

Search for Neutral Higgs Bosons Decaying to Pairs of τ Leptons at $\sqrt{s} = 7$ TeV

By

EVAN KLOSE FRIIS

B.S. (University of California at San Diego) 2005

DISSERTATION

Submitted in partial satisfaction of the requirements for the degree of

DOCTOR OF PHILOSOPHY

in

Physics

in the

OFFICE OF GRADUATE STUDIES

of the

UNIVERSITY OF CALIFORNIA

DAVIS

Approved:

Professor John Conway (Chair)

Professor Robin Erbacher

Professor Mani Tripathi

Committee in Charge

2011

3 Abstract

4 This thesis describes a search for the Higgs boson, a new particle predicted by a theory called
5 the minimal supersymmetric extension to the standard model (MSSM). The standard model
6 of particle physics, the MSSM, and Higgs boson phenomenology are introduced briefly. The
7 search presented in this thesis uses a single final state configuration, in which the Higgs
8 boson decays to two tau leptons, where one tau decays to a muon and neutrinos, and
9 the other decays to pions and a single neutrino. Two new methods are introduced in this
10 analysis, the Tau Neural Classifier tau identification algorithm, and the Secondary Vertex
11 fit tau pair mass reconstruction method. Both methods are discussed in detail. The analysis
12 uses the 2010 dataset from the Compact Muon Solenoid (CMS) experiment, which contains
13 36 pb^{-1} of integrated luminosity at a center of mass energy of 7 TeV. In total, 573 events
14 are selected in the analysis. We fit the observed tau pair mass spectrum and measure the
15 composition of the events. The result is compatible with the standard model expectation.
16 No excess of signal events is observed, and we set an upper limit on cross section times
17 branching ratio of a Higgs boson. This limit is interpreted in the parameter space of the
18 MSSM.

¹⁹ **Acknowledgments**

²⁰

Hooray for everybody.

21 Table of Contents

22	Introduction	1
23	1 The Standard Model and Beyond	3
24	1.1 The Standard Model	3
25	1.1.1 Quantum Electrodynamics and Gauge Invariance	4
26	1.1.2 The Weak Interactions	6
27	1.1.3 Spontaneous Symmetry Breaking	9
28	1.1.4 The Higgs Mechanism	11
29	1.1.5 Electroweak Unification	13
30	1.1.6 Quantum Chromodynamics	18
31	1.2 Beyond the Standard Model	20
32	1.2.1 The Hierarchy Problem	21
33	1.2.2 Supersymmetry	22
34	1.2.3 The Minimal Supersymmetric Extension to the Standard Model	22
35	1.3 Searches for the Higgs Boson	25
36	1.3.1 Standard Model Higgs Boson Phenomenology	25
37	1.3.2 MSSM Higgs Boson Phenomenology	31
38	1.3.3 Results from LEP and Tevatron	32
39	1.3.4 The Physics of the Tau Lepton	37
40	2 The Compact Muon Solenoid Experiment	39
41	2.1 The Large Hadron Collider	40
42	2.2 Solenoid Magnet	40
43	2.3 Charged Particle Tracking Systems	42
44	2.4 Electromagnetic Calorimeter	45
45	2.5 Hadronic Calorimeter	48
46	2.6 Muon System	49
47	2.7 Trigger System	51
48	3 Tau Identification: The Tau Neural Classifier	54
49	3.1 Geometric Tau Identification Algorithms	55
50	3.2 Decay Mode Tau Identification: Motivation	55
51	3.3 The Tau Neural Classifier	56
52	3.3.1 Decay Mode Reconstruction	57
53	3.3.2 Photon Merging	57
54	3.3.3 Quality Requirements	58
55	3.3.4 Performance	59
56	3.3.5 Neural Network Classification	63
57	3.3.6 Neural Network Training	63

58	3.3.7	Discriminants	67
59	3.3.8	Neural Network Performance	68
60	3.4	Summary	75
61	3.5	HPS+TaNC: A Hybrid Algorithm	76
62	3.5.1	Decay Mode Reconstruction	76
63	3.5.2	Hadronic Tau Discrimination	80
64	3.6	Electron and Muon Rejection	81
65	4	Mass Reconstruction: The Secondary Vertex Fit	84
66	4.1	Existing Mass Reconstruction Algorithms	84
67	4.2	The Secondary Vertex Fit	86
68	4.3	Parametrization of Tau Decays	87
69	4.4	Likelihood for Tau Decays	88
70	4.4.1	Likelihood for Reconstructed E_T^{miss}	89
71	4.4.2	Likelihood for Tau Transverse Momentum Balance	90
72	4.4.3	Secondary Vertex Information	92
73	4.5	Performance	94
74	5	Analysis Selections	97
75	5.1	High Level Trigger	97
76	5.2	Particle Identification	98
77	5.2.1	Muons	98
78	5.2.2	Hadronic Taus	99
79	5.2.3	Missing Transverse Energy	100
80	5.3	Event Selections	100
81	6	Data–Driven Background Estimation	105
82	6.1	Background Enriched Control Regions	106
83	6.2	The Fake–rate Method	107
84	6.2.1	Parameterization of Fake–rates	110
85	6.2.2	Measurement of Fake–rates	111
86	6.2.3	Application of Fake–rates	111
87	6.2.4	“Simple” Weight Method	112
88	6.2.5	“CDF–type” Weights	114
89	6.2.6	k–Nearest Neighbor Fake–rate Calculation	117
90	6.2.7	Results of Fake–Rate Background Estimation	118
91	6.3	Template Method	120
92	7	Monte Carlo Corrections	133
93	7.1	Muon Identification Efficiency	133
94	7.2	Hadronic Tau Identification Efficiency	136
95	7.3	Muon and Tau Momentum Scale	138
96	7.4	Missing Transverse Energy Correction	139
97	7.5	Pile-up Event Weighting	140
98	8	Systematics and Limit Extraction	142
99	8.1	Signal Normalization Uncertainties	144
100	8.2	Background Normalization Uncertainties	144

101	8.3 Shape Uncertainties	145
102	8.4 Theory Uncertainties	146
103	8.5 Limit Extraction Method	146
104	9 Results	153
105	9.1 Selected Events	153
106	9.2 Limits on Higgs Boson Production	154
107	9.3 Interpretation in the MSSM	155
108	Conclusions	164
109	Bibliography	164

110 List of Figures

111	1.1	Fermi contact interaction diagram	8
112	1.2	Muon decaying through intermediate gauge boson	8
113	1.3	QCD Feynman Diagrams	19
114	1.4	Loop corrections to Higgs boson mass	21
115	1.5	Higgstrahlung production diagram at e^+e^- colliders	26
116	1.6	Gluon fusion Higgs boson production diagram	27
117	1.7	Vector boson fusion Higgs boson production diagram	27
118	1.8	Parton luminosity comparison of the LHC and Tevatron	28
119	1.9	SM Higgs boson cross sections at the LHC	29
120	1.10	SM Higgs boson branching fractions	29
121	1.11	Cross sections of interest at hadron colliders	30
122	1.12	MSSM Higgs boson production with association b -quarks	31
123	1.13	MSSM Higgs boson cross sections at the LHC	32
124	1.14	LEP SM Higgs boson limit plot	34
125	1.15	Tevatron low mass standard model Higgs boson limit plot	35
126	1.16	Tevatron high mass standard model Higgs boson limit plot	36
127	1.17	LEP MSSM exclusion limits	36
128	1.18	Tevatron MSSM exclusion limits	37
129	2.1	Schematic drawings of the CMS detector	41
130	2.2	Material budget of the CMS tracker	44
131	2.3	Momentum and impact parameter resolutions of CMS tracker	45
132	2.4	Energy resolution of the CMS ECAL	47
133	2.5	Muon system material budget and identification efficiency	50
134	3.1	Visible invariant mass of τ lepton decay products	56
135	3.2	Invariant mass photon pairs in reconstructed π^0 mesons	58
136	3.3	Neutral energy fraction in visible τ decays	59
137	3.4	Tau decay mode reconstruction performance	61
138	3.5	Kinematic dependence of decay mode reconstruction	62
139	3.6	Neural network over-training validation plots	66
140	3.7	Kinematic weighting of training sample	67
141	3.8	Neural network output in each decay mode	70
142	3.9	Performance curves for the neural networks used in the TaNC	71
143	3.10	Tau Neural Classifier performance curves for different p_T ranges	72
144	3.11	Tau Neural Classifier transformation performance	74
145	3.12	Transformed neural network output	75
146	3.13	Tau Neural Classifier performance comparison	77
147	3.14	Tau Neural Classifier kinematic performance	78

148	3.15 Invariant mass distribution of PF photon pairs	80
149	4.1 Coordinate system of the SVfit	89
150	4.2 Effect of p_T -balance term on SVfit performance	92
151	4.3 Effect of the visible p_T requirements on muon and hadronic τ decays	93
152	4.4 Effect of the visible p_T requirements for Z and Higgs boson events	94
153	4.5 Comparison of SVfit with the collinear approximation algorithm	95
154	4.6 Comparison of SVfit with the visible mass observable	96
155	5.1 Distributions of M_T and muon isolation discriminants	102
156	5.2 Reconstruction and distribution of P_ζ discriminant	103
157	6.1 Visible mass distribution of the backgrounds in the signal and control regions	108
158	6.2 SVfit mass distribution of the backgrounds in the signal and control regions	109
159	6.3 p_T and η dependency of tau ID performance	123
160	6.4 Comparison of fake-rate contribution from genuine taus in the simple and CDF methods	125
162	6.5 Muon transverse momentum in the fake-rate method	126
163	6.6 Tau-jet transverse momentum in the fake-rate method	127
164	6.7 Visible mass in the fake-rate method	128
165	6.8 k -Nearest Neighbor classifier example	129
166	6.9 Comparison of visible mass and SVfit mass	130
167	6.10 Comparison of background shapes in the signal and control regions	131
168	6.11 Visible mass distribution in the final fit of the template method	132
169	7.1 Tag-probe muon isolation method	135
170	7.2 Muon isolation correction factors	137
171	7.3 Measurement of hadronic tau identification efficiency	138
172	7.4 Distribution of number of reconstructed primary vertices per event	141
173	9.1 Transverse momentum distributions of muon and tau in the final selected events	157
175	9.2 Distributions of the η and ϕ of the muon and tau candidates in the final selected events	158
176	9.3 Distributions of final selected events	159
178	9.4 Observed and expected limits on Higgs boson $\sigma \times \text{BR}$	162
179	9.5 Excluded regions of MSSM $\tan \beta - m_{A^0}$ parameter space	163
180	9.6 CMS combined exclusion of MSSM $\tan \beta - m_{A^0}$ parameter space	165

List of Tables

182	1.1	Chiral supermultiplets in the MSSM	23
183	1.2	Gauge supermultiplets in the MSSM	23
184	1.3	Higgs boson search channels at LEP	33
185	1.4	Decay modes of the τ lepton	38
186	3.1	Decay mode performance – naive reconstruction	60
187	3.2	Decay mode performance – TaNC reconstruction	60
188	3.3	Neural network training event statistics	64
189	3.4	Variables used in the different TaNC neural networks	83
190	5.1	High Level Trigger paths used to select $\mu + \tau_h$ events	98
191	5.2	Analysis backgrounds that include fake taus	100
192	5.3	Event selection summary	104
193	6.1	Criteria used to select background enriched control regions	121
194	6.2	Comparison of background control region yields in data and the prediction from simulation	122
195	6.3	Fake-rate “simple” method closure test results	124
196	6.4	Fake-rate “CDF” method closure test results	125
197	6.5	Fake-rate method results	129
198	6.6	Fake-rate method predicted yields in like-sign control region	130
199	6.7	Background yields measured using the template method	130
200	7.1	Muon trigger, identification, and isolation correction factors	136
201	8.1	Effect of normalization uncertainties on signal efficiency times acceptance .	147
202	8.2	Correspondence of confidence levels and $2\Delta \ln \mathcal{L}$ intervals	150
203	8.3	Summary of systematic uncertainties	152
204	9.1	Final analysis yield and background expectations	154
205	9.2	Expected signal yields at $\tan \beta = 30$	160
206	9.3	Expected and observed 95% CL $\sigma \times \text{BR}$ upper limits	161
207	9.4	Contributions of different MSSM Higgs boson types at different m_{A^0}	161

209 Introduction

210 This thesis describes a search for the Higgs boson, a new particle predicted by the standard
211 model of particle physics. The search is optimized for a particular extension of the stan-
212 dard model, a theory called the minimal supersymmetric extension to the standard model
213 (MSSM). The analysis uses the 2010 dataset from the Compact Muon Solenoid (CMS) ex-
214 periment, which contains 36 pb^{-1} of integrated luminosity at a center of mass energy of
215 7 TeV. The Higgs boson is hypothesized to be the catalyst of electroweak symmetry break-
216 ing, the phenomenon strongly believed to impart mass to particles that form our natural
217 world.

218 Chapter 1 begins with an introduction to the standard model (SM) of particle physics.
219 Emphasis is given to electroweak symmetry breaking and the Higgs mechanism, the theo-
220 retical phenomena that motivate the presence of a Higgs boson. The theoretical issues which
221 motivated the development of the MSSM are discussed, and a brief introduction is given.
222 Finally, the phenomenology of Higgs bosons in the SM and MSSM is discussed, with an
223 overview of searches for the Higgs boson performed at LEP and the Tevatron.

224 This thesis then documents the development of a complete search for MSSM Higgs
225 bosons at CMS. The CMS experiment is introduced briefly in Chapter 2. Chapters 3 and 4
226 document in detail two fundamental components of the search, an advanced tau identifi-
227 cation algorithm, and a novel method for reconstructing the neutrinos associated to tau
228 decays. The development of these algorithms was motivated by the challenges of this anal-
229 ysis, and precipitated significant improvements in the final result. Finally, in Chapters 5-8,
230 we describe the methods and results of the event selection, background estimation, and the
231 systematic uncertainties, and finally compute an upper limit on the presence of an MSSM
232 Higgs boson.

233 The studies presented herein were part of a larger effort at CMS to search for an MSSM
234 Higgs boson decaying to tau lepton pairs. In addition to the $\mu - \tau_h$ channel described in
235 this thesis, final states with an electronic and hadronic tau decay ($e - \tau$) and electronic and
236 muonic ($e - \mu$) were considered. The combination of all three was used to set a limit on
237 the MSSM [1]. This result has recently been accepted for publication in Physical Review
238 Letters B. At the time of this writing, the CMS analysis sets the world's strongest limit on
239 the MSSM Higgs boson using a direct search.

240

Chapter 1

241

The Standard Model and Beyond

242 1.1 The Standard Model

243 The standard model (SM) is a “theory of almost everything” that describes the interactions
244 of elementary particles. The SM is a quantum field theory, first appearing in its modern
245 form in the middle of the 20th century. The model is the synthesis of the independent
246 theories of electromagnetism, and the weak and strong nuclear forces. Each of these theories
247 was used to describe different phenomena, which each have extremely different strengths
248 and act at different scales. The interaction of light and matter is described by quantum
249 electrodynamics (QED), a relativistic field extension of the theory of electromagnetism.
250 The physics of radioactivity and nuclear decay was described by the Fermi theory of weak
251 interactions and the forces that strong nuclear force binds the nuclei of atoms was described
252 by Yukawa. An overview of these theories will be presented in this chapter.

253 The feature that united the disparate theories into the SM was the application of the
254 principle of local gauge invariance. The principle of gauge invariance first found success in
255 QED, which predicted electromagnetic phenomenon with astounding accuracy. Local gauge
256 invariance is now believed to a fundamental feature of nature that underpins all theories of
257 elementary particles. Furthermore, the development of the complete SM as it is known today
258 was precipitated by Goldstones’s work on spontaneous symmetry breaking [2, 3], which
259 produces an effective Lagrangian with additional massless “Goldstone” bosons. Higgs (and
260 others) [4, 5, 6] developed these ideas into what is ultimately called the “Higgs mechanism,”
261 which uses a combination of new fields with broken symmetry to give mass to the Goldstone
262 bosons.

263 In the 1960s, Glashow [7], Weinberg [8], and Salam [9] developed the above ideas into
 264 the electroweak model, which unified QED with the weak force using intermediate weak
 265 bosons in a gauge theory with symmetry that is spontaneously broken using the Higgs
 266 mechanism. This unified theory has been incredibly experimentally successful and is the
 267 foundation of modern particle theory.

268 1.1.1 Quantum Electrodynamics and Gauge Invariance

269 The theory of QED is a modern extension of Maxwell's theory of electromagnetism, describ-
 270 ing the interaction of matter with light. The development of QED is a result of efforts to
 271 develop a quantum mechanical formulation of electromagnetism compatible with the the-
 272 ory of special relativity. QED is a *gauge* theory, which means that the physical observables
 273 are invariant under local gauge transformations. Requiring local gauge invariance gives rise
 274 to a “gauge” field, which can be interpreted as particles that are exchanged during an
 275 interaction.

276 In the following, we first describe the Dirac equation for a free electron, which is the
 277 relativistic extension of the Schroedinger equation for spin 1/2 particles. We then show that
 278 requiring the corresponding Lagrangian of the free charged particle to be invariant under
 279 local gauge transformations creates an effective gauge boson field. This “gauge field” creates
 280 terms in the Lagrangian that represent interactions between the particles.

The Dirac equation is the equation of motion of a free spin 1/2 particle of mass m and
 is derived from the energy–momentum relationship of relativity

$$p^\mu p_\mu - m^2 c^2 = 0. \quad (1.1)$$

Dirac sought to express this relationship in the framework of quantum mechanics by applying the transformation

$$p_\mu \rightarrow i\hbar\partial_\mu \quad (1.2)$$

to equation Equation 1.1, but with the requirement that the resulting equation be first

order in time.¹ To achieve this, Dirac factorized Equation 1.1 into

$$(\gamma^\kappa p_\kappa + mc)(\gamma^\mu p_\mu - mc) = 0, \quad (1.3)$$

where γ^μ is a set of four 4×4 matrices referred to as the Dirac matrices. The equation of motion is obtained by choosing either term (they are equivalent) from the left hand side of Equation 1.3 and making the substitution in Equation 1.2.

$$i\hbar\gamma^\mu\partial_\mu\psi - mc\psi = 0. \quad (1.4)$$

- 281 The solutions ψ of the Dirac equation are called “Dirac spinors,” and represent the quantum
- 282 mechanical state of spin 1/2 particles.

The Lagrangian corresponding to the Dirac equation (1.4) is

$$\mathcal{L} = \bar{\psi}(i\hbar c\gamma^\mu\partial_\mu - mc^2)\psi, \quad (1.5)$$

where ψ is the spinor field of the particle in question, \hbar is Planck’s constant, c the speed of light, and γ^μ are the Dirac matrices. As $\bar{\psi}$ is the Hermitian conjugate of ψ , the Lagrangian is invariant under the global gauge transformation

$$\psi' \rightarrow e^{i\theta}\psi. \quad (1.6)$$

The Lagrangian is invariant under *local* gauge translations if θ can be defined differently at each point in space, i.e. if $\theta = \theta(x)$ in Equation 1.6. However, as the derivative operator ∂_μ in Equation 1.5 does not commute with $\theta(x)$, the Lagrangian must be modified to satisfy local gauge invariance. This modification is accomplished with the use of a “gauge covariant derivative.” By making the replacement

$$\partial_\mu \rightarrow D_\mu = \partial_\mu - \frac{ie}{\hbar}A^\mu$$

in Equation 1.5, where $A^\mu = \partial^\mu\theta(x)$ and e is the electric charge, the Lagrangian becomes

¹A detailed discussion of this topic is available in [10].

locally gauge invariant:

$$\mathcal{L} = \bar{\psi}(i\hbar c\gamma^\mu D_\mu - mc^2)\psi. \quad (1.7)$$

The difference between the locally (1.7) and the globally (1.5) gauge invariant Lagrangian is then

$$\mathcal{L}_{int} = \frac{e}{\hbar}\bar{\psi}\gamma^\mu\psi A_\mu.$$

This term can be interpreted as the coupling between the particle and the gauge boson (force carrier) fields. The coupling is proportional to the constant e , which is associated with the electric charge. This is consistent with the experimental observation that particles with zero electric charge do not interact electromagnetically with each other. In this interpretation, the electromagnetic force between two charged particles is caused by the exchange of gauge bosons (photons). The existence of this “minimal coupling” is *required* if the Lagrangian is to satisfy local gauge invariance. The addition of a term with the gauge Field Strength Tensor to represent the kinetic term of the gauge (photon) field yields the QED Lagrangian:

$$\mathcal{L}_{QED} = \bar{\psi}(i\hbar c\gamma^\mu D_\mu - mc^2)\psi - \frac{1}{4\mu_0}F_{\mu\nu}F^{\mu\nu}.$$

283 The gauge symmetry group of QED is $U(1)$, the unitary group of degree 1. This sym-
 284 metry can be visualized as a rotation of a two-dimensional unit vector. (The application
 285 of the gauge transformation $e^{i\theta}$ rotates a number in the complex plane.) In a gauge theory
 286 the symmetry group of the gauge transformation defines the behavior of the gauge bosons
 287 and thus the interactions of the theory.

288 1.1.2 The Weak Interactions

The theory of Weak Interactions was created to describe the physics of radioactive decay. The first formulation of the theory was done by Fermi [11] to explain the phenomenon of the β decay of neutrons. The initial theory was a four-fermion “contact” theory. In a contact theory, all four fermions come involved in the β -decay are connected at a single vertex. The

Fermi theory Hamiltonian for the β -decay of a proton is then [12]

$$H = \frac{G_\beta}{\sqrt{2}} [\bar{\psi}_p \gamma_\mu (1 - g_A \gamma_5) \psi_n] [[\bar{\psi}_e \gamma^\mu (1 - \gamma_5) \psi_\nu] + h.c., \quad (1.8)$$

where G_β is the Fermi constant and g_A is the relative fraction of the interaction with axially Lorentz structure. The value of g_A was determined experimentally to be 1.26. One of the most notable things discovered about the weak force is that weak interactions violate parity; that is, the physics of the interaction change (or become disallowed) under inversion of the spatial coordinates. This is evidenced by the $(1 - \gamma_5)$ term in Equation 1.8. This term is the “helicity operator”; the left and right “handed” helicity states are eigenstates states of this term.

$$h = (1 - \gamma_5)/2$$

$$\begin{aligned} h\psi_R &= \frac{1}{2}\psi_R \\ h\psi_L &= -\frac{1}{2}\psi_L \end{aligned}$$

It is observed that only left-chiral neutrinos (or right-chiral anti-neutrinos) participate in the weak interaction.

The Fermi interaction can describe both nuclear β decay ($p \rightarrow n + e^+ + \bar{\nu}_e$) as well as the decay of a muon into an electron ($\mu \rightarrow \nu_\mu + e + \bar{\nu}_e$, Figure 1.1). Furthermore, the coupling constant G is found to be a *universal* constant in weak interactions, in that it is the same for interactions regardless of the particle species participating in the interaction. That is, $G_\mu = G_e = G_F$. Using an Hamiltonian analogous to Equation 1.8 for muon decay, the decay amplitude M is found to be

$$M = \frac{G_F}{\sqrt{2}} \left[\bar{u}_{\nu_\mu} \gamma_\rho \frac{1 - \gamma_5}{2} u_\mu \right] \left[\bar{u}_{\nu_e} \gamma_\rho \frac{1 - \gamma_5}{2} u_e \right]. \quad (1.9)$$

However, the contact interaction form of Fermi’s theory is not complete. When applied to scattering processes, the interaction violates unitarity: the calculated cross section grows with the center of mass energy, so that for some energy the probability for an interaction

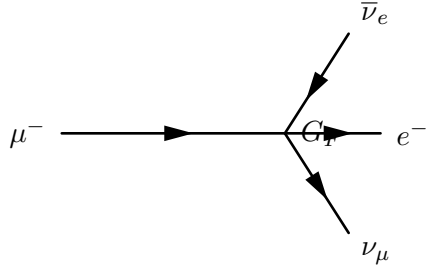


Figure 1.1: Feynmann diagram of muon decay in Fermi contact interaction theory.

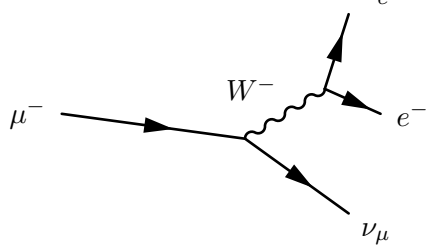


Figure 1.2: Feynmann diagram of muon decay proceeding through an intermediate gauge boson W^- .

- ³⁰¹ is greater than one. Furthermore, the techniques successfully used to “renormalize”² QED
³⁰² fail when applied to the Fermi interaction.

The first attempt to solve the problems with the Fermi theory was made by introducing an intermediate weak boson [7]. The contact interaction is replaced by a massive propagator, the W^\pm bosons. The decay of a muon to an electron and two neutrinos then proceeds as pictured in Figure 1.2 with an amplitude given [12] by

$$M = - \left[\frac{g}{\sqrt{2}} \bar{u}_{\nu_\mu} \gamma_\rho \frac{1 - \gamma_5}{2} u_\mu \right] \frac{-g^{\rho\sigma} + \frac{q^\rho q^\sigma}{M_W^2}}{q^2 - M_W^2} \left[\frac{g}{\sqrt{2}} \bar{u}_{\nu_e} \gamma_\rho \frac{1 - \gamma_5}{2} u_e \right]. \quad (1.10)$$

The presence of the large gauge boson mass term M_W^2 in the denominator of the central term of Equation 1.10 is the reason why the contact interaction original formulated by Fermi effectively described low-energy weak phenomenon. When the momentum transfer q in the interaction is small compared to M_W , the effect of the propagator is an effective constant. In the low energy limit, the full propagator in Equation 1.10 is equivalent to the Fermi contact interaction in 1.9 as

$$\lim_{q/M_W \rightarrow 0} \frac{g^2}{8(q^2 - M_W^2)} = \frac{G_F}{\sqrt{2}}. \quad (1.11)$$

²Renormalization of quantum field theories is a broad topic beyond the scope of this thesis. Briefly, the process involves “absorbing” infinite divergences that occur in higher-order interactions into physical observables [10].

303 Unfortunately, the weak boson exchange model did not solve the problems of unitarity
 304 and renormalizability in the weak interaction. However, the form of the boson-exchange
 305 propagator in Equation 1.11 suggests the observed “weakness” of the weak interactions is
 306 an artifact of the presence of the massive propagator (M_W) and that the fundamental scale
 307 of the interaction g is the same order of magnitude as that of QED, $g \approx e$. This observation
 308 lead to the unification of the electromagnetic and weak forces, which we describe in the
 309 next sections.

310 1.1.3 Spontaneous Symmetry Breaking

311 In the early 1960s Glashow, Weinberg, and Salam published a series of papers describing
 312 how the electromagnetic and weak forces could be unified into a common “electroweak”
 313 force. The fact that at low energy the electromagnetic and weak forces appear to be sep-
 314 arate phenomena is due to the fact that the symmetry of the electroweak gauge group is
 315 “spontaneously broken.” Modern field theories (both the SM and beyond) are predicated
 316 on the idea that the all interactions are part of a single, unified symmetry group and the
 317 differences between various scales (electromagnetic, weak, etc.) at lower energies are due to
 318 the unified symmetry being spontaneously broken.

A symmetry of a Lagrangian is spontaneously broken when the ground state, or vacuum, is at a value about which the Lagrangian is not symmetric. In quantum field theories, a particle is interpreted as quantized fluctuations of its corresponding field about some constant (vacuum) ground state. The “effective” Lagrangian that we observe in the (low energy) laboratory would be the expansion of the Lagrangian about this stable point. The effective Lagrangian no longer obeys the original symmetry, which has been “broken.” We give a brief example of the phenomenological effects of a spontaneously broken symmetry in a toy model, following the treatment in [12].

$$\mathcal{L} = \frac{1}{2}\partial_\mu\phi_1\partial^\mu\phi_1 + \frac{1}{2}\partial_\mu\phi_2\partial^\mu\phi_2 - V(\phi_1^2 + \phi_2^2) \quad (1.12)$$

319 The toy Lagrangian in Equation 1.12 has a global $U(1)$ ³ symmetry and consists of two
 320 real-valued fields, ϕ_1 and ϕ_2 . The particle mass spectra of the theory is given by expanding
 321 the field potential $V(\phi_1, \phi_2)$ about its minimum, $(\phi_1^{min}, \phi_2^{min})$. The first three terms in the
 322 series are found by

$$\begin{aligned} V(\phi_1, \phi_2) &= V(\phi_1^{min}, \phi_2^{min}) + \sum_{a=1,2} \left(\frac{\partial V}{\partial \phi_a} \right)_0 (\phi_a - \phi_a^{min}) \\ &+ \frac{1}{2} \sum_{a,b=1,2} \left(\frac{\partial^2 V}{\partial \phi_a \partial \phi_b} \right)_0 (\phi_a - \phi_a^{min})(\phi_b - \phi_b^{min}) + \dots \end{aligned} \quad (1.13)$$

Since at the minimum the partial derivative of V is zero with respect to all fields, the second term in Equation 1.13 is zero. The third term determines the masses of the particles in the theory. Since a mass term for a particle corresponding to a field ϕ_n in the Lagrangian appears as $\frac{1}{2}m^2\phi_n\phi_n$, we can identify

$$\left(\frac{\partial^2 V}{\partial \phi_a \partial \phi_b} \right)_{\phi^{min}} \quad (1.14)$$

323 as the a th row and b th column in the “mass matrix”. Off diagonal terms in this matrix
 324 indicate mixing terms between the fields. By diagonalizing the matrix, the combinations of
 325 fields which correspond to the physical particles (the “mass eigenstates”) are found. The
 326 m^2 of each particle is then the corresponding entry in the diagonal of the mass matrix.

The particle spectra of the model depends heavily on the form of the potential. An illustrative form (that is renormalizable and bounded from below) of a possible configuration for the potential V in Equation 1.12 is

$$V(\phi_1^2, \phi_2^2) = \frac{m^2}{2}(\phi_1^2 + \phi_2^2) + \frac{\lambda}{4}(\phi_1^2 + \phi_2^2)^2. \quad (1.15)$$

327 If the parameters m^2 and λ are both positive, then the minimum of V is at the origin ($\phi_1 =$

³Technically, the symmetric transformation is

$$\begin{pmatrix} \phi_1 \\ \phi_2 \end{pmatrix} \rightarrow \begin{pmatrix} \phi'_1 \\ \phi'_2 \end{pmatrix} = \begin{pmatrix} \cos \theta & -\sin \theta \\ \sin \theta & \cos \theta \end{pmatrix} \begin{pmatrix} \phi_1 \\ \phi_2 \end{pmatrix},$$

which is $\mathcal{O}(2)$. However, this transformation is equivalent to $U(1)$, as the two real fields ϕ_1 and ϕ_2 can be seen to correspond to the real and imaginary parts of a complex field ϕ that does transform according to $U(1)$.

328 $\phi_2 = 0$). In this case, the mass matrix term in Equation 1.13 takes the form $\left(\frac{\partial^2 V}{\partial \phi_a \partial \phi_b}\right)_0 =$
 329 $\frac{m^2}{2} \delta_{ab}$, where δ_{ab} is the Kronecker delta function. Therefore the mass matrix is already
 330 diagonalized, and the ϕ_1 and ϕ_2 both correspond to particles with mass m . If the m^2
 331 parameter in Equation 1.15 is negative, the spectrum is dramatically different. After making
 332 the replacement $m^2 = -\mu^2 (\mu^2 > 0)$, the extrema of V are no longer unique. The requirement
 333 of $\frac{\partial V}{\partial \phi_i} = 0$ for all i is satisfied in two cases:

$$(\phi_1^{min}, \phi_2^{min}) = (0, 0) \quad (1.16)$$

$$(\phi_1^{min})^2 + (\phi_2^{min})^2 = \frac{\mu^2}{\lambda} = \nu^2. \quad (1.17)$$

If the vacuum state is defined at the point in Equation 1.16, the symmetry is unbroken and the mass spectra is unchanged. However, the system is unstable at this point, as it is a local maximum. The true global minimum is defined as the set of points which satisfy Equation 1.17, which form a continuous circle in $\phi_1 - \phi_2$ space (and is therefore infinitely degenerate). We can choose any point on the circle as the vacuum expectation value (VEV). If the point $(\phi_1^{min} = \nu, \phi_2^{min} = 0)$ ⁴ is chosen, evaluating Equation 1.14 yields the mass matrix

$$\left(\frac{\partial^2 V}{\partial \phi_a \partial \phi_b}\right)_{\phi^{min}} = \begin{pmatrix} v^2 & 0 \\ 0 & 0 \end{pmatrix}.$$

334 Breaking the symmetry has changed the mass spectrum of the physical particles in the
 335 model. There is now a massive particle with $m = v^2$ and a massless particle. This massless
 336 particle is called the “Goldstone boson.” Goldstone found [2] that a massless particle appears
 337 for each generator in the symmetry group that is broken.

338 1.1.4 The Higgs Mechanism

339 As in Section 1.1.1, extending the gauge symmetry requirement to be *locally* invariant
 340 creates interesting consequences for models that have spontaneously broken symmetry. This
 341 gives rise to the “Higgs mechanism,” which we overview here. For simplicity we will again

⁴The point chosen for the VEV here is not arbitrary. One can chose any point that satisfies Equation 1.17 as the VEV. However, after the mass matrix is diagonalized, there will always be one physical field with a VEV= ν and one with a VEV= 0. Therefore the physical content of the theory does not depend on the choice of VEV.

³⁴² consider a model with $U(1)$ symmetry. The model is identical to the one presented in
³⁴³ Section 1.1.3, with two exceptions. First, we express the two real fields ϕ_1 and ϕ_2 as a single
³⁴⁴ complex-valued field ϕ . Second, the model is required to be locally $U(1)$ invariant, and so
³⁴⁵ uses the gauge-covariant derivatives, minimal coupling to the gauge field, and contains the
³⁴⁶ kinetic term for the gauge field, as discussed in Section 1.1.1. The unbroken Lagrangian is

$$\mathcal{L} = -\frac{1}{4}F_{\mu\nu}F^{\mu\nu} + (D_\mu\phi^*)(D^\mu\phi) - V(\phi^*\phi) \quad (1.18)$$

$$V(\phi^*\phi) = -\mu^2\phi^*\phi + \lambda(\phi^*\phi)^2, \quad (1.19)$$

³⁴⁷ where $F_{\mu\nu}$ is related to the gauge field by $F_{\mu\nu} = \partial_\mu A_\nu - \partial_\nu A_\mu$. The Lagrangian is invariant
³⁴⁸ under the local $U(1)$ gauge transformation

$$\begin{aligned} \phi \rightarrow \phi' &= e^{-i\alpha(x)}\phi \\ A_\mu \rightarrow A'_\mu &= A_\mu - \frac{1}{2}\partial_\mu\alpha(x). \end{aligned}$$

The potential is minimized when $\phi^*\phi = \frac{\mu^2}{2\lambda}$. To simplify the algebra, we can re-parameterize the field into a real part $\eta(x)$ defined about ν , the minimum of V , and a complex phase parameterized by $\theta(x)/\nu$

$$\phi(x) = \frac{1}{\sqrt{2}}(\nu + \eta(x))e^{i\theta(x)/\nu}. \quad (1.20)$$

³⁴⁹ If the gauge transform is chosen to be $\alpha(x) = \theta(x)/\nu$, the fields of are defined in the so-called
³⁵⁰ “unitary gauge”⁵ and have the special forms

$$\begin{aligned} \phi(x) \rightarrow \phi'(x) &= \frac{1}{\sqrt{2}}(\nu + \eta(x)) \\ A_\mu(x) \rightarrow B_\mu(x) &= A_\mu(x) - \frac{1}{e\nu}\partial_\mu\theta(x) \end{aligned} \quad (1.21)$$

³⁵¹ The kinetic term of the gauge field $F_{\mu\nu}$ is invariant under this transformation. If the gauge
³⁵² transformations of Equation 1.21 are substituted into the Lagrangian (1.18) the effective

⁵In the unitary gauge, the choice of gauge ensures that the mass matrix is diagonalized.

353 Lagrangian at the minimum of V is

$$\begin{aligned}\mathcal{L} &= \frac{1}{2}\partial_\mu\eta\partial^\mu\eta - \mu^2\eta^2 \\ &- \frac{1}{4}F_{\mu\nu}F^{\mu\nu} + \frac{1}{2}(e\nu)^2B_\mu B^\mu \\ &+ \frac{1}{2}e^2B_\mu B^\mu\eta(\eta + 2\nu) - \lambda\nu\eta^3 - \frac{\lambda}{4}\eta^4.\end{aligned}\quad (1.22)$$

354 The breaking of the original symmetry has dramatically altered the physical consequences
355 of the model. In its unbroken form, the model described by Equation 1.18 would produce
356 two real massive particles and one massless gauge boson mandated by local gauge invari-
357 ance. After symmetry breaking, the effective Lagrangian in Equation 1.22 contains a massive
358 scalar η with $m = \sqrt{2\mu^2}$ and a *massive* gauge boson B_μ with mass $m = \sqrt{2}e\nu$. By acquiring
359 a mass, the gauge boson B_μ has acquired the degree of freedom (as it can now be longitudi-
360 nally polarized) previously associated to the second degree of freedom in the scalar ϕ field.
361 This phenomenon, known as the Higgs mechanism, is a simplified version of the techniques
362 successfully used to unify the electromagnetic and weak forces that we will discuss in the
363 next section.

364 1.1.5 Electroweak Unification

365 In the 1960s, the ideas of local gauge invariance in field theories, spontaneous symme-
366 try breaking, and the Higgs mechanism were combined by Glashow [7], Weinberg [8] and
367 Salam [9] to form the unified theory of electroweak interactions, the nucleus of the SM. This
368 model successfully unified the electromagnetic and weak interactions into a unified theory
369 with a larger symmetry group. The reason for the empirically observed difference in scales
370 between two interactions is due to the larger, unified symmetry group being broken. This
371 broken symmetry creates heavy gauge bosons via the Higgs mechanism, whose large mass
372 decreases the strength of “weak” interactions at low energy, as discussed in Section 1.1.2.
373 The model successfully predicted the existence and approximate masses of the weak force
374 carriers, the W^\pm and Z bosons. These particles were later observed [13, 14, 15, 16] with the
375 predicted masses at the UA1 and UA2 experiments.

376 To provide a simple introduction to the mechanisms of the model, we will start with a
 377 model that includes only one family of leptons, the electron e and its associated neutrino
 378 ν_e . Following once again the treatment of [12], we describe the representation of the e and
 379 ν_e in the chosen symmetry group of the model. We then construct a locally gauge invariant
 380 Lagrangian with spontaneously broken symmetry, and examine the particle content of the
 381 resulting model.

The form of the charged current $J_\mu(x) = \bar{u}_{\nu_e} \gamma_\rho \frac{1-\gamma_5}{2} u_e$ in the weak interaction amplitudes (1.9) indicates that the left-handed electron and neutrino (remember that the $(1-\gamma_5)$ kills any right-handed spinors) can be combined into a doublet L of $SU(2)$.

$$L = \frac{1-\gamma_5}{2} \begin{pmatrix} \nu_e \\ e^- \end{pmatrix} = \begin{pmatrix} \nu_e \\ e^- \end{pmatrix}_L \quad (1.23)$$

382 The operators that operate on “weak isospin,” the quantum of $SU(2)_L$, are

$$\tau^+ = \frac{\tau^1 + i\tau^2}{2} = \begin{pmatrix} 0 & 1 \\ 0 & 0 \end{pmatrix} \quad (1.24)$$

$$\tau^- = \frac{\tau^1 - i\tau^2}{2} = \begin{pmatrix} 0 & 0 \\ 1 & 0 \end{pmatrix}, \quad (1.25)$$

where the τ^i are the Pauli matrices. The weak currents J_μ^\pm can be written by combining Equations 1.23–1.25

$$J_\mu^\pm = \bar{L} \gamma_\mu \tau^\pm L. \quad (1.26)$$

383 Since τ^1 , τ^2 , and τ^3 are the generators of the $SU(2)$ group, we can complete the group
 384 by adding a neutral current to the charged currents of Equation 1.26. The τ^3 generator is

385 diagonal, so the charge of the current is zero and no mixing of the fields occur:

$$\begin{aligned}
 J_\mu^3 &= \bar{L} \gamma_\mu \frac{\tau^3}{2} L \\
 &= \bar{L} \gamma_\mu \frac{1}{2} \begin{pmatrix} 1 & 0 \\ 0 & -1 \end{pmatrix} L \\
 &= \frac{1}{2} \bar{\nu}_e \gamma_\mu \nu_e - \frac{1}{2} \bar{e}_L \gamma_\mu e_L.
 \end{aligned} \tag{1.27}$$

386 Naively one might hope that the neutral current of Equation 1.27 would correspond to the
 387 electromagnetic (photon) current of QED. However, this is impossible for two reasons. First,
 388 the right-handed component e_R does not appear in the current, so this interaction violates
 389 parity, a known symmetry of the electromagnetic interactions. Second, the current couples to
 390 neutrinos, which have no electric charge. Therefore, the “charge” corresponding to the $SU(2)$
 391 gauge symmetry generators $T^i = \int J_0^i(x) d^3x$ cannot be that of the QED, and the gauge
 392 group must be enlarged to include an additional $U(1)$ symmetry. The generator of the new
 393 symmetry must commute with the generators of the $SU(2)_L$ group. The symmetry cannot
 394 be directly extended with $U(1)_{em}$ as the electromagnetic charge $Q = \int (e_L^\dagger e_L + e_R^\dagger e_R) d^3x$
 395 does not commute with T^i . The solution is to introduce the “weak hypercharge” $\frac{Y}{2} = Q - T^3$,
 396 which commutes the generators of $SU(2)_L$. Thus the symmetry group of the electroweak
 397 model is $SU(2)_L \times U(1)_Y$.

398 The $SU(2)_L \times U(1)_Y$ gauge invariant Lagrangian is written

$$\begin{aligned}
 \mathcal{L} &= \bar{L} i \gamma^\mu (\partial_\mu - ig \frac{\vec{\tau}}{2} \cdot \vec{A}_\mu + \frac{i}{2} g' B_\mu) L \\
 &+ \bar{R} i \gamma^\mu (\partial_\mu + \frac{i}{2} g' B_\mu) R \\
 &- \frac{1}{4} F_{\mu\nu}^i F^{i\mu\nu} - \frac{1}{4} B_{\mu\nu} B^{\mu\nu}.
 \end{aligned}$$

399 As R is a singlet in $SU(2)$, it does not couple to the $SU(2)$ gauge bosons A_μ^i . For this
 400 Lagrangian to correspond to empirical observations at low energy, the $SU(2)_L \times U(1)_Y$
 401 must be broken. As $U(1)_{em}$ symmetry is observed to be good symmetry at all scales the
 402 broken Lagrangian must be invariant under $U(1)_{em}$.

403 To accomplish the symmetry breaking, we introduce a new $SU(2)$ doublet of complex

⁴⁰⁴ Higgs fields ϕ that have hypercharge $Y = 1$, and contribute \mathcal{L}_S to the Lagrangian:

$$\begin{aligned}\phi &= \begin{pmatrix} \phi^+ \\ \phi^0 \end{pmatrix} \\ \mathcal{L}_S &= (D_\mu \phi)^\dagger (D^\mu \phi) - V(\phi^\dagger \phi),\end{aligned}$$

where D_μ is the gauge covariant derivative containing couplings to both the $SU(2)_L$ and $U(1)_Y$ gauge fields, and V has a form analogous to V in Equation 1.19. At this point we also add $SU(2)_L \times U(1)_Y$ invariant “Yukawa” terms

$$\mathcal{L}_Y = -G_e (\bar{L} \phi R + \bar{R} \phi^\dagger L) + h.c. \quad (1.28)$$

⁴⁰⁵ to the Lagrangian which couple the fermions (L and R) to the Higgs field. After symmetry ⁴⁰⁶ breaking these terms will allow the fermions to acquire masses. By choosing the m^2 and λ ⁴⁰⁷ parameters of V appropriately, the new ϕ field acquires a non-zero VEV and the symmetry ⁴⁰⁸ is spontaneously broken.

At the minimum of V , the Higgs field satisfies $\phi^\dagger \phi = \frac{\nu^2}{2}$ and the Higgs fields has a VEV of

$$\phi_{min} = \begin{pmatrix} 0 \\ v/\sqrt{2} \end{pmatrix}.$$

The new symmetry of the model can be confirmed by looking at the action of the different symmetry generators on the VEV. If the generator acting on the vacuum state has a non-zero value, then the corresponding symmetry is broken. It can then be seen that the original symmetry generators T^+ , T^- , T^3 , and Y are all broken. The vacuum *is* invariant under Q , the generator of $U(1)_{em}$:

$$Q\phi_{min} = (T^3 + \frac{Y}{2}) \begin{pmatrix} 0 \\ v/\sqrt{2} \end{pmatrix} = 0,$$

⁴⁰⁹ so the broken Lagrangian contains the correct symmetry properties.

The gauge boson content of the electroweak interaction is obtained by parameterizing

the Higgs field in the magnitude–phase notation of Equation 1.20 and using the unitary gauge (see Section 1.1.4), where the gauge transformation is chosen so Higgs field is real.

The Higgs scalar doublet is then

$$\phi' = \begin{pmatrix} 0 \\ \frac{1}{\sqrt{2}}(\nu + H(x)) \end{pmatrix} = \frac{1}{\sqrt{2}}(\nu + H(x))\chi.$$

The mass spectrum of the gauge bosons of the electroweak interaction (the photon, W^\pm , and Z) is determined by the interaction of the gauge field terms in the covariant derivative with the non-zero vacuum expectation value ν of the scalar Higgs field ϕ

$$(D_\mu \phi)' = (\partial_\mu - ig \frac{\vec{\tau}}{2} \cdot \vec{A}'_\mu - \frac{i}{2} g' B'_\mu) \frac{1}{\sqrt{2}}(\nu + H)\chi.$$

The terms in the expansion of the kinetic term of the Higgs field that are quadratic in ν^2 and a gauge boson field give the mass associated to that boson, and can be written as

$$\mathcal{L}_{mass} = \frac{\nu^2}{8}(g^2 A'_\mu{}^1 A'^1{}^\mu + g^2 A'_\mu{}^2 A'^2{}^\mu + (g A'_\mu{}^3 - g' B'_\mu)^2). \quad (1.29)$$

The $A'_\mu{}^1$ and $A'_\mu{}^2$ fields can be combined such that the first two terms in Equation 1.29 are equivalent to the mass term of a charged boson

$$W_\mu^\pm = \frac{A'_\mu{}^1 \mp i A'_\mu{}^2}{2}.$$

410 This is the familiar W^\pm boson of β and muon decay, and has mass $M_W = \frac{1}{2}g\nu$. The third
411 term in Equation 1.29 can be written in matrix form and then diagonalized into mass
412 eigenstates

$$\begin{aligned} & \frac{\nu^2}{8} (A'_\mu{}^3 \ B'_\mu) \begin{pmatrix} g^2 & -gg' \\ -gg' & g'^2 \end{pmatrix} \begin{pmatrix} A'^3{}^\mu \\ B'^\mu \end{pmatrix} \\ & \rightarrow \frac{\nu^2}{8} (Z_\mu \ A_\mu) \begin{pmatrix} g^2 + g'^2 & 0 \\ 0 & 0 \end{pmatrix} \begin{pmatrix} Z^\mu \\ A^\mu \end{pmatrix}, \end{aligned}$$

giving a massive Z boson with

$$M_Z = \frac{\nu}{2} \sqrt{g^2 + g'^2} \quad (1.30)$$

and the massless photon A_μ of QED. The mass of the Z is related to the mass of the W^\pm by

$$M_Z \equiv \frac{M_W}{\cos \theta_W},$$

where θ_W is the “Weinberg angle,” which must be determined from experiment. As the Fermi contact interaction of Section 1.1.2 is an effective theory of the weak sector, the value of G_F obtained from β and muon decay experiments give clues to the masses of the W and Z .

$$\begin{aligned} M_W &= \frac{1}{2} \left(\frac{e^2}{\sqrt{2} G_F} \right)^{(1/2)} \frac{1}{\sin \theta_W} \approx \frac{38 \text{ GeV}}{\sin \theta_W} > 37 \text{ GeV} \\ M_Z &\approx \frac{76 \text{ GeV}}{\sin 2\theta_W} > 76 \text{ GeV}. \end{aligned}$$

The discovery of the W [13, 14] and Z [15, 16] at the CERN SPS was a huge triumph for the electroweak model.

The model that is presented in this section assumes only one species of leptons, the electron and its associated neutrino. The electroweak model is trivially extended [12] to include the other species (μ, τ) of leptons and the three families of quarks. The masses of the fermions are determined by the Yukawa terms in Equation 1.28. Each particle species has a Yukawa term relating the Higgs VEV to its mass that is not constrained by the theory, and must be determined by experiment.

1.1.6 Quantum Chromodynamics

After electroweak unification, the SM is completed by the theory of quantum chromodynamics (QCD), which describes the interactions between quarks and gluons. QCD is a broad field and only a brief introduction to its motivations and the phenomenology relevant to the analysis presented in this thesis is contained in this section. The existence of quarks as composite particles of hadrons was first proposed by Gell–Man and Zweig to explain the spectroscopy of hadrons. QCD is an $SU(3)$ non–Abelian gauge theory which is invariant

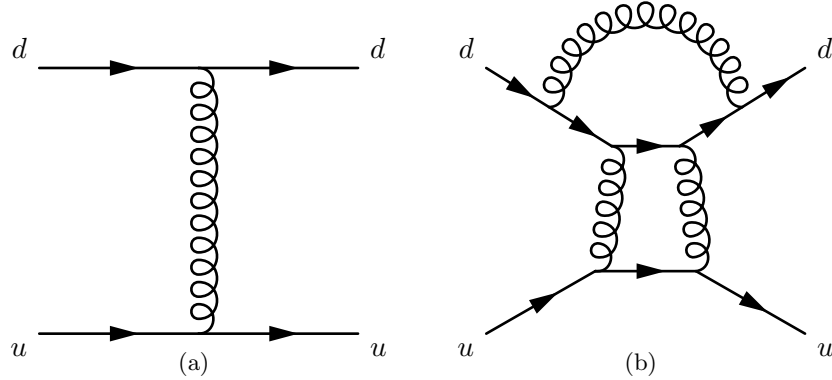


Figure 1.3: Feynman diagrams of a first–order (a) QCD interaction and a multi–loop (b) QCD interaction that have the same initial and final states. Each internal gluon propagator contributes a factor of g_s , the strong coupling constant, to the the amplitude. Since $g_s > 1$, multi–loop diagrams have a larger contribution than simpler diagrams.

under *color* transformations. Color is the charge of QCD and comes in three types: red, green and blue. The gauge boson that carries the force of QCD is called the gluon, which is massless as the $SU(3)_c$ color symmetry is unbroken.

There are three marked differences between the photon of QED and the gluon of QCD. First, the gluon carries a color charge, while the photon is electrically neutral. This has the consequence that a gluon can couple to other gluons. Secondly, it is found that no colored object exists in nature. The corollary of this is that it is believed to be impossible for a single “bare” quark or gluon to be observed. The mechanism that gives rise to this effect is called “color confinement.” The strength of the strong force between two interacting colored objects increases with distance. If two colored objects in a hadron are pulled apart, the energy required to separate them will eventually be large enough to produce new (anti-)colored objects, resulting in two (or more) colorless hadrons. Finally, at low energy, QCD is non–perturbative. What this means in practice is that when computing an amplitude from a QCD Feynman diagram, additional gluon interactions contribute a value greater than one. The dominance of multi–loop diagrams is illustrated in Figure 1.1.6. Thus higher order diagrams with many internal loops cannot be ignored in QCD as is possible in the QED or Electroweak models. In practice what is done is to “factorize” QCD interaction amplitudes into a perturbative (high–energy) part and a non–perturbative part. The perturbative portion is calculable using the Feynman calculus; the non–perturbative must be estimated from parameterization functions that are experimentally measured.

452 The practical consequence of color confinement to a physicist studying electroweak phe-
 453 nomenon at a high–energy particle physics experiment is the production of quark and gluon
 454 “jets,” which are high multiplicity sprays of particles observed in the detector. In a proton–
 455 proton collision, quarks and gluons can be knocked off the incident protons. These quarks
 456 and gluons immediately “hadronize,” surrounding themselves with additional hadrons, the
 457 majority of which are charged and neutral pions. Heavier quarks, such as the charm, beauty,
 458 and top quarks undergo a flavor–changing weak decays, which can give rise to structure
 459 (leptons, sub–jets) within the jet. Furthermore, due to the relative strength of the strong
 460 interaction compared that of the electroweak, collision events involving only strong inter-
 461 actions are produced at rates many orders of magnitudes larger than that of electroweak
 462 interactions. This makes life difficult for physicists studying the electroweak force at hadron
 463 colliders. Sections 2.7, and Chapters 3 and 5 will discuss the techniques used to identify and
 464 remove QCD events from the data at different stages of the analysis.

465 1.2 Beyond the Standard Model

466 The standard model is one of the most successful theories of the natural world ever created.
 467 The predictions of the SM have been tested to many orders of magnitude and no experiment
 468 to date⁶ has found a result statistically incompatible with the SM. However, there is a
 469 general consensus in the physics community that the SM is not complete. It is believed that
 470 it is only an effective theory that is valid below some energy scale Λ . Above this energy,
 471 there must exist some other “new physics,” which unifies the forces of the SM and correctly
 472 describes the natural world at all scales, while maintaining equivalence to the SM at low
 473 energy. This concept is analogous to the relationship between the effective Fermi contact
 474 theory of Section 1.1.2 and the unified electroweak theory of Section 1.1.5. The size of
 475 the cutoff scale Λ is estimated [12] to be $\mathcal{O}(10^{15})$ GeV for a unified theory with $SU(5)$
 476 symmetry and even larger, $\mathcal{O}(10^{19})$ GeV = M_{planck} if the theory is unified with gravity.

477 There are many compelling reasons that indicate that the SM is incomplete. One is
 478 the fact that the model does not include gravity, which has still not been successfully

⁶The SM predicts that lepton number is a good quantum number and that the neutrinos are massless. It has recently been found that the neutrinos do have non–zero mass, and that they undergo oscillations between different neutrino species, violating lepton number.

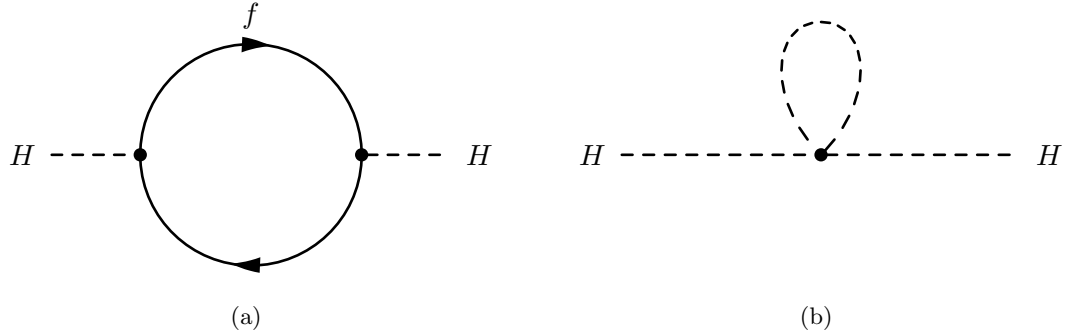


Figure 1.4: Feynman diagram of fermion (a) and scalar (b) loop corrections to Higgs boson mass.

479 reformulated into a quantum mechanical theory. Another is that cosmological observations
 480 indicate the presences of massive amounts of “dark matter” in the universe. Dark matter is
 481 expected to be composed of a stable massive neutral particle which interacts very weakly
 482 with other matter; no SM particle fits this description. Finally, there is the “hierarchy,”
 483 or fine-tuning problem. This problem strongly affects the Higgs sector, and motivated the
 484 development of Supersymmetry, which are the targets of the search presented in this thesis.
 485 An short overview of the hierarchy problem and Supersymmetry are presented in the next
 486 sections.

487 1.2.1 The Hierarchy Problem

The enormous size of the cutoff scale Λ in the SM causes a major theoretical problem in the SM. During renormalization of the SM, amplitudes with divergent integrals are cut off at Λ . These large constant terms are “absorbed” into the physical observables. The cutoff term appears directly in quantum corrections to the Higgs boson mass [17]. The Yukawa term $-\lambda_f H \bar{f} f$ coupling the fermion f to the Higgs boson H produces loop corrections to Higgs boson mass. The two types of corrections due to fermion loops and scalar loops are illustrated in Figure 1.4. The contribution [17] of the loop correction in Figure 1.4(a) to the Higgs boson mass is

$$m_H^2 = -\frac{|\lambda_f|^2}{8\pi^2} \Lambda^2 + \dots \quad (1.31)$$

488 The correction scales with Λ^2 , which is many orders of magnitude larger than the electroweak
 489 (M_W) scale. The physical mass of the Higgs boson is expected to have the same scale as M_W ,

490 $\mathcal{O}(100 \text{ GeV}/c^2)$. The fact that each fermion contributes a loop correction (Equation 1.31)
 491 requires that the “bare mass” of the Higgs boson to be tuned to the precision of $(M_W/\Lambda)^2 \approx$
 492 10^{-26} for the renormalized mass to be correct! This is the so-called fine-tuning problem: it
 493 is believed that in a natural theory there will be only one scale. The electroweak unification
 494 analogy is in Equation 1.11, where it was noticed that the difference between the QED and
 495 weak scale was due to the massive M_W propagator term, and that the fundamental scale
 496 g of the intermediate weak boson theory was compatible with QED. The most promising
 497 solution to the hierarchy problem is the introduction of a new, “super” symmetry.

498 1.2.2 Supersymmetry

499 Supersymmetry extends the SM by positing that there exists a symmetry between the
 500 integer-spin bosons (γ, W^\pm, Z, H) and the half integer-spin fermions (quarks and leptons).
 501 In Supersymmetry, every particle in the SM has a “superpartner” with a spin differs by $1/2$.
 502 All of the other quantum numbers (including mass) of the superpartners are the same. The
 503 introduction of this symmetry immediately solves the hierarchy problem. For every scalar
 504 loop correction (Figure 1.4(b)) to the Higgs boson mass there is now a corresponding fermion
 505 loop correction (Figure 1.4(a)). As the fermion and the scalar have the same quantum
 506 numbers (except for spin) it turns out that these two diagrams have the same value, but
 507 *opposite* sign. Thus the large Λ^2 superpartner loop corrections to the Higgs boson mass
 508 exactly cancel out the problematic SM corrections. It is clear that if Supersymmetry exists,
 509 it must be broken. We have not observed a scalar charged particle with the same mass as the
 510 electron, for example. An excellent overview of possible mechanisms that create spontaneous
 511 symmetry breaking in supersymmetric models is given in Chapter 6 of [17].

512 1.2.3 The Minimal Supersymmetric Extension to the Standard Model

513 The simplest possible supersymmetric extension to the SM is MSSM. The model groups
 514 superpartner pairs into chiral (a left or right-handed fermion field plus a complex scalar
 515 field) and gauge (a spin-1 vector boson and a left or right-handed *gaugino* fermion) “su-
 516 permultiplets.” As the weak interactions of the SM fermions are chiral, they (and their
 517 superpartners) must belong in a chiral supermultiplet. It is interesting to note that there

Names		spin 0	spin 1/2	$SU(3)_C, SU(2)_L, U(1)_Y$
squarks, quarks ($\times 3$ families)	Q	$(\tilde{u}_L \ \tilde{d}_L)$	$(u_L \ d_L)$	$(\mathbf{3}, \mathbf{2}, \frac{1}{6})$
	\bar{u}	\tilde{u}_R^*	u_R^\dagger	$(\bar{\mathbf{3}}, \mathbf{1}, -\frac{2}{3})$
	\bar{d}	\tilde{d}_R^*	d_R^\dagger	$(\bar{\mathbf{3}}, \mathbf{1}, \frac{1}{3})$
sleptons, leptons ($\times 3$ families)	L	$(\tilde{\nu} \ \tilde{e}_L)$	$(\nu \ e_L)$	$(\mathbf{1}, \mathbf{2}, -\frac{1}{2})$
	\bar{e}	\tilde{e}_R^*	e_R^\dagger	$(\mathbf{1}, \mathbf{1}, 1)$
Higgs, higgsinos	H_u	$(H_u^+ \ H_u^0)$	$(\tilde{H}_u^+ \ \tilde{H}_u^0)$	$(\mathbf{1}, \mathbf{2}, +\frac{1}{2})$
	H_d	$(H_d^0 \ H_d^-)$	$(\tilde{H}_d^0 \ \tilde{H}_d^-)$	$(\mathbf{1}, \mathbf{2}, -\frac{1}{2})$

Table 1.1: Chiral supermultiplets in the MSSM. The spin-0 fields are complex scalars, and the spin-1/2 fields are left-handed two-component Weyl fermions. Source: [17]

Names	spin 1/2	spin 1	$SU(3)_C, SU(2)_L, U(1)_Y$
gluino, gluon	\tilde{g}	g	$(\mathbf{8}, \mathbf{1}, 0)$
winos, W bosons	$\tilde{W}^\pm \ \tilde{W}^0$	$W^\pm \ W^0$	$(\mathbf{1}, \mathbf{3}, 0)$
bino, B boson	\tilde{B}^0	B^0	$(\mathbf{1}, \mathbf{1}, 0)$

Table 1.2: Gauge supermultiplets in the MSSM. Source: [17]

is a different superpartner for the left and right-handed components of the fermions, even though the superpartners are spin-0 and cannot have any handedness. It is found that there must be two Higgs supermultiplets for the MSSM to be viable. As there are now fermionic particles in the Higgs sector (the Higgsinos), if only one supermultiplet is introduced the MSSM suffers from non-renormalizable gauge anomalies.⁷ By introducing an additional Higgs supermultiplet with opposite hypercharge, the anomaly is canceled. The scalar portion of the MSSM Higgs sector then contains two complex doublet fields $H_u = (H_u^+, H_u^0)$ (up-type) and $H_d = (H_d^0, H_d^-)$ (down-type). The complete chiral and gauge supermultiplets of the MSSM are enumerated in Tables 1.1 and 1.2, respectively.

The superpotential (like the scalar potential of Section 1.1.3 but invariant under supersymmetric transformations) of the MSSM is then [17]

$$W_{\text{MSSM}} = \bar{u}\mathbf{y_u}QH_u - \bar{d}\mathbf{y_d}QH_d - \bar{e}\mathbf{y_e}LH_d + \mu H_u H_d ,$$

⁷A gauge anomaly is a linear divergence that occurs in diagrams containing a fermion loop with three gauge bosons (total) in the initial and final states. In the Electroweak model, the sum of the fermion contributions cancel the anomaly. Interestingly, the requirement of anomaly cancellation is only achieved in the SM is achieved only by requiring there be three types of color in QCD.

527 where H_u , H_d , Q , L , \bar{u} , \bar{d} , and \bar{e} are the superfields defined in Table 1.1. The \mathbf{y} terms are
 528 Yukawa 3×3 matrices which act on the different families. It is important to note that the
 529 up-type quarks couple to the up-type Higgs doublet H_u , while the down-type quarks and
 530 leptons couple to the down-type Higgs doublet. This feature has large phenomenological
 531 consequences, which are discussed in Section 1.3.2. The scalar portion of the W_{MSSM} poten-
 532 tial defines the spontaneous symmetry breaking. Similar to the scalar potential V symmetry
 533 breaking of Section 1.1.3, the potential of V at the minimum is found⁸ to be

$$\begin{aligned} V = & (|\mu|^2 + m_{H_u}^2)|H_u^0|^2 + (|\mu|^2 + m_{H_d}^2)|H_d^0|^2 \\ & - (bH_u^0H_d^0 + c.c.) + \frac{1}{8}(g^2 + g'^2)(|H_u^0|^2 - |H_d^0|^2)^2. \end{aligned} \quad (1.32)$$

Under suitable choices⁹ of the parameters in Equation 1.32, the up-type and down-type neutral Higgs fields acquire a VEV, ν_u and ν_d , respectively. The VEVs are related to the VEV of electroweak symmetry breaking (Equation 1.30) in the SM,

$$\nu_u^2 + \nu_d^2 = \nu^2 = \frac{2M_Z^2}{g^2 + g'^2} \approx (174 \text{ GeV})^2.$$

The ratio of the VEVs is expressed as

$$\tan \beta \equiv \frac{\nu_u}{\nu_d},$$

534 which is an important parameter of the MSSM. As there are two complex doublets, there are
 535 a total of eight degrees of freedom in the MSSM Higgs sector. After the symmetry breaking,
 536 three of the degrees of freedom are (like the Standard Model) eaten by the W^\pm and Z weak
 537 gauge bosons. The remaining five degrees of freedom create five massive Higgs bosons: two
 538 CP-even neutral scalars h^0 and H^0 , a CP-odd neutral scalar A^0 , and two (positive and
 539 negative) charged scalars H^\pm . The masses are of the different Higgs boson mass eigenstates

⁸A clever choice of the $SU(2)_L$ gauge has removed any contributions from the charged fields. The charged Higgs fields cannot have a VEV without breaking $U(1)_{em}$.

⁹See Chapter 7 of [17] for a detailed overview.

⁵⁴⁰ are related to each other and $\tan \beta$ at tree level by

$$\begin{aligned} m_{h^0}^2 &= \frac{1}{2}(m_{A^0}^2 + m_Z^2 - \sqrt{(m_{A^0}^2 - m_Z^2)^2 + 4m_Z^2 m_{A^0}^2 \sin^2(2\beta)}) \\ m_{H^0}^2 &= \frac{1}{2}(m_{A^0}^2 + m_Z^2 + \sqrt{(m_{A^0}^2 - m_Z^2)^2 + 4m_Z^2 m_{A^0}^2 \sin^2(2\beta)}). \end{aligned} \quad (1.33)$$

It can be seen that the tree level mass m_{h^0} of Equation 1.33 is bounded from above by $m_{h^0} < m_Z |\cos(2\beta)| < 90 \text{ GeV}/c^2$. If this is true the model would have been excluded by the LEP experiment (see next section). However, there are important quantum corrections to m_{h^0} from the top–quark and top–squark loop diagrams which increase m_{h^0} . The Yukawa couplings in the MSSM depend on $\tan \beta$. The relationships for the most massive members of each family are

$$m_t = y_t v \sin \beta, \quad m_b = y_b v \cos \beta, \quad m_\tau = y_\tau v \cos \beta.$$

⁵⁴¹ The Yukawa couplings are free parameters determined by experimentally observed masses.
⁵⁴² This means that when $\tan \beta$ is large ($\beta \rightarrow \pi$), the Yukawa terms y for the b quarks and τ
⁵⁴³ leptons must be enhanced to maintain the observed masses. The effect of $\tan \beta$ on the Higgs
⁵⁴⁴ boson mass spectrum and couplings in the MSSM will be discussed further in Section 1.3.2.

⁵⁴⁵ 1.3 Searches for the Higgs Boson

⁵⁴⁶ The discovery of the Higgs boson is one of the biggest prizes in science today. Dozens of
⁵⁴⁷ experiments, thousands of scientists and billions of dollars (a human hierarchy problem)
⁵⁴⁸ have been spent in efforts to discover the Higgs boson. In this section we discuss how the
⁵⁴⁹ Higgs boson and the MSSM could appear in modern colliders (with an emphasis on the
⁵⁵⁰ LHC) and the current limits placed on the Higgs boson by the Large Electron–Positron
⁵⁵¹ Collider (LEP) and Tevatron experiments.

⁵⁵² 1.3.1 Standard Model Higgs Boson Phenomenology

The phenomenology of the Higgs boson is strongly coupled to its relationship with mass. The coupling of the Higgs boson to the fermions is determined by the Yukawa terms (Equation 1.28) in the Lagrangian. Taking the electron as an example, after symmetry breaking,

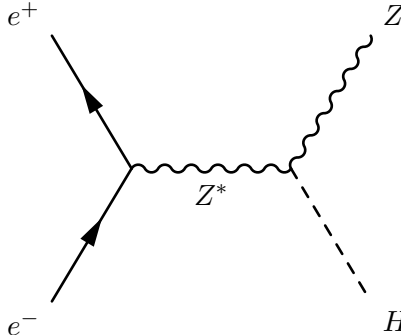


Figure 1.5: Higgstrahlung production diagram at e^+e^- colliders

the Yukawa term is found to be

$$\mathcal{L}_e = -\frac{G_e}{\sqrt{2}}(\nu + H(x))\bar{e}e = -\frac{G_e\nu}{\sqrt{2}}\bar{e}e - \frac{G_e}{\sqrt{2}}H(x)\bar{e}e. \quad (1.34)$$

The value of G_e is a free parameter of the theory and is thus determined by the measurement of the electron mass and ν , the VEV of the Higgs field

$$\frac{G_e\nu}{\sqrt{2}} = \frac{m_e}{\nu}. \quad (1.35)$$

553 The left-hand side of Equation 1.35 is the same as the constant in the electron–Higgs boson
 554 coupling term ($H(x)\bar{e}e$) in Equation 1.34. Therefore the coupling between the fermions
 555 and Higgs boson is proportional to their mass! This remarkable fact shapes the possible
 556 production modes and the branching fractions of Higgs boson decays.

557 The dominant modes of Higgs boson production depend on the type of experiment.
 558 In general, Higgs boson production is favored through high-mass intermediate states, due
 559 to the mass² proportional coupling. At the Tevatron and LEP experiments, which will be
 560 introduced in the next section, the dominant SM Higgs boson production mode is “Hig-
 561 gstrahlung,” where a virtual W^\pm or Z gauge boson is produced and then radiates a Higgs
 562 boson. Higgstrahlung is illustrated in Figure 1.3.1. At the Large Hadron Collider, higher
 563 gluon luminosities (see Figure 1.8) result in the favored cross section being “gluon fusion,”
 564 (illustrated in Figure 1.3.1) where two gluons from the incident protons combine in a quark
 565 (dominated by the massive top quark) loop which then radiates a Higgs boson. Another
 566 important channel [19] is “vector boson fusion,” (Figure 1.3.1) where weak gauge bosons
 567 (W^\pm or Z) are radiated from the incoming quarks and fuse to produce a Higgs boson.

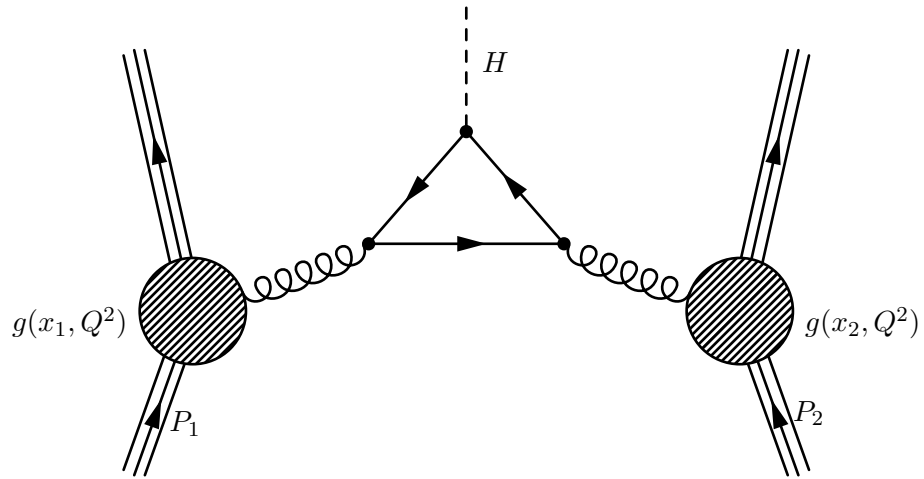


Figure 1.6: Gluon fusion Higgs boson production mechanism in a proton–proton collision. The Higgs mass coupling favors the heavy top quark in the central loop. Image credit: [18]

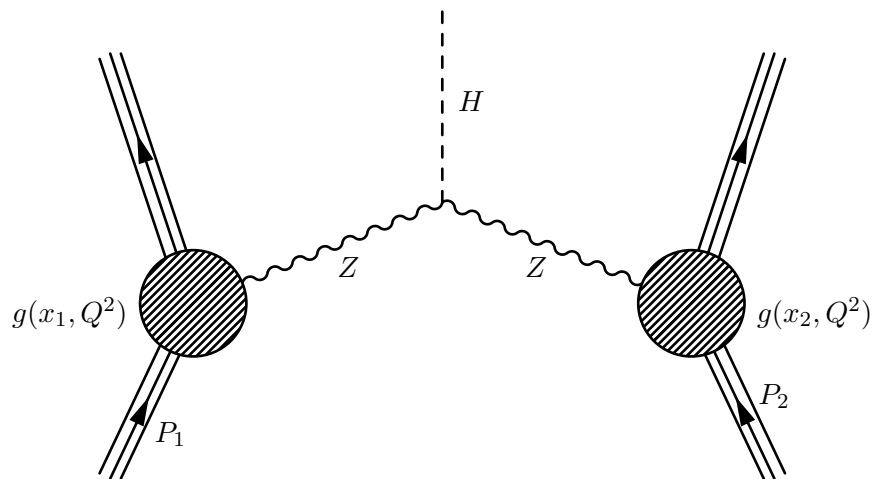


Figure 1.7: Vector boson fusion (VBF) Higgs boson production mechanism in proton–proton collisions. The VBF mechanism is notable for the lack of color–flow between the two incident protons, producing events with low jet activity in the central region.

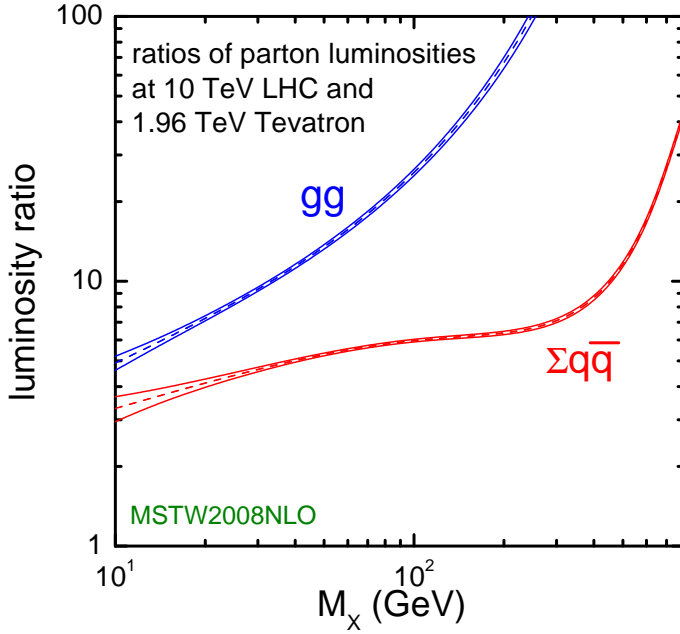


Figure 1.8: Ratio of the parton luminosity (the amount of luminosity contributed by the different species that compose the proton) of the LHC (at $\sqrt{s} = 10$ TeV) and the Tevatron. The large increase in gluon–gluon luminosity affects the favored production mechanisms of the Higgs boson.

568 This is a notable channel due to the lack of “color-flow” (gluons) between the two protons,
 569 producing an event with low central jet activity and two “tag-jets” in the forward and
 570 backward regions. The theoretical cross sections for the SM Higgs boson at the LHC are
 571 shown for the various production mechanisms in Figure 1.9.

572 The branching fractions of the different decay modes of the SM Higgs boson depend
 573 strongly on the mass of the Higgs boson. In general, the Higgs prefers (due to the Yukawa
 574 couplings) to decay pairs of the particles with the highest mass possible. Below the threshold
 575 to decay to pairs of weak bosons ($M_H < 160 \text{ GeV}/c^2$), the Higgs boson decays predominantly
 576 to either b -quarks ($b\bar{b}$, 90%) or a pair of τ leptons ($\tau^+\tau^-$, $\approx 10\%$). Above the $W^\pm W^\mp$ thresh-
 577 old, decays to vector bosons ($H \rightarrow W^\pm W^\mp$ and $H \rightarrow ZZ$) dominate. The dependence of
 578 branching fraction on M_H and the other rare decay modes are illustrated in Figure 1.10.
 579 For low mass Higgs bosons, the $\tau^+\tau^-$ decay mode plays a particularly important role. The
 580 dominant decay mode $H \rightarrow b\bar{b}$ suffers from enormous backgrounds from QCD jet produc-
 581 tion. It is important to understand the magnitude of difference between expected Higgs
 582 boson production and the rates of various backgrounds. Figure 1.11 illustrates the cross

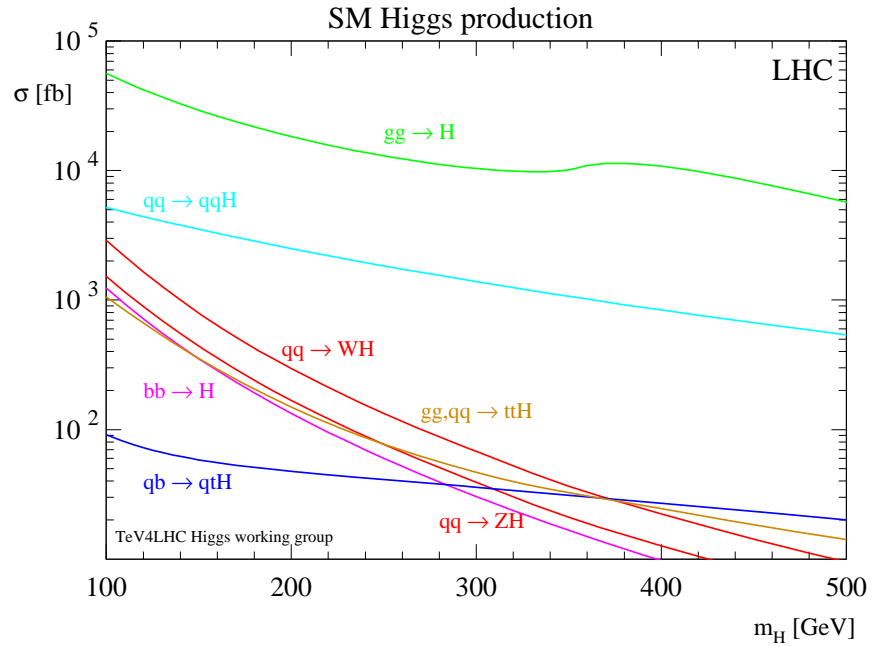


Figure 1.9: Cross section of the SM Higgs boson versus the Higgs boson mass. The different curves give the contribution to the cross section from different production mechanisms. Source: [20].

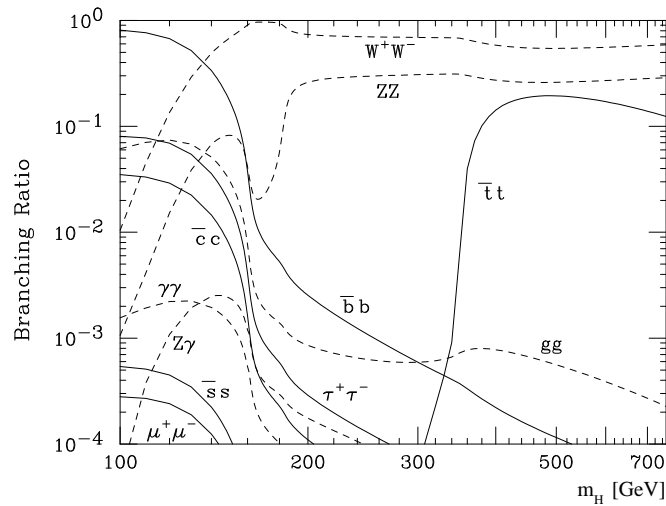


Figure 1.10: Branching fraction of the SM Higgs bosons for different values of M_H . Source: [20].

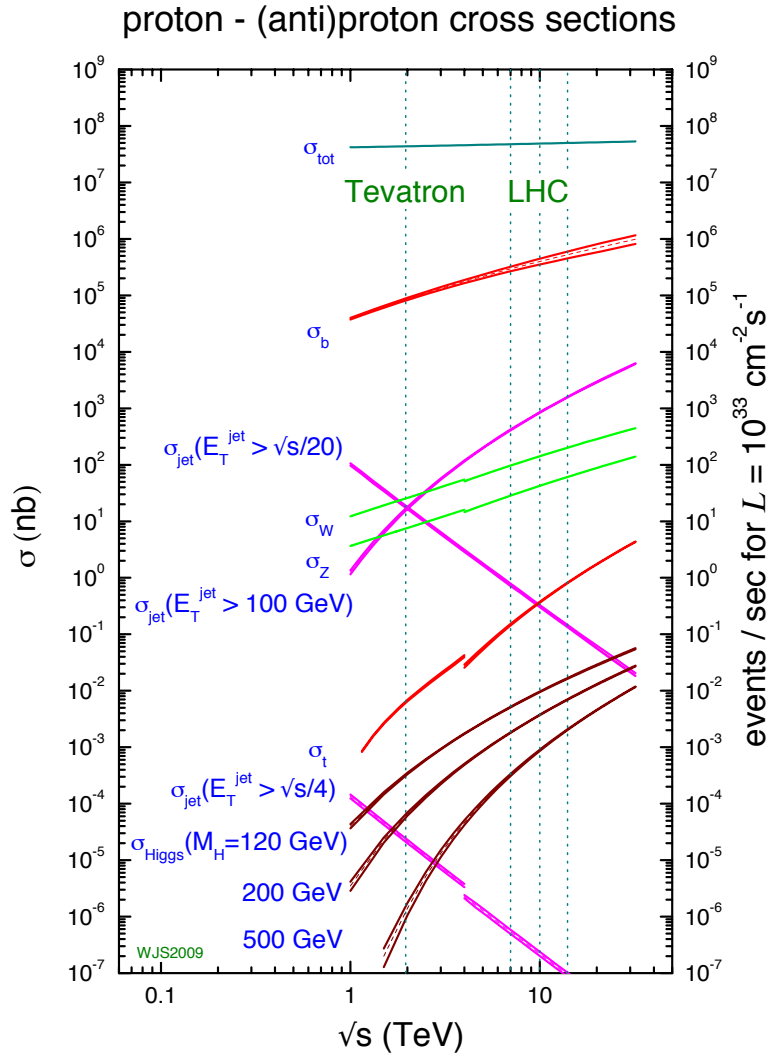


Figure 1.11: Cross sections of various processes at hadron colliders. The horizontal axis represents the center of mass energy of the collision. Of note is the vast difference in scales between Higgs boson production (maroon lines, $\mathcal{O}(10^{-2} \text{ nb})$) and the QCD cross section to produce $b\bar{b}$ pairs (red line, $\mathcal{O}(10^4 \text{ nb})$). Source: [21].

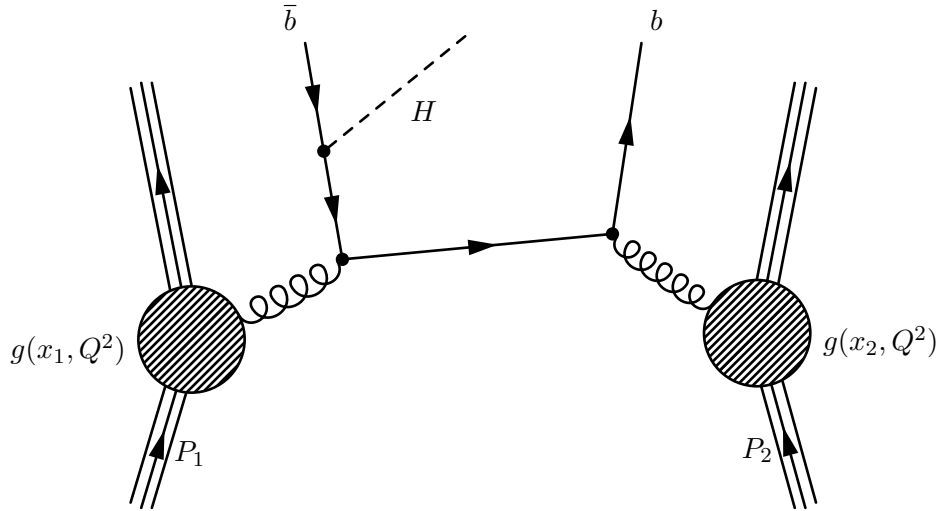


Figure 1.12: One possible diagram for an MSSM Higgs boson produced with associated b -quarks in a proton–proton collision.

sections for different SM processes at hadron colliders. The rate of Higgs boson production is many orders of magnitude ($\mathcal{O}(10^{-7})$) smaller than that of QCD production. It is important to therefore design searches to use handles that can reject the vast majority of the uninteresting events at hadron colliders.

1.3.2 MSSM Higgs Boson Phenomenology

The phenomenology of the Higgs sector of the MSSM is similar to the SM in some respects, but differs in some key aspects which have important implications for final states involving τ leptons and b quarks. When the parameter $\tan \beta$ is large, the coupling factor between the Higgs bosons and the down-type quarks and leptons (effectively the τ and b quark) is enhanced by $\tan \beta$. The gluon–gluon cross section is therefore increased by $\tan^2 \beta$, where the top quark loop in Figure 1.3.1 is replaced by a ($\tan \beta$ enhanced) b quark loop. Additionally, MSSM Higgs production with associated b -quarks, illustrated in Figure 1.3.2, becomes an important production mode. At tree-level, the MSSM can be defined by the mass of the CP-odd Higgs boson m_{A^0} and $\tan \beta$. For a reasonably high $\tan \beta$, there is always one CP-even Higgs boson (h^0 or H^0) which is mass-degenerate with the A^0 . When $\tan \beta$ and m_{A^0} are both large, associated b production dominates the total cross section [22]. The cross sections of the different MSSM neutral Higgs bosons are shown in Figure 1.13.

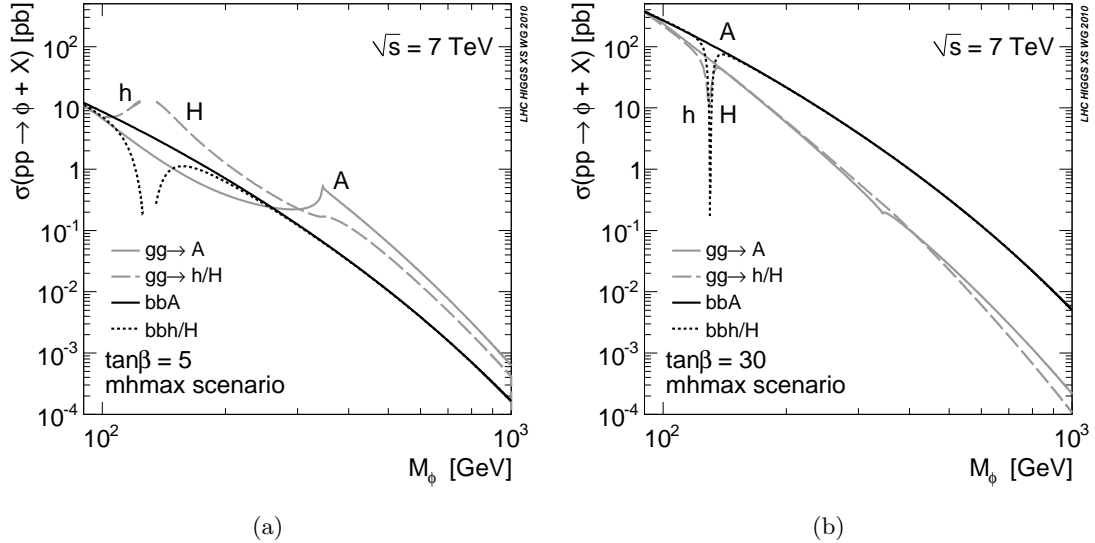


Figure 1.13: Cross sections for the different MSSM Higgs bosons versus m_{A^0} in the $m_{h^{max}}$ benchmark scenario [23] scenario for $\tan \beta = 5$ (a) and $\tan \beta = 30$ (b). Source: [22]

600 The $\tan \beta$ enhancement of the MSSM Higgs boson coupling to the b quarks and τ leptons
 601 causes the branching fraction of all neutral MSSM Higgs states to be $H \rightarrow b\bar{b}$ (90%) and
 602 $H \rightarrow \tau^+\tau^-$ (10%) across the entire range of m_{A^0} . The enhanced production rate and the
 603 high branching fraction to τ leptons make the MSSM Higgs bosons decaying to τ leptons
 604 an exciting and promising channel to search for Higgs bosons and supersymmetric physics
 605 at colliders.

606 1.3.3 Results from LEP and Tevatron

607 The LEP and Tevatron experiments have both set limits on the existence of the SM
 608 and MSSM Higgs boson. Precision electroweak measurements give additional hints on the
 609 prospects for both models.

610 LEP was an e^+e^- collider at CERN and has effectively excluded the presence of a low
 611 (less than 114 GeV/c^2) mass Higgs boson. The dominant SM Higgs boson production mode
 612 at LEP is Higgstrahlung, where the Higgs boson is produced in association with a Z boson
 613 (see Figure 1.3.1). The search at LEP utilized a number of different decay channels [20].
 614 The decay channels used in the LEP search are summarized in Table 1.3.3.

Higgs Decay	Z Decay
$b\bar{b}$	$q\bar{q}$
$\tau^+\tau^-$	$q\bar{q}$
$b\bar{b}$	$t\bar{t}$
$b\bar{b}$	$\nu\bar{\nu}$
$b\bar{b}$	$\mu^+\mu^-$
$b\bar{b}$	e^+e^-

Table 1.3: Different channels used at LEP to search for Higgs bosons produced with the Higgstrahlung mechanism.

615 The results using all channels from the four LEP experiments¹⁰ have been combined into
 616 a single limit, shown in Figure 1.14. The analysis sets a limit on the ratio $\xi^2 = (g_{HZZ}/g_{HZZ})^2$,
 617 the upper limit on the HZZ coupling divided by the predicted value of the SM. For Higgs
 618 boson masses below 114 GeV/c², the ratio is below unity at the 95% confidence level, ruling
 619 out a SM Higgs boson below that mass.

620 The Tevatron is a proton–antiproton collider with a center-of-mass energy of $\sqrt{s} =$
 621 1.96 TeV. There are two general purpose detectors at the Tevatron, CDF and DØ. The
 622 dominant Higgs boson production modes at the Tevatron are Higgstrahlung and gluon fusion
 623 (see Figure 1.3.1). For low mass ($m_H < 135$ GeV/c²) Higgs bosons the dominant channel
 624 at the Tevatron is the Higgstrahlung production mode and $H \rightarrow b\bar{b}$ decays. Large multi-
 625 jet backgrounds prevent the $H \rightarrow b\bar{b}$ decay mode from being useful for searching for Higgs
 626 bosons produced by gluon fusion. The $H \rightarrow \tau^+\tau^-$ and $H \rightarrow \gamma\gamma$ decays are additionally
 627 used in an inclusive search at low mass, but do not dominate the search sensitivity. The
 628 combined low-mass limit on the SM Higgs boson from both Tevatron experiments is shown
 629 in Figure 1.15. The Tevatron currently sets an upper limit on the SM Higgs boson cross
 630 section of about 2.5 times the SM expectation.

631 When ($m_H < 135$ GeV/c²) the $H \rightarrow W^+W^-$ decay mode becomes significant. Low
 632 diboson backgrounds allow this decay mode to probe both the Higgstrahlung and gluon
 633 fusion production modes. The combined results of the CDF and DØ searches using the

¹⁰ALEPH, DELPHI, L3, and OPAL

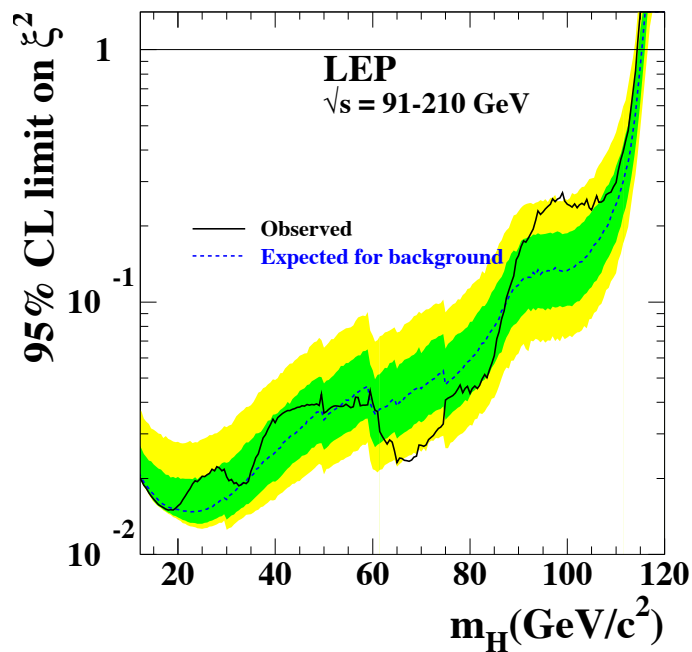


Figure 1.14: Combined LEP upper limit set on the quantity $\xi^2 = (g_{HZZ}/g_{HZZ})^2$ at 95% confidence level. Regions where the observed ratio is less than one exclude the SM. The dashed line gives the expected limit for the null (background only) hypothesis, with the green and yellow bands representing the expected variance at one and two sigma, respectively, of the limit. The solid line is the observed limit from the combined LEP data. Reference: [20]

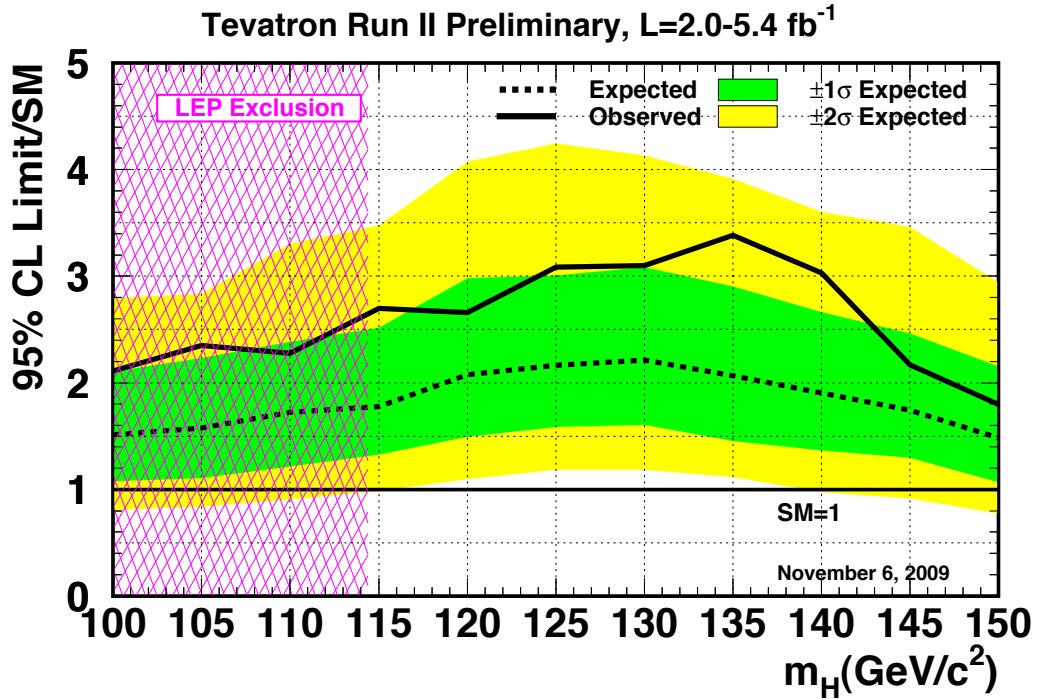
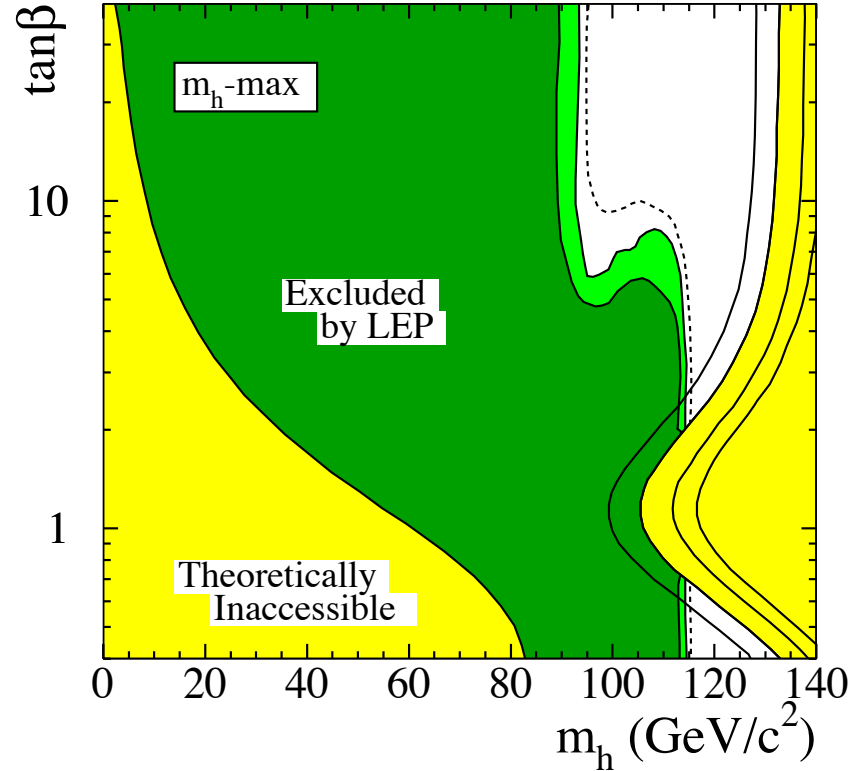
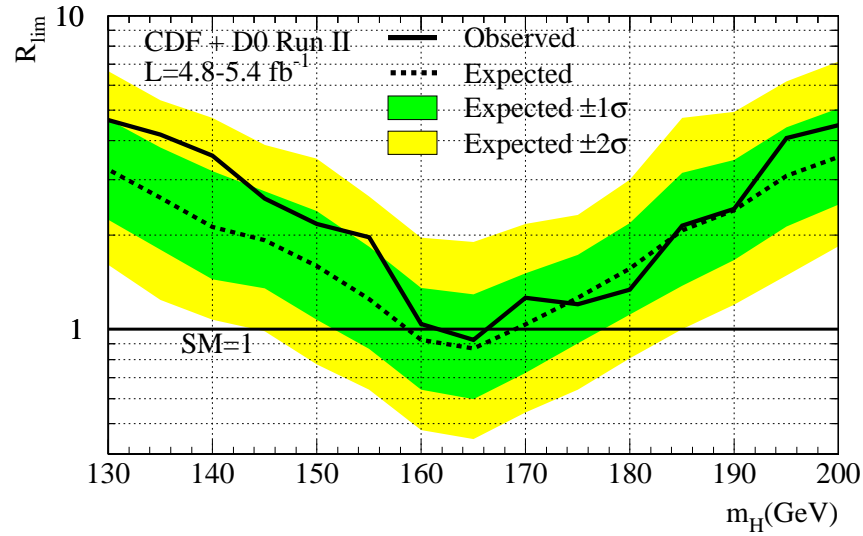


Figure 1.15: Combined CDF and DØ RunII upper limit on the cross section of a standard model-like Higgs boson. The LEP limit is shown in pink. Reference: [20]

634 W^+W^- have decay mode recently excluded (See Figure 1.16) a SM Higgs boson with a
 635 mass between 162 and 166 GeV/c^2 . This is the first exclusion in SM Higgs boson mass
 636 parameter space since the LEP result.

637 Analyses at LEP and Tevatron have also addressed excluded regions of the MSSM. At
 638 LEP, the dominant production modes of the MSSM Higgs bosons are Higgstrahlung and
 639 pair production, where $e^+e^- \rightarrow h^0A^0$ or H^0A^0 . For the Higgstrahlung production mode,
 640 the SM search can be reinterpreted in terms of the MSSM. To address the pair production
 641 mode, searches were performed in the $e^+e^- \rightarrow h^0A^0 \rightarrow b\bar{b}b\bar{b}$ and $\tau^+\tau^-q\bar{q}$ decay modes.
 642 Finally, LEP is also sensitive to associated MSSM Higgs boson production at low m_{A^0} and
 643 high $\tan\beta$ to $e^+e^- \rightarrow \{\bar{\phi}$, where the associated fermions $\{\$ are b -quarks or tau leptons.
 644 The combined limits from LEP in the $m_{A^0} - \tan\beta$ plane are shown in Figure 1.17.

645 At the Tevatron, CDF and DØ have set a combined limit on the MSSM using the
 646 inclusive $H \rightarrow \tau^+\tau^-$ channel. The analysis presented in this thesis is very similar to the
 647 approaches used at the Tevatron. Results from the Tevatron have excluded the MSSM for



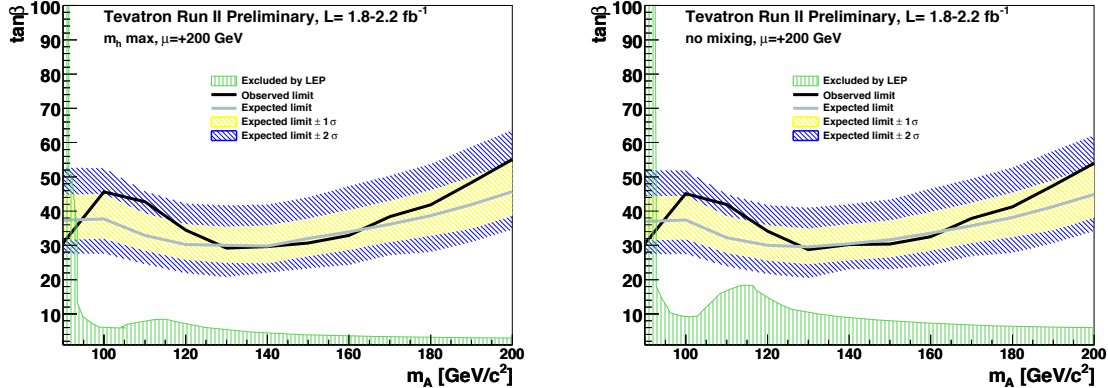


Figure 1.18: Combined Tevatron limits on the MSSM. The grey line and blue and yellow bands gives the expected limit and its one and two sigma contours. The black line is the observed limit. The results are interpreted in the context of the m_h -max benchmark (left) and “no mixing” (right) MSSM scenarios. The limit from LEP is shown in green. Reference: [20]

648 $\tan \beta$ greater than approximately 35 for MSSM Higgs boson mass $m_{A^0} < 200$ GeV/c^2 . The
 649 full exclusion plot for the m_h -max and “no mixing” MSSM benchmark scenarios are shown
 650 in Figure 1.18.

651 1.4 The Physics of the Tau Lepton

652 As discussed in Sections 1.3.1 and 1.2.3, the τ lepton is an important probe of Higgs physics.
 653 The τ lepton has some unusual properties which make it particularly challenging at hadron
 654 colliders. With a mass of 1.78 GeV/c^2 , the τ lepton is heaviest of the leptons. The nominal
 655 decay distance $c\tau$ of the τ lepton is 87 μm , which in practice means that the τ will always
 656 decay before reaching the first layer of the detector. Tau decays can be effectively classified
 657 into two types. “Leptonic” decays consist of a τ decaying to a light lepton ($\ell = e, \mu$) and two
 658 neutrinos $\tau^+ \rightarrow \ell^+ \nu_\tau \bar{\nu}_\ell$. “Hadronic” decays consist of a low-multiplicity collimated group of
 659 hadrons, typically π^\pm and π^0 mesons. The hadronic decays of the τ lepton compose approx-
 660 imately 65% of the τ lepton branching fraction, with the remainder shared approximately
 661 equally by the leptonic decays. The branching fractions for the leptonic and most common
 662 hadronic decays are shown in Table 1.4.

663 The tau is also a challenging object in that the decay of the tau always includes neu-
 664 trinos. The associated neutrinos are weakly interacting and do not create a signal in any

Visible Decay Products	Resonance	Mass (MeV/c ²)	Fraction [20]
Leptonic modes			
$e^- \nu_\tau \bar{\nu}_e$	-	0.5	17.8%
$\mu^- \nu_\tau \bar{\nu}_\mu$	-	105	17.4%
Hadronic modes			
$\pi^- \nu_\tau$	-	135	10.9%
$\pi^- \pi^0 \nu_\tau$	ρ	770	25.5%
$\pi^- \pi^0 \pi^0 \nu_\tau$	$a1$	1200	9.3%
$\pi^- \pi^- \pi^+ \nu_\tau$	$a1$	1200	9.0%
$\pi^- \pi^- \pi^+ \pi^0 \nu_\tau$	$a1$	1200	4.5%
Total			94.4%

Table 1.4: Resonances and branching ratios of the dominant decay modes of the τ lepton. The decay products listed correspond to a negatively charged τ lepton; the table is identical under charge conjugation.

665 detector at CMS. The only sign that the neutrinos are there is an imbalance in the total
 666 transverse¹¹ energy in the event. This thesis will describe a novel way to reconstruct the
 667 neutrinos associated to tau decays in Chapter 4.

A tau with produced with energy E travels on average

$$\gamma c\tau = \frac{E}{1.78 \text{ GeV}} 87 \text{ } \mu\text{m}$$

668 before decaying in the detector. These lengths are comparable to the resolution of the CMS
 669 tracker, therefore it is possible to reconstruct a vertex corresponding to a tau decay that is
 670 displaced with respect to the primary vertex. This can be used as an additional discriminant
 671 against QCD, which is expected to decay promptly. Furthermore, in Chapter 4 we will see
 672 it may be possible to use it when reconstructing the associated neutrinos.

¹¹At proton colliders, the constituent quarks/gluons of the proton share the total proton momentum. As the total fraction of momentum carried by the parton involved in a hard collision is unknown, longitudinal momentum is not conserved.

Chapter 2

673 **The Compact Muon Solenoid Experiment**

675 The Compact Muon Solenoid (CMS) Experiment is a general-purpose particle detector
 676 designed to measure collision events at the Large Hadron Collider (LHC), a proton-proton
 677 synchrotron located at the CERN laboratory in Geneva, Switzerland. The design goals of
 678 the CMS experiment are [24], in order of priority:

- 679 • Excellent muon identification and momentum resolution over a large solid angle. Par-
 ticularly important is the ability to determine the muon charge for any muon with
 $p < \text{TeV}/c$.
- 682 • Charged particle tracking with excellent momentum. Triggering on b -jets requires an
 excellent vertex resolution, and requires pixel detectors close to the interaction region;
- 684 • An electromagnetic calorimeter with an energy resolution precise enough to measure
 the mass of diphoton and dielectron events with a resolution of $\approx 1\%$ at 100 GeV/c^2 .
 The calorimeter must have high granularity to determine isolated photons and elec-
 trons during high luminosity running.;
- 688 • The design goal of excellent missing-transverse-energy and dijet-mass resolution, re-
 quiring require hadron calorimeters large solid angle coverage and high granularity.

690 The detector uses a hermetic design that maximizes the solid-angle of the fiducial region to
 691 capture as much information about the collisions as possible. The general geometry of the
 692 detector is cylindrical. A cutaway diagram of the detector is shown in Figure 2.1. Each of
 693 the sub-detector components consists of “barrel” and “endcap” components. As its name
 694 suggests, the detector is centered around a four Tesla superconducting solenoid magnet.
 695 The individual sub-detectors of CMS are arranged in a manner that permits identification

696 of different species of particles. The central (closest to interaction point) sub-detectors
 697 are the charged particle tracking systems (the “tracker”). The tracker is designed to be
 698 a non-destructive instrument, which means that ideally that the momentum of particles
 699 are unchanged after passing through it. Outside of the tracker is the electromagnetic and
 700 hadronic calorimeters, which are abbreviated ECAL and HCAL, respectively. The outer
 701 layers of CMS are designed to measure muons, the one¹ species of particle that is nearly
 702 immune to the stopping power of the calorimeter. The arrangement of destructive and non-
 703 destructive sub-detectors facilitates the identification of different types of particles. This
 704 concept is illustrated in Figure 2.1(b). In this chapter we give an brief overview of the LHC
 705 machine, and then describe the individual sub-detector systems of CMS.

706 2.1 The Large Hadron Collider

707 The Large Hadron Collider is a proton–proton synchrotron, with a design collision energy
 708 of 14 TeV. At the time of this writing (and for the foreseeable future), the LHC is the
 709 world’s largest and highest energy particle accelerator. A synchrotron is a machine that
 710 accelerates beams of charged particles by using magnets to steer them in a circle through
 711 radio-frequency resonating cavities which accelerate the particles. As the LHC is a collider,
 712 there are two beams that are accelerated in opposite directions. The maximum beam energy
 713 of a synchrotron is determined by its radius and the maximum strength of the magnetic
 714 fields used to bend the path of the beam. The dipole magnets used by the LHC to steer the
 715 particles are superconducting niobium–titanium. To maintain them in a superconducting
 716 state, they are cooled using superfluid liquid helium to 1.9 Kelvin. To store the beam at the
 717 injection energy of 450 GeV, the magnetic dipole fields must be maintained at 1/2 Tesla. As
 718 the energy of each beam energy is increased to its (design) maximum of 7 TeV, the dipole
 719 fields are ramped to a maximum field of over 8 Tesla.

720 2.2 Solenoid Magnet

The four-Tesla field of the CMS solenoid magnet is a critical factor in ability of CMS
 to precisely measure the particles produced in collisions at the LHC. The momentum of

¹Neutrinos of course fulfill this requirement as well, but are so weakly interacting that they are effectively invisible.

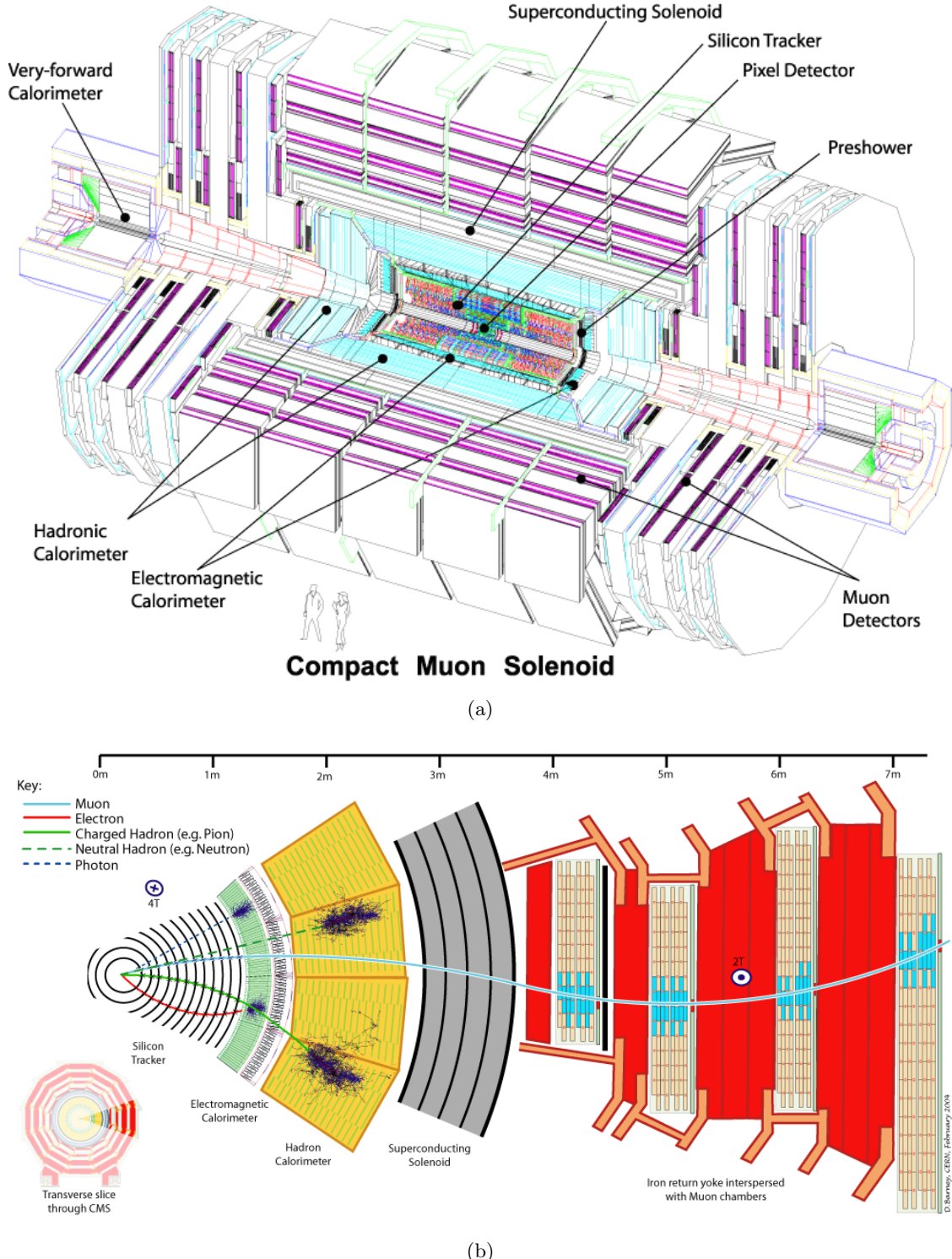


Figure 2.1: Figure (a), top, shows a schematic drawing of the CMS detector. The individual sub-detectors are labeled. Two humans are shown in the foreground for scale. Figure (b) shows a radial cross section of the detector and demonstrates how the (non-)destructiveness of different sub-detectors facilitates particle identification.

charged particles is measured in the tracking detector by examining the curvature of the particles path as it travels through the magnetic field. The radius of curvature r of a charged particle in a magnetic field is given by

$$r = \frac{p_{\perp}}{|q|B}, \quad (2.1)$$

where q is the charge of the particle, B is strength of the magnetic field, and p_{\perp} is the component of the particle's relativistic momentum perpendicular to the direction of the magnetic field. From Equation 2.1, it is evident that the ability to measure high momentum charged particles (a critical goal of CMS) requires a high magnetic field. Even at very high particle energies where the resolution becomes poor, the strength of the magnetic field is still very important for identifying the bending direction of the particle; the direction corresponds to the particle's electric charge. Furthermore, the homogeneity of the magnetic field is important to minimize systematic errors in the measurement of tracks.

The CMS solenoid is extremely large. The radial bore of the magnet is 6.3 meters; the magnet is 12.5 meters in length and weighs 220 tons. The large bore of the magnet allows the tracker and calorimeter systems to be located inside the solenoid. The internal windings of solenoid is arranged in four layers to increase the total field strength and are cooled by liquid helium to a temperature of 4.5 Kelvin. The windings are magnetically coupled to the support superstructure. This coupling allows the magnet to heat uniformly during a “quench” event², reducing localized stresses. The nominal current at full field of the solenoid is 19.14 kA. The solenoid itself is surrounded by an iron return yoke with a total mass of 10,000 tons. The return yoke surrounding the solenoid minimizes the fringing field. The muon detector system is interspersed inside the yoke, and takes advantage of the return field in the yoke to measure the momentum and charge of muons.

2.3 Charged Particle Tracking Systems

The charged particle tracking system measures the trajectories of charged particles emerging from the event. The tracker measures the trajectory of a charged particle by measuring

²A quench event occurs when some part of the magnet is suddenly no longer in a superconducting state. The coil becomes resistive and the large current in the magnet creates large amounts of heat.

743 “hits” along the trajectory. Each hit corresponds to the global position of the trajectory
 744 on a given surface. The trajectory can then be reconstructed by a helix to the points.
 745 The tracker is designed to have a resolution that permits the reconstruction of “secondary
 746 vertices” in b –quark and τ lepton decays. To accomplish this, there are two types of tracking
 747 detectors in CMS. The “pixel detector” comprises the inner layers (three in the barrel, two
 748 in the endcaps). The pixel detector is situated as close as possible (4.4 cm) to the interaction
 749 point and has a very high resolution. Outside of the pixel detector is the silicon strip tracker,
 750 with ten layers in the barrel and 12 layers in the endcaps. A secondary vertex occurs when a
 751 particle is semi–stable, traveling some non–negligible distance in the detector, but decaying
 752 before the first layer of the tracking system. The pixel and strip tracking detectors have a
 753 fiducial region which extends to a pseudorapidity of approximately $|\eta| \approx 2.5$.

754 Both the pixel and strip trackers are silicon–based. The principle of operation is similar
 755 to that of a charged–coupled device (CCD) in a modern digital camera. The sensitive portion
 756 of the detector is a silicon chip that is arranged with diode junctions formed by a p –doped
 757 layer and an n –doped layer³. Each $p – n$ junction is electrically isolated from adjacent layers.
 758 The size of each junction region determines⁴ the spatial resolution of the sensor. In the pixel
 759 detector, each sensor region “pixel” is $100 \mu\text{m} \times 150 \mu\text{m}$. In the strip tracker, The rear side
 760 of the chip is mounted to readout electronics. During operation, a high–voltage reverse bias
 761 is applied to each $p – n$ junction to achieve full depletion. When a charged particle passes
 762 through the detector, the diode junction breaks down and the readout system registers the
 763 hit.

764 The tracking system has been specifically designed for the high radiation environment
 765 around the interaction point. The detector is cooled to -27°C during operation to minimize
 766 damage. Radiation exposure produced in LHC collisions can change behavior of the tracking
 767 detector in three ways. Over time, radiation can induce positive holes in oxide layers fond
 768 in the read–out electrons which increase the signal–to–noise ratio. In the sensor mass itself,

³The pixel detector actually uses a more complicated multi–layered scheme to improve radiation hardness. For details, see Section 3.2.2 of [24].

⁴Additionally, the size of the sensitive area needs to be small enough such that the hit occupancy during a typically LHC event is not too large, which would cause overlaps and spoil the ability to reconstruct tracks. The expected occupancy depends on the distance r^2 from the interaction. The expected occupancy in the pixel detector for LHC collisions is 10^{-4} .

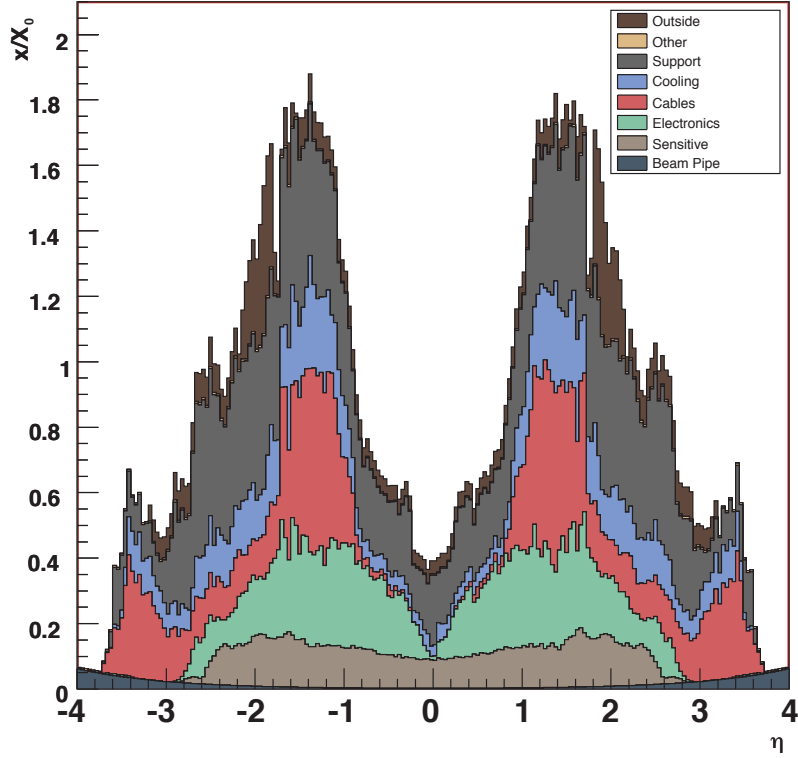


Figure 2.2: Material budget of the CMS tracker in units of radiation lengths X_0 versus pseudorapidity. The material budget is broken down into the contributions from the different components of the tracker. The amount of material is largest in the “transition region” between the barrel and endcap.

769 radiation damage changes the doping from n to p over time. The required voltage to deplete
 770 the sensor will thus increase over time. The readout electronics, bias voltage supplies, and
 771 cooling systems are designed to scale with the radiation damage and maintain a signal-to-
 772 noise ration of 10:1 or greater for 10 years of LHC operation. The final radiation effect is not
 773 an integrating effect. A “single event upset” is transient effect where an ionizing charged
 774 particle passes through the readout electronics and changes the state of the digital circuitry.

775 In the ideal case, the tracker would be a non-destructive instrument. However, charged
 776 particles can interact with the mass of the tracker (and its support infrastructure). These
 777 interactions limit the resolution of the tracker. The amount of matter in the tracker is
 778 referred to as the “material budget”. The material budget of the CMS tracker depends
 779 heavily on the pseudorapidity η and is illustrated in Figure 2.2. The relatively large ma-

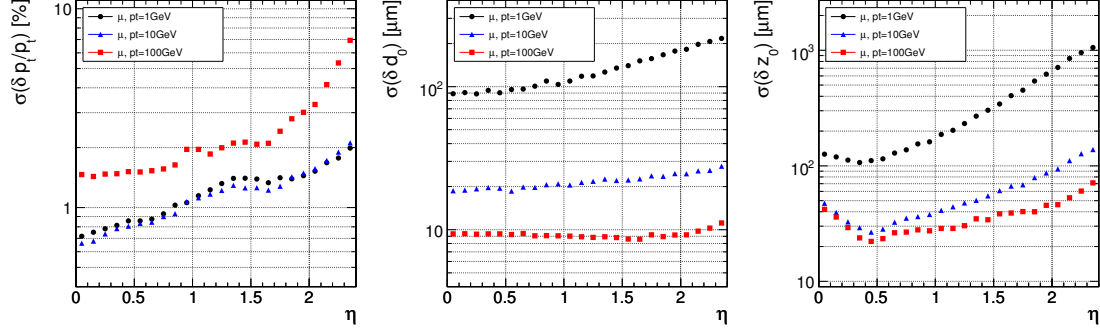


Figure 2.3: Expected resolutions of reconstructed transverse momentum (left), transverse impact parameter (center), and longitudinal impact parameter (right) versus absolute pseudorapidity $|\eta|$. The resolution is shown for three different cases of particle p_T , 1 GeV/c (black), 10 GeV/c (blue), and 100 GeV/c (red).

780 terial budget of the CMS tracker has two effects: charged particles can undergo “multiple
 781 scattering,” interacting with material in the tracker. This can cause “kinks” in the recon-
 782 structed track. Hadronic particles (charged and neutral) can undergo nuclear interactions,
 783 which are a hard collisions between the incident particle and a nucleus in tracker material.
 784 This typically produces a spray of hadrons from the point of interaction. Finally, the ma-
 785 terial budget can cause “photon conversions.” A photon conversion occurs when a photon
 786 (which typically does not interact with the tracker) converts into an electron–positron pair
 787 while passing through material in the tracker.

788 The expected (from simulation) impact parameter and transverse momentum resolu-
 789 tion of the tracker is shown in Figure 2.3. The momentum scale of the tracker has been
 790 measured [25] in 7 TeV 2010 CMS data using $J/\psi \rightarrow \mu^+ \mu^-$ decays and is found to agree
 791 with the prediction from simulation within 5%. The impact parameter and vertex resolu-
 792 tions have also been measured [26] in data and found to be in excellent agreement with the
 793 simulation.

794 2.4 Electromagnetic Calorimeter

795 The electromagnetic calorimeter (ECAL) of CMS is designed to measure the energy of par-
 796 ticles which interact electromagnetically with high precision.⁵. The ECAL is a *scintillation*

⁵One of the design goals of the CMS experiment is to be able to conduct a search for Standard Higgs bosons decaying to pairs of photons. The branching fraction to photons is illustrated in Figure 1.10.

797 detector, and functions by counting the number of photons produced in an electromagnetic
 798 shower inside a crystal. Upon entering the crystal, a charged particle or photon will inter-
 799 act electromagnetically with the crystal, producing a shower of electrons and photons. The
 800 shower will expand until it consists entirely of photons. The crystal is optically clear, so
 801 these photons travel to the rear face of the crystal where they are then counted by a pho-
 802 tomultiplier. The number of detected photons can then be related to the energy that was
 803 deposited in the crystal. At 18°C, about 4.5 photoelectrons will be produced per MeV of de-
 804 posited energy. The ECAL has excellent solid angle coverage, extending to a pseudorapidity
 805 of $|\eta| = 3.0$.

806 The ECAL uses lead tungstate (PbWO_4) crystals as the scintillation medium. The
 807 crystals have a very large density, which allows the calorimeter to be relatively compact.
 808 To be able to correctly measure the energy of electrons and photons, an incident photon or
 809 electron must be completely stopped by interactions with the calorimeter. The quantities
 810 that determine if an electron or photon will be completely contained is the total depth of
 811 the crystal, the crystal density, and the radiation length property X_0 of the crystal. The
 812 radiation length X_0 is defined as the mean distance (normalized to material density) after
 813 which an electron will have lost $(1 - \frac{1}{e})$ of its energy. The PbWO_4 crystals of the CMS
 814 ECAL have a density of 8.28 g/cm^3 and a depth of 230 mm. A single crystal thus has a
 815 total radiation length of $25.8 X_0$, and will capture on average 99.9993% of the energy of an
 816 incident electron. The front face of the crystal is $22 \text{ mm} \times 22 \text{ mm}$, which corresponds to an
 817 $\eta - \phi$ area of 0.00174×0.00174 . The Molière radius of a material is the average radial profile
 818 size of an electromagnetic shower, and for PbWO_4 is 2.2 cm. The fact that the Molière
 819 radius is larger than the size of the individual crystals improves the spatial resolution of
 820 the measurement. As the shower is shared between multiple crystals, the relative amounts
 821 deposited in each crystal allows the true impact point to be determined with a resolution
 822 smaller than the individual crystal size.

823 The transparency of the CMS ECAL crystals change as they are exposed to radiation.
 824 However, at the working temperature of the ECAL (18°C), the crystal transparency will
 825 naturally return to its nominal value. The transparency of the crystals thus decreases during
 826 the course of a run of collisions, then increases during the following collision-less period.

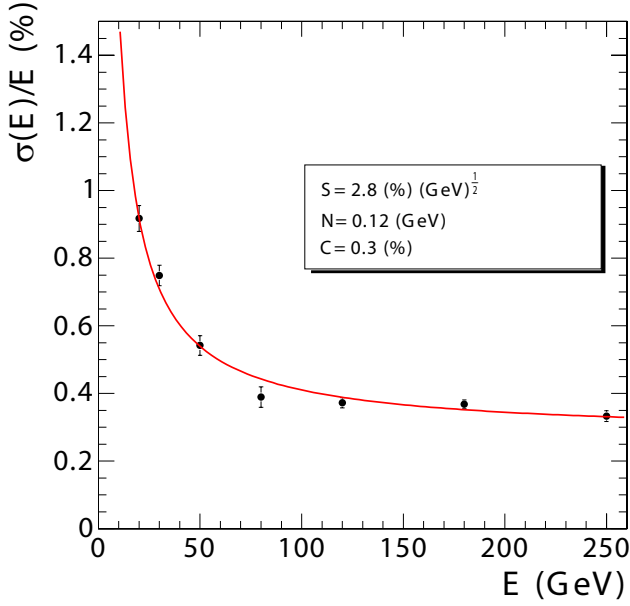


Figure 2.4: Energy resolution (in %) of the CMS ECAL measured at an electron test beam. The resolution depends on the incident energy of the electron. The points are fitted to function with the form given in Equation 2.2. The fitted parameters are given in the legend.

827 The changing transparency conditions need to be continuously monitored and corrected
 828 for to ensure a stable detector response. The transparency of the crystals are measured
 829 continuously using two lasers. One laser has wavelength $\lambda = 400$ nm which corresponds to
 830 the color of light produced in the scintillations and is sensitive to changes in transparency.
 831 The other laser is in the near-infrared and is used to monitor the overall stability of the
 832 crystal. The lasers are synchronized to pulse between LHC bunch trains so the transparency
 833 can be continuously monitored while collisions are occurring.

The energy resolution of the ECAL is given by

$$\left(\frac{\sigma}{E}\right)^2 = \left(\frac{S}{\sqrt{E}}\right)^2 + \left(\frac{N}{E}\right)^2 + C^2, \quad (2.2)$$

834 where S is a stochastic noise term (due to photon counting statistics), N is a noise term, and
 835 C is a constant term. The parameters of Equation 2.2 have been measured at an electron
 836 test-beam (see Figure 2.4). The energy resolution is better than 1% for electron energies
 837 greater than 20 GeV.

838 2.5 Hadronic Calorimeter

839 The hadronic calorimeter (HCAL) surrounds the CMS ECAL and is located within the coil
 840 of the CMS solenoid magnet. To ensure incident particles are completely contained within
 841 the calorimeter volume, in the barrel region the HCAL employs a “tail–catcher”, an extra
 842 layer of calorimetry outside of the magnet. The hadronic calorimeter measures the energy
 843 of charged and neutral hadronic particles. The HCAL is a *sampling* calorimeter. Layers of
 844 plastic scintillating tiles are interspersed between brass absorber plates. An incident hadron
 845 produces a hadronic shower as it passes through the absorber. The particles in the shower
 846 produce light as they pass through the scintillating tiles. Measuring the light produced in
 847 each layer of tile allows the reconstruction of the radial profile of the shower which can be
 848 related to the deposited energy. The response of the scintillator tiles are calibrated using a
 849 radioactive source, either Cs¹³⁷ or Co⁶⁰. Small stainless tubes permit the radioactive sources
 850 to be moved into the center of the tile during calibration. The granularity of the HCAL is
 851 0.087 × 0.087 and 0.17 × 0.17 in $\eta - \phi$ in the barrel ($|\eta| < 1.6$) and endcap ($|\eta| > 1.6$),
 852 respectively.

853 The outer HCAL (HO), or “tail catcher” is designed to capture showers which begin
 854 late in the ECAL or HCAL and ensure they do not create spurious signals in the muon
 855 system (“punch through”). The HO is installed outside of the solenoid magnet in the first
 856 layer between the first two layers of the iron return yoke. The total depth of the HCAL,
 857 including the HO is then 11.8 interaction lengths.

858 The HCAL includes a specially designed forward calorimeter (HF). The design of the
 859 forward calorimeter is constrained by the extreme amount of radiation it is exposed to,
 860 particularly at the highest rapidities. The active material of the HF are quartz fibers. The
 861 fibers are installed inside grooves inside of a steel absorber. Charged particles created in
 862 showers in the absorber create light in the fibers, provided they have energy greater than
 863 the with energy greater than the Cherenkov threshold. As Cherenkov light is created by
 864 the passage of charged particles through matter, the HF design is not sensitive to neutrons
 865 emitted by radionucleids that may be created in the absorber material durin operation.
 866 The fibers are grouped into two sets: one set of fibers are installed over the full depth of

867 the detector, the other only cover half the depth. A crude form of particle identification
 868 is possible, as showers created by electrons and photons will deposit the majority of the
 869 energy in the front of the detector.

870 2.6 Muon System

871 The ability to detect and measure muons is one of the most valuable tools an experimentalist
 872 has at a hadron collider experiment. Muons have particular properties that cause them to
 873 leave extremely unique signatures in the detectors.

874 • Muons are stable particles, for the typical energies and distances considered at a
 875 collider.

876 • Muons have non-zero charge, so their trajectories can be measured.

877 • Muons are heavy enough and only interact electromagnetically so they lose very little
 878 energy as they pass through the calorimeters.

879 The approach to detecting muons is to build the detector to a thickness such that other
 880 particles (electrons, photons, hadrons) will not penetrate the outermost calorimeter. Any
 881 charged particle that is detected outside of this region can then be identified as a muon. At
 882 CMS, the muon detection systems are built into the magnet return yoke outside of the CMS
 883 calorimeters and magnet, giving them excellent protection (illustrated in Figure 2.5(a))
 884 against hadronic “punch-through.” The purity of particles that reach the muon system
 885 make it especially effective as a “trigger” of interesting physics. The CMS muon system has
 886 the feature that it additionally can trigger on muons above a certain transverse momentum
 887 threshold. The CMS muon system is composed of three types of detectors: drift tubes (DT),
 888 resistive plate chambers (RPC), and cathode strip chambers (CSC).

889 A drift tube detector is of a tube filled with a mixture of argon (85%) and carbon
 890 dioxide (15%) gas with a positively charged ($V = +3.6$ kV) wire running through the
 891 middle of the tube. When a charged particle passes through the tube, it ionizes some gas.
 892 The free electrons are then drawn to the positively charged wire inside the tube, creating a
 893 signal when it reaches it. The speed of the detector is limited by the “drift time,” the maximum

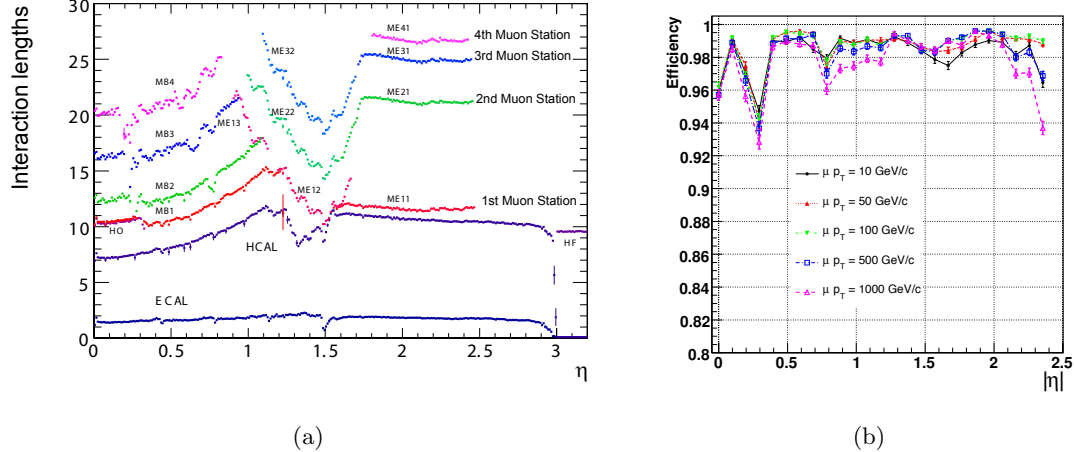


Figure 2.5: The left figure, (a), illustrates the number of interaction lengths versus pseudorapidity η of material that must be traversed before reaching the different layers of the muon system. On the right, (b) shows the efficiency versus η to reconstruct a “global” muon for different transverse momenta.

amount of time it may take for an electron to reach a sensor wire. The precision of the spatial measurement can be increased by recording the time at which each wire records a signal and correlating the measurements across multiple tubes. The time resolution of the CMS DTs is on the order of a few nanoseconds, allowing the DT to provide a trigger on a given proton bunch crossing. The tubes in adjacent layers are offset by one half tube width to take advantage of this effect and ensure there are no gaps in the fiducial region. In CMS, the smallest unit of the DT system is the superlayer, which consists of four layers of tubes. A DT chamber consists of three or two superlayers. The tubes in the two superlayers farthest from the beam are oriented parallel to the beam and measured the bending of the muons in the magnetic field. The inner superlayer is oriented orthogonally to the beam and measures the longitudinal position of incident muons. There are four muon “stations” in the barrel which contain DT chambers. The stations correspond to available areas in the magnetic return yoke.

Cathode strip chambers (CSCs) are used in the endcap muon system, providing coverage in the pseudorapidity range $0.9 < |\eta| < 2.4$. A cathode strip chamber consists of a chamber filled with inert gas that with a number of internal wires held at a high voltage. A

910 number of cathode strips are installed perpendicular⁶ to the wires on the walls of the cham-
 911 ber. When a muon passes through the CSC, it ionizes some of the gas. The high voltage on
 912 a nearby wire causes this ionized gas to break down, forming a conductive passage in the
 913 gas and an “avalanche” current between the wire and a number of the cathode strips. The
 914 spatial position of the hit in two dimensions is found taking one coordinate from the wire
 915 and the other coordinate from the signal average of the cathode strips.

916 The CSCs in the CMS endcap are positioned such that a muon in the pseudorapidity
 917 range $1.2 < |\eta| < 2.4$ will cross three or four CSC detectors. The geometry of the CSC
 918 strips and wires is designed to provided a spatial $r - \phi$ resolution of 2 mm at the L1 trigger
 919 level and a final offline reconstruction resolution of 75 μm for the first layer and 150 μm for
 920 outer layers. The RMS of the response time for a CSC layer is about 11 ns, which is too
 921 long to correctly associate a signal in the CSCs to an LHC bunch crossing (25 ns) with
 922 high efficiency. By grouping the layers into chambers, and taking the shortest response, the
 923 correct bunch crossing can be identified with 98–99% efficiency.

924 The Resistive Plate Chamber (RPC) muon detectors ensure that the muon system can
 925 be used as a fast, first-level trigger. The RPC detector consists of two gaps filled with gas
 926 (up and down) with a common set of strips between the two gaps. The strips are oriented
 927 parallel to the beam line to permit measurement of the transverse momentum of the muons.

928 2.7 Trigger System

929 At the LHC, proton bunches crossings (collisions) occur every 25 ns. This corresponds to
 930 an interaction rate of 40 MHz. At this high rate, and with the huge number of channels
 931 in the CMS detector, the front-end bandwidth readout from the detector is over 1 Pb/s.
 932 Due to bandwidth and storage requirements, the rate at which events are permanently
 933 recorded must be reduced by more than a factor of a million. This reduction is achieved
 934 by CMS trigger system. As only a fraction of the total events can be stored, and the rate
 935 of diffractive and common QCD multi-jet production is many orders of magnitude larger
 936 than “interesting” new physics (see Figure 1.11). The trigger must therefore be designed to

⁶The wires are actually placed at an angle to the perpendicular to compensate for a shifting effect caused by the magnetic field Lorentz force.

937 select “interesting” events. A typical requirement applied at the trigger level might be the
 938 presence of a high- p_T muon, an isolated ECAL deposit, or a large deposit of energy in the
 939 event.

940 The CMS trigger consists of two stages: a fast Level–1 (L1) trigger and a High–Level
 941 Trigger (HLT). The L1 trigger system is built on custom, typically reprogrammable elec-
 942 tronics and interfaces directly to the detector subsystems. The L1 trigger has access to
 943 information from the muon and calorimeter systems. The L1 does not have access to the
 944 full granularity of the muon system and calorimeters but must make the decision based
 945 on coarse segments. The design acceptance rate of the L1 trigger is 100 kHz. The trigger
 946 typically operates at a nominal rate of 30 kHz. The maximum latency of the L1 is 3.2 μ s,
 947 requiring that the output from detector electronics be passed through memory pipelines to
 948 ensure that no bunch crossings go unanalyzed. The High–Level Trigger (HLT) runs on a
 949 farm of about 1000 commercial compute nodes and processes events that are accepted by
 950 the L1 trigger. An HLT decision (“path”) has the ability to reconstruct tracks and do a full
 951 regional unpacking of the recorded hits in a regions of the calorimeter. Each HLT path has
 952 a strict rate budget, as the total rate of the HLT is required to be less than 100 Hz. The
 953 triggers used at CMS change as the conditions change. To limit the total rate to 100 Hz as
 954 the luminosity increases, trigger paths must either increase their thresholds, or apply a
 955 “prescale.” When a prescale is applied, a fraction of events passing the trigger are thrown
 956 away randomly.

957 The CMS trigger is a deep subject and a complete description is beyond the scope of
 958 this thesis. A detailed description can be found in [27]. The triggers used in the analysis
 959 presented in this thesis will be briefly described. Two types of trigger selections were applied
 960 to the 2010 datasets used in this analysis. During the initial period of low luminosity running,
 961 single muon triggers were used. As the luminosity increased, the p_T threshold of the trigger
 962 was increased. In some cases, an “isolated muon” HLT trigger was required, in which a veto
 963 was applied on muons with associated energy deposits in the calorimeter. In the final period
 964 of data taking, two “cross–triggers” were used. These required the presence of both a muon
 965 and a hadronic tau decay in the event. The triggers used in this analysis in the different
 966 2010 run periods are enumerated in Table 5.1.

967 The muon component of all the triggers used in this analysis is based on the “L1 seed
968 trigger” L1_SingleMu7, which nominally selects event which contain a muon with $p_T >$
969 7 GeV/c. The L1 muon trigger decision is determined by the Global Muon Trigger (GMT),
970 which combines information from the DT, CSC, and RPC sub-detectors, and is able to
971 trigger muons up to a pseudorapidity of $|\eta| < 2.1$. Each sub-detector has a “local trigger,”
972 which can reconstruct tracks in the muon system. For the drift tubes, the Bunch Track
973 Identifiers (BTI), a custom integrated circuit, searches for aligned hits in the associated
974 DT chamber. The CSCs and RPCs employ similar strategies to detect local muon tracks.
975 The sub-detectors send the GMT the charge, p_T , η , ϕ , and a quality code of up to four
976 local muons. The measurements from the sub-detectors are combined and a final decision
977 is made by the GMT.

Chapter 3

978

Tau Identification: The Tau Neural Classifier

979

980

981 Excellent tau identification performance is important for the discovery potential of many
 982 possible new physics signals at CMS. The standard model background rates from true tau
 983 leptons are typically the same order of magnitude as the expected signal rate in many
 984 searches for new physics. The challenge of doing physics with taus is driven by the rate
 985 at which objects are incorrectly tagged as taus. In particular, quark and gluon jets have a
 986 significantly higher production cross-section and events where these objects are incorrectly
 987 identified as tau leptons can dominate the backgrounds of searches for new physics using
 988 taus. Efficient identification of hadronic tau decays and low misidentification rate for quarks
 989 and gluons is thus essential to maximize the significance of searches for new physics at CMS.

990 Tau leptons are unique in that they are the only type of leptons which are heavy enough
 991 to decay to hadrons. The hadronic decays comprise approximately 65% of all tau decays, the
 992 remainder being split nearly evenly between $\tau^- \rightarrow \mu^- \bar{\nu}_\mu \nu_\tau$ and $\tau^- \rightarrow e^- \bar{\nu}_e \nu_\tau$. The hadronic
 993 decays are typically composed of one or three charged pions and zero to two neutral pions.
 994 The neutral pions decay almost instantaneously to pairs of photons.

995 In this chapter, we describe a technique to identify hadronic tau decays. Tau decays
 996 to electrons and muons are difficult to distinguish from prompt production of electrons and
 997 muons in pp collisions. Analyses that use exclusively use the leptonic (e, μ) decays of taus
 998 typically require that the decays be of opposite flavor. With the Tau Neural Classifier, we
 999 aim to improve the discrimination of true hadronic tau decays from quark and gluon jets
 1000 using a neural network approach.

1001 3.1 Geometric Tau Identification Algorithms

1002 The tau identification strategies used in previously published CMS analyses are fully de-
 1003 scribed in [28]. A summary of the basic methods and strategies is given here. There are
 1004 two primary methods for selecting objects used to reconstruct tau leptons. The CaloTau
 1005 algorithm uses tracks reconstructed by the tracker and clusters of hits in the electromag-
 1006 netic and hadronic calorimeter. The other method (PFTau) uses objects reconstructed by
 1007 the CMS particle flow algorithm, which is described in [29]. The particle flow algorithm
 1008 provides a global and unique description of every particle (charged hadron, photon, elec-
 1009 tron, etc.) in the event; measurements from subdetectors are combined according to their
 1010 measured resolutions to improve energy and angular resolution and reduce double counting.
 1011 All of the tau identification strategies described in this thesis use the particle flow objects.

1012 Both methods typically use an “leading object” and an isolation requirement to reject
 1013 quark and gluon jet background. Quark and gluon jets are less collimated and have a higher
 1014 constituent multiplicity and softer constituent p_T spectrum than a hadronic tau decay of
 1015 the same transverse momentum. The “leading track” requirement is applied by requiring a
 1016 relatively high momentum object near the center of the jet; typically a charged track with
 1017 transverse momentum greater than 5 GeV/c within $\Delta R < 0.1$ about the center of the jet
 1018 axis. The isolation requirement exploits the collimation of true taus by defining an isolation
 1019 annulus about the kinematic center of the jet and requiring no detector activity about a
 1020 threshold in that annulus. This approach yields a misidentification rate of approximately 1%
 1021 for QCD backgrounds and a hadronic tau identification efficiency of approximately 50% [28].

1022 3.2 Decay Mode Tau Identification: Motivation

1023 The tau identification strategy described previously can be extended by looking at the dif-
 1024 ferent hadronic decay modes of the tau individually. The dominant hadronic decays of taus
 1025 consist of a one or three charged π^\pm mesons and up to two π^0 mesons and are enumerated
 1026 in Table 1.4. The majority of these decays proceed through intermediate resonances and
 1027 each of these decay modes maps directly to a tau final state multiplicity. Each intermediate
 1028 resonance has a different invariant mass (see Figure 3.1). This implies that the problem of

hadronic tau identification can be re-framed from a global search for collimated hadrons satisfying the tau mass constraint into a ensemble of searches for single production of the different hadronic tau decay resonances. The Tau Neural Classifier algorithm implements this approach using two complimentary techniques: a method to reconstruct the decay mode and an ensemble of neural network classifiers used to identify each decay mode resonance and reject quark and gluon jets with the same final state topology.

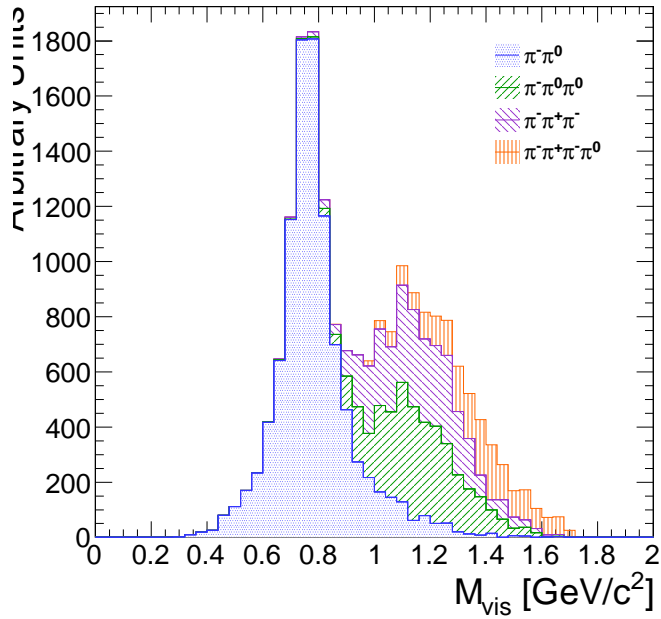


Figure 3.1: The invariant mass of the visible decay products in hadronic tau decays. The decay mode $\tau^- \rightarrow \pi^- \nu_\tau$ is omitted. The different decay modes have different invariant masses corresponding to the intermediate resonance in the decay.

3.3 The Tau Neural Classifier

The Tau Neural Classifier (TaNC) algorithm reconstructs the decay mode of the tau candidate and then feeds the tau candidate to a discriminator associated to that decay mode to make the classification decision. Each discriminator therefore maps to a reconstructed decay mode in a one-to-one fashion. To optimize the discrimination for each of the different decay modes, the TaNC uses an ensemble of neural nets. Each neural net corresponds to one of the dominant hadronic decay modes of the tau lepton. These selected hadronic decays

1042 constitute 95% of all hadronic tau decays. Tau candidates with reconstructed decay modes
 1043 not in the set of dominant hadronic modes are immediately tagged as background.

1044 3.3.1 Decay Mode Reconstruction

1045 The major task in reconstructing the decay mode of the tau is determining the number of
 1046 π^0 mesons produced in the decay. A π^0 meson decays almost instantaneously to a pair of
 1047 photons. The photon objects are reconstructed using the particle flow algorithm [29]. The
 1048 initial collection of photon objects considered to be π^0 candidates are the photons in the
 1049 signal cone described by using the “shrinking-cone” tau algorithm, described elsewhere [28].

1050 The reconstruction of photons from π^0 decays present in the signal cone is complicated
 1051 by a number of factors. To suppress calorimeter noise and underlying event photons, all
 1052 photons with minimum transverse energy less than 0.5 GeV are removed from the signal
 1053 cone, which removes some signal photons. Photons produced in secondary interactions,
 1054 pile-up events, and electromagnetic showers produced by signal photons that convert to
 1055 electron–positron pairs can contaminate the signal cone with extra low transverse energy
 1056 photons. Highly boosted π^0 mesons may decay into a pair of photons with a small opening
 1057 angle, resulting in two overlapping showers in the ECAL being reconstructed as one photon.
 1058 The π^0 meson content of the tau candidate is reconstructed in two stages. First, photon
 1059 pairs are merged together into candidate π^0 mesons. The remaining unmerged photons are
 1060 then subjected to a quality requirement.

1061 3.3.2 Photon Merging

1062 Photons are merged into composite π^0 candidates by examining the invariant mass of all
 1063 possible pairs of photons in the signal region. Only π^0 candidates (photon pairs) with a
 1064 composite invariant mass less than 0.2 GeV/c are considered. The combination of the high
 1065 granularity of the CMS ECAL and the particle flow algorithm provide excellent energy
 1066 and angular resolution for photons; the π^0 mass peak is readily visible in the invariant
 1067 mass spectrum of signal photon pairs (see figure 3.3.2). The π^0 candidates that satisfy the
 1068 invariant mass requirement are ranked by the difference between the composite invariant
 1069 mass of the photon pair and the invariant mass of the π^0 meson given by the PDG [20]. The

1070 best pairs are then tagged as π^0 mesons, removing lower-ranking candidate π^0 s as necessary
 1071 to ensure that no photon is included in more than one π^0 meson.

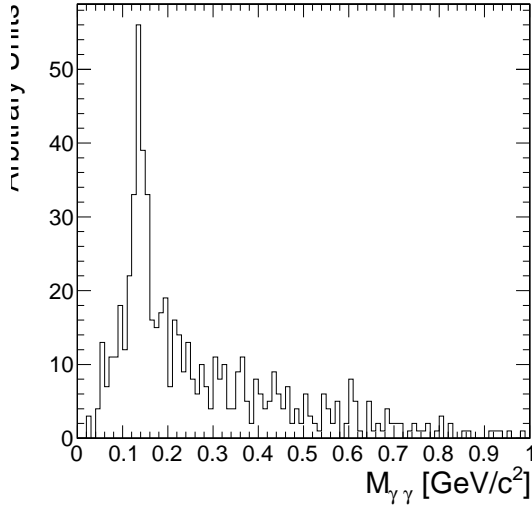


Figure 3.2: Invariant mass of the photon pair for reconstructed tau candidates with two reconstructed photons in the signal region that are matched to generator level $\tau^- \rightarrow \pi^- \pi^0 \nu_\tau$ decays.

1072 3.3.3 Quality Requirements

1073 Photons from the underlying event and other reconstruction effects cause the number of
 1074 reconstructed photons to be greater than the true number of photons expected from a given
 1075 hadronic tau decay. Photons that have not been merged into a π^0 meson candidate are
 1076 recursively filtered by requiring that the fraction of the transverse momentum carried by
 1077 the lowest p_T photon be greater than 10% with respect to the entire (tracks, π^0 candidates,
 1078 and photons) tau candidate. In the case that a photon is not merged but meets the minimum
 1079 momentum fraction requirement, it is considered a π^0 candidate. This requirement removes
 1080 extraneous photons, while minimizing the removal of single photons that correspond to a
 1081 true π^0 meson (see Figure 3.3). A mass hypothesis with the nominal [20] value of the π^0
 1082 is applied to all π^0 candidates. All objects that fail the filtering requirements are moved to
 1083 the isolation collection.

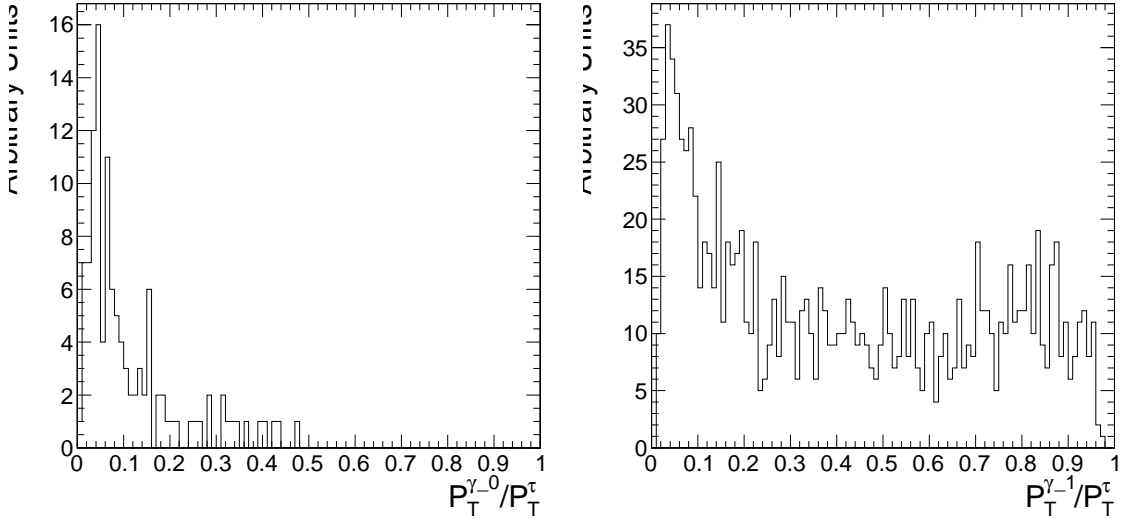


Figure 3.3: Fraction of total τ -candidate transverse momenta carried by the photon for reconstructed taus containing a single photons for two benchmark cases. On the left, the reconstructed tau candidate is matched to generator level $\tau^- \rightarrow \pi^- \nu_\tau$ decays, for which no photon is expected. On the right, the reconstructed tau candidate is matched to generator level $\tau^- \rightarrow \pi^- \pi^0 \nu_\tau$ decays and the photon is expected to correspond to a true π^0 meson. The requirement on the p_T fraction of the lowest p_T photon improves the purity of the decay mode reconstruction.

1084 3.3.4 Performance

1085 The performance of the decay mode reconstruction can be measured for tau candidates that
 1086 are matched to generator level hadronically decaying tau leptons by examining the correla-
 1087 tion of the reconstructed decay mode to the true decay mode determined from the Monte
 1088 Carlo generator level information. Figure 3.4 compares the decay mode reconstruction per-
 1089 formance of a naive approach where the decay mode is determined by simply counting
 1090 the number of photons to the performance of the photon merging and filtering approach
 1091 described in Section 3.3.1. The correlation for the merging and filtering algorithm is much
 1092 more diagonal, indicating higher performance. The performance is additonally presented for
 1093 comparison in tabular form in Table 3.3.4 (merging and filtering approach) and Table 3.3.4
 1094 (naive approach).

1095 The performance of the decay mode reconstruction is dependent on the transverse
 1096 momentum and η of the tau candidate and is shown in Figure 3.5. The p_T dependence
 1097 is largely due to threshold effects; high multiplicity decay modes are suppressed at low

1098 transverse momentum as the constituents are below the minimum p_T quality requirements.
 1099 In the forward region, nuclear interactions and conversions from the increased material
 1100 budget enhances modes containing π^0 mesons.

True decay mode	Reconstructed Decay Mode					
	$\pi^- \nu_\tau$	$\pi^- \pi^0 \nu_\tau$	$\pi^- \pi^0 \pi^0 \nu_\tau$	$\pi^- \pi^+ \pi^- \nu_\tau$	$\pi^- \pi^+ \pi^- \pi^0 \nu_\tau$	Other
$\pi^- \nu_\tau$	14.8%	1.6%	0.4%	0.1%	0.0%	0.7%
$\pi^- \pi^0 \nu_\tau$	6.0%	17.1%	9.0%	0.1%	0.1%	5.5%
$\pi^- \pi^0 \pi^0 \nu_\tau$	0.9%	3.8%	4.2%	0.0%	0.1%	5.9%
$\pi^- \pi^+ \pi^- \nu_\tau$	0.8%	0.3%	0.1%	9.7%	1.6%	6.2%
$\pi^- \pi^+ \pi^- \pi^0 \nu_\tau$	0.1%	0.2%	0.1%	1.7%	2.7%	4.5%

Table 3.1: Decay mode correlation table for the selected dominant decay modes for the naive approach. The percentage in a given row and column indicates the fraction of hadronic tau decays from $Z \rightarrow \tau^+ \tau^-$ events that are matched to a generator level decay mode given by the row and are reconstructed with the decay mode given by the column. Entries in the “Other” column are immediately tagged as background.

True decay mode	Reconstructed Decay Mode					
	$\pi^- \nu_\tau$	$\pi^- \pi^0 \nu_\tau$	$\pi^- \pi^0 \pi^0 \nu_\tau$	$\pi^- \pi^+ \pi^- \nu_\tau$	$\pi^- \pi^+ \pi^- \pi^0 \nu_\tau$	Other
$\pi^- \nu_\tau$	16.2%	1.0%	0.1%	0.1%	0.0%	0.3%
$\pi^- \pi^0 \nu_\tau$	10.7%	21.4%	3.6%	0.2%	0.1%	1.9%
$\pi^- \pi^0 \pi^0 \nu_\tau$	1.8%	7.1%	4.4%	0.1%	0.0%	1.5%
$\pi^- \pi^+ \pi^- \nu_\tau$	0.9%	0.2%	0.0%	11.5%	0.6%	5.4%
$\pi^- \pi^+ \pi^- \pi^0 \nu_\tau$	0.1%	0.3%	0.0%	3.2%	2.9%	2.7%

Table 3.2: Decay mode correlation table for the selected dominant decay modes for the merging and filtering approach. The percentage in a given row and column indicates the fraction of hadronic tau decays from $Z \rightarrow \tau^+ \tau^-$ events that are matched to a generator level decay mode given by the row and are reconstructed with the decay mode given by the column. Entries in the “Other” column are immediately tagged as background.

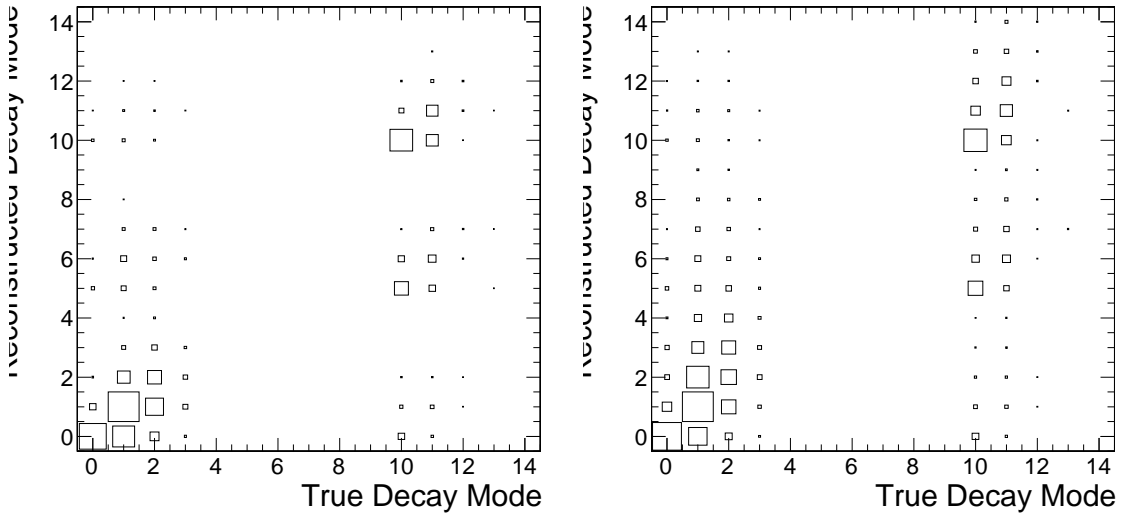


Figure 3.4: Correlations between reconstructed tau decay mode and true tau decay mode for hadronic tau decays in $Z \rightarrow \tau^+\tau^-$ events. The correlation when no photon merging or filtering is applied is shown on the right, and the correlation for the algorithm described in Section 3.3.1 is on the right. The horizontal and vertical axis are the decay mode indices of the true and reconstructed decay mode, respectively. The decay mode index N_{DM} is defined as $N_{DM} = (N_{\pi^\pm} - 1) \cdot 5 + N_{\pi^0}$. The area of the box in each cell is proportional to the fraction of tau candidates that were reconstructed with the decay mode indicated on the vertical axis for the true tau decay on the horizontal axis. The performance of a decay mode reconstruction algorithm can be determined by the spread of the reconstructed number of π^0 mesons about the true number (the diagonal entries) determined from the generator level Monte Carlo information. If the reconstruction was perfect, the correlation would be exactly diagonal.

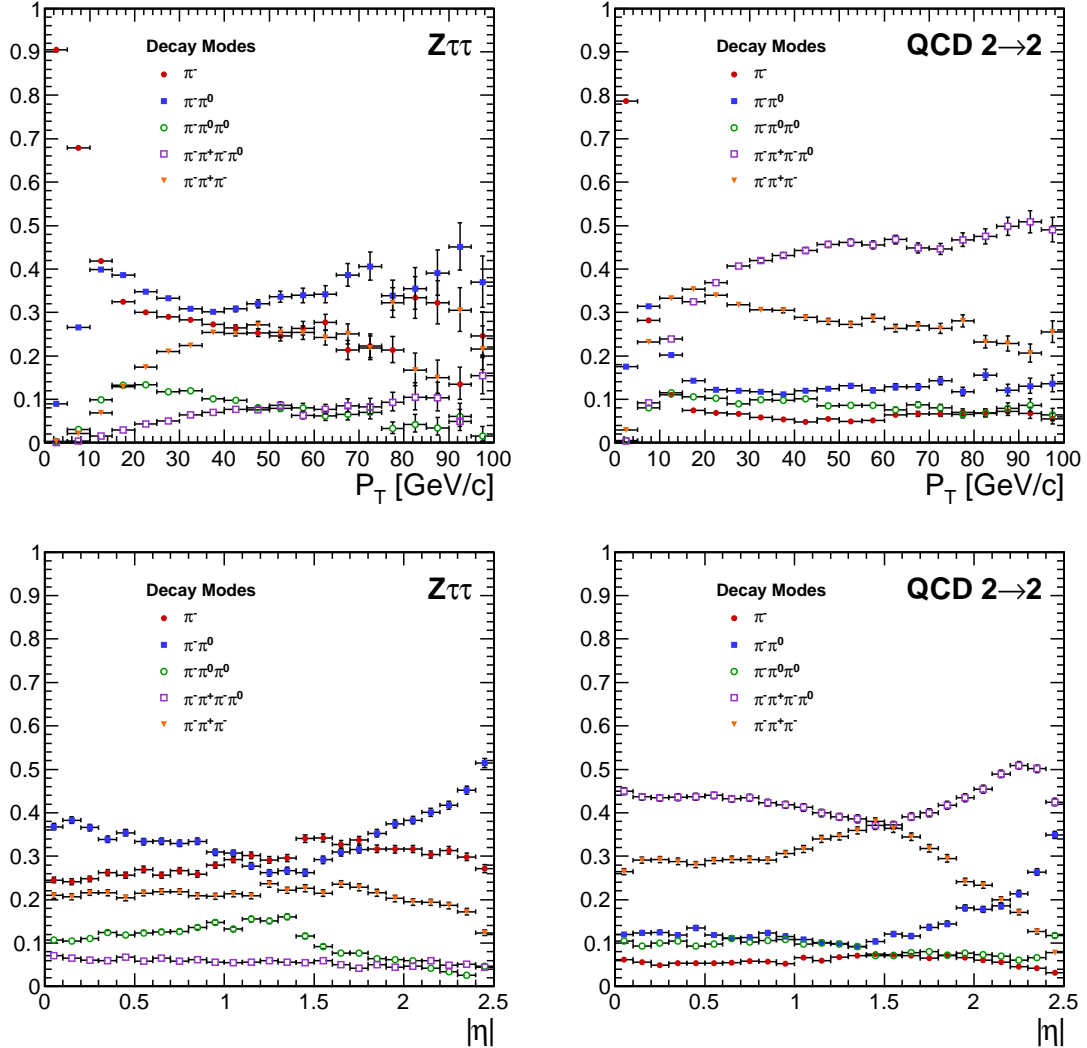


Figure 3.5: Kinematic dependence of reconstructed decay mode for tau candidates in $Z \rightarrow \tau^+\tau^-$ (left) and QCD dijets (right) events versus transverse momentum (top) and pseudo-rapidity (bottom). Each curve is the probability for a tau candidate to be reconstructed with the associated decay mode after the leading pion and decay mode preselection has been applied.

1101 3.3.5 Neural Network Classification

1102 3.3.6 Neural Network Training

1103 The samples used to train the TaNC neural networks are typical of the signals and back-
 1104 grounds found in common physics analyses using taus. The signal-type training sample is
 1105 composed of reconstructed tau candidates that are matched to generator level hadronic tau
 1106 decays coming from simulated $Z \rightarrow \tau^+ \tau^-$ events. The background training sample consists
 1107 of reconstructed tau candidates in simulated QCD $2 \rightarrow 2$ hard scattering events. The QCD
 1108 p_T spectrum is steeply falling, and to obtain sufficient statistics across a broad range of p_T
 1109 the sample is split into different \hat{p}_T bins. Each binned QCD sample imposes a generator
 1110 level cut on the transverse momentum of the hard interaction. During the evaluation of
 1111 discrimination performance the QCD samples are weighted according to their respective
 1112 integrated luminosities to remove any effect of the binning.

1113 The signal and background samples are split into five subsamples corresponding to
 1114 each reconstructed decay mode. An additional selection is applied to each subsample by
 1115 requiring a “leading pion”: either a charged hadron or gamma candidate with transverse
 1116 momentum greater than 5 GeV/c. A large number of QCD training events is required as
 1117 both the leading pion selection and the requirement that the decay mode match one of the
 1118 dominant modes given in Table 1.4 are effective discriminants. For each subsample, 80% of
 1119 the signal and background tau candidates are used for training the neural networks, with
 1120 half (40%) used as a validation sample used to ensure the neural network is not over-trained.
 1121 The number of signal and background entries used for training and validation in each decay
 1122 mode subsample is given in Table 3.3.6.

1123 The remaining 20% of the signal and background samples are reserved as a statisti-
 1124 cally independent sample to evaluate the performance of the neural nets after the training
 1125 is completed. The TaNC uses the Multi-layer Perceptron (MLP) neural network implemen-
 1126 tation provided by the TMVA software package, described in [30]. The MLP classifier is a
 1127 feed-forward artificial neural network. There are two layers of hidden nodes and a single
 1128 node in the output layer. The hyperbolic tangent function is used for the neuron activation
 1129 function.

	Signal	Background
Total number of tau candidates	874266	9526176
Tau candidates passing preselection	584895	644315
Tau candidates with $W(p_T, \eta) > 0$	538792	488917
Decay Mode	Training Events	
π^-	300951	144204
$\pi^-\pi^0$	135464	137739
$\pi^-\pi^0\pi^0$	34780	51181
$\pi^-\pi^-\pi^+$	53247	155793
$\pi^-\pi^-\pi^+\pi^0$	13340	135871

Table 3.3: Number of events used for neural network training and validation for each selected decay mode.

The neural networks used in the TaNC have two hidden layers and single node in the output layers. The number of nodes in the first and second hidden layers are chosen to be $N + 1$ and $2N + 1$, respectively, where N is the number of input observables for that neural network. According to the Kolmogorov's theorem [31], any continuous function $g(x)$ defined on a vector space of dimension d spanned by x can be represented by

$$g(x) = \sum_{j=1}^{j=2d+1} \Phi_j \left(\sum_{i=1}^d \phi_i(x) \right) \quad (3.1)$$

for suitably chosen functions for Φ_j and ϕ_j . As the form of Equation 3.1 is similar to the topology of a two hidden-layer neural network, Kolmogorov's theorem suggests that *any* classification problem can be solved with a neural network with two hidden layers containing the appropriate number of nodes.

The neural network is trained for 500 epochs. At ten epoch intervals, the neural network error is computed using the validation sample to check for over-training (see Figure 3.6). The neural network error E is defined [30] as

$$E = \frac{1}{2} \sum_{i=1}^N (y_{ANN,i} - \hat{y}_i)^2 \quad (3.2)$$

1134 where N is the number of training events, $y_{ANN,i}$ is the neural network output for the i th
 1135 training event, and y_i is the desired (-1 for background, 1 for signal) output the i th event.
 1136 No evidence of over-training is observed.

1137 The neural networks use as input observables the transverse momentum and η of the
 1138 tau candidates. These observables are included as their correlations with other observables
 1139 can increase the separation power of the ensemble of observables. For example, the opening
 1140 angle in ΔR for signal tau candidates is inversely related to the transverse momentum,
 1141 while for background events the correlation is very small [32]. In the training signal and
 1142 background samples, there is significant discrimination power in the p_T spectrum. However,
 1143 for a general-purpose tau identification algorithm, it is desirable to eliminate any systematic
 1144 dependence of the neural network output on p_T and η , as in practice the TaNC will be
 1145 presented with tau candidates whose $p_T - \eta$ spectrum will be analysis dependent. The
 1146 optimal situation would be to train the neural networks using the signal and backgrounds
 1147 that are present in the analysis where the algorithm is applied. In practice, it is difficult to
 1148 collect enough training samples for each analysis situation. The dependence on p_T and η is
 1149 removed by applying a p_T and η dependent weight to the tau candidates when training the
 1150 neural nets.

The weights are defined such that in any region in the vector space spanned by p_T
 and η where the signal sample and background sample probability density functions are
 different, the sample with higher probability density is weighted such that the samples have
 identical $p_T - \eta$ probability distributions. This removes regions of $p_T - \eta$ space where the
 training sample is exclusively signal or background. The weights are computed according to

$$W(p_T, \eta) = \text{less}(p_{sig}(p_T, \eta), p_{bkg}(p_T, \eta))$$

$$w_{sig}(p_T, \eta) = W(p_T, \eta)/p_{sig}(p_T, \eta)$$

$$w_{bkg}(p_T, \eta) = W(p_T, \eta)/p_{bkg}(p_T, \eta)$$

1151 where $p_{sig}(p_T, \eta)$ and $p_{bkg}(p_T, \eta)$ are the probability densities of the signal and background
 1152 samples after the “leading pion” and dominant decay mode selections. Figure 3.7 shows the
 1153 signal and background training p_T distributions before and after the weighting is applied.

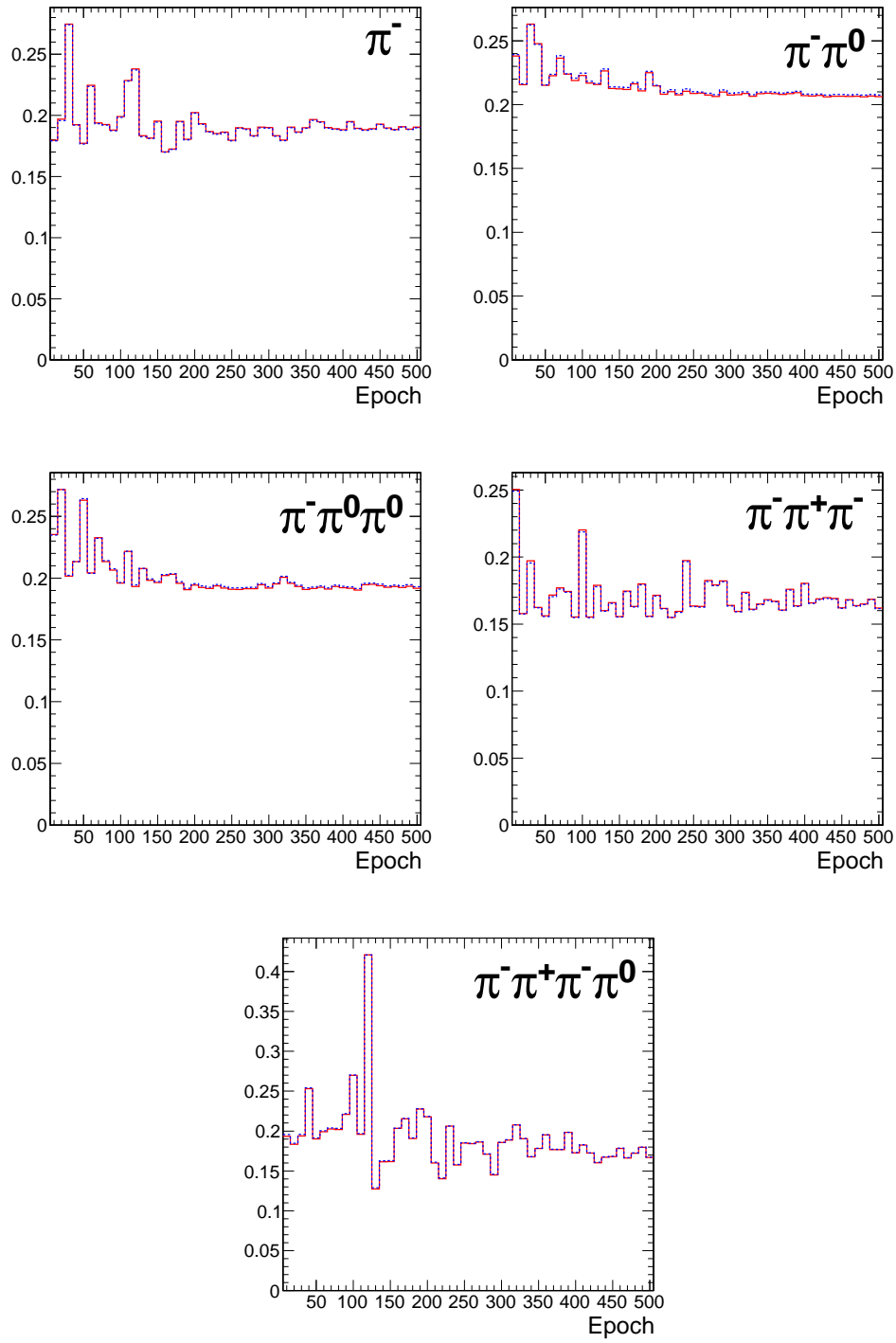


Figure 3.6: Neural network classification error for training (solid red) and testing (dashed blue) samples at ten epoch intervals over the 500 training epochs for each decay mode neural network. The vertical axis represents the classification error, defined by equation 3.2. N.B. that the choice of hyperbolic tangent for neuron activation functions results in the desired outputs for signal and background to be 1 and -1, respectively. This results in the computed neural network error being larger by a factor of four than the case where the desired outputs are (0, 1). Classifier over-training would be evidenced by divergence of the classification error of the training and testing samples, indicating that the neural net was optimizing about statistical fluctuations in the training sample.

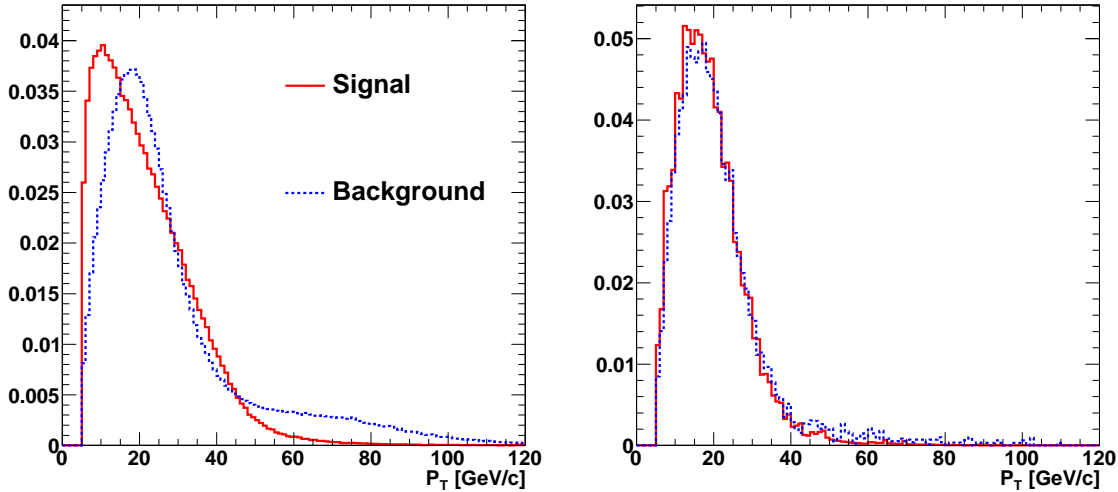


Figure 3.7: Transverse momentum spectrum of signal and background tau candidates used in neural net training before (left) and after (right) the application of $p_T - \eta$ dependent weight function. Application of the weights lowers the training significance of tau candidates in regions of $p_T - \eta$ phase space where either the signal or background samples has an excess of events.

1154 3.3.7 Discriminants

1155 Each neural network corresponds to a different decay mode topology and as such each
 1156 network uses different observables as inputs. However, many of the input observables are
 1157 used in multiple neural nets. The superset of all observables is listed and defined below.
 1158 Table 3.4 maps the input observables to their associated neural networks. In three prong
 1159 decays, the definition of the “main track” is important. The main track corresponds to the
 1160 track with charge opposite to that of the total charge of the three tracks. This distinction is
 1161 made to facilitate the use of the “Dalitz” observables, allowing identification of intermediate
 1162 resonances in three-body decays. This is motivated by the fact that the three prong decays
 1163 of the tau generally proceed through $\tau^- \rightarrow a_1^- \nu_\tau \rightarrow \pi^- \rho^0 \nu_\tau \rightarrow \pi^- \pi^+ \pi^- \nu_\tau$; the oppositely
 1164 charged track can always be identified with the ρ^0 decay.

1165 **ChargedOutlierAngleN** ΔR between the Nth charged object (ordered by p_T) in the
 1166 isolation region and the tau candidate momentum axis. If the number of isolation
 1167 region objects is less than N, the input is set at one.

1168 **ChargedOutlierPtN** Transverse momentum of the Nth charged object in the isolation
 1169 region. If the number of isolation region objects is less than N, the input is set at zero.

1170 **DalitzN** Invariant mass of four vector sum of the “main track” and the Nth signal region
 1171 object.

1172 **Eta** Pseudo-rapidity of the signal region objects.

1173 **InvariantMassOfSignal** Invariant mass of the composite object formed by the signal
 1174 region constituents.

1175 **MainTrackAngle** ΔR between the “main track” and the composite four–vector formed
 1176 by the signal region constituents.

1177 **MainTrackPt** Transverse momentum of the “main track.”

1178 **OutlierNCharged** Number of charged objects in the isolation region.

1179 **OutlierSumPt** Sum of the transverse momentum of objects in the isolation region.

1180 **PiZeroAngleN** ΔR between the Nth π^0 object in the signal region (ordered by p_T) and
 1181 the tau candidate momentum axis.

1182 **PiZeroPtN** Transverse momentum of the Nth π^0 object in the signal region.

1183 **TrackAngleN** ΔR between the Nth charged object in the signal region (ordered by p_T)
 1184 and the tau candidate momentum axis, exclusive of the main track.

1185 **TrackPtN** Transverse momentum of the Nth charged object in the signal region, exclusive
 1186 of the main track.

1187 3.3.8 Neural Network Performance

1188 The classification power of the neural networks is unique for each of the decay modes.
 1189 The performance is determined by the relative separation of the signal and background
 1190 distributions in the parameter space of the observables used as neural network inputs. A
 1191 pathological example is the case of tau candidates with the reconstructed decay mode of

1192 $\tau^- \rightarrow \pi^- \nu_\tau$. If there is no isolation activity, the neural net has no handle with which it
 1193 can separate the signal from the background. The neural net output for tau candidates in
 1194 the testing sample (independent of the training and validation samples) for each of the five
 1195 decay mode classifications is shown in Figure 3.8.

1196 When a single neural network is used for classification, choosing an operating point is
 1197 relatively straightforward: the requirement on neural network output is tuned such that the
 1198 desired purity is attained. However, in the case of the TaNC, multiple neural networks are
 1199 used. Each network has a unique separation power (see Figure 3.9) and each neural network
 1200 is associated to a reconstructed decay mode that composes different relative fractions of the
 1201 signal and background tau candidates. Therefore, a set of five numbers is required to define
 1202 an “operating point” (the signal efficiency and background misidentification rate) in the
 1203 TaNC output. All points in this five dimensional cut–space map to an absolute background
 1204 fake–rate and signal efficiency rate. Therefore there must exist a 5D “performance curve”
 1205 which for any attainable signal efficiency gives the lowest fake–rate. A direct method to
 1206 approximate the performance curve is possible using a Monte Carlo technique.

1207 The maximal performance curve can be approximated by iteratively sampling points in
 1208 the five–dimensional cut space and selecting the highest performance points. The collection
 1209 of points in the performance curve are ordered by expected fake rate. During each iteration,
 1210 the sample point is compared to the point before the potential insertion position of the
 1211 sample in the ordered collection. The sample point is inserted into the collection if it has
 1212 a higher signal identification efficiency than the point before it. The sample point is then
 1213 compared to all points in the collection after it (i.e. those with a larger fake rate); any point
 1214 with a lower signal efficiency than the sample point is removed. After the performance curve
 1215 has been determined, the set of cuts are evaluated on an independent validation sample
 1216 to ensure that the measured performance curve is not influenced by favorable statistical
 1217 fluctuations being selected by the Monte Carlo sampling. The performance curves for two
 1218 different transverse momentum ranges are shown in Figure 3.10.

The 5D performance curve can also be parameterized by using the probability for a tau candidate to be identified for a given decay mode. An artificial neural network maps a point in the space of input observables to some value of neural network output x . The

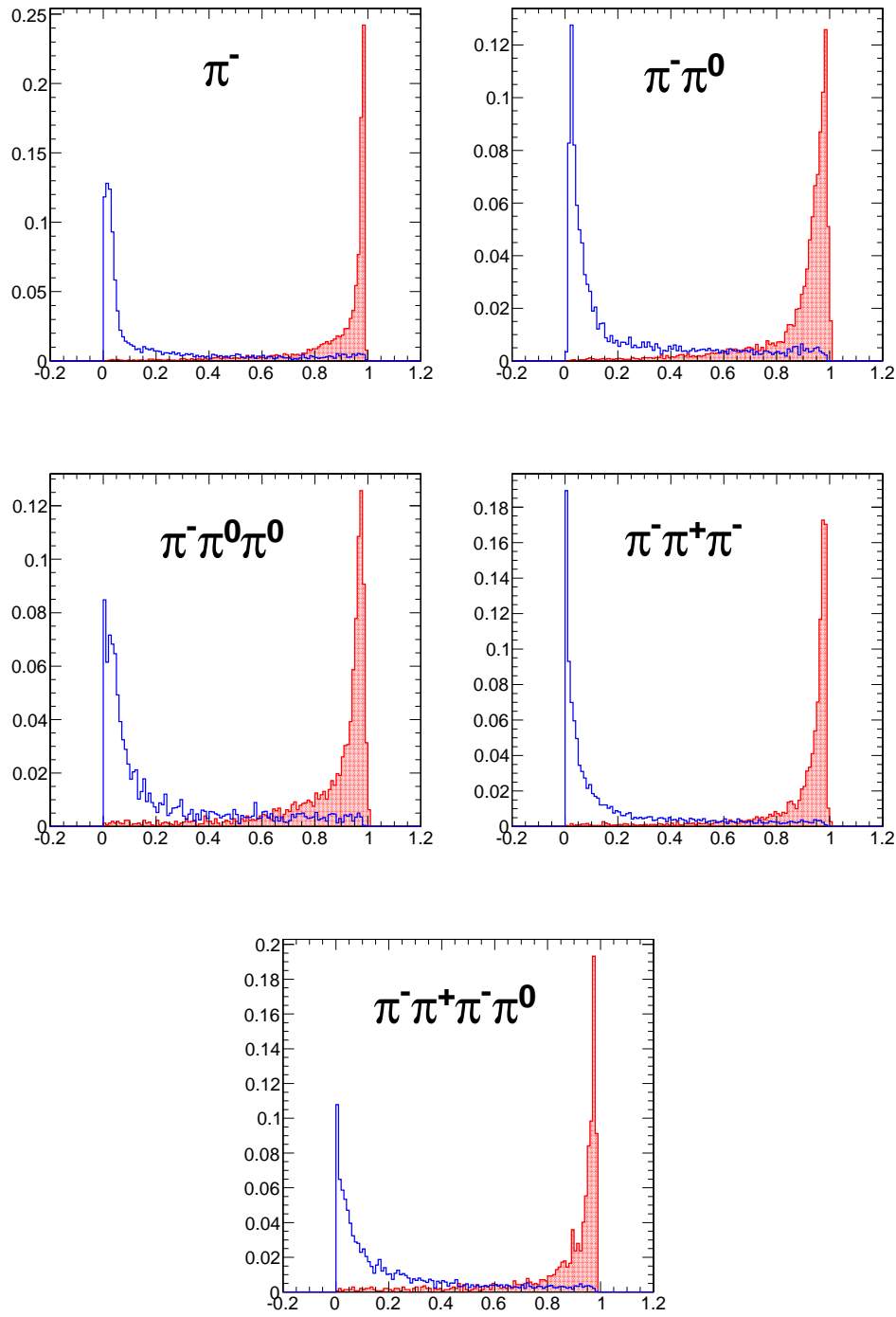


Figure 3.8: Neural network output distributions for the five reconstructed tau candidate decay modes used in the TaNC for $Z \rightarrow \tau^+\tau^-$ events (red) and QCD dijet events (blue).

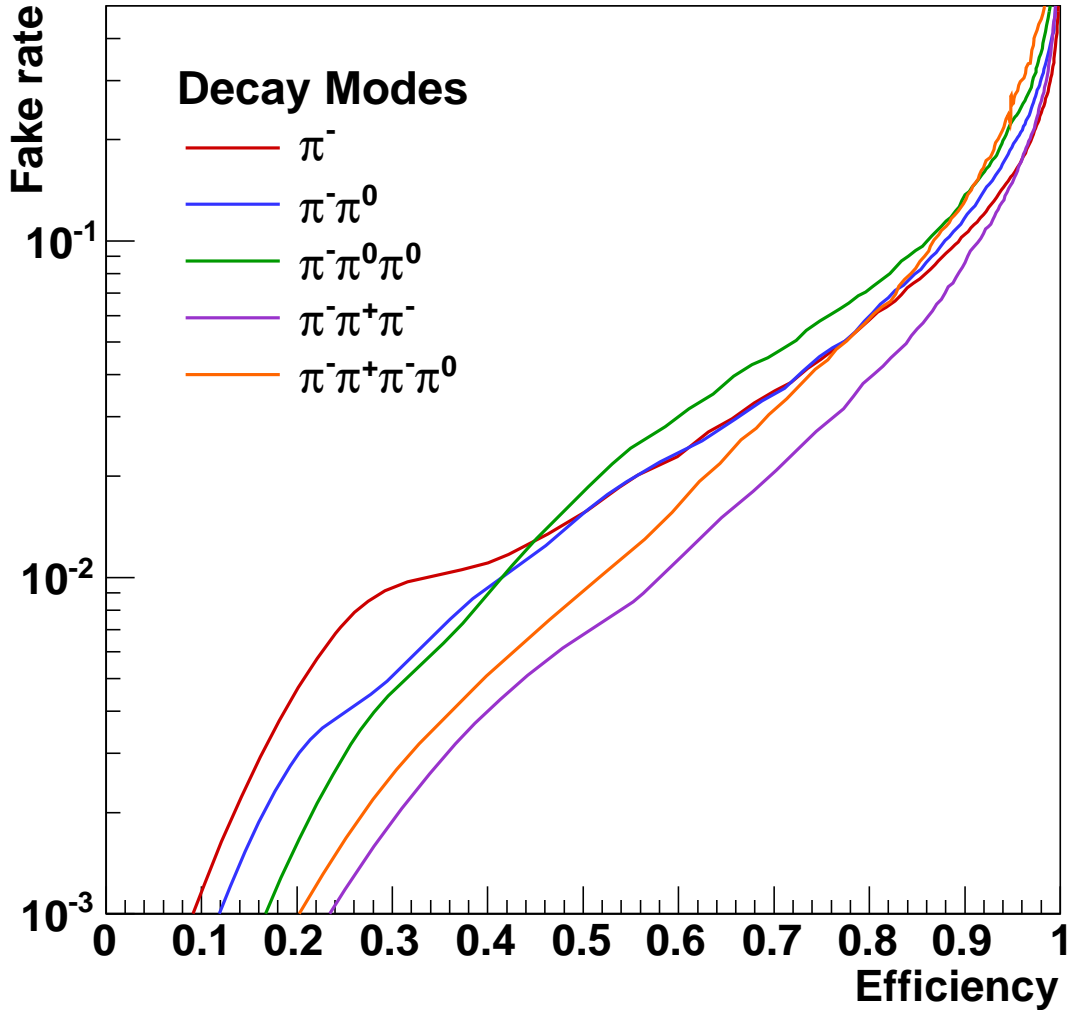


Figure 3.9: Performance curves for the five neural networks used by the TaNC for tau candidates with transverse momentum greater than 20 GeV/c. Each curve represents the signal efficiency (on the horizontal axis) and background misidentification rate (vertical axis) for a scan of the neural network selection requirement for a single neural network. The efficiency (or misidentification rate) for each neural network performance curve is defined with respect to the preselected tau candidates that have the reconstructed decay mode associated with that neural network. Each neural network has a different ability so separate signal and background as each classifier uses different observables as inputs.

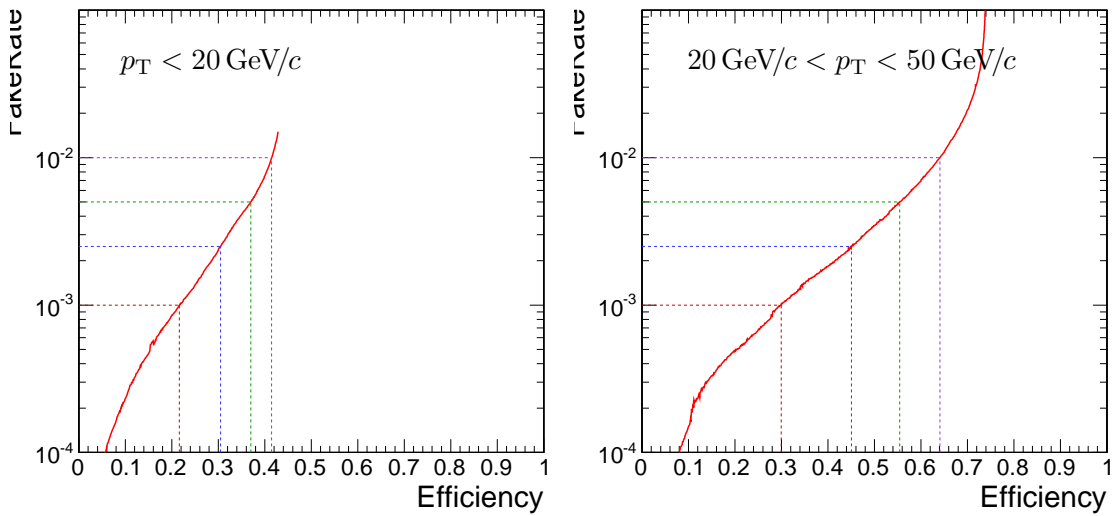


Figure 3.10: Tau Neural Classifier performance curves for tau candidates with $p_T < 20 \text{ GeV}/c$ (left) and $20 < p_T < 50 \text{ GeV}/c$ (right). The vertical axis represents the expected fake-rate of QCD jets and the horizontal axis the expected signal efficiency for hadronic tau decays. The performance curve for the low transverse momentum range is worse due to leading pion selection. While both true taus and QCD are removed by this cut, the selection preferentially keeps the QCD tau candidates with low multiplicities, which increases the number of QCD tau candidates passing the decay mode selection.

neural network training error is given by Equation 3.2. A given point in the vector space spanned by the neural network input observables (denoted as “feature space”) contributes to the neural network training error E by

$$E' = (1 - x)^2 \cdot \rho^\tau + x^2 \cdot \rho^{QCD}$$

1219 where $\rho^\tau(\rho^{QCD})$ denotes the training sample density of the τ signal and QCD-jet back-
1220 ground at that point in feature space.

The value x assigned by the neural network to this region in feature space should satisfy the requirement of minimal error:

$$\begin{aligned} \frac{\partial E'}{\partial x} &= 0 \\ 0 &= -2(1 - x) \cdot \rho^\tau + 2x \cdot \rho^{QCD} \\ x &= \frac{\rho^\tau}{\rho^\tau + \rho^{QCD}} \end{aligned} \tag{3.3}$$

$$\begin{aligned} \rho^\tau &= x(\rho^\tau + \rho^{QCD}) \\ \frac{\rho^{QCD}}{\rho^\tau} &= \frac{1}{x} - 1 \end{aligned} \tag{3.4}$$

1221 The ratio $\frac{\rho^{QCD}}{\rho^\tau}$ corresponds to the ratio of the normalized probability density functions of
1222 signal and background input observable distributions, i.e. $\int \rho^\tau d\vec{x} = 1$.

In the case of multiple neural networks, one can derive a formula that maps the output x_j of the neural network corresponding to decay mode j according to the “prior probabilities” $p_j^\tau(p_j^{QCD})$ for true τ lepton hadronic decays (quark and gluon jets) to pass the preselection criteria and be reconstructed with decay mode j . By substituting $\rho^s \rightarrow \rho^s p_j^s$ for $s \in \{\tau, QCD\}$ in Equation 3.3, the output x_j can be related to $p_j^\tau(p_j^{QCD})$ by

$$x'_j = \frac{\rho^\tau \cdot p_j^\tau}{\rho^\tau \cdot p_j^\tau + \rho^{QCD} \cdot p_j^{QCD}} = \frac{p_j^\tau}{p_j^\tau + \frac{\rho^{QCD}}{\rho^\tau} \cdot p_j^{QCD}} \tag{3.5}$$

Substituting Equation 3.4 into Equation 3.5 yields the transformation of the output x_j of the neural network corresponding to any selected decay mode j to a single discriminator output x'_j which for a given point on the optimal performance curve should be independent

of j .

$$x'_j = \frac{p_j^\tau}{p_j^\tau + \left(\frac{1}{x_j} - 1\right) \cdot p_j^{QCD}} \quad (3.6)$$

In this manner a single number (the “transform cut”) given by Equation 3.6 can be used to specify any point on the performance curve. The training sample neural network output after the transformation has been applied is shown in Figure 3.12. The performance curve for the cut on the transformed output is nearly identical to the optimal performance curve determined by the Monte Carlo sampling technique.

The discriminator output of the TaNC algorithm is a continuous quantity, enabling analysis specific optimization of the selection to maximize sensitivity. For the convenience of the user, four operating point benchmark selections are provided in addition to the continuous output. The four operating points are chosen such that for tau candidates with transverse momentum between 20 and 50 GeV/c, the expected QCD dijet fake rate will be 0.1%, 0.25%, 0.50% and 1.0%, respectively.

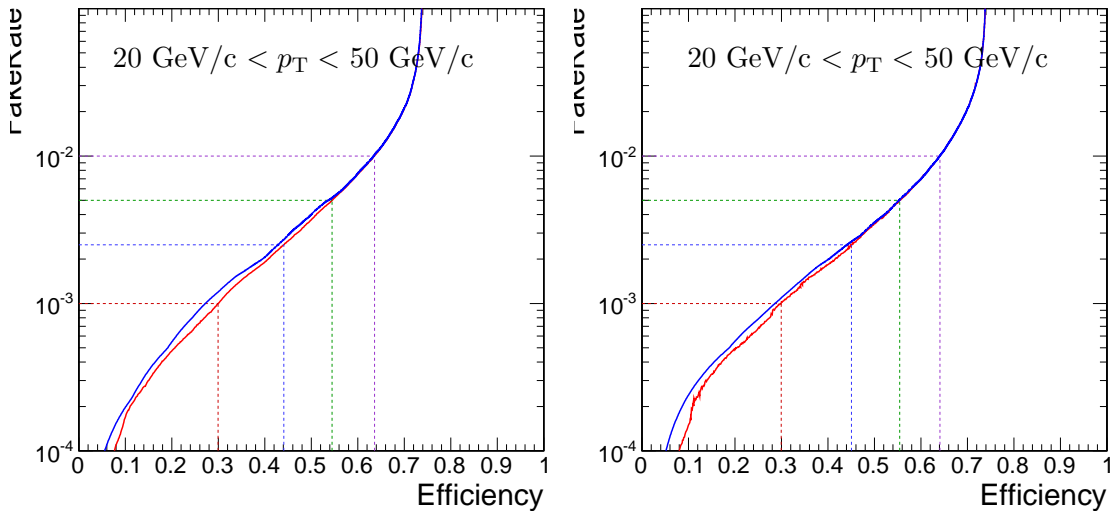


Figure 3.11: Tau Neural Classifier performance curves for tau candidates with $20 < p_T < 50$ GeV/c. The figure on the left compares the optimal performance curve determined by the Monte Carlo sampling method (red) to the performance curve obtained by scanning the “transform cut” (blue) defined in Equation 3.6 from zero to one. The figure on the right is the same set of cuts (and cut transformation values) applied on an independent sample to remove any biases introduced by the Monte Carlo sampling. The four dashed lines indicate the performance for the four benchmark points.

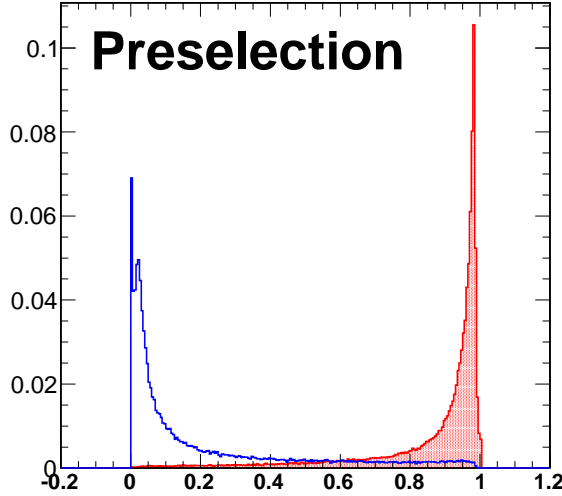


Figure 3.12: Transformed TaNC neural network output for tau candidates with transverse momentum between 20 and 50 GeV/c that pass the pre-selection criteria. The neural network output for each tau candidate has been transformation according to Equation 3.6. The decay mode probabilities ρ_i^{bkg} , ρ_i^{signal} are computed using the entire transverse momentum range of the sample.

1234 3.4 Summary

1235 The Tau Neural classifier introduces two complimentary new techniques for tau lepton
 1236 physics at CMS: reconstruction of the hadronic tau decay mode and discrimination from
 1237 quark and gluon jets using neural networks. The decay mode reconstruction strategy pre-
 1238 sented in Section 3.3.1 significantly improves the determination of the decay mode. This
 1239 information has the potential to be useful in studies of tau polarization and background
 1240 estimation.

1241 The Tau Neural classifier tau identification algorithm significantly improves tau dis-
 1242 crimination performance compared to isolation-based approaches [28] used in previous CMS
 1243 analyses. Figure 3.13 compares the performance of the “shrinking cone” isolation tau-
 1244 identification algorithm [28] to the performance of the TaNC for a scan of requirements
 1245 on the transformed neural network output. The signal efficiency and QCD dijet fake rate
 1246 versus tau candidate transverse momentum and pseudo-rapidity for the four benchmark
 1247 points and the isolation based tau identification are show in Figure 3.14. For tau candi-

1248 dates with transverse momentum between 20 and 50 GeV/ c , the TaNC operating cut can
 1249 be chosen such that the two methods have identical signal efficiency; at this point the TaNC
 1250 algorithm reduces the background fake rate by an additional factor of 3.9. This reduction
 1251 in background will directly improve the significance of searches for new physics using tau
 1252 leptons at CMS.

1253 3.5 HPS+TaNC: A Hybrid Algorithm

1254 The techniques used in the TaNC have been hybridized with techniques used by the “Hadrons
 1255 plus Strips” (HPS) algorithm [33]. The combined algorithm is referred to “Hadrons plus
 1256 Strips and Tau Neural Classifier” (HPS + TaNC) identification algorithm. The algorithm
 1257 combines the HPS methods of constructing the signal components of the tau candidate
 1258 and the discrimination methods of the TaNC algorithm. Both algorithms are based on re-
 1259 constructing individual tau lepton hadronic decay modes, which has been demonstrated to
 1260 improve the tau identification performance significantly with respect to previously used cone
 1261 isolation based algorithms [34]. The HPS + TaNC algorithm first reconstructs the hadronic
 1262 decay mode of the tau, and applies different discriminants based on the reconstructed de-
 1263 cay mode. Identification of hadronic tau decays by the HPS + TaNC algorithm proceeds in
 1264 two stages: first, the hadronic decay mode of the tau is reconstructed and then different
 1265 discriminators are applied, based on the reconstructed decay mode. In the decay mode re-
 1266 construction particular attention is paid to the reconstruction of neutral pions, which are
 1267 expected for the majority of hadronic decay modes.

1268 3.5.1 Decay Mode Reconstruction

1269 The decay mode reconstruction algorithm is seeded by particle-flow jets reconstructed by
 1270 the anti- k_T algorithm [35]. In order to reconstruct the decay mode, the algorithm needs to
 1271 merge photon candidates into candidate π^0 mesons. The π^0 candidates are reconstructed by
 1272 two algorithms which are executed concurrently. The “combinatoric” π^0 algorithm produces
 1273 a π^0 candidate for every possible pair of photons within the jet. The “strips” algorithm clus-
 1274 ters photons strips in $\eta - \phi$. The results of both algorithms are combined and then “cleaned”,

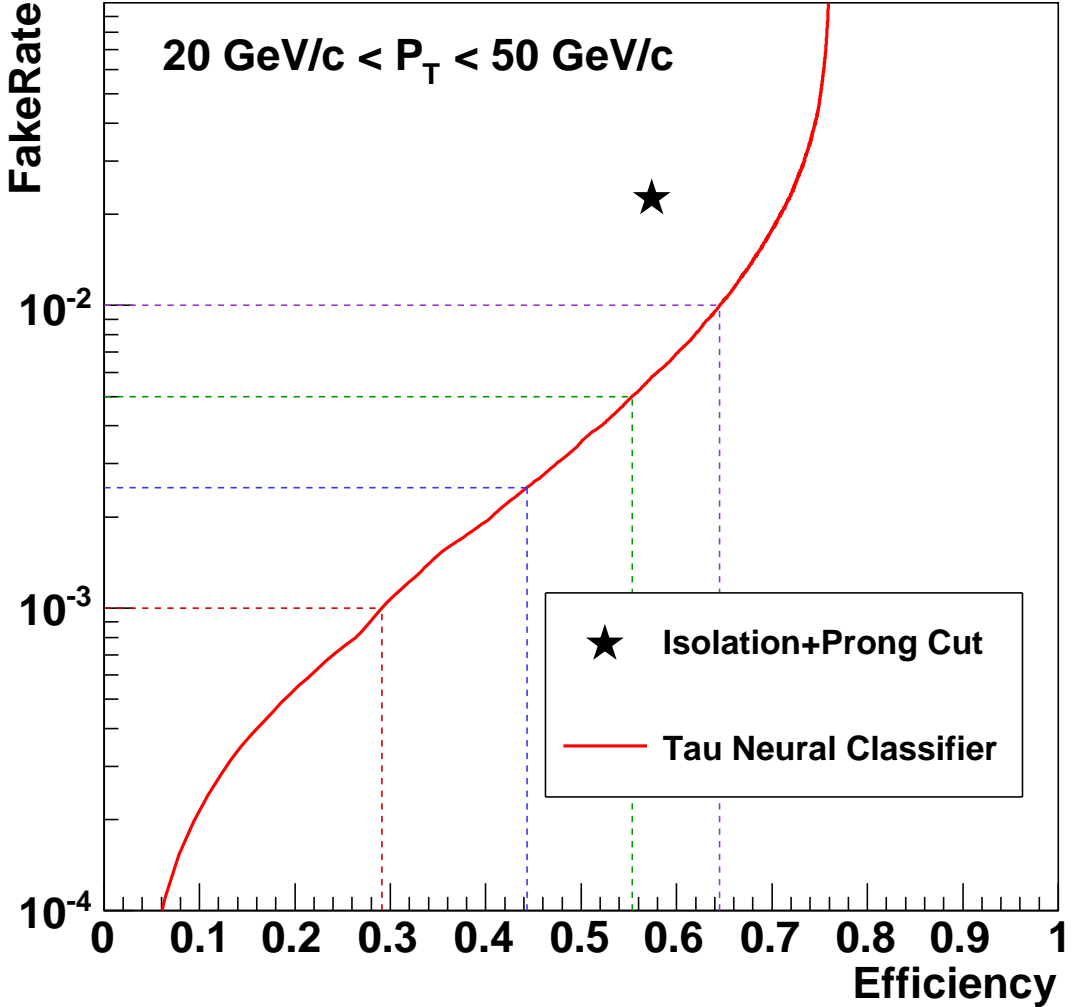


Figure 3.13: Performance curve (red) of the TaNC tau identification for various requirements on the output transformed according to Equation 3.6. The horizontal axis is the efficiency for true taus with transverse momentum between 20 and 50 GeV/c to satisfy the tau identification requirements. The vertical axis gives the rate at which QCD di-jets with generator-level transverse momentum between 20 and 50 GeV/c are incorrectly identified as taus. The performance point for the same tau candidates using the isolation based tau-identification [28] used in many previous CMS analyses is indicated by the black star in the figure. An additional requirement that the signal cone contain one or three charged hadrons (typical in a final physics analysis) has been applied to the isolation based tau-identification to ensure a conservative comparison.

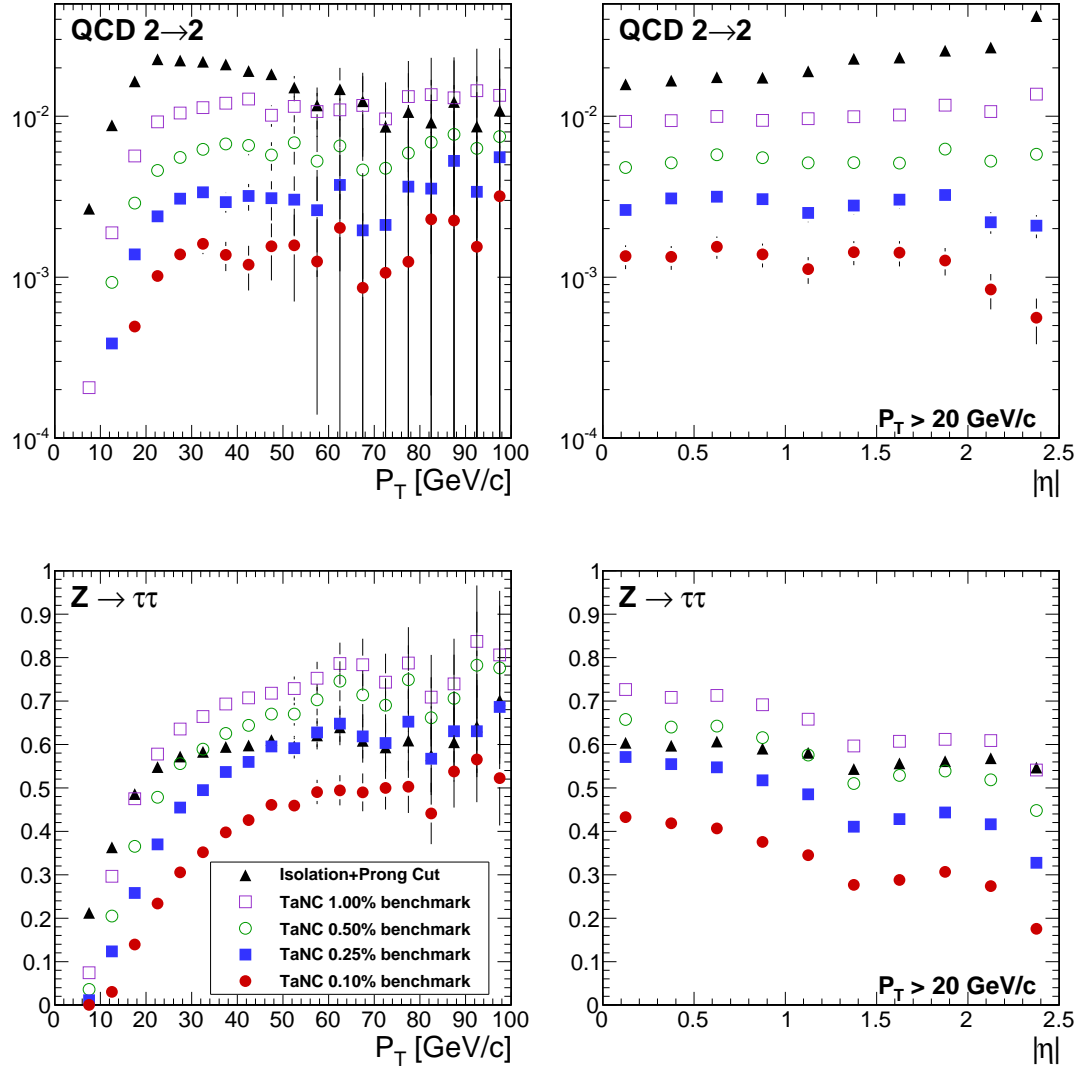


Figure 3.14: Comparison of the identification efficiency for hadronic tau decays from $Z \rightarrow \tau^+\tau^-$ decays (bottom row) and the misidentification rate for QCD dijets (top row) versus tau candidate transverse momentum (left) and pseudo-rapidity (right) for different tau identification algorithms. The efficiency (fake-rate) in a given bin is defined as the quotient of the number of true tau hadronic decays (generator level jets) in that bin that are matched to a reconstructed tau candidate that passes the identification algorithm divided by the number of true tau hadronic decays (generator level jets) in that bin. In the low transverse momentum region both the number of tau candidates in the denominator and the algorithm acceptance vary rapidly with respect to p_T for both signal and background; a minimum transverse momentum requirement of 20 GeV/c is applied to the pseudorapidity plots to facilitate interpretation of the plots.

1275 resolving multiple hypotheses. The quality of a π^0 candidate is determined according to the
 1276 following categorical rankings:

- 1277 • The π^0 candidate is in the ECAL barrel region ($|\eta| < 1.5$) and has invariant mass
 1278 $|m_{\gamma\gamma} - m_{\pi^0}| < 0.05 \text{ GeV}/c^2$.
- 1279 • The π^0 candidate is in the ECAL endcap region ($|\eta| > 1.5$) and has invariant mass
 1280 $m_{\gamma\gamma} < 0.2 \text{ GeV}/c^2$.
- 1281 • The π^0 candidate contains two or more photons within an $\eta - \phi$ strip of size 0.05×0.20 .
- 1282 • Photons not satisfying any of the other categories are considered as unresolved π^0
 1283 candidates in case they have $p_T > 1.0 \text{ GeV}/c$.

1284 The symbol m_{π^0} denotes the nominal neutral pion mass [20]. The size of the invariant mass
 1285 windows in the ECAL endcap and barrel regions is motivated by the resolution of the π^0
 1286 mass (illustrated in Figure 3.15) measured during the commissioning of the particle-flow
 1287 algorithm in early CMS data [36]. Multiple π^0 candidates in the same category are ranked
 1288 in quality according to the difference of the reconstructed photon pair mass to the nominal
 1289 π^0 mass. After the π^0 candidates are ranked, the highest ranked candidate is selected for
 1290 the final collection. The photon constituents of the highest ranked candidate are removed
 1291 from remaining π^0 candidates not yet selected for the final collection in order to prevent
 1292 photons from entering more than one π^0 candidate. The rank of remaining π^0 candidates
 1293 is reevaluated and the π^0 candidate with the next highest rank is selected for the output
 1294 collection. The process is repeated until no more π^0 candidates are remaining.

1295 Once the final collection of π^0 candidates is determined, tau reconstruction in the
 1296 HPS + TaNC algorithm proceeds by building tau candidates from reconstructed π^0 candi-
 1297 dates and charged hadrons reconstructed by the particle-flow algorithm. A combinatoric
 1298 approach is again employed for the tau candidate building. A tau candidate hypothesis is
 1299 built for every combination of jet constituents (π^0 candidates plus charged hadrons) which
 1300 has a multiplicity consistent with a hadronic tau decay. The tau candidates are ranked anal-
 1301 ogous to the ranking utilized for the π^0 reconstruction, but with the following categorical
 1302 rankings:

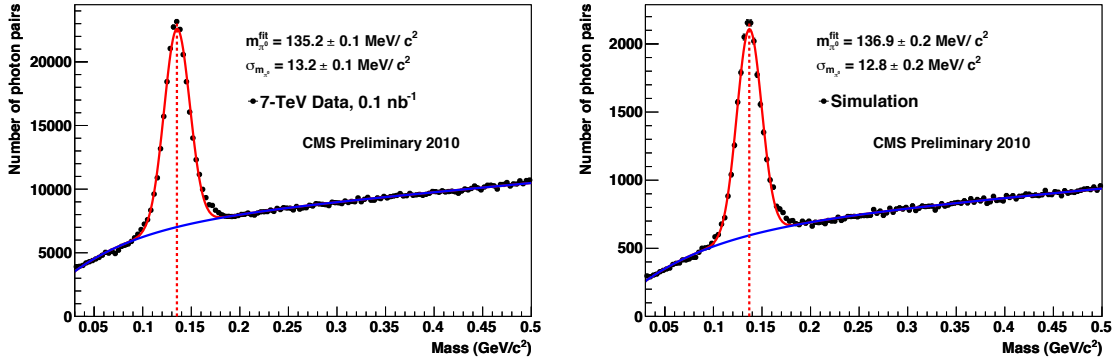


Figure 3.15: Invariant mass distribution of photon pairs reconstructed by the particle-flow in 2010 CMS minimum bias events (left), and predicted by the simulation (right). A clear resonant pick corresponding to the π_0 meson is visible above the combinatoric background. Reference: [36]

- 1303 • In each decay mode category, the tau candidate with the highest neural network
- 1304 output is selected.
- 1305 • The tau candidate has unit charge.
- 1306 • The tau candidate passes the “lead pion” criteria, requiring that there is a photon or
- 1307 charged pion candidate with $p_T > 5 \text{ GeV}/c$.
- 1308 • The tau candidate passes the HPS invariant mass and collimation¹ requirements.
- 1309 In case multiple tau candidates satisfy all four categorical requirements, the tau candidate
- 1310 with the highest energy sum of charged and neutral pions is selected as the highest ranking
- 1311 one.

1312 3.5.2 Hadronic Tau Discrimination

- 1313 The final level of discrimination is performed by an ensemble of neural networks, with each
- 1314 neural network corresponding to a specific decay mode, analogously to the method used
- 1315 original TaNC algorithm (Section 3.3.5). The inputs of each neural network are different and
- 1316 correspond to the observables (invariant mass, Dalitz masses) available for its associated

¹The invariant mass of the signal candidates is required to be compatible with the resolution for that decay mode. The collimation selection requires the maximum ΔR between any two signal candidates to be less than $2.8/E_T$, where E_T is the total transverse energy of the signal candidates. A full description is available in [33].

1317 decay mode. The neural networks are trained on samples simulated $Z \rightarrow \tau^+\tau^-$ events
 1318 (“signal”) and QCD dijet events selected in the 7 TeV data collected by CMS in 2010
 1319 (“background”). All of the tau hypothesis from a given jet reconstructed in data are used
 1320 for training. The $Z \rightarrow \tau^+\tau^-$ signal sample is generated by PYTHIA [37] which has been
 1321 interfaced to TAUOLA [38] for the purpose of generating the decays of the tau leptons using
 1322 the full matrix element information. After generation, the events passed through the “full”
 1323 GEANT [39] based simulation of the CMS detector. Only tau candidates which have been
 1324 reconstructed in a decay mode matching the true decay mode of the tau on generator
 1325 level enter the signal training sample. The neural network implementation, network layout,
 1326 and training strategies are the same as in the original TaNC algorithm described in this
 1327 chapter. To account for differences in the input signal purity and separation power of the
 1328 neural networks between decay modes, the outputs of each neural network are transformed
 1329 according to the method described in Section 3.3.8. Multiple working-points corresponding
 1330 to different purities are provided. The “loose” working point corresponds to an approximate
 1331 fake-rate of 1%, and has slightly higher signal efficiency performance at high p_T than the
 1332 corresponding HPS isolation-only working point.

1333 3.6 Electron and Muon Rejection

1334 Additional discriminators must be applied to prevent electrons and muons from being iden-
 1335 tified as hadronic tau decays. This is especially important for removing $Z \rightarrow e^+e^-$ and
 1336 $Z \rightarrow \mu^+\mu^-$ contributions when selecting events with two taus and requiring one of them
 1337 to decay leptonically and the other hadronically. The electron and muon discrimination
 1338 algorithms and performance are described in detail elsewhere [28]. A cursory overview of
 1339 the techniques used are given here. Muon removal is achieved with high purity by requiring
 1340 that no track in the signal collection of the tau candidate is matched to a segment² in the
 1341 muon system. The rejections of true electrons is more difficult. Electrons leave no signal in
 1342 the muon system and produce bremsstrahlung photons as they travel through the magnetic
 1343 field. The most significant difference from a true hadronic tau is that an electron is not
 1344 expected to deposit any energy in the hadronic calorimeter. Electrons are thus rejected by

²A track reconstructed in the DT or CSC sub-detectors.

¹³⁴⁵ requiring that there is an HCAL energy deposit with a magnitude that is greater than 10%
¹³⁴⁶ of the momentum of the leading track in the tau.

Input observable	Neural network				
	$\pi^- \nu_\tau$	$\pi^- \pi^0 \nu_\tau$	$\pi^- \pi^0 \pi^0 \nu_\tau$	$\pi^- \pi^+ \pi^- \nu_\tau$	$\pi^- \pi^+ \pi^- \pi^0 \nu_\tau$
ChargedOutlierAngle1	•	•	•	•	•
ChargedOutlierAngle2	•	•	•	•	•
ChargedOutlierPt1	•	•	•	•	•
ChargedOutlierPt2	•	•	•	•	•
ChargedOutlierPt3	•	•	•	•	•
ChargedOutlierPt4	•	•	•	•	•
Dalitz1			•	•	•
Dalitz2			•	•	•
Eta	•	•	•	•	•
InvariantMassOfSignal		•	•	•	•
MainTrackAngle		•	•	•	•
MainTrackPt	•	•	•	•	•
OutlierNCharged	•	•	•	•	•
OutlierSumPt	•	•	•	•	•
PiZeroAngle1		•	•		•
PiZeroAngle2			•		
PiZeroPt1		•	•		•
PiZeroPt2			•		
TrackAngle1				•	•
TrackAngle2				•	•
TrackPt1				•	•
TrackPt2				•	•

Table 3.4: Input observables used for each of the neural networks implemented by the Tau Neural Classifier. The columns represents the neural networks associated to various decay modes and the rows represent the superset of input observables (see Section 3.3.7) used in the neural networks. A dot in a given row and column indicates that the observable in that row is used in the neural network corresponding to that column.

Chapter 4

Mass Reconstruction: The Secondary Vertex Fit

1347
 1348 The dominant background in the search for a Higgs boson decaying to a $\tau^+\tau^-$ pair is
 1349 standard model $Z \rightarrow \tau^+\tau^-$ events. The most “natural” observable to discriminate between
 1350 a Higgs boson signal and the Z background is the invariant mass of the ditau system,
 1351 utilizing the fact that the Z resonance is well known ($m_Z = 91.1876 \pm 0.0021$ GeV/c²) and
 1352 has a narrow width ($\Gamma_Z = 2.4952 \pm 0.0023$ GeV) [20]. The experimental complication in this
 1353 approach is due to the neutrinos produced in the tau lepton decays, which escape detection
 1354 and carry away an unmeasured amount of energy, making it difficult to reconstruct the
 1355 tau lepton four-vectors. In this chapter we give an overview of techniques used in previous
 1356 literature [19, 40, 41] to construct an observable related to the tau pair invariant mass. We
 1357 then introduce a new algorithm, called the Secondary Vertex (SV) fit. The SVfit reconstructs
 1358 the “full” tau pair mass, and provides increased performance with respect to techniques
 1359 previously used in the literature.
 1360

4.1 Existing Mass Reconstruction Algorithms

1361 The simplest observable related to the $\tau^+\tau^-$ mass is the invariant mass of the visible (re-
 1362 constructible) decay products associated with each tau decays. This quantity, referred in
 1363 this document as the “visible mass,” has the advantages of simplicity and lack of exposure
 1364 to systematic errors associated with the reconstruction of the E_T^{miss} . However, no attempt
 1365 is made to reconstruct the neutrinos in the event. The reconstructed mass is thus system-
 1366 atically smaller than mass of the resonance which produced the tau leptons. The visible
 1367 mass is typically on the order of half of the resonance mass, depending on the kinematic
 1368 requirements applied to the visible products of the tau decays.
 1369

The collinear approximation is a technique previously used [19] to reconstruct the full $\tau^+\tau^-$ mass. In an event with two tau decays, there are a total of six¹ unknowns associated with the missing energy: the three components of the momentum of each neutrino. The collinear approximation makes the assumption that the neutrinos have the same direction as their associated visible decay products. This assumption reduces the number of unknown quantities to two, corresponding to the total energy of each neutrino. These two unknowns can be solved for by using the two components of the reconstructed missing transverse energy, which in the ideal case corresponds to the transverse component of the vector sum of the two neutrino's four momentum. The characteristic equation of the collinear approximation is

$$\begin{pmatrix} E_x^{\text{miss}} \\ E_y^{\text{miss}} \end{pmatrix} = \begin{pmatrix} \cos \phi_1 & \cos \phi_2 \\ \sin \phi_1 & \sin \phi_2 \end{pmatrix} \begin{pmatrix} E_1 \\ E_2 \end{pmatrix} \quad (4.1)$$

where $(E_x^{\text{miss}}, E_y^{\text{miss}})$ are the two components of the reconstructed missing transverse energy, $\phi_{1(2)}$ is the azimuthal angle of the visible component of the first (second) tau decay, and $E_{1(2)}$ is the reconstructed energy of neutrino of the first (second) tau decay. E_1 and E_2 can be extracted by inverting the matrix on the right hand side of Equation 4.1.

$$\begin{pmatrix} E_1 \\ E_2 \end{pmatrix} = \frac{1}{\sin(\phi_2 - \phi_1)} \begin{pmatrix} \sin \phi_2 & -\cos \phi_2 \\ -\sin \phi_1 & \cos \phi_1 \end{pmatrix} \begin{pmatrix} E_x^{\text{miss}} \\ E_y^{\text{miss}} \end{pmatrix} \quad (4.2)$$

1371 The collinear approximation suffers from two problems. The approximation can fail
 1372 (yielding unphysical negative energies for the reconstructed neutrinos) when the missing
 1373 transverse energy is mis-measured. The events with unphysical solutions must be removed
 1374 from the analysis, leading to a dramatic reduction in acceptance (on the order of 50% in
 1375 this analysis). Improvements to the collinear approximation algorithm have recently been
 1376 made which aim to recover part of the events with unphysical solutions [42]. But even with
 1377 these improvements, no physical solution is still found for a large fraction of signal events.

¹Technically, there is an extra unknown for each leptonic tau decay, which has two associated neutrinos. This is a small effect compared to the overall resolution of the collinear approximation.

1378 Additionally, the method is numerically unstable when the two τ lepton are nearly back-
 1379 to-back in azimuth. In these cases the $\sin(\phi_2 - \phi_1)^{-1}$ term in Equation 4.2 is very large
 1380 and small mis-measurements of the missing transverse energy can produce a large tail on
 1381 the reconstructed mass. This tail is particularly large for low-mass resonances. The large
 1382 tail for high mass is predominantly due to the fact (discussed in Section 4.4.2) that the
 1383 kinematic requirements² applied on the visible decay products preferentially selects events
 1384 where the visible decay products carry the majority of the energy of the original τ lepton,
 1385 reducing the amount of true missing energy in the event.

1386 4.2 The Secondary Vertex Fit

1387 A novel algorithm is presented in the following, which succeeds in finding a physical solution
 1388 for every event. As an additional benefit, the new algorithm is found to improve the ditau
 1389 invariant mass resolution, making it easier to separate the Higgs boson signal from the
 1390 $Z \rightarrow \tau^+\tau^-$ background.

1391 The novel Secondary Vertex fit (SVfit) algorithm for ditau invariant mass reconstruc-
 1392 tion that we present in the following utilizes a likelihood maximization to fit a $\tau^+\tau^-$ in-
 1393 variant mass hypothesis for each event. The likelihood is composed of separate terms which
 1394 represent probability densities of:

- 1395 • the tau decay kinematics,
- 1396 • the matching between the momenta of neutrinos produced in the tau decays and the
 1397 reconstructed missing transverse momentum,
- 1398 • a regularization “ p_T -balance” term which accounts for the effects on the ditau invari-
 1399 ant mass of acceptance cuts on the visible tau decay products,
- 1400 • and the compatibility of tau decay parameters with the position of reconstructed
 1401 tracks and the known tau lifetime of $c\tau = 87 \mu\text{m}$ [20].

1402 The likelihood is maximized as function of a set of parameters which fully describe the tau
 1403 decay.

²The kinematic requirements on the visible decay products are necessary to reduce backgrounds and maintain compatibility with un-preserved event triggers. This topic is discussed in detail in Chapter 5.

1404 4.3 Parametrization of Tau Decays

1405 The decay of a tau with visible four-momentum p_{vis} measured in the CMS detector (“laboratory”) frame can be parametrized by three variables. The invisible (neutrino) momentum
 1406 is fully determined by these parameters.

1408 The “opening-angle” θ is defined as the angle between the boost direction of the tau
 1409 lepton and the momentum vector of the visible decay products in the rest frame of the
 1410 tau. The azimuthal angle of the tau in the lab frame is denoted as $\bar{\phi}$ (we denote quantities
 1411 defined in the laboratory frame by a overline). A local coordinate system is defined such
 1412 that the \bar{z} -direction lies along the visible momentum and $\bar{\phi} = 0$ lies in the plane spanned
 1413 by the momentum vector of the visible decay products and the proton beam direction. The
 1414 third parameter, $m_{\nu\nu}$, denotes the invariant mass of the invisible momentum system.

Given θ , $\bar{\phi}$ and $m_{\nu\nu}$, the energy and direction of the tau lepton can be computed by means of the following equations: The energy of the visible decay products in the rest frame of the tau lepton is related to the invariant mass of the neutrino system by:

$$E^{vis} = \frac{m_\tau^2 + m_{vis}^2 - m_{\nu\nu}^2}{2m_\tau} \quad (4.3)$$

1415 Note that for hadronic decays, $m_{\nu\nu}$ is a constant of value zero, as only a single neutrino is
 1416 produced. Consequently, the magnitude of P^{vis} depends on the reconstructed mass of the
 1417 visible decay products only and is a constant during the SVfit.

The opening angle $\bar{\theta}$ between the tau lepton direction and the visible momentum vector in the laboratory frame is determined by the rest frame quantities via the (Lorentz invariant) component of the visible momentum perpendicular to the tau lepton direction:

$$\begin{aligned} p_\perp^{vis} &= \bar{p}_\perp^{vis} \\ \Rightarrow \sin \bar{\theta} &= \frac{p^{vis} \sin \theta}{\bar{p}^{vis}} \end{aligned} \quad (4.4)$$

Substituting the parameters $m_{\nu\nu}$ and θ into Equations 4.3 and 4.4, the energy of the tau is obtained by solving for the boost factor γ in the Lorentz transformation between the

tau rest frame and laboratory frame of the visible momentum component parallel to the tau direction:

$$\begin{aligned}\bar{p}^{vis} \cos \bar{\theta} &= \gamma \beta E^{vis} + \gamma p^{vis} \cos \theta \\ \Rightarrow \gamma &= \frac{E^{vis}[(E^{vis})^2 + (\bar{p}^{vis} \cos \bar{\theta})^2 - (p^{vis} \cos \theta)^2]^{1/2} - p^{vis} \cos \theta \bar{p}^{vis} \cos \bar{\theta}}{(E^{vis})^2 - (p^{vis} \cos \theta)^2}, \\ E^\tau &= \gamma m_\tau\end{aligned}$$

1418 The energy of the tau lepton in the laboratory frame as function of the measured visible
 1419 momentum depends on two of the three parameters only - the rest frame opening angle θ and
 1420 the invariant mass $m_{\nu\nu}$ of the neutrino system. The direction of the tau lepton momentum
 1421 vector is not fully determined by θ and $m_{\nu\nu}$, but is constrained to lie on the surface of a
 1422 cone of opening angle $\bar{\theta}$ (given by Equation 4.4), the axis of which is given by the visible
 1423 momentum vector. The tau lepton four–vector is fully determined by the addition of the
 1424 third parameter $\bar{\phi}$, which describes the azimuthal angle of the tau lepton with respect to the
 1425 visible momentum vector. The spatial coordinate system used is illustrated in Figure 4.1.

1426 4.4 Likelihood for Tau Decays

The probability density functions for the tau decay kinematics are taken from the kinematics review of the PDG [20]. The likelihood is proportional to the phase–space volume for two–body ($\tau \rightarrow \tau_{had}\nu$) and three–body ($\tau \rightarrow e\nu\nu$ and $\tau \rightarrow \mu\nu\nu$) decays. For two–body decays the likelihood depends on the decay angle θ only:

$$d\Gamma \propto |\mathcal{M}|^2 \sin \theta d\theta$$

For three–body decays, the likelihood depends on the invariant mass of the neutrino system also:

$$d\Gamma \propto |\mathcal{M}|^2 \frac{((m_\tau^2 - (m_{\nu\nu} + m_{vis})^2)(m_\tau^2 - (m_{\nu\nu} - m_{vis})^2))^{1/2}}{2m_\tau} m_{\nu\nu} dm_{\nu\nu} \sin \theta d\theta \quad (4.5)$$

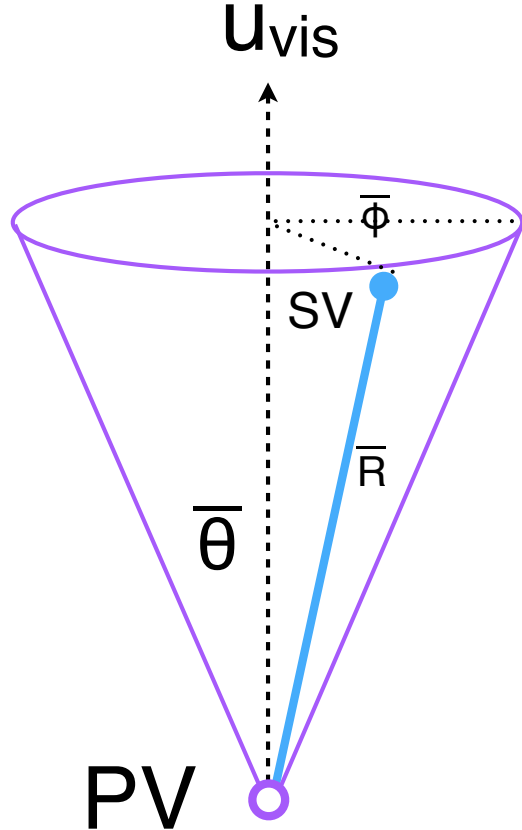


Figure 4.1: Illustration of the coordinate system used by the SVfit to describe the decays of tau leptons.

¹⁴²⁷ In the present implementation of the SVfit algorithm, the matrix element is assumed to be
¹⁴²⁸ constant, so that the likelihood depends on the phase-space volume of the decay only ³.

¹⁴²⁹ 4.4.1 Likelihood for Reconstructed E_T^{miss}

¹⁴³⁰ Momentum conservation in the plane perpendicular to the beam axis implies that the
¹⁴³¹ vectorial sum of the momenta of all neutrinos produced in the decay of the tau lepton pair
¹⁴³² matches the reconstructed missing transverse momentum. Differences are possible due to
¹⁴³³ the experimental resolution and finite p_T of particles escaping detection in beam direction
¹⁴³⁴ at high $|\eta|$.

³The full matrix elements for tau decays may be added in the future, including terms for the polarization of the tau lepton pair, which is different in Higgs boson and Z decays [43].

The E_T^{miss} resolution is measured in $Z \rightarrow \mu^+\mu^-$ events selected in the 7 TeV data collected by CMS in 2010. Corrections are applied to the distribution of E_T^{miss} in the Monte Carlo simulated events to match the resolution measured in data. The uncertainty on this correction factor is taken as a “shape systematic.” The treatment of this correction and its corresponding uncertainty are described in Chapters 7 and 8. The momentum vectors of reconstructed E_T^{miss} and neutrino momenta given by the fit parameters are projected in direction parallel and perpendicular to the direction of the $\tau^+\tau^-$ momentum vector. For both components, a Gaussian probability function is assumed. The width and mean values of the Gaussian in parallel (“ \parallel ”) and perpendicular (“ \perp ”) direction are:

$$\sigma_{\parallel} = \max(7.54(1 - 0.00542 \cdot q_T), 5.)$$

$$\mu_{\parallel} = -0.96$$

$$\sigma_{\perp} = \max(6.85(1 - 0.00547 \cdot q_T), 5.)$$

$$\mu_{\perp} = 0.0,$$

¹⁴³⁵ where q_T denotes the transverse momentum of the tau lepton pair.

¹⁴³⁶ 4.4.2 Likelihood for Tau Transverse Momentum Balance

The tau lepton transverse momentum balance likelihood term represents the probability density $p(p_T^{\tau}|M_{\tau\tau})$ of the tau transverse momentum, given the condition that the tau is produced in the decay of a resonance of mass $M_{\tau\tau}$. The likelihood is constructed by parametrizing the shape of the tau lepton p_T distribution in simulated $H \rightarrow \tau^+\tau^-$ events as a function of the Higgs boson mass. The functional form of the parametrization is taken to be the sum of two terms. The first term, denoted by $p^*(p_T|M)$, is derived by assuming an isotropic two-body decay, that is

$$dp^* \propto \sin \theta d\theta.$$

Performing a variable transformation from θ to $p_T \sim \frac{M}{2} \sin \theta$, we obtain

$$\begin{aligned} p^*(p_T|M) &= \frac{dp}{dp_T} = \frac{dp}{d \cos \theta} \left| \frac{d \cos \theta}{dp_T} \right| \\ &\propto \left| \frac{d}{dp_T} \sqrt{1 - \left(2 \frac{p_T}{M} \right)^2} \right| \\ &= \frac{1}{\sqrt{\left(\frac{M}{2p_T} \right)^2 - 1}}. \end{aligned} \quad (4.6)$$

The first term of the p_T -balance likelihood is taken as the convolution of Equation 4.6 with a Gaussian of width s . The second term is taken to be a Gamma distribution with scale parameter θ and shape parameter k , in order to account for tails in the p_T distribution of the tau lepton pair. The complete functional form is thus given by

$$p(p_T|M) \propto \int_0^{\frac{M}{2}} p^*(p'_T|M) e^{-\frac{(p_T-p'_T)^2}{2s^2}} dp'_T + a\Gamma(p_T, k, \theta). \quad (4.7)$$

Numerical values of the parameters s , θ and k are determined by fitting the PDF in Equation 4.7 to the tau lepton p_T distribution in simulated $H \rightarrow \tau^+\tau^-$ events. The relative weight of the two terms is also determined in the fit. Replacing the integrand in Equation 4.7 by its Taylor expansion so that the integration can be carried out analytically, keeping polynomial terms up to fifth order, and assuming the fit parameters to depend at most linearly on the Higgs boson mass, we obtain the following numerical values for the parameters:

$$s = 1.8 + 0.018 \cdot M_{\tau\tau}$$

$$k = 2.2 + 0.0364 \cdot M_{\tau\tau}$$

$$\theta = 6.74 + 0.02 \cdot M_{\tau\tau}$$

$$a = 0.48 - 0.0007 \cdot M_{\tau\tau}.$$

¹⁴³⁷ The motivation for the p_T -balance likelihood is to add a “regularization” term which
¹⁴³⁸ compensates for the effect of p_T cuts applied on the visible decay products of the two tau

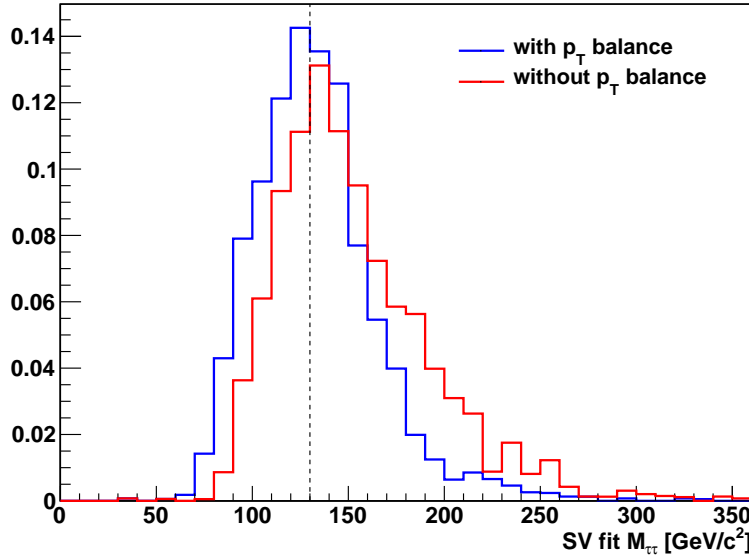


Figure 4.2: Distribution of ditau invariant mass reconstructed by the SVfit algorithm in simulated Higgs boson events with $m_{A^0} = 130$ GeV/c^2 . The SVfit algorithm is run in two configurations, with (blue) and without (red) the p_T -balance likelihood term included in the fit.

leptons. In particular for tau lepton pairs produced in decays of resonances of low mass, the visible p_T cuts significantly affect the distribution of the visible momentum fraction $x = E_{vis}/E_\tau$. The effect is illustrated in Figures 4.3 and 4.4. If no attempt would be made to compensate for this effect, Equations 4.4 and 4.5 would yield likelihood values that are too high at low x , resulting in the SVfit underestimating the energy of the visible decay products (and overestimating the energy of neutrinos) produced in the tau decay. This effect produces a significant tail of the reconstructed mass distribution in the high mass region. The $\tau^+\tau^-$ invariant mass distribution reconstructed with and without the p_T -balance likelihood term is shown in Figure 4.2. A significant improvement in resolution and in particular a significant reduction of the non-Gaussian tail in the region of high masses is seen.

4.4.3 Secondary Vertex Information

The parametrization of the tau decay kinematics described in section 4.3 can be extended to describe the production and decay of the tau. As the flight direction of the tau is already fully determined by the parameters θ , $\bar{\phi}$ and $m_{\nu\nu}$, the position of the secondary (decay)

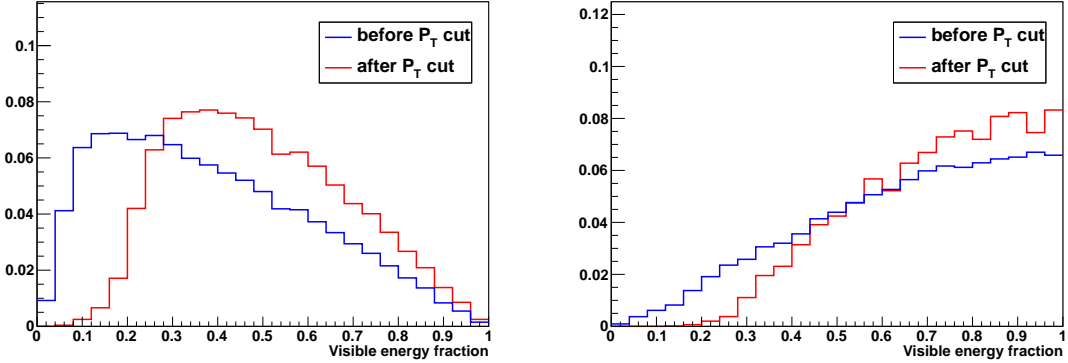


Figure 4.3: Normalized distributions of the fraction of total tau decay energy carried by the muon (left) and hadronic constituents (right) in simulated Higgs boson events with $m_{A^0} = 130 \text{ GeV}/c^2$. The distribution is shown before (blue) and after (red) the requirement on the p_T of the visible decay products described in Chapter 5.

1453 vertex is hence fully determined by addition of a single parameter for the flight distance,
 1454 r . The tau lifetime $c\tau = 87 \mu\text{m}$ is large enough to allow the displacement of the tau decay
 1455 vertex from the primary event vertex to be resolved by the CMS tracking detector. The
 1456 resolution provided by the CMS tracking detector is utilized to improve the resolution on
 1457 the $\tau^+\tau^-$ invariant mass reconstructed by the SVfit algorithm. The likelihood term based on
 1458 the secondary vertex information represents the compatibility of the decay vertex position
 1459 with the reconstructed tracks of charged tau decay products. Perhaps surprisingly, it turns
 1460 out that the flight distance parameter R is sufficiently constrained even for tau decays into
 1461 a single charged hadron, electron or muon.

The parameter R can be constrained further by a term which represents the probability for a tau lepton of momentum P to travel a distance d before decaying:

$$p(d|P) = \frac{m_\tau}{P c\tau} e^{-\frac{m_\tau d}{P c\tau}}$$

1462 The likelihood terms for the secondary vertex fit have been implemented in the SVfit
 1463 algorithm. In the analysis presented in this note, the decay vertex information is not used,
 1464 however, because of systematic effects arising from tracker (mis-)alignment which are not
 1465 yet fully understood.

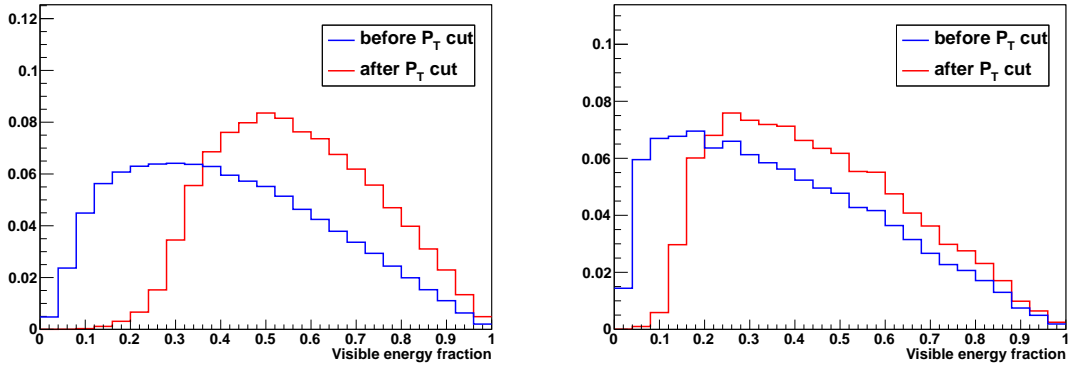


Figure 4.4: Normalized distributions of the fraction of total tau decay energy carried by the muon in simulated $Z \rightarrow \tau^+\tau^-$ (left) and Higgs boson events with $m_{A^0} = 200$ GeV/c 2 (right). The distribution is shown before (blue) and after (red) the requirement that the p_T of the muon be greater than 15 GeV/c.

1466 4.5 Performance

1467 The tau pair invariant mass reconstructed by the Secondary Vertex fit (“SVfit mass”)
 1468 provides the observable with the largest separation between signal Higgs boson events and
 1469 the dominant $Z \rightarrow \tau^+\tau^-$ background. The mean of the SVfit mass is located at the true
 1470 mass of the ditau pair. The SVfit algorithm has a higher acceptance and better resolution
 1471 than the collinear approximation algorithm. The SVfit always finds a physical solution,
 1472 improving on the efficiency of the collinear approximation by a factor of two. Additionally,
 1473 it has a much better resolution. The collinear approximation reconstructed mass distribution
 1474 has a large tail at high mass due to events with poorly measured E_T^{miss} . The shape of the
 1475 SVfit distribution is nearly Gaussian. The comparison is illustrated in Figure 4.5. Previous
 1476 searches for Higgs bosons decaying to tau leptons [40] have in general used the “visible mass”
 1477 as the observable used to search for new resonances. The SVfit method has the obvious
 1478 difference that it reconstructs the “full” tau pair invariant mass, which is the most natural
 1479 observable corresponding to a particle decaying to tau leptons. In addition, the relative
 1480 resolution⁴ of the SV fit is superior to that of the visible mass. This feature is illustrated in
 1481 Figure 4.6. In Figure 4.6, the visible mass distribution is scaled by an arbitrary number such
 1482 that the scaled mean of the distribution matches the true invariant mass of the tau pair

⁴We define this metric of performance as the variance of a distribution divided by its mean.

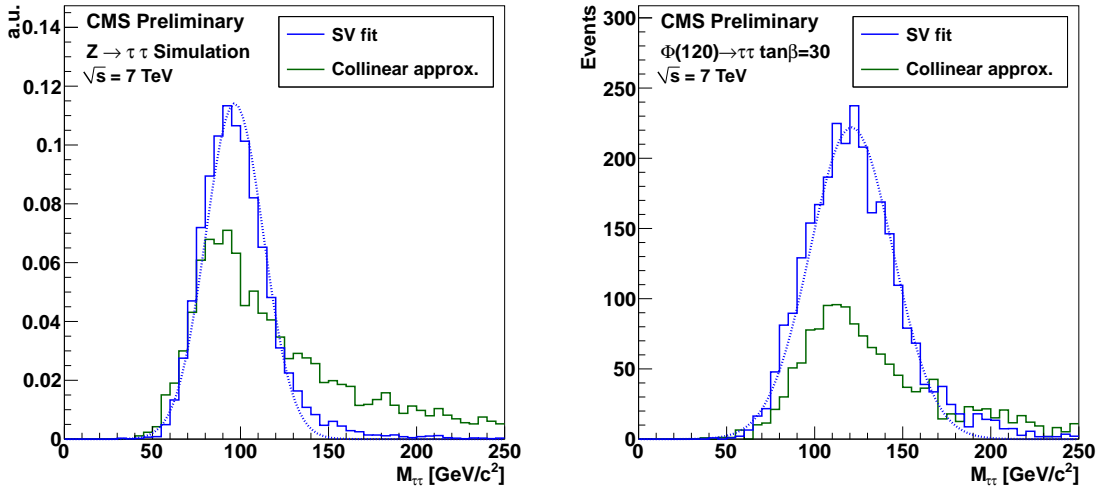


Figure 4.5: Comparison of the reconstructed tau pair invariant mass spectrum in $Z \rightarrow \tau^+\tau^-$ (left) and MSSM $H(120) \rightarrow \tau^+\tau^-$ (right) events after the selections described in chapter 5. The mass spectrum reconstructed by the Secondary Vertex fit is shown in blue, the result of the collinear approximation algorithm is given in green. In the left plot, both distributions are normalized to unity, illustrating the improvement in resolution (shape) provided by the SVfit. In the right plot, the distributions are normalized to an (arbitrary) luminosity, illustrating the loss of events that occurs due to unphysical solutions in the application of the collinear approximation.

1483 (and the SVfit mass). The width of the SVfit distribution is smaller than that of the scaled
 1484 visible mass distribution, indicating better performance. The increase in relative resolution
 1485 allows an excess in the spectrum due to the presence of signal events to be more easily
 1486 distinguished from the $Z \rightarrow \tau^+\tau^-$ background. This increases the power of the search for
 1487 the new signal.

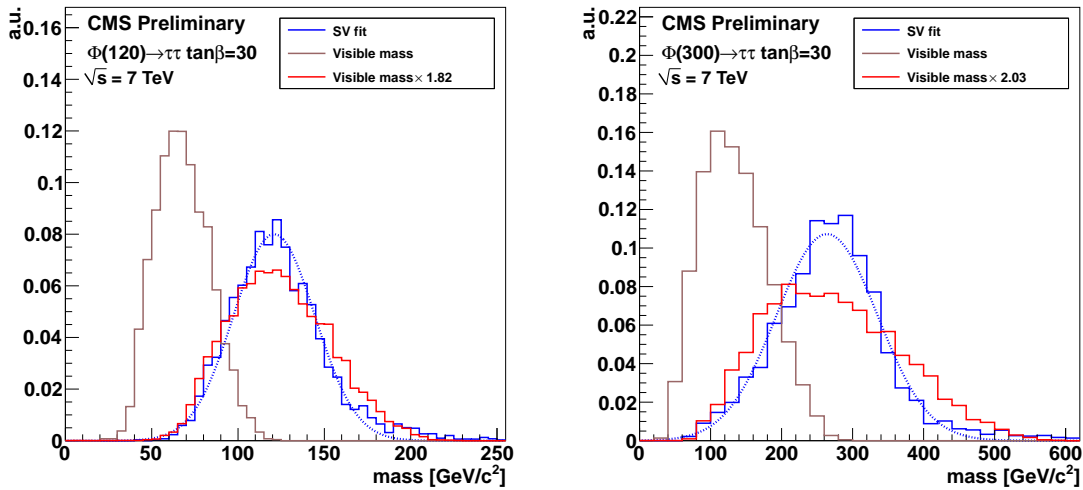


Figure 4.6: Comparison of the invariant mass of the muon and τ_{jet} (the “visible mass”) with the full $\tau^+\tau^-$ mass reconstructed by the SVfit. The spectrum is shown for two simulated MSSM Higgs boson samples, with $m_{A^0} = 120 \text{ GeV}/c^2$ (left), and $m_{A^0} = 200 \text{ GeV}/c^2$ (right). To illustrate that relative resolution of the SVfit is superior to that of the visible mass, the visible mass is also shown scaled up such that the mean of the two distributions are identical.

1488

Chapter 5

1489

Analysis Selections

1490 The selections applied to events in this analysis are designed to maximize the significance
 1491 of Higgs boson signal events in the final set of selected events. The analysis presented in
 1492 this thesis is an inclusive analysis, meaning that no preference is given to any single Higgs
 1493 boson production mechanism. The analysis looks specifically at the channel in which one tau
 1494 decays to a muon and the other decays to hadrons. Therefore the first step in the analysis
 1495 selection is to find HLT selection that is highly efficient for the signal and is not highly
 1496 prescaled¹. After the trigger selection, events are required to contain at least a good muon
 1497 and a good tau. Vetoos on extra leptons are applied to reduce backgrounds from dimuon
 1498 events. Finally, kinematic and charge selections are applied to the event to reduce $W + \text{jets}$
 1499 and QCD backgrounds.

1500

5.1 High Level Trigger

1501 Because only data which passes the HLT is recorded, it is critical that an appropriate
 1502 trigger path is found. The events in this analysis are triggered by a combination of muon
 1503 and muon + hadronic tau “cross–channel” triggers. For the muon triggers, the HLT paths
 1504 with lowest p_T thresholds are used as long as the path remained unprescaled (see Ta-
 1505 ble 5.1). The muon + tau-jet “cross–channel” trigger paths increase the trigger efficiency
 1506 for events containing muons of transverse momenta close to the $p_T^\mu > 15$ GeV/c cut thresh-
 1507 old. The trigger efficiency is measured in data via the tag-and-probe technique. Details of
 1508 the muon trigger efficiency measurement are given in Section 7.1. Monte Carlo simulated

¹If a trigger has high background rates, it may exceed its rate budget with increasing luminosity. When this happens, it is generally “prescaled,” and some fraction of the events that pass this trigger are randomly thrown it away to reduce the rate. In general, it is better to use an unprescaled trigger with lower efficiency than a prescaled trigger.

Trigger path	run-range
HLT_Mu9	132440 - 147116
HLT_IsoMu9	147196 - 148058
HLT_Mu11	147196 - 148058
HLT_Mu15	147196 - 149442
HLT_IsoMu13	148822 - 149182
HLT_IsoMu9_PFTau15	148822 - 149182
HLT_Mu11_PFTau15	148822 - 149182

Table 5.1: Muon and muon + tau “cross–channel” trigger paths utilized to trigger events in different data–taking periods.

1509 events are required to pass the HLT_Mu9 trigger path. Weights are applied to simulated
 1510 events to account for the difference between the simulated HLT_Mu9 efficiency and the com-
 1511 bined efficiency of the set HLT_Mu9, HLT_IsoMu9, HLT_Mu11, HLT_IsoMu13, HLT_Mu15,
 1512 HLT_IsoMu9_PFTau15 and HLT_Mu11_PFTau15 used to trigger the data.

1513 5.2 Particle Identification

1514 5.2.1 Muons

1515 Muon candidates are required to be reconstructed as global and as tracker muons, meaning
 1516 that a full track is reconstructed in the muon system and is well matched to a track in the
 1517 silicon strip and pixel trackers. Additionally, they are required to pass the “Vector Boson
 1518 Task Force” (VBF) muon identification criteria developed for the $Z \rightarrow \mu^+ \mu^-$ cross–section
 1519 measurement [44], which consist of:

- 1520 • ≥ 1 pixel hits,
- 1521 • ≥ 10 hits in silicon pixel and strip detectors,
- 1522 • ≥ 1 hit(s) in muon system,
- 1523 • ≥ 2 matched segments,

- 1524 • $\chi^2/DoF < 10$ for global track fit,
- 1525 • and an inner track transverse impact parameter $d_{\text{IP}} < 2$ mm with respect to the
1526 beamspot.

1527 In order to reduce background contributions from muons originating from heavy quark
1528 decays in QCD multi-jet events, muons are required to be isolated. Isolation is computed
1529 as the p_{T} sum of charged and neutral hadrons plus photons reconstructed by the CMS
1530 particle-flow algorithm [29] within a cone of size $\Delta R_{\text{iso}} = 0.4$ around the muon direction
1531 divided by the muon p_{T} . The innermost region of size $\Delta R_{\text{veto}} = 0.08$ (0.05) is excluded
1532 from the computation of the isolation p_{T} sum with respect to neutral hadrons (photons),
1533 in order to avoid energy deposits in the electromagnetic and hadronic calorimeters which
1534 are due to the muon to enter the sum. In order to reduce pile-up effects, particles entering
1535 the isolation p_{T} sum are required to have transverse momenta $p_{\text{T}} > 1.0$ GeV/c. Charged
1536 particles are additionally required to originate from the same vertex as the muon. The
1537 muons are required to be isolated with respect to charged hadrons of $p_{\text{T}} > 1.0$ GeV/c and
1538 photons of $p_{\text{T}} > 1.5$ GeV/c as reconstructed by the particle-flow algorithm [29] in a cone
1539 of size $\Delta R = 0.4$ around the direction of the muon. The distribution of the muon isolation
1540 discriminant is shown in Figure 5.1(a).

1541 5.2.2 Hadronic Taus

1542 Hadronic decays of taus are identified by the HPS + TaNC hybrid algorithm described in
1543 Section 3.5. The expected sensitivity of the search was evaluated using each of the hadronic
1544 tau identification work points. The “loose” working point, corresponding to an expected
1545 QCD fake-rate of about 1%, was found to have the highest performance and is used in this
1546 analysis. $Z \rightarrow \mu^+ \mu^-$ background contributions are largely due to muons which failed to
1547 get reconstructed as global muons (thus failing the muon identification requirement) and
1548 are misidentified as tau candidates. These muons are typically isolated and have a large
1549 chance to pass the hadronic tau ID discriminators. To reject these events, hadronic taus are
1550 additionally required to pass an anti-muon veto described in Section 3.6.

Background	Cross Section (pb)
QCD Heavy Flavor	84679 ³
$W \rightarrow \mu\nu + \text{jets}$	10435
$Z \rightarrow \mu\mu + \text{jets}$	1666
$t\bar{t} + \text{jets}$	158

Table 5.2: The different backgrounds to the analysis presented in this thesis that include misidentified hadronic taus.

1551 5.2.3 Missing Transverse Energy

1552 The missing transverse energy E_T^{miss} , in the event is reconstructed based on the vectorial
 1553 momentum sum of particle candidates reconstructed by the particle-flow algorithm [29, 45].
 1554 In the ideal case, the E_T^{miss} corresponds to the vector sum of the transverse components of
 1555 all neutrinos in the event. The E_T^{miss} resolution in simulated $Z \rightarrow \mu^+\mu^-$ events is found
 1556 to be smaller (better) than in the data. The reconstructed E_T^{miss} in the simulated events is
 1557 “smeared” by a correction factor such that the data and simulation are in agreement. The
 1558 “Z-recoil” E_T^{miss} correction procedure is described in Section 7.4.

1559 5.3 Event Selections

1560 The selections applied to the analysis are designed to reject large fractions of the back-
 1561 ground while maintaining a high efficiency for identifying signal Higgs boson events. The
 1562 backgrounds can be divided into two classifications: “fake” backgrounds, in which there is
 1563 at least one misidentified hadronic tau decay, and the irreducible $Z \rightarrow \tau^+\tau^-$ background,
 1564 which cannot² be distinguished from the potential presence of a Higgs boson of the same
 1565 mass. Strategies for dealing with the irreducible Z background will be discussed in the Chap-
 1566 ter 9. The different fake backgrounds, their cross section, and the basic removal strategies
 1567 are outlined in Table 5.2.

²Due to the differences in spin between the Z (spin 1) and the Higgs boson (spin 0), in the future it may be possible to separate the two using spin correlations of the two tau decays.

Events are selected by requiring a muon of $p_T^\mu > 15$ GeV/c within $|\eta_\mu| < 2.1$ and a tau-jet candidate of $p_T^{\tau\text{-jet}} > 20$ GeV/c within $|\eta_{\tau\text{-jet}}| < 2.3$. The η requirement on the muon ensures that it is within the fiducial region of the muon trigger system. The η requirement on the hadronic tau ensures it is well within the fiducial region of the tracker ($|\eta| < 2.5$) and minimizes exposure to large QCD backgrounds in the very forward region.

The muon and tau candidate are required to be of opposite charge, as the Higgs boson is neutral and charge is conserved. The muon is required to pass the identification criteria described in Section 5.2.1. The tau-jet candidate is required to pass the “loose” TaNC tau identification discriminator.

Additional event selection criteria are applied to reduce contributions of specific background processes. In order to reject $Z \rightarrow \mu^+ \mu^-$ background, a dedicated discriminator against muons is applied [28]. The remaining dimuon background is suppressed by rejecting events which have a track of $p_T > 15$ GeV/c and for which the sum of energy deposits in ECAL plus HCAL is below $0.25 \cdot P$ within a cylinder of radius 15 cm (ECAL) and 25 cm (HCAL), respectively. Contamination from $Z \rightarrow \tau^+ \tau^-$ events in which the reconstructed tau candidate is due to a $\tau \rightarrow e \nu \nu$ decay is reduced by applying a dedicated tau ID discriminator against electrons.

The $t\bar{t}$ and $W + \text{jets}$ backgrounds are suppressed by cuts on the transverse mass of the $\mu - E_T^{\text{miss}}$ system and the P_ζ variable. The transverse mass (M_T) cut is defined as the quantity

$$M_T = p_T^\mu E_T^{\text{miss}} \sqrt{1 - \cos \Delta\phi},$$

where $\Delta\phi$ is the angle between the muon and the reconstructed \vec{E}_T^{miss} in the transverse plane. The M_T quantity is much higher in events $W \rightarrow \mu\nu$ decays than in signal Higgs boson events. In $W \rightarrow \mu\nu$ decays, the neutrino expected to be produced in the opposite to the muon in azimuth. In signal events, there are three neutrinos produced, with the majority (two) of the neutrinos being associated to the $\tau \rightarrow \mu\nu\nu$ decay. Accordingly, we expect that the \vec{E}_T^{miss} is on average collinear with the muon in signal events. The M_T distribution immediately before the M_T cut is applied is illustrated in Figure 5.1(b) for the different background sources and 2010 data.

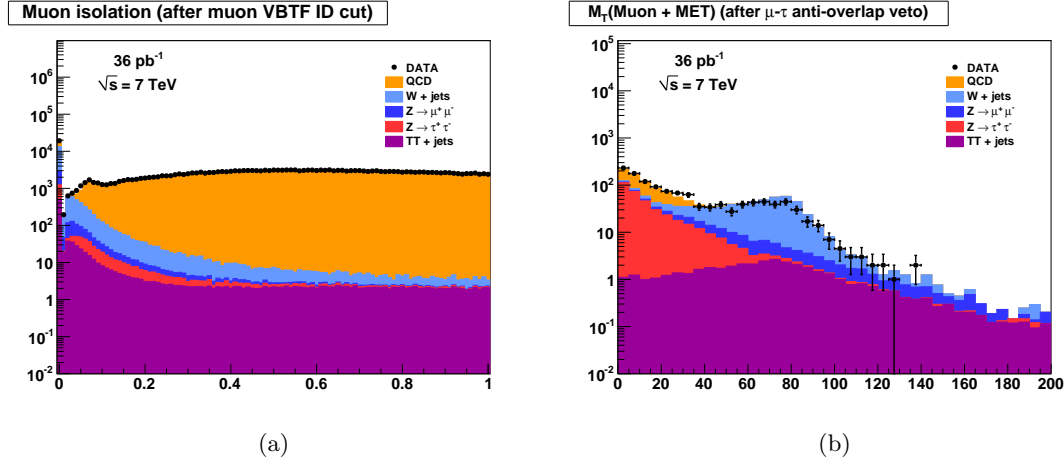


Figure 5.1: Distributions of the muon isolation (a) and M_T (b) discriminant variables. The muon isolation discriminant rejects the QCD background at a high rate. The M_T cut is designed to reject $W + \text{jets}$ and $t\bar{t} + \text{jets}$ backgrounds. The distributions shown are computed immediately before the corresponding selection is applied.

The P_ζ variable is another quantity with discriminant power against $W + \text{jets}$ and $t\bar{t}$ backgrounds. The observable has been introduced in the search for $H \rightarrow \tau^+\tau^-$ events performed by the CDF collaboration [46]. The observable is motivated by the fact that in $\tau^+\tau^-$ signal events the neutrinos are produced nearly collinear with their associated visible decay products. It is therefore expected that the direction of the missing transverse energy vector in these events points in a direction between⁴ the visible τ decay products. This event topology is not preferred in $W + \text{jets}$, $t\bar{t}$ and QCD background events. The observable is computed as the difference of the projections:

$$P_\zeta = \vec{P}_T^{vis_1} + \vec{P}_T^{vis_2} + E_T^{\text{miss}}$$

on the axis ζ bisecting the directions $\vec{P}_T^{vis_1}$ and $\vec{P}_T^{vis_2}$ of the visible τ lepton decay products in the transverse plane (see Figure 5.2(a) for an illustration). The distribution of P_ζ after the M_T selection has been applied is shown in Figure 5.2(b). The complete set of event selection criteria applied are summarized in Table 5.3.

⁴In other words, the projection of \vec{E}_T^{miss} is positive along the bisector of the muon and hadronic tau momenta.

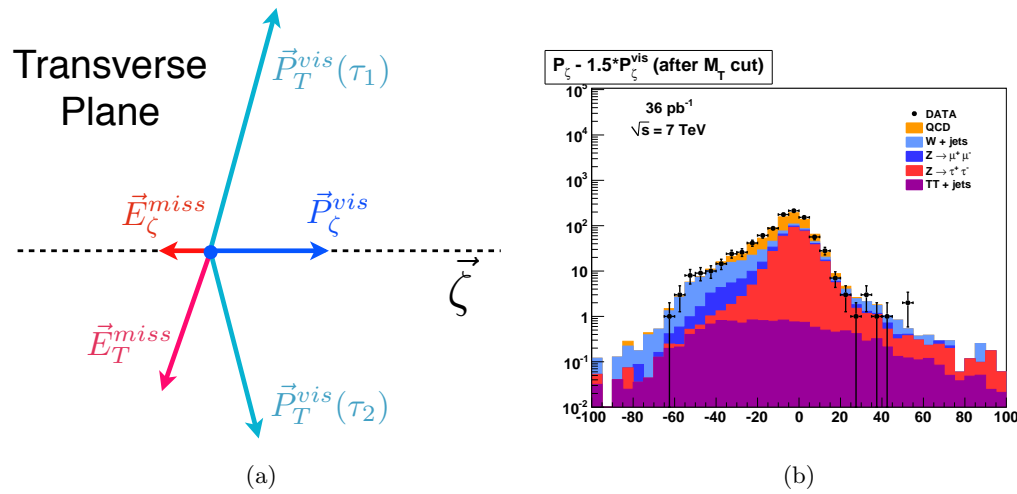


Figure 5.2: The vector quantities used in construction of the quantity $P_\zeta - 1.5 \cdot P_\zeta^{\text{vis}}$ are illustrated in Figure (a). Image credit: [46] The distribution of the P_ζ variable in the different background sources and 2010 data after the M_T cut has been applied is shown at right in (b).

Requirement	
Trigger	HLT Mu9 for MC <i>cf.</i> table 5.1 for Data
Vertex	reconstructed with beam-spot constraint:
Muon	$-24 < z_{vttx} < +24 \text{ cm}$, $ \rho < 2 \text{ cm}$, $N_{\text{DOF}} > 4$ reconstructed as global Muon with: $p_T > 15 \text{ GeV}/c$, $ \eta < 2.1$, VBF Muon ID passed, isolated within $\Delta R = 0.4$ cone with respect to charged hadrons of $p_T > 1.0 \text{ GeV}/c$ and neutral electromagnetic objects of $E_T > 1.5 \text{ GeV}$
Tau Candidate	reconstructed by HPS + TaNC combined Tau ID algorithm TaNC “medium” Tau ID discriminator and discriminators against electrons and muons passed, calorimeter muon rejection passed
Muon + Tau	$\text{charge}(\text{Muon}) + \text{charge}(\text{Tau}) = 0$, $\Delta R(\text{Muon}, \text{Tau}) > 0.5$
Kinematics	$M_T(\text{Muon-MET}) < 40 \text{ GeV}$ $P_\zeta - 1.5 \cdot P_\zeta^{\text{vis}} > -20 \text{ GeV}$

Table 5.3: Event selection criteria applied to select $H \rightarrow \tau^+ \tau^- \rightarrow \mu \tau_{had}$ events.

Chapter 6

1605

1606 Data–Driven Background Estimation

1607 For the result of this analysis to be reliable, it is of paramount importance that the back-
 1608 grounds be well understood. If at all possible, all background processes should be measured
 1609 in a “data–driven” way. By requiring that the background comes from data, biases due to
 1610 incorrectly modeling background processes in simulation can be minimized or eliminated.
 1611 In general, the data–driven methods also have the advantage that they are independent of
 1612 the uncertainty on the integrated luminosity. This analysis measures the backgrounds using
 1613 two complementary methods, the “template method” and the “fake–rate method.” In both
 1614 cases, predictions are made about backgrounds in the signal region using measurements
 1615 obtained in background enriched control regions of the data.

1616 The template method fits the sum of background shape templates to the M_{vis} spec-
 1617 trum of events selected in the final analysis and is described in Section 6.3. The results of
 1618 template method presented in this chapter cannot be used directly in the final result of this
 1619 analysis, as the final likelihood fit (see Chapter 8) implicitly performs a template fit of the
 1620 background shapes. Nonetheless, we present the results here as an additional cross–check
 1621 of the simulation performance, and to give an overview of the method.

1622 The fake–rate method is based on applying probabilities for quark and gluon jets to
 1623 be misidentified as hadronic tau decays to events passing all event selection criteria except
 1624 the tau identification requirements. The probabilities with which jets fake hadronic tau
 1625 signatures are measured in data. Contrary to the template method, the fake–rate method
 1626 estimates the sum of the contributions of backgrounds that contain incorrectly identified
 1627 taus. The fake–rate method is detailed in Section 6.2. The two methods are complementary
 1628 as the template method uses only information about the different visible mass distribution

1629 shapes of the backgrounds, while the fake–rate method uses only information about the
 1630 hadronic tau fake–rate.

1631 6.1 Background Enriched Control Regions

1632 The criteria applied to select events in the background enriched control regions for the
 1633 template method is based on the work described in [47]. With respect to that work, the muon
 1634 isolation criteria applied to select $Z \rightarrow \mu^+ \mu^-$, $W + \text{jets}$, $t\bar{t} + \text{jets}$ and QCD background
 1635 enriched control samples has been changed to relative isolation with respect to charged
 1636 hadrons and neutral electromagnetic objects reconstructed by the particle–flow algorithm.
 1637 The selection of the enriched backgrounds is accomplished by disabling or inverting specific
 1638 selections of Chapter 5 that were implemented to reject the given background. The selection
 1639 of control regions used to measure the fake–rates for different types of background processes
 1640 are very similar to the selections used for the template method. The details of the fake–rate
 1641 measurement selections may be found in [48].

1642 All control regions are selected from the 2010 CMS muon primary datasets using single
 1643 muon HLT trigger paths. The set of triggers and run–ranges used to select events in the
 1644 background enriched control samples is the same as for the analysis (see Table 5.1). The
 1645 Monte Carlo simulated events used for comparison with the control region selections are
 1646 required to pass the HLT_Mu9 trigger path and are weighted according to the description
 1647 in Chapter 7 to account for the difference in efficiency between HLT_Mu9 and the trigger
 1648 paths required to have passed in the data.

1649 QCD dijet events containing a muon (originating from the leptonic decay of a b or
 1650 c quark) are selected by applying an anti–isolation requirement on the jet containing a
 1651 muon. $W + \text{jets}$ and $t\bar{t} + \text{jets}$ are selected by requiring an isolated muon, and inverting
 1652 the transverse mass (M_T) and P_ζ selections. Tau candidates considered in the $Z \rightarrow \mu^+ \mu^-$
 1653 sample where the reconstructed tau candidate is faked by a misidentified muon and in
 1654 the $t\bar{t} + \text{jets}$ control sample are required to pass the “loose” TaNC discriminator. For the
 1655 template method, the $Z \rightarrow \mu^+ \mu^-$ sample where the reconstructed tau candidate is faked by
 1656 a misidentified quark or gluon jet, the $W + \text{jets}$ and the QCD enriched control samples have
 1657 a loose hadronic tau “preselection” applied. The tau candidates are required to pass the

1658 “very loose”, but fail the “loose” TaNC discriminator. The criteria applied to select events
 1659 in the different background enriched control samples are summarized in Table 6.1. The goal
 1660 of the background enriched selection process is to select different background processes with
 1661 high purity. A highly pure background control sample improves the stability of inferences
 1662 about the signal region made using information in the enriched control region. The purity
 1663 of the control regions (estimated using simulation) are summarized in Table 6.2.

1664 The number of events observed in the different control samples is compared to the
 1665 Monte Carlo expectation in Table 6.2. Except for the contribution of $Z \rightarrow \mu^+\mu^-$ events
 1666 in which the reconstructed tau candidate is due to a misidentified quark or gluon jet,
 1667 good agreement between data and Monte Carlo simulation is observed. Differences observed
 1668 between data and simulation will be accounted for as systematic uncertainties.

1669 The distributions of visible and “full” $\tau^+\tau^-$ invariant mass reconstructed by the SVfit
 1670 algorithm (see Chapter 4) observed in the background enriched control regions is compared
 1671 to the Monte Carlo simulation in Figures 6.1 and 6.2. The template for the $W +$ jets back-
 1672 ground has been corrected for the bias on the $M_{vis}^{\mu\tau_{had}}$ shape caused by the $M_T^{\mu E_T^{\text{miss}}} <$
 1673 $50 \text{ GeV}/c^2$ and $P_\zeta - 1.5 \cdot P_\zeta^{\text{vis}} > -20 \text{ GeV}$ requirements applied in the final analysis via the
 1674 reweighting procedure described in [47]. In the $t\bar{t} +$ jets enriched control region a peak at the
 1675 Z mass is observed in data, which is not modeled by the Monte Carlo samples considered.
 1676 The peak could be due to $Z \rightarrow \mu^+\mu^-$ events produced in association with b quarks. On
 1677 the other hand, the contribution from $t\bar{t} +$ jets events to that sample seems to be overesti-
 1678 mated. The origin of the Z mass peak merits further investigation, but overall the $t\bar{t} +$ jets
 1679 is a negligible background contribution.

1680 6.2 The Fake-rate Method

1681 The probabilities with which quark and gluon jets get misidentified as taus may be utilized
 1682 to obtain an estimate of background contributions in physics analyses. As an illustrative
 1683 example and in order to demonstrate the precision achievable with the method, we introduce
 1684 the method in the context of a “closure test,” using a simulated samples, a simple method of

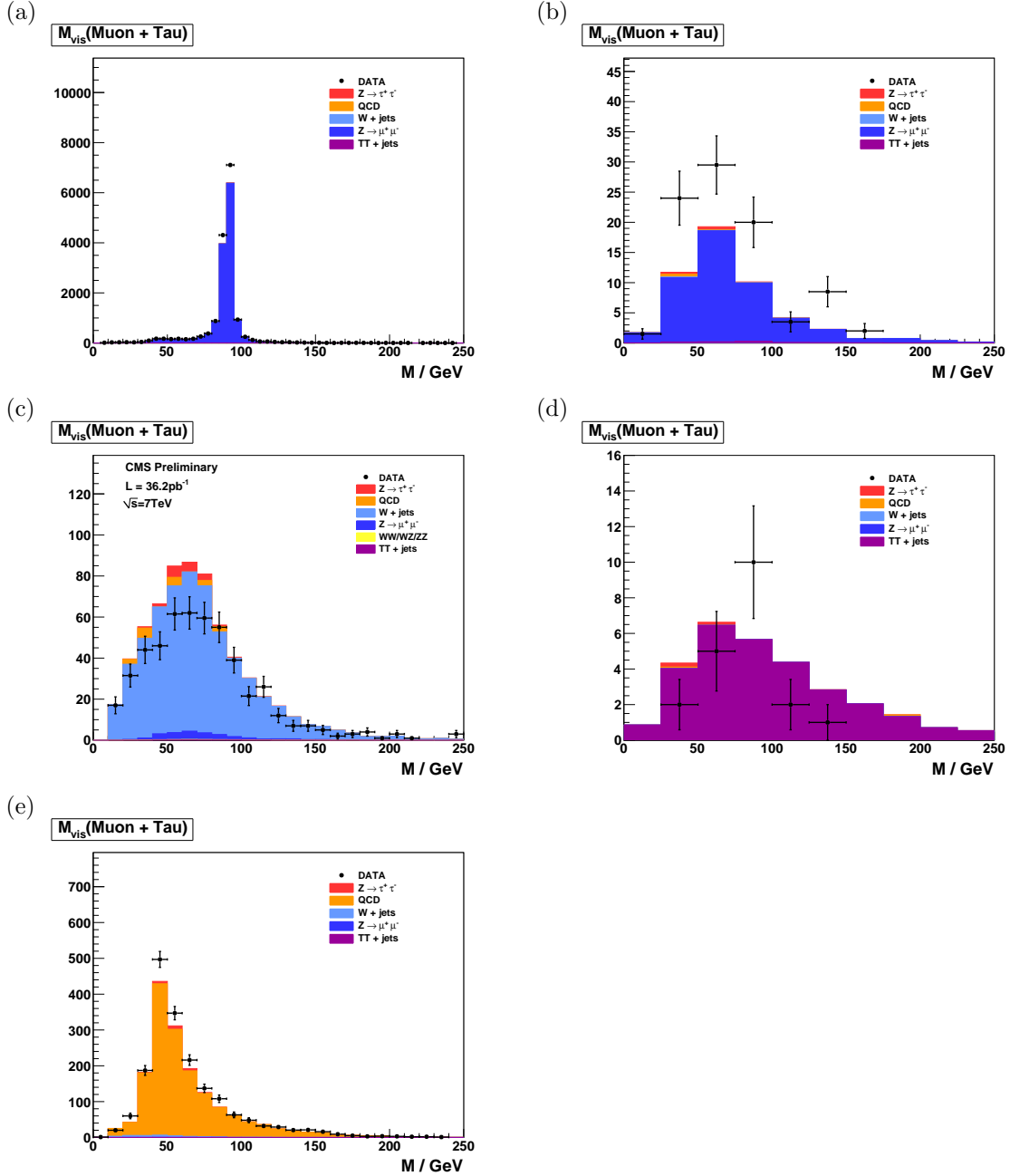


Figure 6.1: Distribution of visible mass of muon plus the tau candidate reconstructed in the background enriched control samples for $Z \rightarrow \mu^+ \mu^-$ (a) and (b), $W + \text{jets}$ (c), $t\bar{t} + \text{jets}$ (d) and QCD multi-jet (e) backgrounds. In (a) reconstructed tau candidates are expected to be dominantly due to misidentified muons, while in (b) they are expected to be mostly due to misidentified misidentified quark or gluon jets.

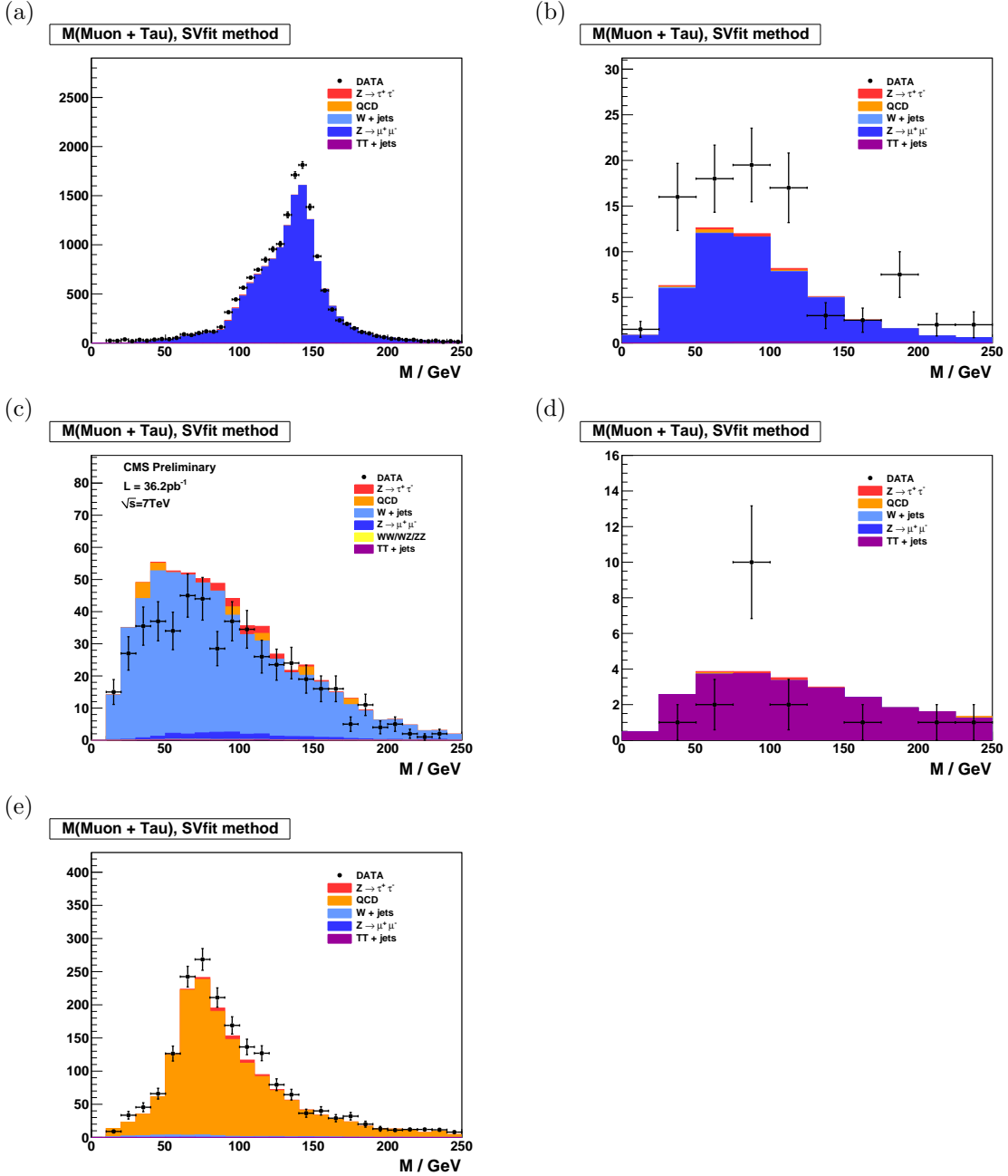


Figure 6.2: Distribution of “full” invariant mass reconstructed by the SVfit algorithm in the background enriched control samples for $Z \rightarrow \mu^+ \mu^-$ (a) and (b), $W + \text{jets}$ (c), $t\bar{t} + \text{jets}$ (d) and QCD multi-jet (e) backgrounds. In (a) reconstructed tau candidates are expected to be dominantly due to misidentified muons, while in (b) they are expected to be mostly due to misidentified misidentified quark or gluon jets.

1685 computing the fake–rate, and a simpler¹ hadronic tau identification algorithm. The closure
 1686 test demonstrates that the method is self–consistent, and that the fake–rate technique can be
 1687 used to estimate the contributions of QCD, $W + \text{jets}$, $t\bar{t} + \text{jets}$ and $Z \rightarrow \mu^+\mu^-$ backgrounds.
 1688 The analysis selections used in the closure test are almost identical to the selections used
 1689 in this analysis. Exact details of the selections can be found in reference analysis [44]. The
 1690 method is then extended to use fake–rates measured in data, a multivariate method of
 1691 computing the fake–rates, and the HPS + TaNC tau identification algorithm used in this
 1692 analysis.

1693 6.2.1 Parameterization of Fake–rates

1694 Efficiencies and fake–rates of the tau identification algorithm based on requiring no tracks
 1695 of $p_T > 1$ GeV/ c and ECAL energy deposits of $p_T > 1.5$ GeV/ c reconstructed within
 1696 an “isolation cone” of size $\Delta R_{iso} = 0.5$ and outside of a “shrinking signal cone” of size
 1697 $\Delta R_{sig} = 5.0/E_T$ as it is used in the $Z \rightarrow \tau^+\tau^- \rightarrow \mu + \tau$ -jet analysis [44] are displayed
 1698 in Figure 6.3. In order to account for the visible p_T and η dependence, we parametrize
 1699 the fake–rates in bins of transverse momentum and pseudo–rapidity. As we will show in
 1700 Section 6.2.3, the parametrization of the fake–rates by p_T and η makes it possible to not
 1701 only estimate the total number of background events contributing to physics analyses, but
 1702 to model the distributions of kinematic observables with a precision that is sufficient to
 1703 extract information on the background shape.

We add a third quantity, the E_T -weighted jet–width R_{jet} , to the parametrization in
 order to account for differences between the fake–rates of quark and gluon jets, which on
 average have differing widths and different fake–rates. The jet width quantity R_{jet} is defined
 as

$$R_{jet} = \sqrt{E(\eta^2) + E(\phi^2)}$$

1704 where $E(\eta^2)$, $E(\phi^2)$ is the second η , ϕ moment of the jet constituents, weighted by con-
 1705 stituent transverse energy. Analyses performed by the CDF collaboration [40, 49, 46] found

¹The closure test uses the “shrinking cone” tau identification algorithm, which is described briefly in Section 3.1. A full description can be found in [28].

1706 that systematic uncertainties on background estimates obtained from the fake–rate method
 1707 are reduced in case differences between quark and gluon jets are accounted for in this way.

1708 6.2.2 Measurement of Fake–rates

Efficiencies and fake–rates are obtained by counting the fraction of tau candidates passing all tau identification cuts and discriminators in a given bin² of p_T^{jet} , η_{jet} and R_{jet} :

$$P_{fr} \left(p_T^{jet}, \eta_{jet}, R_{jet} \right) := \frac{N_{jets} \left(p_T^{jet}, \eta_{jet}, R_{jet} | \text{tau ID passed} \right)}{N_{jets} \left(p_T^{jet}, \eta_{jet}, R_{jet} | \text{preselection passed} \right)} \quad (6.1)$$

1709 The pre–selection in the denominator of Equation 6.1 in general refers to p_T and η cuts,
 1710 which are applied with thresholds matching those applied on the final analysis level, but
 1711 may include loose tau identification criteria (which may be applied e.g. already during event
 1712 skimming). It is critical that the selection used in the denominator be identical to that of
 1713 the final analysis to ensure the fake–rates are not biased by different selections.

1714 Different sets of fake–rates are determined for the highest p_T and for the second highest
 1715 p_T jet in QCD dijet events, for jets in a QCD event sample enriched by the contribution
 1716 of heavy quarks and gluons by requiring the presence of a muon reconstructed in the final
 1717 state, and for jets in “electroweak” events selected by requiring a W boson in the final state.

1718 6.2.3 Application of Fake–rates

1719 Knowledge of the tau identification efficiencies and fake–rates as function of the parameters
 1720 p_T^{jet} , η_{jet} and R_{jet} as defined by Equation 6.1 is utilized to obtain an estimate for the con-
 1721 tributions of background processes to physics analyses involving tau lepton hadronic decays
 1722 in the final state. The basic idea is to replace tau identification cuts and discriminators by
 1723 appropriately chosen weights.

1724 Application of the fake–rate technique consists of two stages. The first stage consists of
 1725 loosening the tau identification cuts and discriminators and applying only the preselection
 1726 requirements defined by the denominator of Equation 6.1, in order to obtain an event
 1727 sample dominated by contributions of background processes. After disabling the selections

²The example presented in the closure tests bins the fake–rate calculation in bins of the parameterization variables. In Section 6.2.6 we describe a more robust multivariate method to compute the fake–rates.

on hadronic tau identification, the relative contributions of the backgrounds are expected to increase by the inverse of the (average) fake–rate, typically by a factor $\mathcal{O}(100)$. In the second stage, weights are applied to all events in the background dominated control sample, according to the probabilities $P_{fr} \left(p_T^{jet}, \eta_{jet}, R_{jet} \right)$ for jets to fake the signature of a hadronic tau decay. After application of the weights, an estimate for the total number of background events passing the tau identification cuts and discriminators and thus contributing to the final analysis sample is obtained.

The fake–rate technique works best if all background contributions to the analysis arise from misidentification of quark and gluon jets as hadronic tau decays. Corrections to the estimate obtained from the fake–rate technique are needed in case of background processes contributing to the final analysis sample which either produce genuine tau leptons in the final state (e.g. $t\bar{t} + \text{jets}$) or in which tau candidates are due to misidentified electrons or muons (e.g. $Z \rightarrow \mu^+\mu^-$, $Z \rightarrow e^+e^-$), as the latter may fake signatures of hadronic tau decays with very different probabilities than quark and gluon jets.

In the “simple” fake–rate method described in detail in the next section, the corrections are taken from Monte Carlo simulations. Corrections based on Monte Carlo are needed also to compensate for signal contributions to the background dominated control sample. An alternative to Monte Carlo based corrections is to utilize additional information contained in the background dominated control sample. The modified version is described in Section 6.2.5. It has been used to estimate background contributions in searches for Higgs boson production with subsequent decays into tau lepton pairs performed by the CDF collaboration in Tevatron Run II data [40, 49, 46]. We will refer to the modified version as “CDF–type” method in the following.

6.2.4 “Simple” Weight Method

In the “simple” method, all tau candidates within the background dominated event sample are weighted by the probabilities of quark and gluon jets to fake the signature of a hadronic tau decay

$$w_{jet}^{simple} \left(p_T^{jet}, \eta_{jet}, R_{jet} \right) := P_{fr} \left(p_T^{jet}, \eta_{jet}, R_{jet} \right). \quad (6.2)$$

1752 These weights are applied to all jets in the background dominated control sample which
 1753 pass the preselection defined by the denominator of Equation 6.1. Note that the weights
 1754 defined by Equation 6.2 can be used to estimate the contributions of background processes
 1755 to distributions of tau related observables. They cannot be used as event weights.

In order to compare distributions of event–level quantities or per–particle quantities for particles of types different from tau leptons decaying hadronically, event weights need to be defined. Neglecting the small fraction of background events in which multiple tau candidates pass the complete set of all tau identification cuts and discriminators, event weights can be computed by summing up the per–jet weights defined by Equation 6.2 over all tau candidates in the event which pass the preselection:

$$W_{\text{event}}^{\text{simple}} := \sum w_{\text{jet}}^{\text{simple}} \quad (6.3)$$

A bit of care is needed in case one wants to compare distributions of observables related to “composite particles,” the multiplicity of which depends on the multiplicity of tau candidates in the event (e.g. combinations of muon + tau pairs in case of the $Z \rightarrow \tau^+ \tau^- \rightarrow \mu + \tau$ -jet analysis). Per–particle weights need to be computed for such “composite particles”, depending on $p_{\text{T}}^{\text{jet}}$, η_{jet} , R_{jet} of its tau candidate constituent, according to:

$$w_{\text{comp-part}}^{\text{simple}}(p_{\text{T}}^{\text{jet}}, \eta_{\text{jet}}, R_{\text{jet}}) := w_{\text{jet}}^{\text{simple}}(p_{\text{T}}^{\text{jet}}, \eta_{\text{jet}}, R_{\text{jet}}) \quad (6.4)$$

1756 Different estimates are obtained for the fake–rate probabilities determined for the high-
 1757 est and second highest p_{T} jet in QCD dijet events, jets in a muon enriched QCD sample
 1758 and jets in $W + \text{jets}$ events. The arithmetic average of the four estimates of the closure test
 1759 together with the difference between the computed average and the minimum/maximum
 1760 value is given in Table 6.3.

1761 We take the average value as the “best” estimate of the background contribution and
 1762 the difference between the average and the minimum/maximum estimate as its systematic
 1763 uncertainty. We obtain a value of $\mathcal{O}(15\%)$ for the systematic uncertainty and find that
 1764 the true sum of QCD, $W + \text{jets}$, $t\bar{t} + \text{jets}$ and $Z \rightarrow \mu^+ \mu^-$ background contributions agrees

1765 well with the “best” estimate obtained by the fake–rate method within the systematic
 1766 uncertainty.

1767 Note that the estimate for the sum of background contributions which one obtains
 1768 in case one applies the “simple” fake–rate weights defined by Equation 6.3 to a back-
 1769 ground dominated control sample selected in data is likely to overestimate the true value
 1770 of background contributions by a significant amount. The reason is that contributions of
 1771 $Z \rightarrow \tau^+ \tau^-$ events with true taus are non–negligible. In fact, genuine tau contributions to
 1772 the background dominated control sample are expected to be 14.9% and since the per-
 1773 jet weights computed by Equation 6.2 are larger on average in signal than in background
 1774 events, the signal contribution increases by the weighting and amounts to 37.1% of the sum
 1775 of event weights computed by Equation 6.3 and given in Table 6.3.

1766 The contribution of the $Z \rightarrow \tau^+ \tau^-$ signal needs to be determined by Monte Carlo
 1767 simulation and subtracted from the estimate obtained by applying the “simple” fake–rate
 1768 method to data, in order to get an unbiased estimate of the true background contributions.

1779 6.2.5 “CDF–type” Weights

1780 Instead of subtracting from the estimate obtained for the sum of background contributions a
 1781 correction determined by Monte Carlo simulation, the genuine tau contribution contribution
 1782 to the background dominated event sample selected in data can be corrected for by adjusting
 1783 the weights, based solely on information contained in the analyzed data sample, avoiding
 1784 the need to rely on Monte Carlo based corrections.

1785 In the “CDF–type” method, additional information, namely whether or not tau can-
 1786 didates pass or fail the tau identification cuts and discriminators, is drawn from the data.
 1787 The desired cancellation of signal contributions is achieved by assigning negative weights
 1788 to those tau candidates which pass all tau identification cuts and discriminators, i.e. to a
 1789 fair fraction of genuine hadronic tau decays, but to a small fraction of quark and gluon jets
 1790 only. The small reduction of the background estimate by negative weights assigned to quark
 1791 and gluon jets is accounted for by a small increase of the positive weights assigned to those
 1792 tau candidates for which at least one of the tau identification cuts or discriminators fails.
 1793 In this way, an unbiased estimate of the background contribution is maintained.

To be specific, the “CDF–type” weights assigned to tau candidates are computed as:

$$w_{jet}^{CDF}(p_T^{jet}, \eta_{jet}, R_{jet}) := \begin{cases} \frac{P_{fr}(p_T^{jet}, \eta_{jet}, R_{jet}) \cdot \varepsilon(p_T^{jet}, \eta_{jet}, R_{jet})}{\varepsilon(p_T^{jet}, \eta_{jet}, R_{jet}) - P_{fr}(p_T^{jet}, \eta_{jet}, R_{jet})} & \text{all tau ID passed} \\ \frac{P_{fr}(p_T^{jet}, \eta_{jet}, R_{jet}) \cdot (1 - \varepsilon(p_T^{jet}, \eta_{jet}, R_{jet}))}{\varepsilon(p_T^{jet}, \eta_{jet}, R_{jet}) - P_{fr}(p_T^{jet}, \eta_{jet}, R_{jet})} & \text{otherwise} \end{cases} \quad (6.5)$$

For the derivation of Equation 6.5 for the “CDF–type” weights assigned to tau candidates, we will use the following notation: Let n_τ (n_{QCD}) denote the total number of taus (quark and gluon jets) in a certain bin of transverse momentum p_T^{jet} , pseudo-rapidity η_{jet} and jet-width R_{jet} and n_τ^{sel} (n_{QCD}^{sel}) denote the number of taus (quark and gluon jets) in that bin which pass all tau identification cuts and discriminators. By definition of the tau identification efficiency $\varepsilon := \varepsilon(p_T^{jet}, \eta_{jet}, R_{jet})$ and fake-rate $f := f(p_T^{jet}, \eta_{jet}, R_{jet})$:

$$\begin{aligned} n_\tau^{sel} &= \varepsilon \cdot n_\tau \\ n_{QCD}^{sel} &= f \cdot n_{QCD}. \end{aligned} \quad (6.6)$$

Depending on whether or not a given tau candidate passes all tau identification cuts and discriminators or not, we will assign a weight of value w_{passed} or w_{failed} to it. The values of the weights w_{passed} and w_{failed} shall be adjusted such that they provide an unbiased estimate of the background contribution:

$$w_{passed} \cdot f \cdot n_{QCD} + w_{failed} \cdot (1 - f) \cdot n_{QCD} \equiv n_{QCD}^{sel} = f \cdot n_{QCD} \quad (6.7)$$

while averaging to zero for genuine hadronic tau decays:

$$w_{passed} \cdot \varepsilon \cdot n_\tau + w_{failed} \cdot (1 - \varepsilon) \cdot n_\tau \equiv 0.$$

The latter equation yields the relation:

$$w_{passed} = -\frac{1 - \varepsilon}{\varepsilon} \cdot w_{failed}, \quad (6.8)$$

associating the two types of weights. By inserting relation 6.8 into Equation 6.7 we obtain:

$$\begin{aligned} & -\frac{1-\varepsilon}{\varepsilon} \cdot w_{failed} \cdot f \cdot n_{QCD} + w_{failed} \cdot (1-f) \cdot n_{QCD} = f \cdot n_{QCD} \\ \Rightarrow & \left(\frac{-f + \varepsilon \cdot f + \varepsilon - f \cdot \varepsilon}{\varepsilon} \right) \cdot w_{failed} = f \\ \Rightarrow & w_{failed} = \frac{f \cdot \varepsilon}{\varepsilon - f} \end{aligned}$$

and

$$w_{passed} = -\frac{f \cdot (1-\varepsilon)}{\varepsilon - f} \quad (6.9)$$

which matches exactly Equation 6.5 for the “CDF–type” weights applied to tau candidates given in Section 6.2.5.

Event weights and the weights assigned to “composite particles” are computed in the same way as for the “simple” weights, based on the weights assigned to the tau candidates:

$$\begin{aligned} W_{event}^{CDF} &:= \Sigma w_{jet}^{CDF} \\ w_{comp-part}^{CDF} (p_T^{jet}, \eta_{jet}, R_{jet}) &:= w_{jet}^{CDF} (p_T^{jet}, \eta_{jet}, R_{jet}), \end{aligned} \quad (6.10)$$

where the sums extend over all jets in the background dominated control sample which pass the preselection defined by the denominator of Equation 6.1.

The effect of the negative weights to compensate the positive weights in case the “CDF–type” fake–rate method is applied to signal events containing genuine hadronic tau decays is shown in Table 6.4 and illustrated in Figure 6.4. As expected, positive and negative weights do indeed cancel in the statistical average.

Figures 6.5, 6.6 and 6.7 demonstrate that an unbiased estimate of the background contribution by the “CDF–type” weights is maintained. Overall, the estimates obtained are in good agreement with the contributions expected for different background processes, indicating that the adjustment of negative and positive weights works as expected for the background as well.

Results obtained by the “CDF–type” fake–rate method in the closure test are summarized in Table 6.4, in which the total number of background events estimated by Equa-

tion 6.10 is compared to the true background contributions. The “best” estimate of the background contribution obtained from the “CDF-type” method is again taken as the arithmetic average of the estimates obtained by applying the fake-rate probabilities for the highest and second highest p_T jet in QCD dijet events, jets in a muon enriched QCD sample and jets in $W + \text{jets}$ events. Systematic uncertainties are taken from the difference between the computed average value and the minimum/maximum estimate. We obtain a value of $\mathcal{O}(15 - 20\%)$ for the systematic uncertainty of the “CDF-type” method, slightly higher than the systematic uncertainty obtained for the “simple” method. The small increase of systematic uncertainties is in agreement with our expectation for fluctuations of the jet-weights in case weights of negative and positive sign are used.

6.2.6 k-Nearest Neighbor Fake-rate Calculation

For the fake-rate method to give correct results, care must be taken that the measured fake-rate is well defined in all of the regions of phase space where it will be used. In the closure test described above, the computation of the fake-rate was accomplished by binning the numerator (tau ID passed) and denominator (tau ID passed and failed) distributions in the three dimensions of the parameterizations. This method has the disadvantage that the determination of the optimal binning is extremely difficult to determine, and that any bins with no entries in the denominator distribution caused the fake-rate to be undefined in those regions.

To overcome these problems, the fake-rate parameterization is implemented by adapting a multivariate technique known as a k -Nearest Neighbor classifier (k NN). A k NN classifier is typically used to classify events by populating (“training”) an n -dimensional space with signal and background events. The probability for a given point x in the space to be “signal-like” is determined by finding the k nearest neighbors and computing the ratio

$$p_{sig} = \frac{n_{sig}}{n_{sig} + n_{bkg}}, \quad (6.11)$$

where n_{sig} , n_{bkg} are the observed number of signal and background events, respectively. By construction, $k = n_{sig} + n_{bkg}$. The principle of operation is illustrated in Figure 6.8.

1839 The classification feature of a k NN can be trivially adapted to parameterize an efficiency
 1840 (fake–rate) such that it is defined everywhere. Examining the form of Equation 6.11, it is
 1841 clear that by replacing n_{sig} with n_{passed} and n_{bkg} with n_{failed} , p_{sig} is equivalent to the tau–
 1842 fake rate. We thus “train” the k NN with tau candidates which pass the tau identification as
 1843 signal events and those which fail as background events. The resulting classifier is a function
 1844 which returns the expected fake–rate for any point in the space of the parameterization.
 1845 The choice of k must be optimized. When k is low, the small number of neighbors causes
 1846 large counting fluctuations in the fake rate. If k is too large, the k NN effectively averages
 1847 over a large area of the space of the variables³. For the training statistics available in the
 1848 2010 data, $k = 20$ is found to be the optimal choice.

1849 6.2.7 Results of Fake–Rate Background Estimation

1850 An independent estimate of the background contributions to the analysis presented in this
 1851 thesis is obtained by applying the fake–rate method in a manner analogous to the closure
 1852 test. Fake–rates in QCD multi–jet events (light quark enriched sample), QCD events con-
 1853 taining muons (heavy quark and gluon enriched sample) and $W +$ jets events are measured
 1854 in data [34, 48] and applied to events which pass all the event selection criteria listed in
 1855 Table 5.3, with the exceptions of

- 1856 • the “loose” HPS + TaNC discriminator, and
- 1857 • the requirement that the tau have unit charge.

1858 No assumption is made on the composition of $Z \rightarrow \mu^+ \mu^-$, $W +$ jets, $t\bar{t} +$ jets and QCD
 1859 backgrounds contributing to the event sample selected by the analysis. Differences between
 1860 fake–rates obtained for QCD multi–jet, QCD muon enriched and $W +$ jets background
 1861 events are attributed as systematic uncertainties of the fake–rate method. Per jet and per
 1862 event weights have been computed by the “simple” and “CDF-type” weights as described in
 1863 the closure test and the results are found to be compatible within statistical and systematic
 1864 uncertainties. In the following, we present results for “CDF-type” weights. The “CDF-type”

³In the limit $k \rightarrow \inf$, the k NN output reduces to a single number. In this extreme case, all information about the dependence of the fake–rate on the variables is lost.

1865 weights have the advantage that the background estimate obtained does not change, whether
 1866 there is MSSM $H \rightarrow \tau^+\tau^-$ signal present in the data or not.

1867 Tau identification efficiencies need to be known when using “CDF-type” weights. Ded-
 1868 icated studies have checked the tau identification efficiencies in data [48]. Statistical and
 1869 systematic uncertainties of these studies are still sizeable at present, on the order of 20–30%.
 1870 No indication has been found, however, that the Monte Carlo simulation does not correctly
 1871 model hadronic tau decays in data. For the purpose of computing fake-rate weights via
 1872 the “CDF-type” method, tau identification efficiencies are taken from the Monte Carlo
 1873 simulation of hadronic tau decays in $Z \rightarrow \tau^+\tau^-$ events. Systematic uncertainties on the
 1874 background estimate obtained by the fake-rate method are determined by varying the tau
 1875 identification efficiencies by $\pm 30\%$ relative to the value obtained from the Monte Carlo
 1876 simulation.

1877 The results of applying the fake-rate method to the mu + tau channel are summarized
 1878 in Table 6.5. The background prediction has been corrected for the expected⁴ contribution
 1879 of $13.1^{+2.8}_{-0.6}$ events from $Z \rightarrow \mu^+\mu^-$ background events in which the reconstructed tau is due
 1880 to a misidentified muon. The obtained estimate is in good agreement with the Monte Carlo
 1881 expectation.

1882 As an additional cross-check of the method, a sample of events containing a muon plus
 1883 a tau of like-sign charge is selected in data and compared to the background prediction
 1884 obtained by applying the fake-rate method to the like-sign sample. The like-sign sample is
 1885 expected to be dominated by the contributions of $W + \text{jets}$ and QCD background processes
 1886 and allows to verify the fake-rate method in a practically signal free event sample. The
 1887 background estimate obtained by the fake-rate method is compared to the number of events
 1888 observed in the like-sign data sample in Table 6.6. The number of events expected in
 1889 the like-sign control sample from Monte Carlo simulation is indicated in the caption. All
 1890 numbers are in good agreement.

1891 The fake-rate method does not only allow to estimate the total number of background
 1892 events, but allows to model the distributions of background processes as well. The capability
 1893 to model distributions is illustrated in Figure 6.9, which shows good agreement between the

⁴The contribution of $Z \rightarrow \mu^+\mu^-$ is estimated using a simulated sample.

1894 distributions observed in the like-sign data sample and the predictions obtained by the fake–
 1895 rate method for the distributions of muon plus tau visible mass and of the “full” invariant
 1896 mass reconstructed by the SVfit algorithm.

Fixme: THIS
 IS FROM
 THE HPS
 NOTE!

1897 6.3 Template Method

1898 Shape templates for the $\mu + \tau_{had}$ visible mass M_{vis} are obtained from data, using a set of
 1899 dedicated control regions which are chosen to select a high purity sample of one particular
 1900 background process each. The number of events selected in each control region and com-
 1901 parisons to the predictions from Monte Carlo simulations are summarized in Table 6.2. The
 1902 template M_{vis} shapes obtained from data in the background enriched control regions are
 1903 compared to the signal region shapes obtained by Monte Carlo simulation in Figure 6.10.
 1904 The M_{vis} spectrum observed in the final analysis is fitted to the sum of these templates. Es-
 1905 timates for background yields are obtained from the normalization factor of each template,
 1906 determined by the fit. Further details of the method can be found in [47] and [50].

1907 The TaNC (Section 3.3, [51]) discriminators used in [50] are replaced by the correspond-
 1908 ing discriminators of the HPS + TaNC algorithm (Section 3.5, [33]). The $Z/\gamma^* \rightarrow \tau^+\tau^-$ sig-
 1909 nal shape is obtained via the $Z/\gamma^* \rightarrow \mu^+\mu^-$ embedding technique [52]. The $\mu + \tau_{had}$ visible
 1910 mass spectrum observed in the final analysis is compared to the sum of template shapes
 1911 scaled by the normalization factors determined by the fit in Figure 6.11. The corresponding
 1912 estimates for background contributions are summarized in Table 6.7.

Requirement	$Z \rightarrow \mu^+ \mu^-$			Enriched background process		
	Muon fake	$Z \rightarrow \mu^+ \mu^-$ Jet fake	$W + \text{jets}$	$t\bar{t} + \text{jets}$	$W + \text{jets}$	QCD
Muon rel. iso.	< 0.15	< 0.1	< 0.1	< 0.1	< 0.1	> 0.10 $\&\&$ < 0.30
Muon Track IP	-	-	-	-	-	-
Tau TaNC discr.	-	1	1	medium passed	1	1
Tau 1 3-Prong	-	-	-	-	-	-
Charge(Tau) = ± 1	-	-	-	-	-	-
Tau μ -Veto	inverted	applied	applied	applied	applied	applied
Charge(Muon+Tau)	applied	-	-	-	-	-
M_T (Muon-MET)	-	< 40 GeV	-	-	-	< 40 GeV
$P_\zeta - 1.5 \cdot P_\zeta^{vis}$	> -20 GeV	-	-	-	-	> -20 GeV
global Muons	< 2	-	< 2	< 2	< 2	< 2
central Jet Veto	-	-	2	-	-	-
b-Tagging	-	-	-	3	3	-

¹ vloose passed $\&\&$ loose failed ² no Jets of $E_T > 20$ GeV within $|\eta| < 2.1$ (other than the τ -jet candidate) ³ min. two Jets of $E_T > 40$ GeV, at least one of which was at least of which with “TrackCountingHighEff” discriminator > 2.5

Table 6.1: Criteria to select events in different background enriched control samples. Hyphens indicate event selection criteria which are not applied.

Enriched Selection	Data	Σ_{SM}	Contribution from				Purity
			$Z \rightarrow \tau^+ \tau^-$	$Z \rightarrow \mu^+ \mu^-$	$W + \text{jets}$	$t\bar{t} + \text{jets}$	
$Z \rightarrow \mu^+ \mu^-$							
Muon fake	15156	17109.8	331.6	16586.6	55.1	80.4	35.0
Jet fake	85	62.7	2.5	55.5	0.5	1.4	2.4
$W + \text{jets}$	514	642.4	17.9	22.9	581.7	0.8	16.7
$t\bar{t} + \text{jets}$	26	39.7	0.7	< 0.1	0.6	38.4	< 1.0
QCD	2510	2571.8	16.6	0.8	9.3	1.6	2543.4
							98.9%

Table 6.2: Number of events observed in the different background enriched control samples compared to Monte Carlo expectations. Σ_{SM} denotes the sum of $Z \rightarrow \tau^+ \tau^-$, $Z \rightarrow \mu^+ \mu^-$, $W + \text{jets}$ and QCD processes. The expected purity of each control sample is computed as the ratio of contribution of the enriched process to Σ_{SM} .

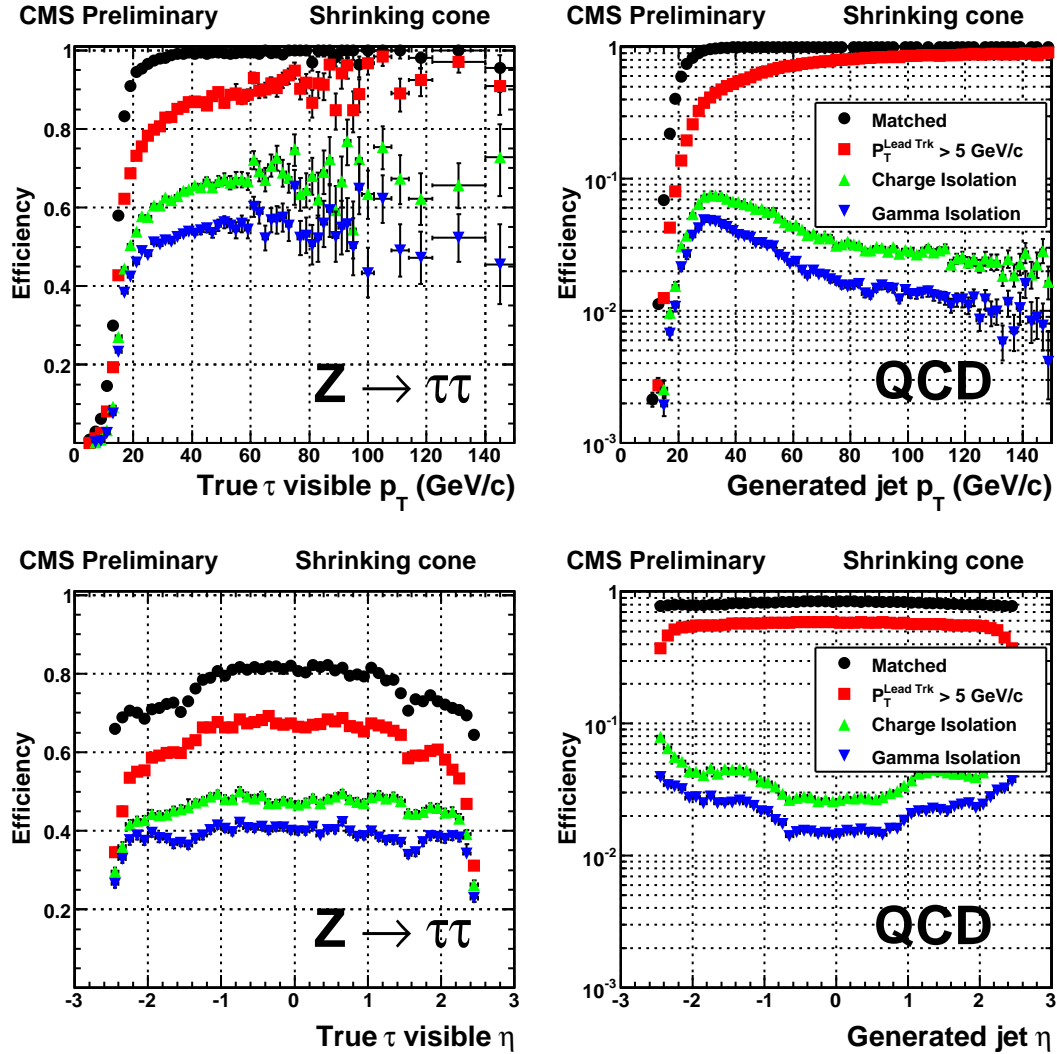


Figure 6.3: Cumulative efficiencies (left) and fake-rates (right) of successively applied tau identification cuts of the “shrinking signal cone” particle-flow based tau identification algorithm described in [28] as function of p_T^{jet} (top) and η^{jet} (bottom) of tau candidates. The efficiencies/fake-rates for the complete set of tau identification criteria are represented by the blue (downwards facing) triangles.

Background Process	Expectation	Estimate obtained by applying weights of type:			Average fake-rate estimate
		QCD lead jet	QCD second jet	QCD μ -enriched	
W+jets	163.0 ± 7.1	157.2 ± 2.8	140.9 ± 2.7	129.9 ± 2.5	177.9 ± 3.2
QCD	246.4 ± 31.8	269.2 ± 14.0	246.5 ± 14.3	219.7 ± 11.8	300.8 ± 15.2
t <bar>t>+jets</bar>	12.2 ± 0.6	14.3 ± 0.3	12.6 ± 0.3	11.6 ± 0.3	16.5 ± 0.3
Z → $\mu^+ \mu^-$	68.6 ± 2.9	58.2 ± 1.3	51.2 ± 1.2	48.5 ± 1.1	65.8 ± 1.4
Σ Background	490.4 ± 32.7	499.9 ± 14.4	451.2 ± 14.6	409.7 ± 12.1	561.1 ± 15.6
Z → $\tau^+ \tau^-$	—	284.3 ± 3.7	269.0 ± 3.9	256.5 ± 3.3	325.3 ± 4.2

Table 6.3: Number of events from W+jets, QCD, tt>+jets and Z → $\mu^+ \mu^-$ background processes expected to pass all selection criteria of the Z → $\tau^+ \tau^- \rightarrow \mu^+ \tau^-$ cross-section analysis compared to the estimates obtained by weighting events in the background dominated control sample with the “simple” fake-rate weights defined by Equation 6.3.

Background Process	Expectation	Estimate obtained by applying weights of type:				Average fake-rate estimate
		QCD lead jet	QCD second jet	QCD μ -enriched	$W + \text{jets}$	
$W + \text{jets}$	163.0 ± 7.1	163.2 ± 3.8	140.6 ± 3.4	128.0 ± 3.1	188.3 ± 4.2	$155.0^{+33.6}_{-27.3}$
QCD	246.4 ± 31.8	300.5 ± 19.5	266.1 ± 19.0	236.0 ± 16.4	335.1 ± 20.4	$284.4^{+55.5}_{-52.0}$
$t\bar{t} + \text{jets}$	12.2 ± 0.6	13.1 ± 0.3	11.5 ± 0.3	10.2 ± 0.3	15.4 ± 0.4	$12.6^{+2.8}_{-2.4}$
$Z \rightarrow \mu^+\mu^-$	68.6 ± 2.9	52.7 ± 1.4	46.7 ± 1.4	41.9 ± 1.2	60.3 ± 1.6	$50.4^{+10.1}_{-8.6}$
Σ Background	490.4 ± 32.7	529.5 ± 19.9	464.9 ± 19.3	416.1 ± 16.8	599.1 ± 20.9	$502.4^{+99.4}_{-88.4}$
$Z \rightarrow \tau^+\tau^-$	–	0.3 ± 2.4	-10.6 ± 2.5	3.8 ± 2.0	-10.8 ± 2.8	$-4.3^{+8.4}_{-7.2}$

Table 6.4: Number of events from $W + \text{jets}$, QCD, $t\bar{t} + \text{jets}$ and $Z \rightarrow \mu^+\mu^-$ background processes expected to pass all selection criteria of the closure test compared to the estimates obtained by weighting events in the background dominated control sample with the “CDF-type” fake-rate weights defined by Equation 6.10.

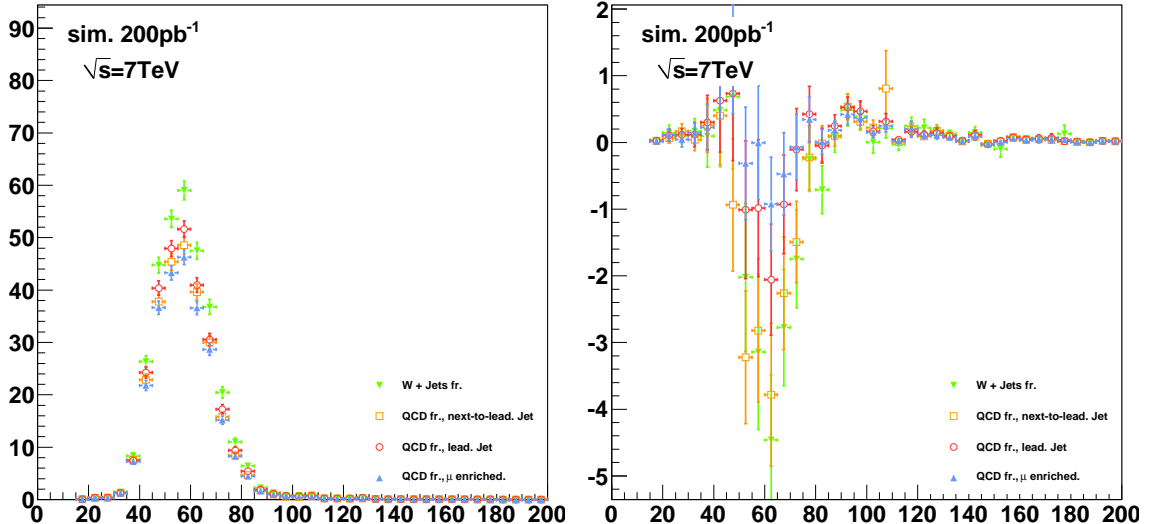


Figure 6.4: Distributions of visible invariant mass of muon plus tau in $Z \rightarrow \tau^+\tau^-$ signal events weighted by “simple” weights computed according to Equation 6.4 (left) and “CDF-type” weights computed according to Equation 6.10 (right). The signal contribution to the background estimate computed by the “simple” method is non-negligible and needs to be corrected for. The “CDF-type” weights achieve a statistical cancellation of positive and negative weights, such that the total signal contribution averages to zero, avoiding the need for Monte Carlo based corrections.

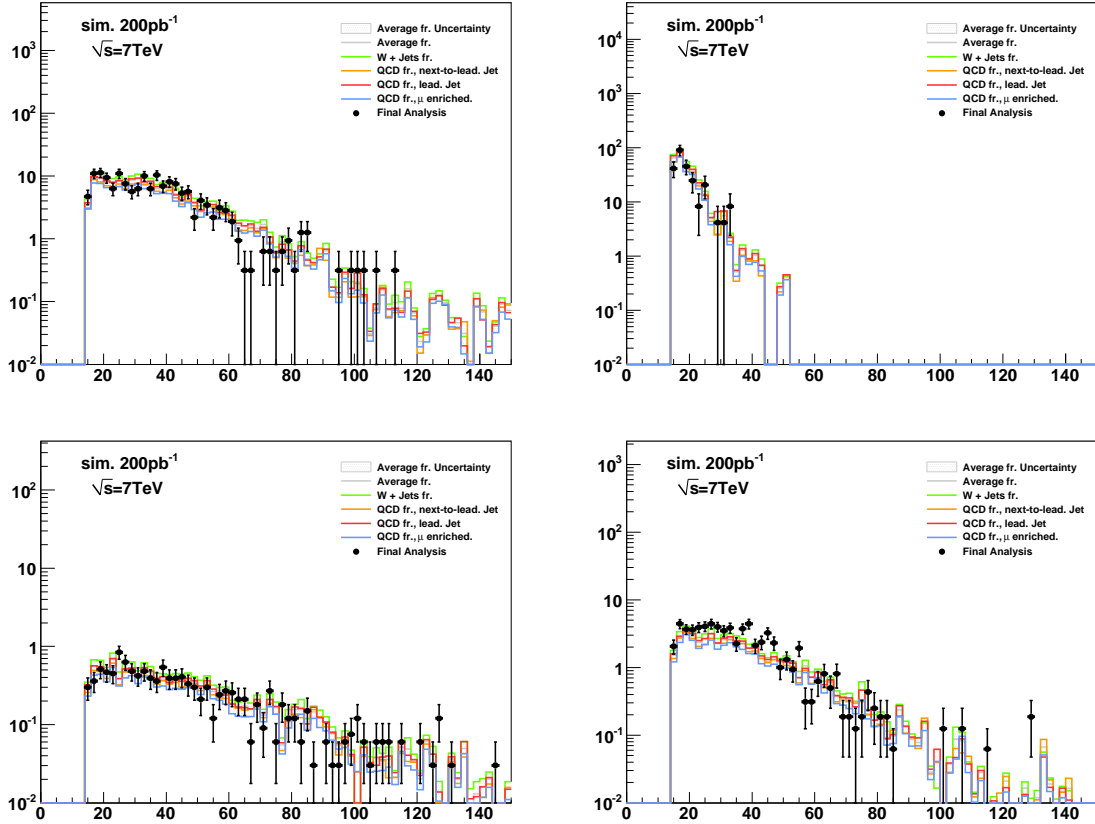


Figure 6.5: Distributions of muon transverse momentum in $W + \text{jets}$ (top left), QCD (top right), $t\bar{t} + \text{jets}$ (bottom left) and $Z \rightarrow \mu^+\mu^- \rightarrow \mu + \tau\text{-jet}$ cross-section analysis [44] compared to the estimate obtained from the “CDF method” fake-rate technique, computed according to Equation 6.10. The expected contribution of background processes is indicated by points. Lines of different colors represent the estimates obtained by applying fake-rate weights determined for different compositions of light quark, heavy quark and gluon jets, as described in Section 6.2.1. The maximum (minimum) estimate is interpreted as upper (lower) bound. The difference between the bounds is taken as systematic uncertainty on the estimate obtained from the “CDF-type” fake-rate method and is represented by the gray shaded area.

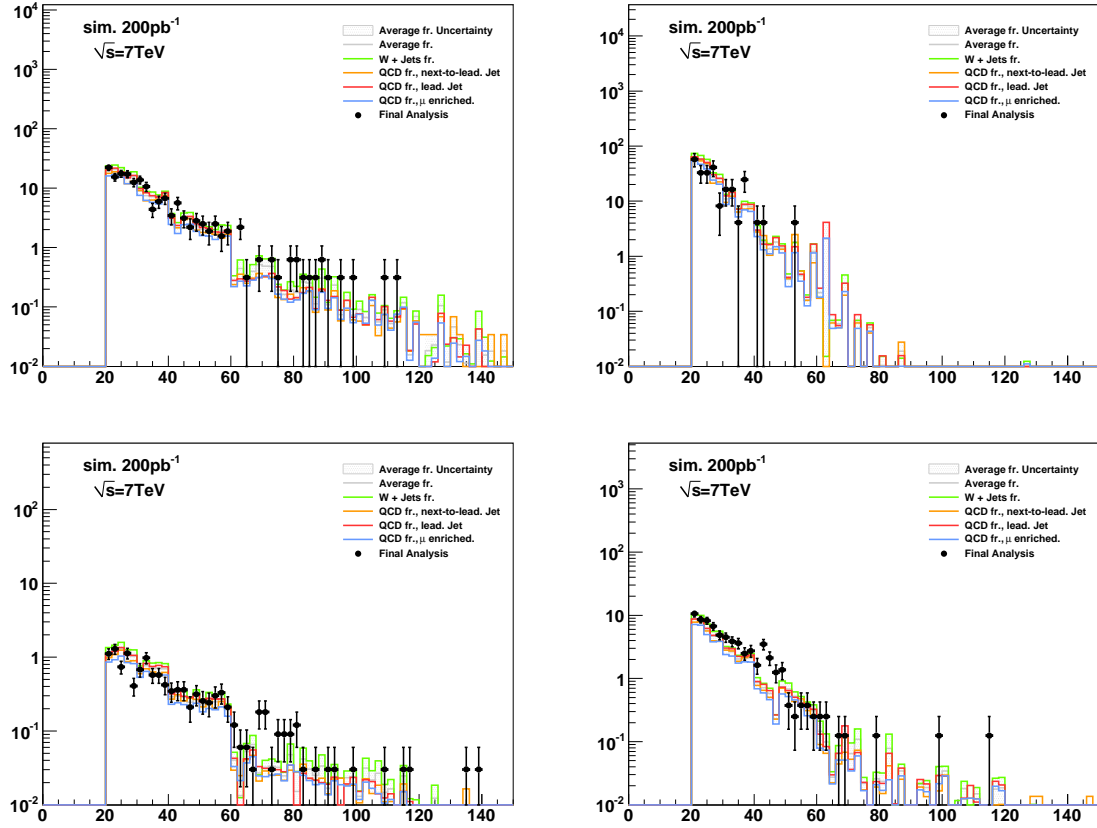


Figure 6.6: Distributions of transverse momenta of the tau candidates in $W + \text{jets}$ (top left), QCD (top right), $t\bar{t} + \text{jets}$ (bottom left) and $Z \rightarrow \mu^+\mu^-$ (bottom right) background events which pass all selection criteria of the $Z \rightarrow \tau^+\tau^- \rightarrow \mu + \tau\text{-jet}$ cross-section analysis compared to the estimate obtained from the fake-rate technique, computed according to Equation 6.5. The expected contribution of background processes is indicated by points. Lines of different colors represent the estimates obtained by applying fake-rate weights determined for different compositions of light quark, heavy quark and gluon jets, as described in Section 6.2.1. The maximum (minimum) estimate is interpreted as upper (lower) bound. The difference between the bounds is taken as systematic uncertainty on the estimate obtained from the “CDF-type” fake-rate method and is represented by the gray shaded area.

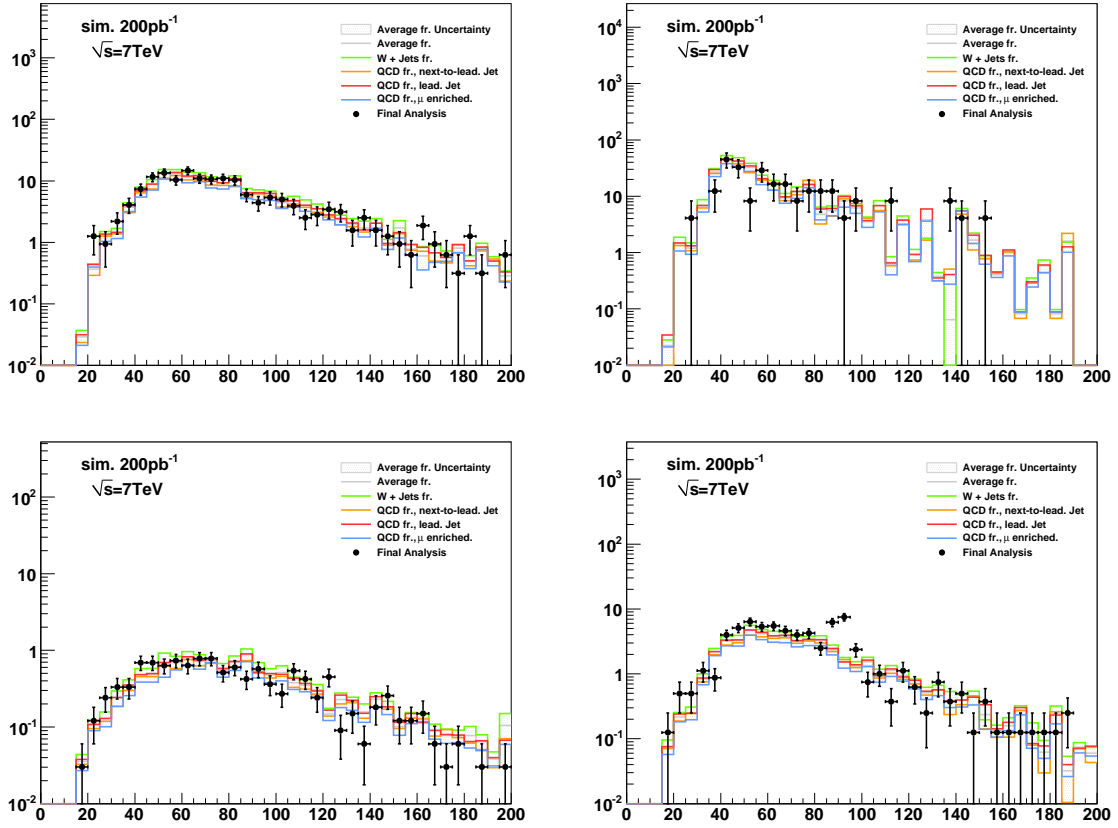


Figure 6.7: Distributions of the visible invariant mass of muon plus tau in $W + \text{jets}$ (top left), QCD (top right), $t\bar{t} + \text{jets}$ (bottom left) and $Z \rightarrow \mu^+\mu^-$ (bottom right) background events which pass all selection criteria of the closure test analysis compared to the estimate obtained from the fake-rate technique, computed according to Equation 6.10. The expected contribution of background processes is indicated by points. Lines of different colors represent the estimates obtained by applying fake-rate weights determined for different compositions of light quark, heavy quark and gluon jets, as described in Section 6.2.1. The maximum (minimum) estimate is interpreted as upper (lower) bound. The difference between the bounds is taken as systematic uncertainty on the estimate obtained from the “CDF-type” fake-rate method and is represented by the gray shaded area.

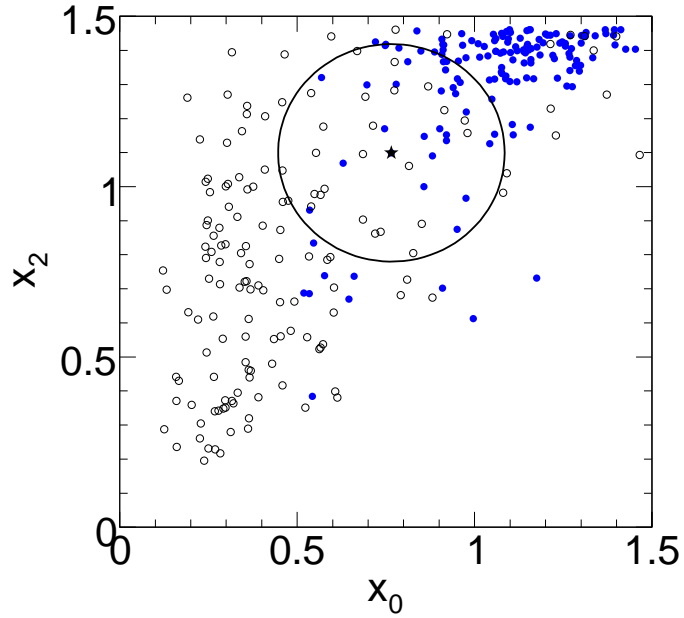


Figure 6.8: Example of the operation of a k NN classifier. The closest $k = 50$ neighbors (those inside the circle) to a test point (indicated by the star marker) are selected. The probability that the star marker is a signal event is given the number of signal neighbors (blue markers) in the circle divided by k . Image credit: [30]

Events weighted by:	Estimate
QCD lead jet	$202.1^{+14.9}_{-74.8}$
QCD second jet	$198.0^{+22.8}_{-79.3}$
QCD μ -enriched	$213.3^{+17.7}_{-82.6}$
$W + \text{jets}$	$232.8^{+21.1}_{-95.0}$
N_{bgr} estimate	$236.1^{+24.1}_{-65.9}$

Table 6.5: Estimate for background contributions obtained by weighting events passing all selection criteria listed in Table 5.3 except for the requirement for tau candidates to pass the “medium” tight TaNC discriminator and have unit charge by fake-rates measured in QCD multi-jet, QCD muon enriched and $W + \text{jets}$ data samples.

Events weighted by:	Estimate
QCD lead jet	$191.7^{+2.3}_{-17.9}$
QCD second jet	$185.1^{+6.0}_{-21.1}$
QCD μ -enriched	$194.7^{+2.0}_{-20.5}$
$W + \text{jets}$	$208.9^{+0.5}_{-14.4}$
Fake-rate estimate	$201.8^{+14.2}_{-18.9}$
Observed	223

Table 6.6: Number of events observed in like-sign control region compared to the estimate obtained by fake-rate method.

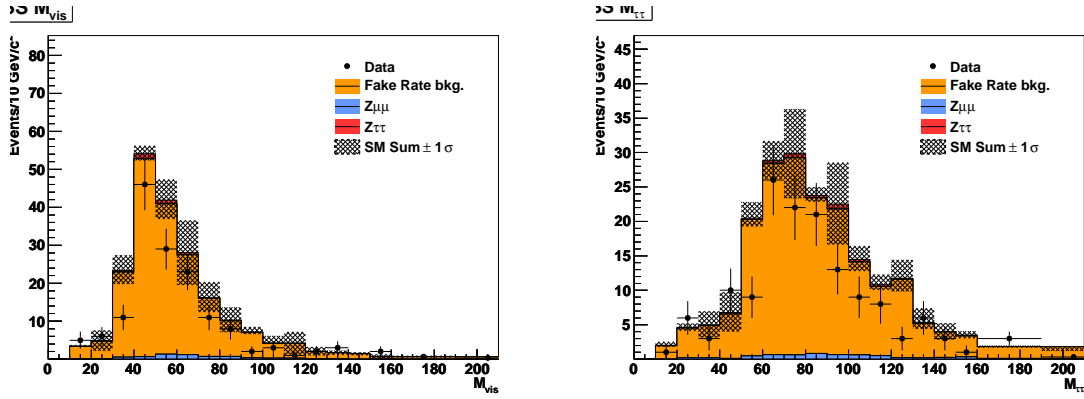


Figure 6.9: Distribution of visible mass (left) and “full” invariant mass reconstructed by the SVfit algorithm (right) observed in the like-sign charge control region compared to the background estimate obtained by the fake-rate method.

Process	Estimate
$Z \rightarrow \mu^+ \mu^-$	
Muon fake	5.7 ± 6.0
Jet fake	< 14.5
$W + \text{jets } t\bar{t} + \text{jets}$	7.6 ± 6.9
QCD	141.3 ± 40.4
N_{bgr} estimate	226.5 ± 33.1

Table 6.7: Estimated contributions of individual background processes to the signal region, obtained via the template method. As the shapes are very similar, the normalization factors for QCD and $W + \text{jets}$ background processes are anti-correlated. As a consequence, the sum of background contributions is determined by the fit more precisely than the individual contributions.

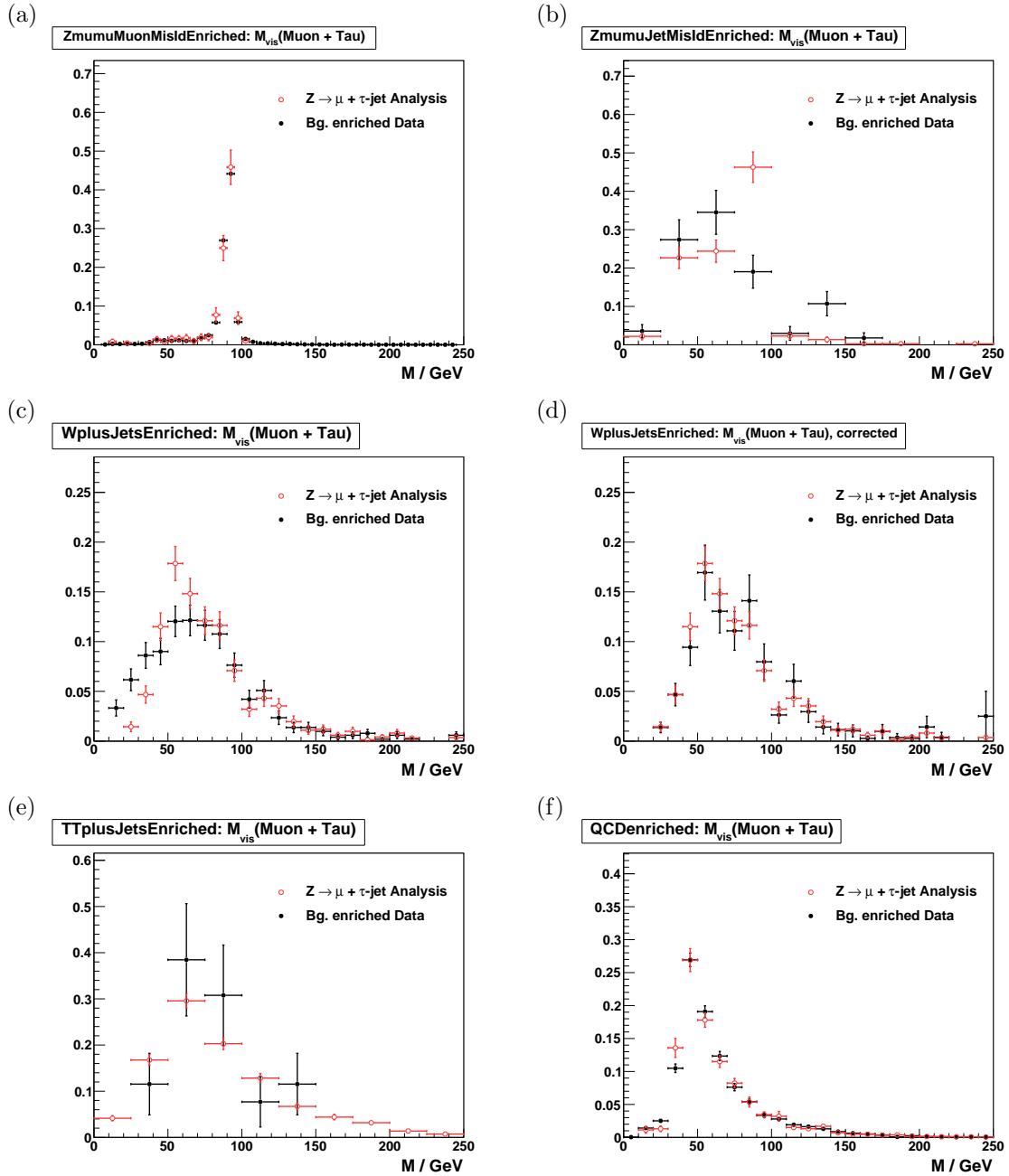


Figure 6.10: $\mu + \tau_{had}$ shape templates obtained from $Z \rightarrow \mu^+ \mu^-$ (a) and (b), $W + \text{jets}$ before (c) and after (d) the bias correction explained in Section 6.3, $t\bar{t} + \text{jets}$ (e) and QCD multi-jet (f) backgrounds enriched control regions compared to the expected distribution of the enriched background process to the signal region, predicted by Monte Carlo simulations. In (a) reconstructed tau candidates are expected to be dominantly due to misidentified muons, while in (b) they are expected to be mostly due to misidentified quark or gluon jets.

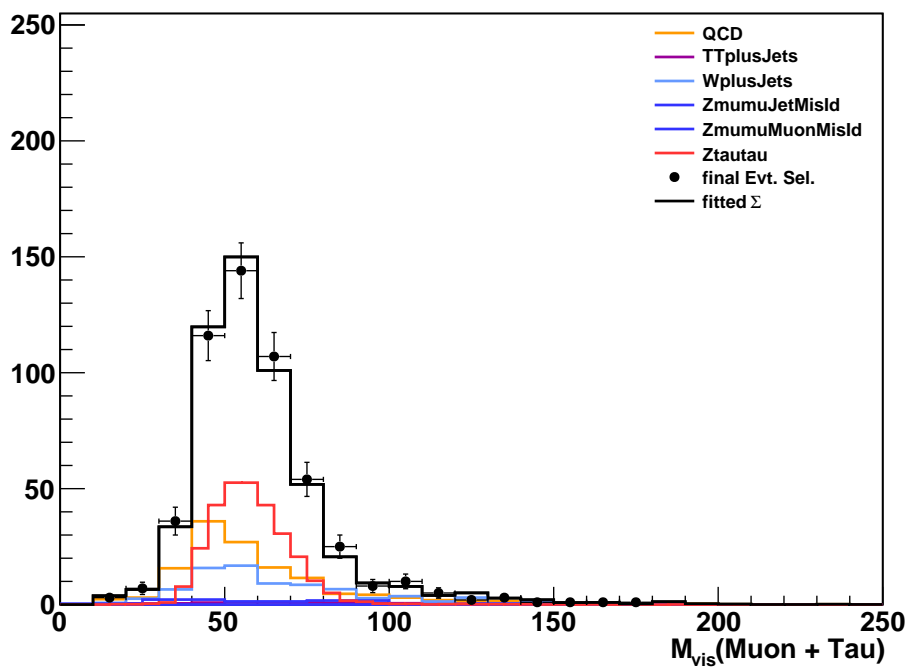


Figure 6.11: M_{vis} distribution of events selected by the $Z/\gamma^* \rightarrow \tau^+\tau^- \rightarrow \mu + \tau_{had}$ cross-section analysis compared to the sum of shape templates for signal and background processes scaled by the normalization factors determined by the fit.

Chapter 7

1913

1914 Monte Carlo Corrections

1915 One of the most important goals of the analysis is to minimize the effect of potentially
 1916 incorrect simulation effects on the final result. While the simulated CMS events have been
 1917 observed to match the 2010 data with surprising results, it is nonetheless critical to measure
 1918 in real data phenomenon which can have significant effects on the analysis whenever possible.
 1919 In practice, these measurements are used to apply a correction factor to the corresponding
 1920 measurement obtained from Monte Carlo. This measured correction factor has an associ-
 1921 ated uncertainty, and is taken into account as a systematic uncertainty. The application of
 1922 systematic uncertainties is described in the next chapter.

1923 The corrections measured and used in this analysis can be divided into two categories,
 1924 efficiency corrections and scale corrections. Identification efficiency corrections scale the
 1925 expected yield (due to a given identification selection) up or down. Scale corrections sys-
 1926 tematically scale the energy of a particle (or E_T^{miss}) up or down. In this analysis we apply
 1927 efficiency corrections for the High Level Trigger muon requirement, all stages of muon iden-
 1928 tification, and the hadronic tau identification. We apply a momentum scale correction to
 1929 the muon and tau legs, and to the resolution of the E_T^{miss} . Finally, events are simulated with
 1930 overlapping “pile-up”¹ events. The simulated events are weighted such that the number of
 1931 pile-up events in the simulation matches that observed in the data.

1932 7.1 Muon Identification Efficiency

1933 The identification efficiencies associated with the muon are measured in $Z \rightarrow \mu^+ \mu^-$ events
 1934 using the “tag and probe” technique [44]. $Z \rightarrow \mu^+ \mu^-$ events are selected from the Muon

¹A pile-up event occurs when there are multiple interactions in one bunch proton bunch crossing. Pile-up increases with the instantaneous luminosity provided by the collider.

1935 7 TeV CMS 2010 datasets² by requiring that the events pass the “loose” Vector Boson Task
 1936 Force (VBTF) event selections [44]. In the selected events, we define the “tag” muons as
 1937 those that have transverse momentum greater than 15 GeV/c and pass the VBTF muon
 1938 selection. The tag muons are further required to pass the “combined relative isolation” de-
 1939 scribed in the VBTF paper. We finally require that the tag muon be matched to an HLT
 1940 object corresponding to the run-dependent requirements listed in Table 5.1. The trigger
 1941 match requirement ensures that the event would be recorded independently of the probe
 1942 muon. After the tag and probe muon pairs have been collected, we compare the muon identi-
 1943 fication performance in the probe collection in events selected in data to the performance in
 1944 simulated $Z \rightarrow \mu^+ \mu^-$ events. The selection of events and tag muon in the simulated sample
 1945 is the same as the data sample, with the notable exception that the only HLT requirement
 1946 applied in MC is that the tag muon is matched to an HLT_Mu9 object. Any difference in ef-
 1947 ficiency between the HLT_Mu9 path and the paths used to select the data (in the tag–probe
 1948 measurement and in the analysis) will be considered implicitly in the correction factor.

1949 The efficiencies for the muon selections applied in this analysis are measured using
 1950 the “probe” objects. We measure the following marginal efficiencies, each relative to the
 1951 previous requirement:

- 1952 • Efficiency of global probe muons to satisfy VBTF muon identification selections.
- 1953 • Efficiency of global probe muons passing the VBTF muon identification selection to
1954 satisfy the isolation criteria described in Section 5.2.1.
- 1955 • Efficiency of probe muons passing the offline analysis selection defined in Chapter 5
1956 to pass the HLT selection.

1957 In each case, the invariant mass spectrum of the tag–probe pair is fitted with a Crystal
 1958 Ball function for the signal ($Z \rightarrow \mu^+ \mu^-$) events and an exponential for the background.
 1959 The fit is done for two cases; where the probe fails the selection and the where it passes.
 1960 The method is illustrated in Figure 7.1. The signal yield N is extracted from each fit and
 1961 the efficiency is computed as $N_{\text{pass}}/(N_{\text{pass}} + N_{\text{fail}})$. Each efficiency is measured in both the

²/Mu/Run2010A-Sep17ReReco²/RECO and /Mu/Run2010B-PromptReco-v2/RECO

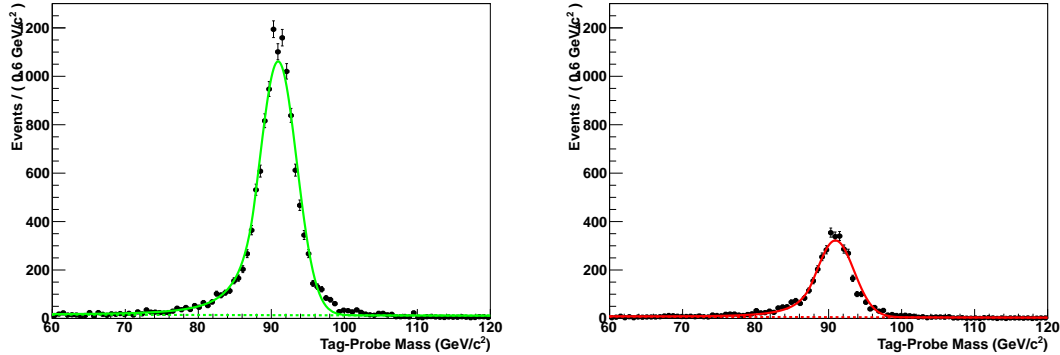


Figure 7.1: The tag–probe dimuon invariant mass spectrum in events in which the probe muon passed (left) and failed (right) the muon isolation requirement. The solid line gives the result of a simultaneous fit of the signal ($Z \rightarrow \mu^+ \mu^-$ events) and background. The fitted background contribution is shown as the dotted line. The muon isolation efficiency is then extracted from the number of signal events in the passing and failing bins.

1962 data and the simulation. The results of the measurements are shown in Table 7.1. In the
 1963 final analysis, the simulated events are weighted by the fractional difference to the measured
 1964 values; the statistical uncertainty on the weight is taken as the sum in quadrature of the
 1965 statistical uncertainties for the data and simulation efficiency measurements. The uncer-
 1966 tainty on this measurement is taken as systematic uncertainty in the final measurement.
 1967

1968 The correction for the trigger efficiency needs to take into account the differences in
 1969 the HLT selections applied during different operating periods (see Table 5.1). To determine
 1970 the overall correction factor, we measure the trigger efficiency in data for each of the op-
 1971 erating periods and compare it to the simulated efficiency of the HLT_Mu9 selection. The
 1972 overall efficiency in data is taken as the average of the three periods, weighted by integrated
 1973 luminosity.

1974 The efficiency of the “cross–triggers” used in the run–range period 148822 – 149182
 1975 (period C) cannot be measured in $Z \rightarrow \mu^+ \mu^-$ events as they require a reconstructed PFTau
 1976 object at the trigger level. A single muon trigger (HLT_Mu15) is also used in period C.
 1977 The contribution of the cross–triggers is taken as a correction to the single muon trigger
 1978 period C efficiency. The “muon leg” of the cross–triggers have the same requirements as
 1979 the single muon triggers used in the run–range 147196 – 148058 (period B). The “cross–

Muon selection	Efficiency		Ratio	Corection
	Data	Simulation		
VBTF identification	$99.2^{+0.1\%}_{-0.1\%}$	$99.1^{+0.1\%}_{-0.1\%}$	$1.001^{+0.001}_{-0.001}$	1.0
Particle Isolation	$76.8^{+0.4\%}_{-0.4\%}$	$78.3^{+0.3\%}_{-0.3\%}$	$0.981^{+0.006}_{-0.006}$	0.98
Trigger	$95.0^{+0.5\%}_{-0.5\%}$	$96.5^{+0.1\%}_{-0.2\%}$	$0.984^{+0.006}_{-0.006}$	0.98

Table 7.1: Efficiency of the various global muon selections applied in the analysis measured in data and simulated $Z \rightarrow \mu^+\mu^-$ events. The “correction” column gives the event weight correction applied to the simulated events in the final analysis. The efficiency for each selection is the marginal efficiency with respect to the selection in the row above it.

trigger” contribution is estimated as the difference between the efficiency in period B and the single-muon period C efficiency multiplied by a correction factor of $0.9 \pm 10\%$ to account for the τ leg efficiency. In the case that the measured single-muon period C efficiency is larger than the period B efficiency (due to statistical fluctuations and improvements in the trigger system), the period B efficiency is increased by 2%.

7.2 Hadronic Tau Identification Efficiency

The hadronic tau identification efficiency has been measured in 2010 7 TeV CMS data. The most straight forward to measure the tau ID efficiency would be to use a resonance which decays to taus and has a known cross section. One could then measure the tau ID efficiency in by comparing the observed yield N_{obs} in data with that expected from the known cross section, according to the cross section equation,

$$\varepsilon = \frac{N_{\text{obs}} - N_{\text{bkg}}}{\mathcal{L} \times \mathcal{A} \times \sigma \times \text{BR}_\tau}.$$

The only suitable resonance for this method is $Z \rightarrow \tau^+\tau^-$. This method has been applied³ in the CMS $Z \rightarrow \tau^+\tau^-$ cross section analysis ??, and measured a tau identification simulation to data correction factor of 0.960 ± 0.067 .

³Actually, a slightly more complicated method is used. The analysis uses three decay channels, and the $Z \rightarrow \tau^+\tau^-$ cross section and tau identification correction factors are fitted simultaneously. The central value of the $Z \rightarrow \tau^+\tau^-$ cross section is driven by the $Z \rightarrow \tau^+\tau^- \rightarrow e\mu$ channel, which is independent of the hadronic tau identification.

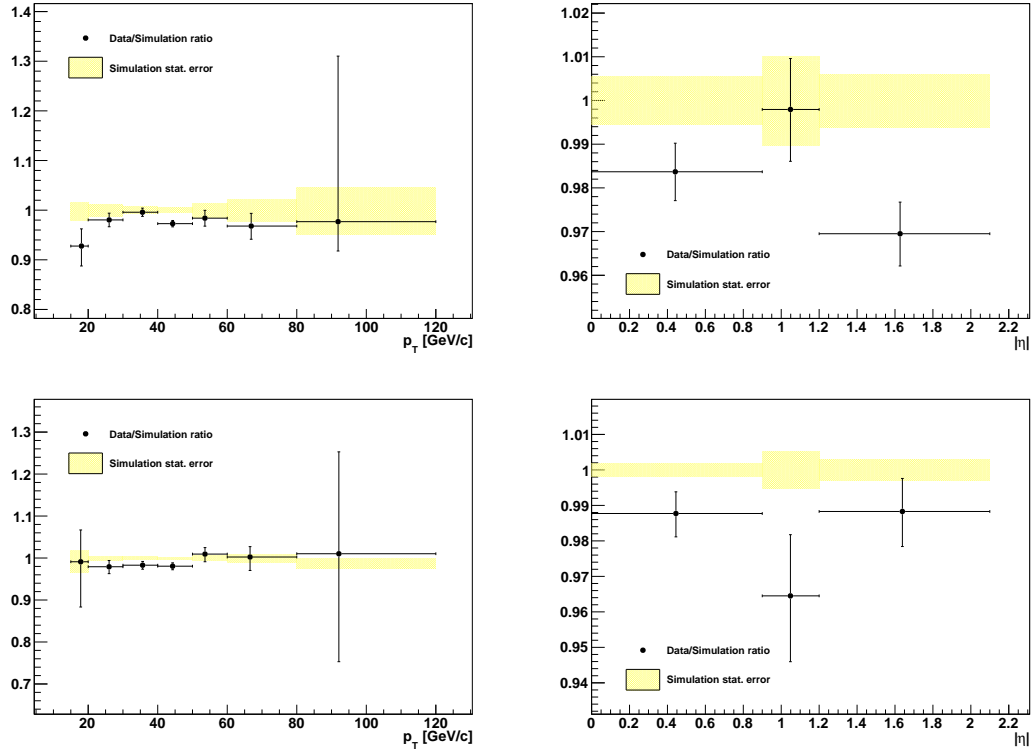


Figure 7.2: Ratio of muon isolation efficiency (top) and HLT trigger efficiency (bottom) measured in data compared to simulated $Z \rightarrow \mu^+\mu^-$ events. The correction factors are measured in bins of p_T (left) and η . In the analysis, the correction factors are taken to be flat.

Unfortunately, this method cannot be used in this analysis. The measurement using the Z resonance operates on the assumption there is no new physics contribution to the events in the Z bump. In the case that there was a Higgs boson signal at $m_{A^0} = 90$ GeV/ c^2 , it would be indistinguishable from the Z and would appear as an increase of N_H in the observed yield. The analysis would be completely insensitive to a Higgs boson on the Z peak, and cause the efficiency to be overestimated by a factor

$$\delta\varepsilon = \frac{N_H}{\mathcal{L} \times \mathcal{A} \times \sigma \times \text{BR}_\tau}.$$

1989 The solution to this problem is to use a “tag and probe” approach analogous to the
1990 muon efficiency measurement of Section 7.1. The tag and probe method is only sensitive to
1991 the shapes of the distributions, and is independent of a Higgs boson contribution to the Z

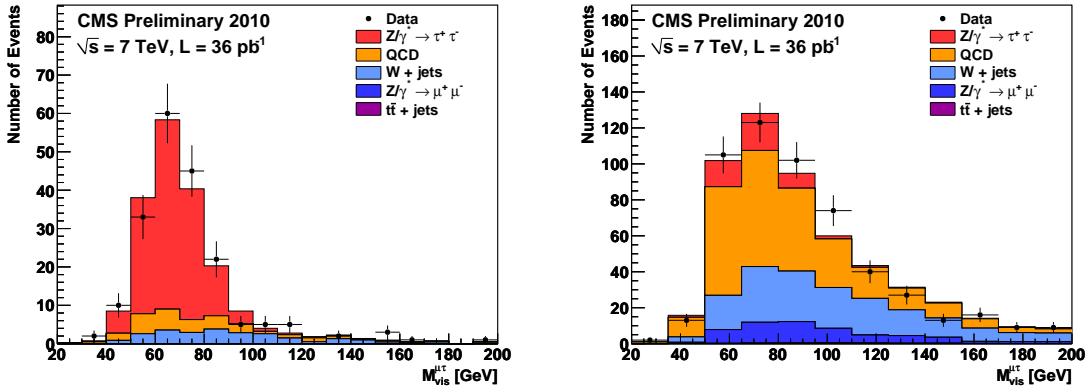


Figure 7.3: Visible mass spectrum of preselected events used to measure the hadronic tau identification efficiency in 2010 CMS 7 TeV data. The figure on the left (right) shows the preselected events that pass (fail) the hadronic tau identification. The different colors indicate the fitted yields of the different signal and background contributions. Reference: [48].

peak. This measurement has been performed by the CMS Tau Physics Object Group [48]. A loose hadronic tau preselection is applied to events which pass the selections (excluding the hadronic tau identification) of the CMS EWK $Z \rightarrow \tau^+\tau^-$ cross section measurement [53]. The preselected sample is then split into two categories, those that pass the hadronic tau identification and those that fail. The signal and background yields in each category are fitted using the Template Method described in Section 6.3. An illustrative example of the fits for the yields is shown in Figure 7.3. The hadronic tau identification efficiency can then be computed using the relative size of the true tau yields in the passing and failing categories. The efficiency is measured [48] for the loose HPS + TaNC tau identification in the 2010 CMS dataset and is found to be 1.06 ± 0.30 .

7.3 Muon and Tau Momentum Scale

Muons are one of the best measured objects at CMS. The momentum scale of CMS muons has been measured [54] using the J/ψ , $\psi(2S)$ and Υ dimuon resonant decays. The muon momentum resolution is found to be 3% or better for muons with $p_T < 100$ GeV/c. We apply the muon momentum correction using the ‘‘MusCleFit’’ algorithm described in [54]. The muon momentum correction and uncertainty varies as a function of

2008 muon p_T and η . The effect of the muon momentum correction uncertainty is a small effect
 2009 in this analysis compared to the τ and E_T^{miss} scale uncertainties.

2010 The uncertainty on the jet energy scale is determined from an analysis of the p_T balance
 2011 between photons and jets in $\gamma + \text{jets}$ events [55]. The jet energy scale uncertainties are
 2012 determined by the JetMET group are applied to tau-jets as well as other jets in the event.
 2013 The tau energy scale correction factor is taken to be 1.0 with an uncertainty of 3%. The QCD
 2014 jet energy scale has been measured to within 3% uncertainty. In the future, the energy scale
 2015 of the tau is expected to be determined to a much better precision, as the neutral hadronic
 2016 activity of a hadronic tau decay is expected to be zero. The jet energy scale of 3% can be
 2017 confidently considered [48] an upper limit⁴, and is used in this analysis as the tau energy
 2018 scale uncertainty.

2019 7.4 Missing Transverse Energy Correction

2020 In practice, the resolution of the reconstructed missing transverse energy is poor as it is
 2021 sensitive to the mis-measurement of any object in the event. Furthermore, a fraction of the
 2022 particles produced in the hard collision can be produced in the very forward region, outside
 2023 of the fiducial region of the calorimeters. The resolution of the E_T^{miss} reconstruction can be
 2024 measured in $Z \rightarrow \mu^+ \mu^-$ events. The true E_T^{miss} in such events is expected to be zero. The
 2025 E_T^{miss} resolution in simulated $Z \rightarrow \mu^+ \mu^-$ events is found to be smaller (better) than in the
 2026 data.

2027 The E_T^{miss} resolution depends on the “recoil” of the Z boson. The reason for this effect
 2028 is that for events where the Z is produced nearly at rest, the associated recoil products have
 2029 very small transverse momentum and are produced at very high pseudorapidity. The E_T^{miss}
 2030 is corrected using a procedure called a “Z-recoil” correction, as described in [56]. The reso-
 2031 lution of the E_T^{miss} is measured in $Z \rightarrow \mu^+ \mu^-$ events in simulation and data. The difference
 2032 in the reconstructed E_T^{miss} resolution in both samples is parameterized by the magnitude of
 2033 the transverse momenta of the particles recoiling against the Z .⁵ The reconstructed E_T^{miss}

⁴The tau energy scale was roughly measured using the invariant mass of the hadronic decay products and shown to be compatible with 1.0, within 3%.

⁵The “recoil” particles are defined as all those not identified as Z decay products. This definition is equivalent to the total decay product transverse momentum q_T added reconstructed E_T^{miss} .

2034 in the simulated $Z \rightarrow \tau^+ \tau^-$, $Z \rightarrow \mu^+ \mu^-$, and $W + \text{jets}$ samples is “smeared” by a random
 2035 amount in each event such that the final resolution matches the observed resolution in the
 2036 data.

2037 Z -recoil corrections are determined as described in [56] and applied to simulated $Z \rightarrow$
 2038 $\tau^+ \tau^-$, $Z \rightarrow \mu^+ \mu^-$ and $W + \text{jets}$ events, in order to correct for residual differences in E_T^{miss}
 2039 response and resolution between data and Monte Carlo simulation [57]. The corrections are
 2040 obtained by an unbinned maximum likelihood fit (in data and simulation) of the transverse
 2041 recoil vector $\vec{u}_T = -(\vec{q}_T + E_T^{\text{miss}})$ as function of the transverse momentum \vec{q}_T of the Z -
 2042 boson in directions parallel and perpendicular to the Z -boson transverse momentum vector.

2043 Two additionally types of corrections are applied to the simulated E_T^{miss} , “clustered”
 2044 and “unclustered.” The overall correction factor from these two effects is taken to be unity.
 2045 However, the uncertainty on these two correction factors is used as a systematic uncertainty
 2046 when setting the final limit. The clustered E_T^{miss} correction varies the scale of all jets with
 2047 $p_T > 10 \text{ GeV}/c$ in the event and recomputes the shifted E_T^{miss} . The unclustered E_T^{miss} cor-
 2048 rection varies the energy scale of all jets/particles in the event with $p_T < 10 \text{ GeV}/c$. The
 2049 scale uncertainty is 3% for the clustered correction and 10% for the unclustered correction.

2050 7.5 Pile-up Event Weighting

2051 The average number of pile-up interactions in the event can effect almost all aspects of
 2052 the analysis. In general, increasing pile-up lowers particle identification efficiencies and
 2053 lowers E_T^{miss} resolution. It is therefore important that the distribution of pile-up events
 2054 in the simulation matches the distribution found in the data. Differences in the number
 2055 of pile-up interactions between the data (averaged over the analyzed run-range) and pile-
 2056 up Monte Carlo samples produced for “BX156⁶” pile-up conditions are corrected for by
 2057 reweighting Monte Carlo simulated events according to the number of reconstructed event
 2058 vertices, in order to match the distribution measured in a $W \rightarrow \mu\nu$ dataset triggered by
 2059 the HLT_Mu15 High Level Trigger path. Vertices considered for this purpose are required
 2060 to pass $-24 < z_{vtx} < +24 \text{ cm}$, $|\rho| < 2 \text{ cm}$, $\text{nDoF} > 4$. In addition, the total transverse

⁶The BX156 name comes from the fact that the pile-up scenario used in this simulation corresponds to an LHC configuration with 156 bunches.

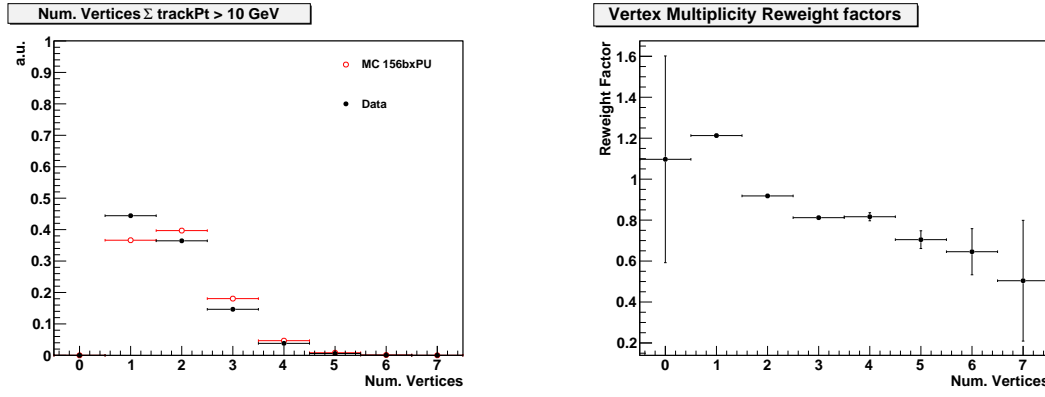


Figure 7.4: Vertex multiplicity distribution measured in the analyzed data-taking period compared to Monte Carlo simulation with “BX156” pile-up conditions (left) and resulting Monte Carlo reweighting factors (right).

2061 momenta of all tracks fitted to the vertex is required to exceed $10 \text{ GeV}/c$, assuming that
 2062 “softer” vertices have little or no effect on the “hard” event to pass event selection criteria.
 2063 The average vertex multiplicity distribution measured in data is compared to Monte Carlo
 2064 simulation with “BX156” pile-up conditions in Figure 7.4. Both distributions are similar,
 2065 resulting in Monte Carlo reweighting factors close to unity.

2066

Chapter 8

2067

Systematics and Limit Extraction

2068 In this chapter we discuss the systematic uncertainties affecting the search for the Higgs
 2069 boson and the statistical techniques used to establish an upper limit on the Higgs $\rightarrow \tau^+\tau^-$
 2070 branching ratio times cross section ($\sigma \times \text{BR}_\tau$). The limit can be interpreted as the largest¹
 2071 signal presence that could exist in the data and still be consistent with the null hypothesis.
 2072 The limit on $\sigma \times \text{BR}_\tau$ is roughly independent of the theoretical model². In the conclusion,
 2073 we will interpret the $\sigma \times \text{BR}_\tau$ limit result in the context of the MSSM theory.

Proper determination of systematic uncertainties is one of the most challenging and important components in performing a measurement correctly. A systematic uncertainty is the effect of the uncertainty of some ancillary measurement (or assumption) that is used in the computation of the final result. An instructive example of how a systematic uncertainty can affect the final result is a counting experiment measuring the cross section of some signal particle in the presence of background. The formula for the cross section times the branching fraction is

$$\sigma \times BR = \frac{N_{sig}}{\mathcal{L} \cdot \mathcal{A} \cdot \epsilon} = \frac{N_{obs} - N_{bkg}}{\mathcal{L} \cdot \mathcal{A} \cdot \epsilon}, \quad (8.1)$$

where N_{obs} is the number of events observed in data, N_{bkg} is the estimated number of background events in the observed data sample, \mathcal{L} is the integrated luminosity, and $\mathcal{A} \cdot \epsilon$ is the acceptance times efficiency of the signal. All of the quantities in Equation 8.1 (with the exception of the observed count N_{obs}) have some uncertainty which will effect the final measurement. Consider a situation where the expected number of background events is determined by fitting some sideband spectrum, and the fitted result has some error δN_{bkg} .

¹At some stated level of statistical confidence; the convention for limits in experimental high energy physics is 95%.

²Provided that the width of the Higgs bosons in the given model is smaller than the resolution of the SVfit mass resolution.

The total relative effect of this error can be obtained by error propagation

$$\frac{\delta(\sigma \times BR)}{\sigma \times BR} = \frac{\partial(\sigma \times BR)}{\partial N_{bkg}} \frac{1}{\sigma \times BR} \delta N_{bkg} = \frac{-\delta N_{bkg}}{N_{obs} - N_{bkg}}. \quad (8.2)$$

2074 It is interesting to examine Equation 8.2 in two scenarios. In the limit that N_{obs} is large
 2075 compared to N_{bkg} , the effect of the error on the background estimate δN_{bkg} does not affect
 2076 the final result. In contrast, in a scenario when the data is dominated by background events,
 2077 the relative error on the signal measurement due to the background estimation approaches
 2078 infinity. The sensitivity of a measurement to a systematic uncertainty on a parameter de-
 2079 pends on the context in which that parameter is used.

2080 Experimental systematic uncertainties relevant for MSSM $H \rightarrow \tau^+ \tau^-$ search presented
 2081 in this thesis are classified in three categories: normalization uncertainties on the signal and
 2082 $Z \rightarrow \tau^+ \tau^-$ background (events with true taus), normalization uncertainties on contribu-
 2083 tions from background with fake taus, and shape uncertainties. Normalization uncertainties
 2084 on events with true taus are due to lepton reconstruction, identification, isolation and trig-
 2085 ger efficiencies. These terms are equivalent to the efficiency ϵ and acceptance terms \mathcal{A} of
 2086 Equation 8.2 and affect the expected yield of MSSM $H \rightarrow \tau^+ \tau^-$ signal and $Z \rightarrow \tau^+ \tau^-$
 2087 background events. The uncertainties on these effects are obtained by measuring the effect
 2088 in data and simulation, according to the procedures of Chapter 7, and calculating a cor-
 2089 rection factor. The uncertainty associated with the measurement of the correction factor
 2090 is the systematic uncertainty. The normalization uncertainties are assumed to be uncor-
 2091 related with the shapes of visible and SVfit mass distributions which are used to extract
 2092 the MSSM $H \rightarrow \tau^+ \tau^-$ signal contribution in the analyzed dataset. Uncertainties on the
 2093 shapes of the distributions are described by “morphing” systematics. These are due to
 2094 uncertainties on the momentum/energy scale of identified electrons, muons, tau and other
 2095 jets in the event. As the SVfit mass reconstruction algorithm uses the missing transverse
 2096 energy, the shape of the SVfit distribution is sensitive to systematic uncertainties on the
 2097 overall scale E_T^{miss} measurement. The “morphing” systematics affect the shapes of signal as
 2098 well as background contributions. Normalization uncertainties on background contributions
 2099 are estimated from the level of agreement between data and Monte Carlo simulation in

2100 background dominated control regions.

2101 8.1 Signal Normalization Uncertainties

2102 The signal normalization uncertainties are due to imperfect knowledge of how improperly
 2103 modeled effects in the simulation could affect the acceptance model, the probability that
 2104 a given signal event will pass one of the selections (detailed in Chapter 5). The general
 2105 procedure to quantify these uncertainties is to measure the effect in some control region
 2106 in both the data and Monte Carlo. The ratio of data to Monte Carlo then gives a cor-
 2107 rection factor which is applied to the simulation. An uncertainty on the measurement of
 2108 the effect in control region (in the data, simulation, or both) is then taken as the system-
 2109 atic uncertainties. The signal normalization uncertainties affecting this analysis on muon
 2110 trigger, reconstruction, identification and isolation efficiencies are taken from the tag and
 2111 probe analysis of $Z \rightarrow \mu^+ \mu^-$ events presented in Section 7.1. A very conservative estimate
 2112 of 30% is taken for the uncertainty on the tau reconstruction and identification efficiency.
 2113 The tau identification uncertainty measurement is discussed briefly in 7.2. The dependency
 2114 of the Higgs boson signal extraction on the tau identification efficiency has been studied,
 2115 the result being that uncertainties on the tau identification efficiency affect the limit on
 2116 cross-section times branching ratio for MSSM $H \rightarrow \tau^+ \tau^-$ production by a few percent
 2117 only. An uncertainty of 11% is attributed to the luminosity measurement [58].

2118 8.2 Background Normalization Uncertainties

2119 Uncertainties on the normalization of background processes are obtained from the study of
 2120 background enriched control regions presented in Chapter 6. The main fake tau backgrounds
 2121 in this analysis are QCD multi-jet and $W + \text{jets}$ events. These backgrounds are produced
 2122 copiously enough for the backgrounds to be studied in control regions dominated by a
 2123 single background process with a purity exceeding 90% and an event statistics exceeding
 2124 the expected contribution of that background to the analysis by more than one order of
 2125 magnitude. Both backgrounds are found to be well modeled by the Monte Carlo simulation.
 2126 The overall background yields used in the final fit are measured in the background enriched
 2127 control regions, and cross-checked using the Fake-rate and Template methods. For a detailed

discussion of the measurements, see Chapter 6. An uncertainty of 10% is attributed to
 the contribution of QCD and $W + \text{jets}$ backgrounds to the analysis. The cross-section for
 $t\bar{t} + \text{jets}$ production makes it difficult to select a high purity sample of $t\bar{t} + \text{jets}$ events of high
 event statistics. From the study of the 19 events selected in the $t\bar{t} + \text{jets}$ background enriched
 control sample we assume an uncertainty on the $t\bar{t} + \text{jets}$ background contribution in the
 analysis of 30%. The $Z \rightarrow \mu^+ \mu^-$ background has been studied with large statistical precision
 in two separate control regions, and is dominated by events in which the reconstructed tau
 candidate is either due to a misidentified quark or gluon jet or due to a misidentified muon.
 Good agreement between data and Monte Carlo simulation is found in both cases. Sizeable
 uncertainties on the $Z \rightarrow \mu^+ \mu^-$ background contribution arise due to the extrapolation
 from the background enriched control regions to the data sample considered in the analysis,
 however: the contribution of $Z \rightarrow \mu^+ \mu^-$ background events to the analysis is due to events
 in which one of the two muons produced in the Z decay either escapes detection or fakes
 the signature of a hadronic tau decay. Both cases may be difficult to model precisely in the
 Monte Carlo simulation. The non-observation of a Z mass peak in the mu + tau visible
 mass distribution studied with the fake-rate method on the other hand sets a limit on
 possible contributions from $Z \rightarrow \mu^+ \mu^-$ background events. Conservatively, we assume an
 uncertainty of 100% on both types of $Z \rightarrow \mu^+ \mu^-$ background contributions.

8.3 Shape Uncertainties

Shape uncertainties on the distributions of visible and “full” invariant mass reconstructed
 by the SVfit algorithm are estimated by varying the electron energy and muon momentum
 scale, the energy scale of taus and other jets in the event and varying the missing transverse
 energy in Monte Carlo simulated events. After each variation the complete event is re-
 reconstructed and passed through the event selection. Shifted visible and “full” invariant
 mass shapes are obtained for each variation from the events passing all event selection
 criteria. The difference between shifted shapes and the “nominal” shapes obtained from
 Monte Carlo simulated events with no variation of energy or momentum scale or of the
 missing transverse energy applied is then taken as shape uncertainty.

2156 The systematic uncertainties on the muon and tau energy scales have been provided
 2157 by the muon and tau CMS Physics Object Groups and are described in Section 7.3. The
 2158 modelling of missing transverse energy in different types of background events has been
 2159 studied in the background enriched control regions described in Chapter 6. No significant
 2160 deviations between data and Monte Carlo simulation have been found. Uncertainties due
 2161 to missing transverse energy are estimated by varying the “clustered” and “unclustered”
 2162 energy scales, described in Section 7.4 and recomputing the total E_T^{miss} .

2163 8.4 Theory Uncertainties

2164 The signal and background normalization as well as the shape uncertainties are all exper-
 2165 imental uncertainties in nature. Additional theoretical uncertainties arise from imprecise
 2166 knowledge of parton–distribution functions (PDFs) and of the exact dependency of signal
 2167 cross–sections and branching ratios on $\tan\beta$ and m_{A^0} . The PDFs describe how the energy
 2168 of the protons is shared between the quarks and gluons. Since the longitudinal boost of
 2169 the hard collisions depends on the PDFs, the signal acceptance is sensitive to errors in the
 2170 PDFs. The uncertainties on the signal acceptance due to PDF uncertainties are estimated
 2171 using tools developed by the CMS Electroweak working group [59]. The acceptance is com-
 2172 puted with respect to MSSM $H \rightarrow \tau^+\tau^-$ decays that have muons of $p_T^\mu > 15$ GeV/c and
 2173 $|\eta_\mu| < 2.1$, jets produced in hadronic tau decays with visible $p_T^{\text{vis}} > 20$ GeV/c and $|\eta_{\text{vis}}| < 2.3$
 2174 on generator level. Acceptance values are computed for the central value and 44 eigenvec-
 2175 tors of the CTEQ66 PDF set [60]. The systematic uncertainty on the signal acceptance is
 2176 computed following the PDF4LHC recommendations [61, 62].

2177 The effect of Monte Carlo normalization, shape and theory uncertainties on the signal
 2178 efficiency times acceptance is summarized in Table 8.1.

2179 8.5 Limit Extraction Method

2180 The search for a new signal is performed by examining the observed distribution of the
 2181 reconstructed ditau invariant mass $m_{\tau\tau}$ as reconstructed by the SVfit algorithm. An “bump”
 2182 in this spectrum would indicate the presence of a new particle. To make a statement about
 2183 the presence of a bump with confidence, the shape under a potential bump must be well

Source	Effect
Normalization uncertainties	
Trigger	0.981 ± 0.006
Muon identification	1.001 ± 0.001
Muon isolation	0.984 ± 0.006
Tau identification	1.00 ± 0.30
Shape uncertainties	
Muon momentum scale	$\ll 1\%$
Tau energy scale	$1 - 4\%^1$
Jet energy scale (JES)	$< 1\%^2$
E_T^{miss} (Z -recoil correction)	1%
Theory uncertainties	
PDF	2% ³

¹ decreasing with m_A

² number quoted for $gg \rightarrow A/H$ and $b\bar{b} \rightarrow A/H$ sample as a whole;
in the subsample of events with b-tagged jets the effect of the JES uncertainty is 4%

³ with small dependence on m_A

Table 8.1: Effect of normalization uncertainties on the $gg \rightarrow A/H$ and $b\bar{b} \rightarrow A/H$ signal efficiency times acceptance.

described. The background shape is decomposed into the combination of shapes from the difference background sources, which we refer to here as “templates.” The data and the templates for each background distribution is binned in the observable $m_{\tau\tau}$ variable. The normalization of each template represents the total yield expected for that source.

We can then define a likelihood for any configuration of our templates given the observed data. The likelihood is a “binned Poisson likelihood,” which is defined as the product of the Poisson probability in each bin. The Poisson probability $P(n|\mu)$ is the probability to observe n events given an expectation of μ events. The Poisson probability is given by the expression

$$P(k|\mu) = \frac{\mu^k e^{-\mu}}{k!}. \quad (8.3)$$

2188 The total likelihood for observed data given some configuration of templates is then simply
 2189 the product of the Poisson probabilities (Equation 8.3) in each of the N_{bin} bins:

$$\mathcal{L} = \prod_{i=1}^{N_{bin}} \frac{\mu_i^{n_i} e^{-\mu_i}}{n_i!}, \quad (8.4)$$

2190 where the expected number of events μ_i in the bin i is the sum of the number of events
 2191 from all sources

$$\mu_i = \sum_{j=1}^{N_{source}} \mu_{ji}.$$

2192 The number of expected events in a source, in turn, can be written

$$\mu_{ji} = L \sigma_j \epsilon_{ji} \quad (8.5)$$

2193 where L is the integrated luminosity, σ_j is the cross section for source j , and ϵ_{ji} is the
 2194 efficiency for source j in bin i .

2195 We incorporate the systematic uncertainties of the analysis by introducing a set of
 2196 “nuisance parameters” $\vec{\beta}$ into the likelihood function. As the name suggests, we are not
 2197 interested in the actual value of the nuisance parameters. Each nuisance parameter pa-
 2198 rameterizes some phenomenon in the analysis. The shape templates (which can be defined
 2199 purely in terms of σ_j and ϵ_{ji} in Equation 8.5) are now interpreted as functions of the set
 2200 of nuisance parameters $\vec{\beta}$. Existing knowledge about the value of the nuisance parameter is
 2201 introduced by extending the likelihood function with a constraint $\mathcal{G}(\vec{\beta})$ that expresses the
 2202 knowledge about the nuisance parameters. The templates μ_{ji} can depend on the nuisance
 2203 parameters in two ways. Normalization uncertainties introduce multiplicative nuisance fac-
 2204 tors on the yield of some (sub)set of the sources defined by Equation 8.5. As an example,
 2205 consider a simplified situation where there are only two sources: $Z \rightarrow \tau^+ \tau^-$ and $W + \text{jets}$
 2206 events. Both sources are sensitive to the efficiency of the muon trigger. Only the $Z \rightarrow \tau^+ \tau^-$
 2207 sample is sensitive to the efficiency of the hadronic tau identification algorithm, as the
 2208 fake-rate in $W + \text{jets}$ is measured in data. We would then introduce two multiplicative nui-

2209 sance parameters, β_μ and β_τ , which respectively correspond to the two uncertainties. The
 2210 expected number of events in the i th bin is then given by a modified form of Equation 8.5

$$\mu_i = L\beta_\mu\sigma^W\epsilon_i^W + L\beta_\mu\beta_\tau\sigma^Z\epsilon_i^Z. \quad (8.6)$$

2211 From Equation 8.6, we can see that β_μ affects both sources but β_τ only affects the $Z \rightarrow \tau^+\tau^-$
 2212 source.

The shape uncertainties discussed in Section 8.3 are incorporated using a technique called “vertical template morphing.” For each source, different templates are created for three different values of the morphing parameter, corresponding to -1, 0, and +1 standard deviation shifts in the nuisance parameter. To determine the number of expected events in the i th bin as a function of the morphing parameter, we interpret quadratically between the i th bin values of the three templates, and extrapolate linearly beyond them. The overall likelihood then, including nuisance parameters, can be written as

$$\mathcal{L} = \prod_{i=1}^{N_{bin}} \frac{[\mu_i(\vec{\beta})]^{n_i} e^{-\mu_i(\vec{\beta})}}{n_i!} \times \prod_{m=1}^{N_\beta} \mathcal{G}(\beta_m). \quad (8.7)$$

2213 In Equation 8.7, we have introduced the assumption that the nuisance parameters are
 2214 uncorrelated.

2215 We wish to determine if the data is compatible with a new signal. To test for the
 2216 presence of a bump, we examine the likelihood as a function of the signal cross-section. If the
 2217 presence of a signal is unambiguous, one can simply determine the likelihood as a function
 2218 of the cross-section. If the signal is known to be non-zero, confidence intervals about the
 2219 maximum likelihood can be constructed by examining the change in the logarithm $2\Delta \ln \mathcal{L}$
 2220 of the likelihood. The Frequentist interpretation of the confidence level $(1 - \alpha)$ is that if
 2221 the experiment were repeated N times, the interval corresponding to $(1 - \alpha)$ would fail
 2222 “cover” the *true* value of the observable in $\alpha \times N$ of the experiments. The correspondence
 2223 between confidence levels and intervals in $2\Delta \ln \mathcal{L}$ is given in Table 8.2. Since the mass of
 2224 a potential Higgs boson is unknown, we repeat this process for different signal masses. If
 2225 there is not a significant signal, we can set upper bounds on the signal cross-section using

Fixme: Did I
mix this up?

$(1 - \alpha)\%$	$m = 1$	$m = 2$	$m = 3$
68.27	1.00	2.30	3.53
90.00	2.71	4.61	6.25
95.00	3.84	5.99	7.82
99.00	6.63	9.21	11.34

Table 8.2: Correspondence between a confidence level defined by $(1 - \alpha)\%$ and the corresponding interval in $2\Delta \ln \mathcal{L}$. The $2\Delta \ln \mathcal{L}$ interval is different depending the number m of parameters which are being simultaneously estimated.

2226 one of several methods, which will be discussed below.

2227 At this point, the likelihood still depends on the nuisance parameters. There are two
 2228 methods of removing the dependence on the nuisance parameters, “marginalization” and
 2229 “profiling.” Marginalization is the process of integrating the likelihood of Equation 8.7
 2230 over the entire range of all nuisance parameters. This effectively averages the effect of
 2231 the different uncertainties into the marginalized likelihood function. The profiling method
 2232 maximizes the likelihood in terms of the nuisance parameters. In the profiling method,
 2233 the “profile likelihood” is created by maximizing the likelihood with respect to all of the
 2234 nuisance parameters. One way to interpret the profiling method is that the values of nuisance
 2235 parameters are being measured *in situ*, constrained by the observed data. While not a
 2236 strictly Bayesian treatment, the profile likelihood method has been shown to give almost
 2237 identical results to marginalization.

2238 An interesting situation relating to the profiling of the nuisance parameters arises in
 2239 this analysis in the context of the hadronic tau identification uncertainty. As discussed in
 2240 Chapter 7, the Higgs–insensitive measurement of the tau identification efficiency has a high
 2241 uncertainty of 30%. If the bump at the $Z \rightarrow \tau^+ \tau^-$ resonance can be considered to free
 2242 of contributions from a Higgs boson, the tau identification efficiency can be measured to
 2243 a much greater precision, approximately 7% [53, 48]. When profiling the likelihood (as a
 2244 function of cross section) for a Higgs boson with a mass $m_{A^0} > m_Z$, the likelihood contains
 2245 the information that there is no Higgs boson contribution to the Z resonance. This fact
 2246 enables the profiling process to constrain the systematic uncertainty on the tau identification

efficiency to the 7% level using the size of the Z resonance. Conversely, when the likelihood is evaluating the likelihood of the presence of a Higgs boson signal with $m_{A^0} = m_Z$, the likelihood cannot distinguish between a potential presence of Higgs boson events in the Z bump or a systematic undershoot of the tau identification efficiency in the simulation. In this case the profiling processing has no power to constrain the systematic to a value lower than the initial 30% value.

In the absence of the signal, or even in the presence of one, we can determine a upper 95% CL bound on the cross-section of the signal using the profile likelihood. In one method we simply use Bayes' Theorem to convert the likelihood to a posterior density in the signal cross-section, and integrate to find the point below which 95% of the probability lies. The Bayesian posterior PDF is computed as

$$\mathcal{P}(\sigma_H | \bar{x}, m_H) = \frac{\mathcal{L}(\bar{x} | \sigma_H m_H) \mathcal{P}(\sigma_H)}{\int \mathcal{L}(\bar{x} | \sigma'_H m_H) \mathcal{P}(\sigma'_H) d\sigma'_H}. \quad (8.8)$$

The left hand side of Equation 8.8 represents the probability density for a given signal cross section, given the observed data \bar{x} and the assumed value m_H for the Higgs boson mass. We refer to this method as the “Bayesian” method of setting limits.

In the other method, which is referred to as the “Delta Log Likelihood” (DLL) method, we compute two likelihoods. The first likelihood is computed for the “null hypothesis” case. The likelihood is profiled (maximized) assuming that no signal is present. We then construct the profile likelihood for increasing values of the signal yield. The upper limit is achieved when the logarithm of the profile likelihood is 1.92 units less than the value of the null hypothesis profile likelihood.

In general the limits computed by the Bayesian and DLL methods are similar. However, the effect of upward or downward statistical fluctuations in the observed data affect the two methods in different ways. When the data fluctuates low, the DLL method will produce a more stringent limit than the DLL method. When the data fluctuates high, creating an apparent signal, the Bayesian method will (correctly) set a more stringent limit.

In the results presented below we use nuisance parameters corresponding to the systematic errors summarized in Table 8.3.

Source	Method	Magnitude
Muon ID/trigger	Multiplicative	20%
Z cross section	Multiplicative	5%
Jet to τ fake rate	Multiplicative	20%
$\mu \rightarrow \tau$ fake rate	Multiplicative	100%
$W + \text{jets}$ cross section	Multiplicative	10%
$t\bar{t}$ cross section	Multiplicative	40%
integrated luminosity	Multiplicative	11%
Tau energy scale	Morphing	3%
Jet energy scale	Morphing	3%
Unclustered energy scale	Morphing	1%
Z -recoil correction	Morphing	-
Muon p_T scale	Morphing	neg.
EM energy scale	Morphing	neg.

Table 8.3: Summary of systematic uncertainties represented by nuisance parameters in the likelihood, their representation method and magnitudes. The Z -recoil correction factor is varied within the uncertainty on the measurement described in Chapter 7.

2269

Chapter 9

2270

Results

2271

9.1 Selected Events

2272

In the 36 pb^{-1} of 7 TeV data collected by CMS in 2010, the analysis selection criteria described in Chapter 5 selects a total of 573 events. The expected yields from each of the background sources, computed by the Template method (Section 6.3) and verified by the Fake-rate method (Section 6.2) are shown in Table 9.1. The total expectation from the standard model background is 577. The data agrees extremely well with the SM background expectation considering the expected statistical variance of the observed data (24 events), as well as the uncertainty on the integrated luminosity¹ and the tau identification uncertainty.

2279

2280

The distributions of the visible mass and SVfit mass in the final selected events are shown in Figure 9.3. Excellent agreement is seen between the shapes of the distributions. The p_T spectrum of the transverse momentum are sensitive to mis-modeling of the kinematics and composition of the various background sources. Control plots showing the transverse momenta of the muon and visible hadronic tau in the final analysis selection are shown in Figure 9.1. The η and ϕ distributions of the muon and tau objects are sensitive to detector effects, and the presence of cosmic muons. For example, muons from cosmic events will preferentially be produced in the $\phi = 0$ direction. Spurious candidates resulting from poorly model noise in one of the CMS subdetectors will in general be localized in $\eta - \phi$. The η and ϕ distributions of the muon and tau candidates are shown in Figure 9.2 and show excellent agreement.

¹The uncertainty on the CMS luminosity measurement was 11% at the time this analysis was performed. The measurement was later improved, and at the time of this writing the uncertainty on CMS 2010 integrated luminosity is 4% [58]. The improved luminosity measurement is not expected to change the results of this analysis significantly.

Process	Events in 36 pb ⁻¹
$t\bar{t} + \text{jets}$	6.6
$W + \text{jets}$	25.6
$Z \rightarrow \mu^+ \mu^-$	10.6
QCD	166.2
$Z \rightarrow \tau^+ \tau^-$	368.1
Standard model sum	577.1
Data	573

Table 9.1: Number of $H \rightarrow \tau^+ \tau^- \rightarrow \mu + \tau_{had}$ candidate events passing the selection criteria described in Chapter 5.

2291 The expected yields from an MSSM Higgs boson signal for $\tan \beta = 30^2$ are summarized
 2292 in . The contributions from the gluon fusion production mode and the associated b -quark
 2293 production modes are given separately. The yields are divided into the exclusive categories
 2294 of events containing a b -tagged jet and those without. For a Higgs boson mass of $m_{A^0} =$
 2295 160 GeV/c², a total of 17 events are expected at $\tan \beta = 30$.

2296 9.2 Limits on Higgs Boson Production

2297 We compute upper limits on the cross section times the branching ratio using the Bayesian
 2298 method described in Section 8.5. We compute an expected limit in the same manner as an
 2299 observed limit, but with simulated data generated in “toy” experiments. A large number
 2300 of pseudo-data sets are generated using the null hypothesis templates using Monte Carlo
 2301 techniques. The nuisance parameters are sampled within their constraints in the generation
 2302 of the pseudo-date. The pseudo-data sets are expected to have the same statistical sensi-
 2303 tivity as the observed dataset. Upper limits are then computed using the pseudo-data. The
 2304 process is repeated many times, and the spread of the obtained upper limits determines the
 2305 expected upper limit band. The expected nominal upper limit, and the ± 1 , and ± 2 confi-
 2306 dence limits are shown in Table 9.3. The observed limit on the MSSM computed from the

²Details of the relationship between the MSSM Higgs boson cross section and $\tan \beta$ are discussed in detail in Section 9.3.

2307 573 events selected in this analysis is given in the right column of Table 9.3. The observed
 2308 limit is compatible with the expected limit, within 1.5 standard deviations. The trend of
 2309 the expected and observed limits versus the Higgs boson mass using both observables are
 2310 shown in Figure 9.4. The use of the SVfit reconstructed mass as the observable increases
 2311 the power of the limit significantly. The limit trend has some interesting features. When
 2312 the Higgs boson mass is close to the mass of the Z resonance, the analysis have little power
 2313 to set a limit on the presence of the Higgs boson. This is due to the large uncertainty on
 2314 the tau identification efficiency. Essentially, when $m_{A^0} = m_Z$, the Higgs boson yield in the
 2315 Z bump would have been larger than 30% of the $Z \rightarrow \tau^+\tau^-$ yield for the profile likelihood to
 2316 be able to recognize an excess of events. Below this value, the profile likelihood can simple
 2317 shift the tau identification efficiency scale factor up by 30% and “eat” any potential excess
 2318 of signal.

2319 9.3 Interpretation in the MSSM

2320 The limits on the cross section times branching ratio are roughly model independent,³ and
 2321 could be applied to set limits on the parameter space of a number of models. In this thesis,
 2322 we interpret the results in the context of the MSSM. Specifically, we exclude a region in the
 2323 $\tan\beta - m_{A^0}$ parameters space of the MSSM. To find the upper limit band on $\tan\beta$, we find
 2324 the minimum value of $\tan\beta$ which provides the cross section and branching ratio product
 2325 found in the corresponding row in Table 9.3.

2326 The mapping between m_{A^0} and $\tan\beta$ and the Higgs boson cross section is provided by
 2327 the LHC Higgs Cross Section working group [63]. The cross sections and branching ratios
 2328 have been computed for the h^0 , H^0 , and A^0 MSSM Higgs boson states in both the ggA
 2329 and qqA production modes, for a grid of points in $\tan\beta - m_{A^0}$ space. In order to combine
 2330 the ggA and qqA production modes, what we call our signal cross-section is the sum of the
 2331 cross-section times branching ratio for both modes, assuming $\tan\beta = 30$. Additionally, as
 2332 discussed in Section 1.2.3, the MSSM Higgs sector consists of two Higgs doublets, yielding

³This assumption is only valid if the shape of the sum of all new physics contributions are also model independent, on the scale of the experimental resolution. For the values of $\tan\beta$ this analysis is sensitive to, this is a valid approximation in the MSSM. In a model where the width of the Higgs boson resonance was larger than the resolution of the SVfit method, the limits of Table 9.3 would not be valid.

2333 five physical Higgs bosons. This search is sensitive to the three neutral Higgs particles the
 2334 h^0 , H^0 , and A^0 . The relative contributions of the three Higgs boson types depends on the
 2335 mass m_{A^0} of the CP-odd Higgs boson. An observed signal will have contributions from at
 2336 least two Higgs boson states. For $m_{A^0} \leq 130$ GeV/ c^2 , the A^0 and h^0 are approximately
 2337 degenerate in mass and width. In this region the H^0 has a very small relative cross section
 2338 and a constant mass of $m_{H^0} \approx 130$ GeV/ c^2 . For $m_{A^0} \geq 130$ GeV/ c^2 , the h_0 reaches a limiting
 2339 mass of ≈ 130 GeV/ c^2 , and the H^0 and A^0 become mass degenerate.

2340 The region in $\tan\beta - m_{A^0}$ MSSM parameter space excluded by this analysis at 95%
 2341 CL is shown in Figure 9.3. The limit is compared to the combined result from Run II of
 2342 the Tevatron (this result is discussed in detail in Section 1.3.3). The result of this analysis
 2343 sets a stronger limit than the Tevatron for large values of m_{A^0} . In the low m_{A^0} region, the
 2344 analysis suffers due to the large tau identification efficiency uncertainty. This effect can be
 2345 mitigated by using the $e - \mu$ channel. The combined CMS result uses this approach, and
 2346 will be discussed briefly in the conclusion.

Fixme:

check this!

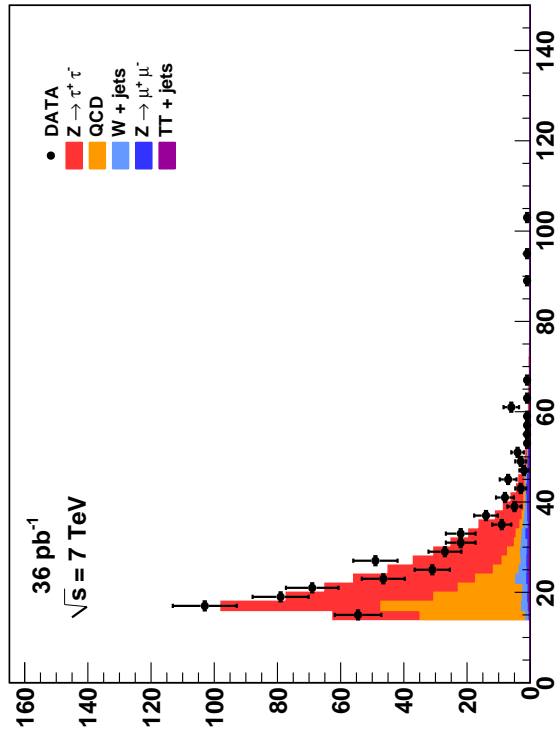
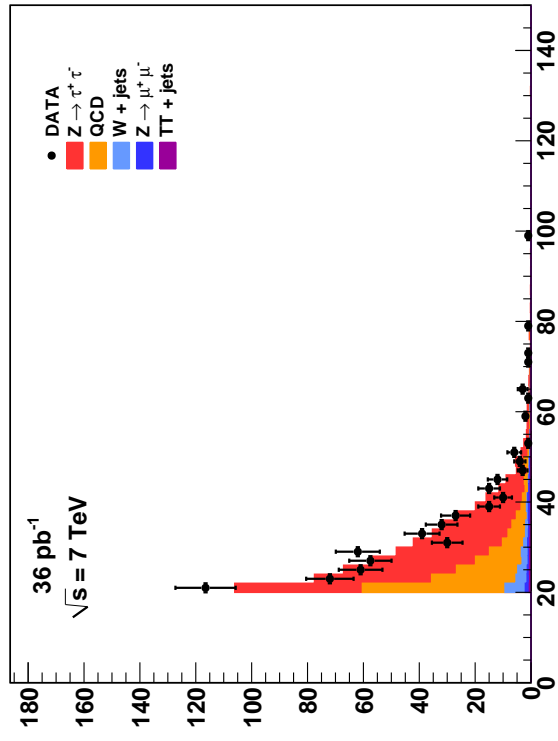
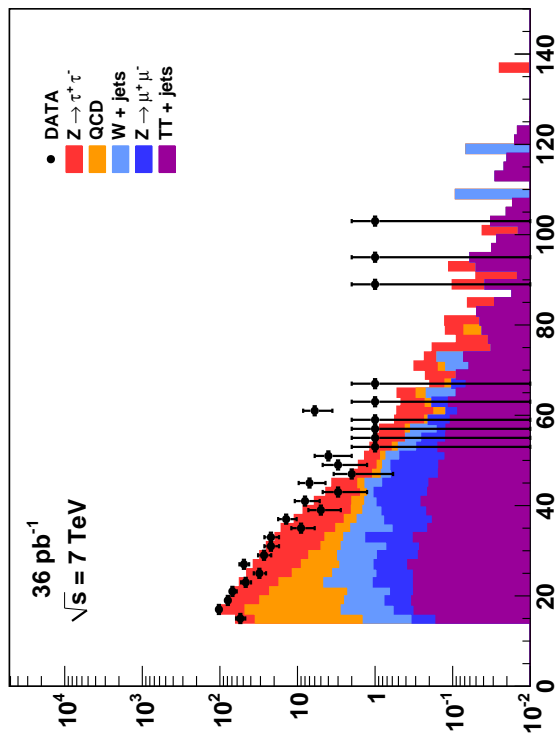
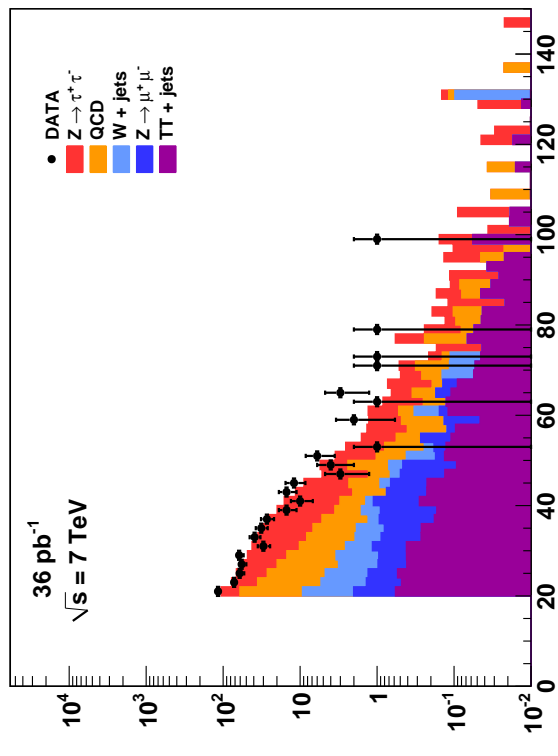
Muon (final event sample)**Tau (final event sample)****Muon (final event sample)****Tau (final event sample)**

Figure 9.1: Distribution of the transverse momentum of the muon (top) and hadronic tau in $H \rightarrow \tau^+ \tau^- \rightarrow \mu + \tau_{had}$ candidate events passing the selection criteria described in Chapter 5. The distributions are shown in linear (logarithmic) scale on the left (right).

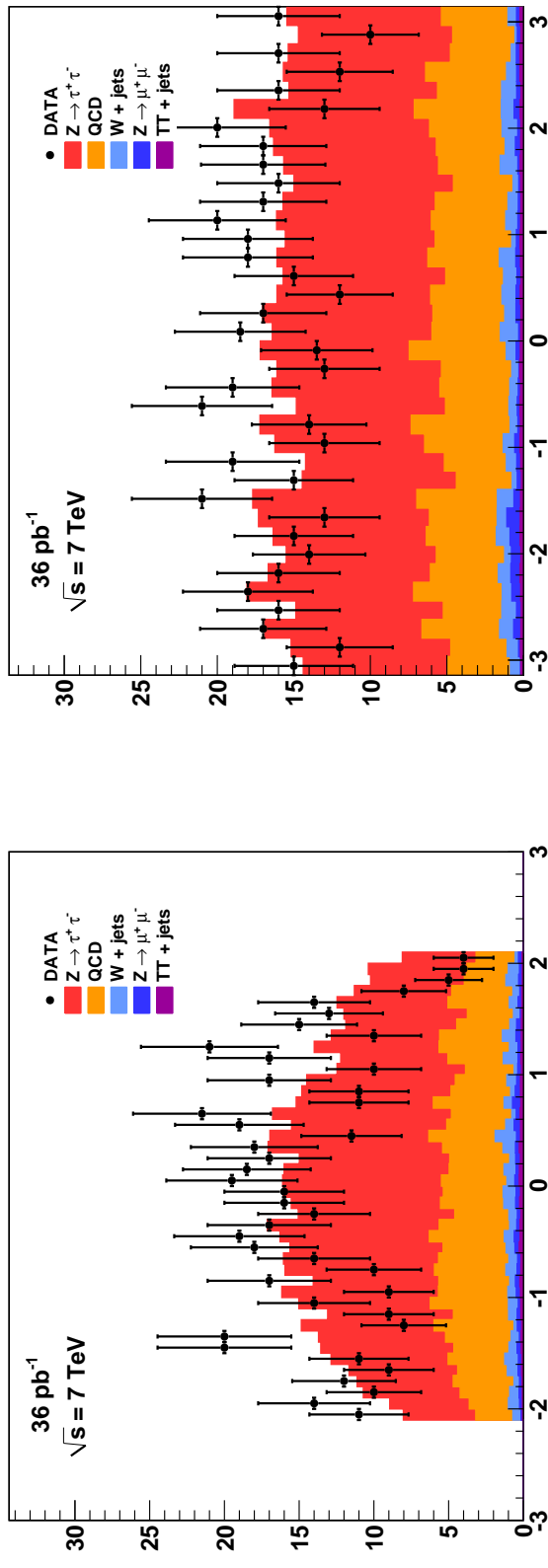
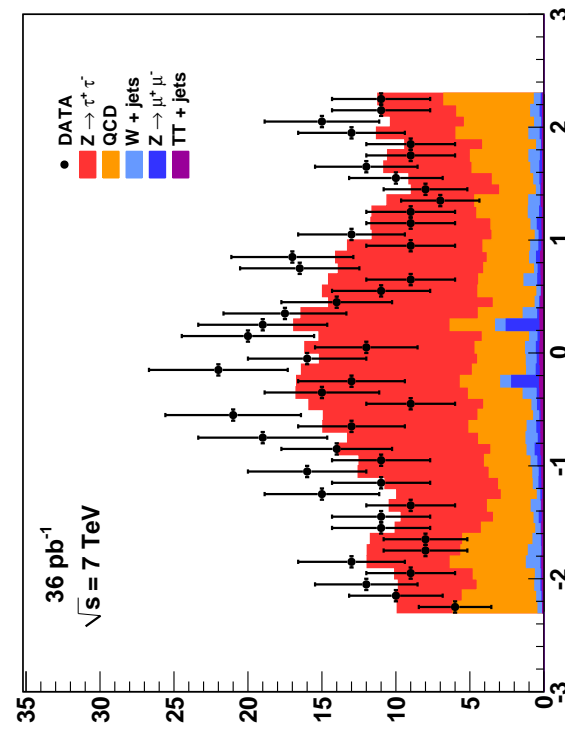
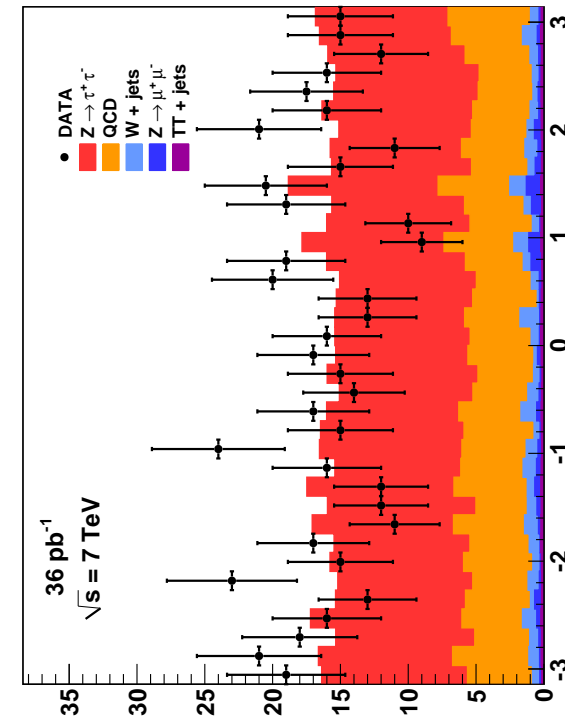
Muon (final event sample)**Tau (final event sample)****Tau (final event sample)**

Figure 9.2: Distribution of the η (left) and ϕ (right) of the muon (top) and hadronic tau (bottom) in $H \rightarrow \tau^+ \tau^- \rightarrow \mu + \tau_{had}$ candidate events passing the selection criteria described in Chapter 5.

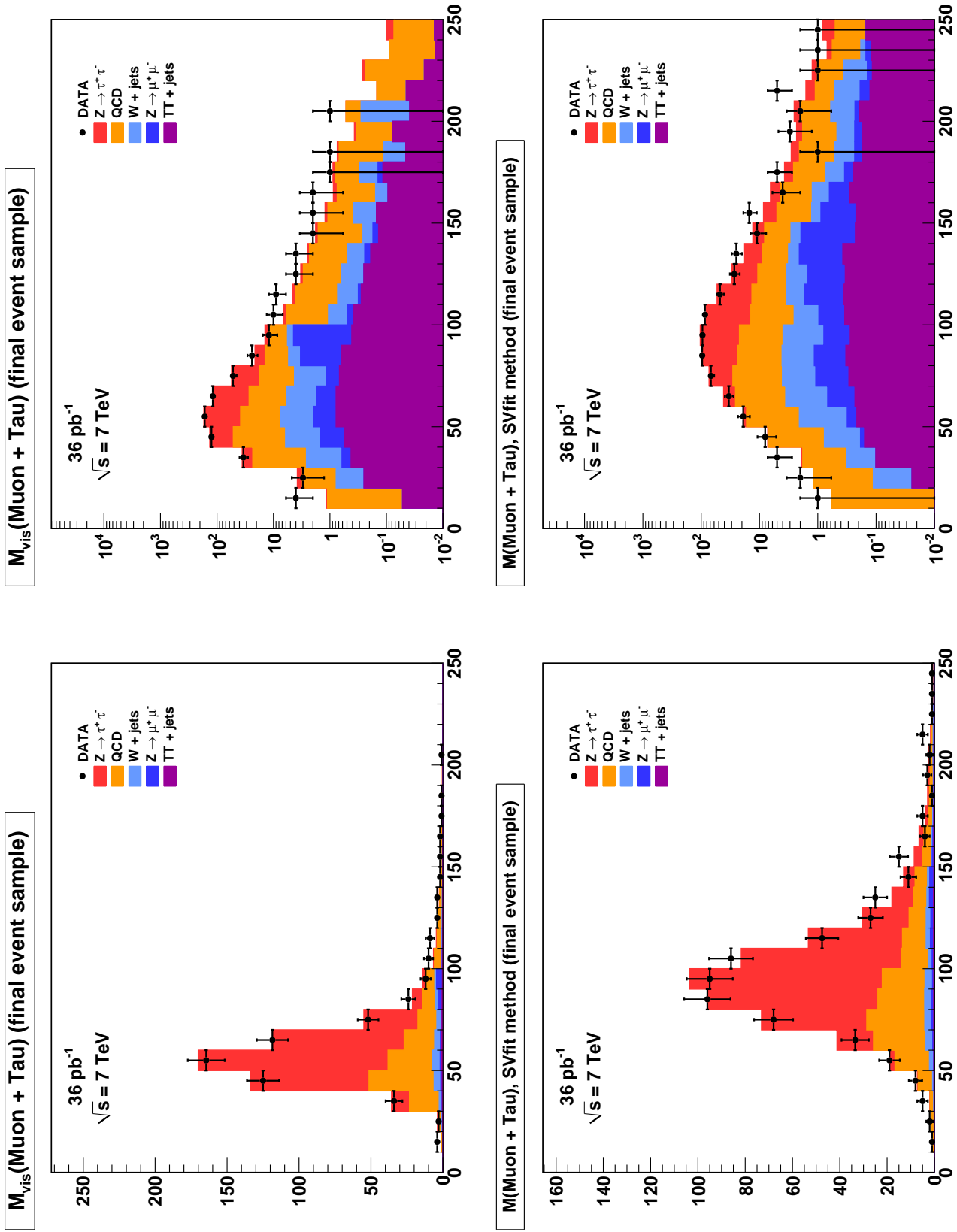


Figure 9.3: Distribution of visible (top) and “full” $\tau^+\tau^-$ invariant mass reconstructed by the SVfit algorithm (bottom) in $H \rightarrow \tau^+\tau^- \rightarrow \mu + \tau_{had}$ candidate events passing the selection criteria described in Chapter 5. The distributions are shown in linear (logarithmic) scale on the left (right).

Process	Events without b -tag	Events with b -tag
Gluon fusion production		
A90	37.21	0.86
A100	27.40	0.40
A120	14.39	0.14
A130	11.81	0.18
A160	4.46	0.09
A200	1.51	0.03
A250	0.47	0.01
A300	0.15	0.0
A350	0.06	0.44
Associated b -quark production		
bbA90	33.07	5.50
bbA100	30.18	4.77
bbA120	21.91	4.02
bbA130	18.34	3.35
bbA160	10.35	2.10
bbA200	4.85	1.29
bbA250	2.11	0.55
bbA300	0.97	0.26
bbA350	0.41	0.13

Table 9.2: Number of Higgs boson signal events expected to pass the selection criteria described in Section 5. The expected signal yield is given for MSSM parameter $\tan \beta = 30$, using the cross sections provided by the LHC Higgs Cross Section working group [63].

Secondary Vertex Fit 95% CL Upper Limit (pb)						
Mass (GeV/c ²)	Expected $\sigma_H \times B_\tau$ (pb)					Observed $\sigma_H \times B_\tau$ (pb)
	-2 σ	-1 σ	Median	+1 σ	+2 σ	
90	329.2	429.2	621.9	862.9	999.1	394.7
120	30.1	41.6	59.8	82.0	116.6	86.5
130	20.7	27.6	40.5	55.6	79.4	59.9
160	10.3	13.2	19.0	26.2	35.8	28.3
200	6.3	8.3	11.2	15.8	20.2	16.4
250	4.0	5.6	7.6	10.6	14.5	12.9
300	2.9	4.0	5.7	7.8	11.1	9.4
Visible Mass 95% CL Upper Limit (pb)						
	90	120	130	160	200	250
90	376.2	523.3	688.2	980.9	998.8	573.8
120	37.0	52.1	75.4	109.2	164.1	82.6
130	26.2	35.9	52.2	74.6	117.5	64.2
160	14.3	18.3	25.1	35.2	55.1	41.2
200	8.9	11.9	16.6	22.4	32.8	31.1
250	5.9	8.1	11.5	15.9	22.3	18.1
300	4.2	5.8	8.4	11.7	15.9	10.8

Table 9.3: Expected 95% CL upper limit bands and the observed limit using the Bayesian prescription. The limit is computed using both the SVfit mass (top) as well as the visible mass (bottom) as the search observable. Use of the SVfit mass significantly improves the strength of the limit considerably.

Higgs State	Included when		
	$m_{A^0} < 130$ GeV/c ²	$m_{A^0} = 130$ GeV/c ²	$m_{A^0} > 130$ GeV/c ²
A^0	yes	yes	yes
H^0	yes	yes	no
h^0	no	yes	yes

Table 9.4: Logic for determining the MSSM Higgs boson cross section for a given mass of the CP-odd A^0 Higgs boson. In some regions of parameter space, the contributions of one of the CP-even Higgs particles is ignored.

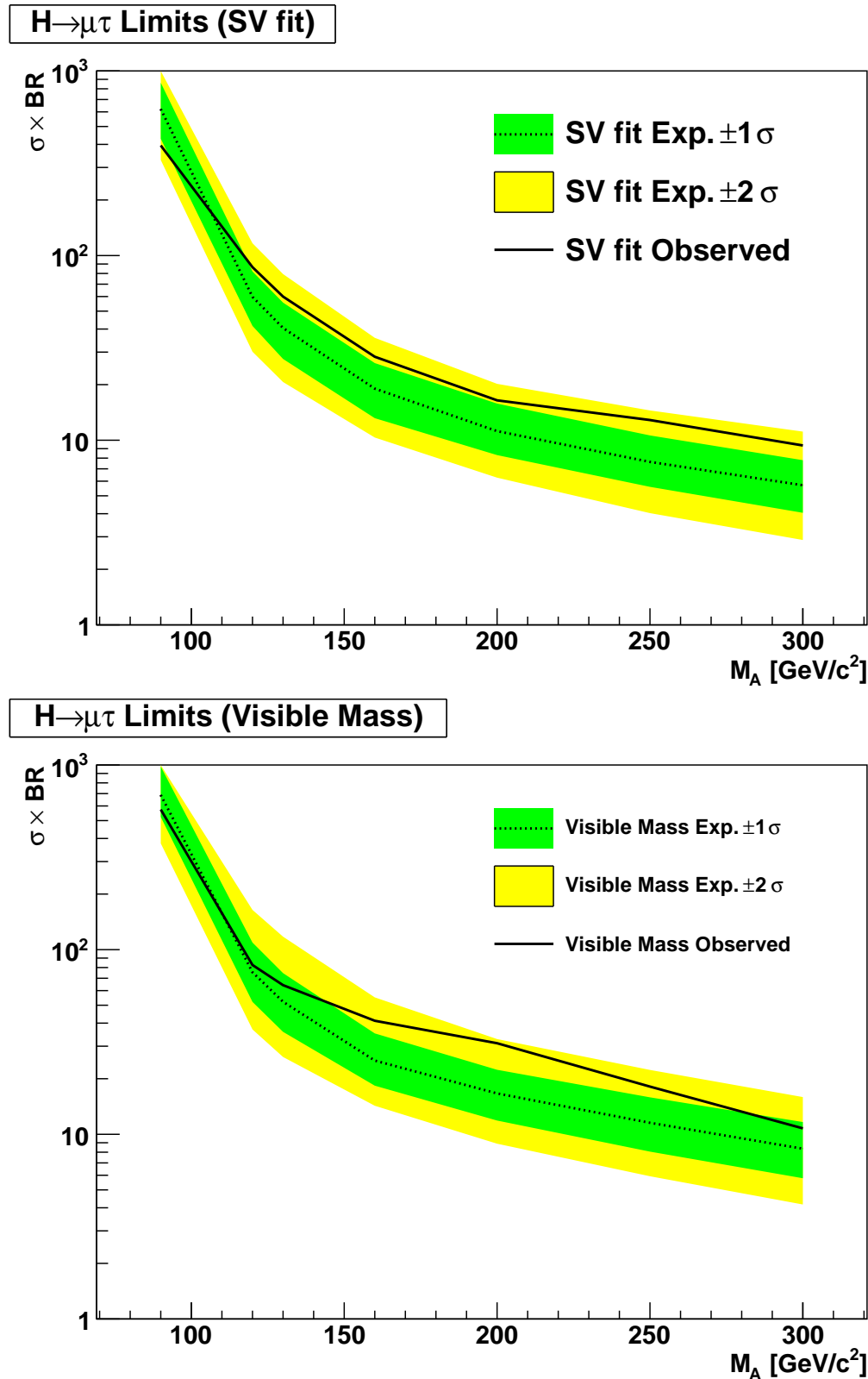


Figure 9.4: Observed and expected limits on the cross section times branching ratio of a Higgs boson versus mass. The top plot gives the limit computed using the SVfit mass as the observable, the bottom plot gives the limit computed using the visible mass. The dashed line gives the nominal expected limit. The green and yellow bands give the +1 and +2 standard deviations on the expected limit.

Figure 9.5: Region of MSSM $\tan \beta - m_{A^0}$ parameter space excluded by this analysis. THIS PLOT IS NOT DONE YET

Conclusions

2347 This analysis has presented a search for MSSM Higgs bosons in the 2010 7 TeV CMS data
 2349 set. Two new experimental methods, the TaNC tau identification algorithm, and the SVfit
 2350 mass reconstruction method have been introduced in this thesis. Both methods increased
 2351 the sensitive of the search. The search was performed using 36 pb^{-1} of data. The expected
 2352 event yield from standard model sources is 577 events. In total, 573 events were selected; the
 2353 observed is compatible with the standard model. No signal-like excess of events is observed.
 2354 We set an upper limit on the production of Higgs bosons, and interpret this limit in the
 2355 context of the MSSM.

2356 The analysis presented in this thesis was part of a larger study [1] performed by the
 2357 CMS collaboration searching for the MSSM Higgs boson decaying to tau leptons. The CMS
 2358 analysis used three channels, the $H \rightarrow \tau\tau \rightarrow e - \tau_h$, $H \rightarrow \tau\tau \rightarrow e - \mu$, and the $\mu - \tau_h$
 2359 channel. The $\mu - \tau_h$ channel search presented in this thesis is very similar to the CMS result.
 2360 While not as pure as the $\mu - \tau$ channel, the inclusion of the high-statistics $e - \tau$ channel
 2361 increases the sensitivity of the CMS analysis. The $e - \mu$ channel has low statistics, but is
 2362 not sensitive to the systematic uncertainty on the hadronic tau identification. The region of
 2363 the MSSM parameter space excluded by combined CMS result is illustrated in Figure 9.3.
 2364 At the time of this writing, the CMS result described in [1] sets the most stringent limits
 2365 on the MSSM using a direct search.

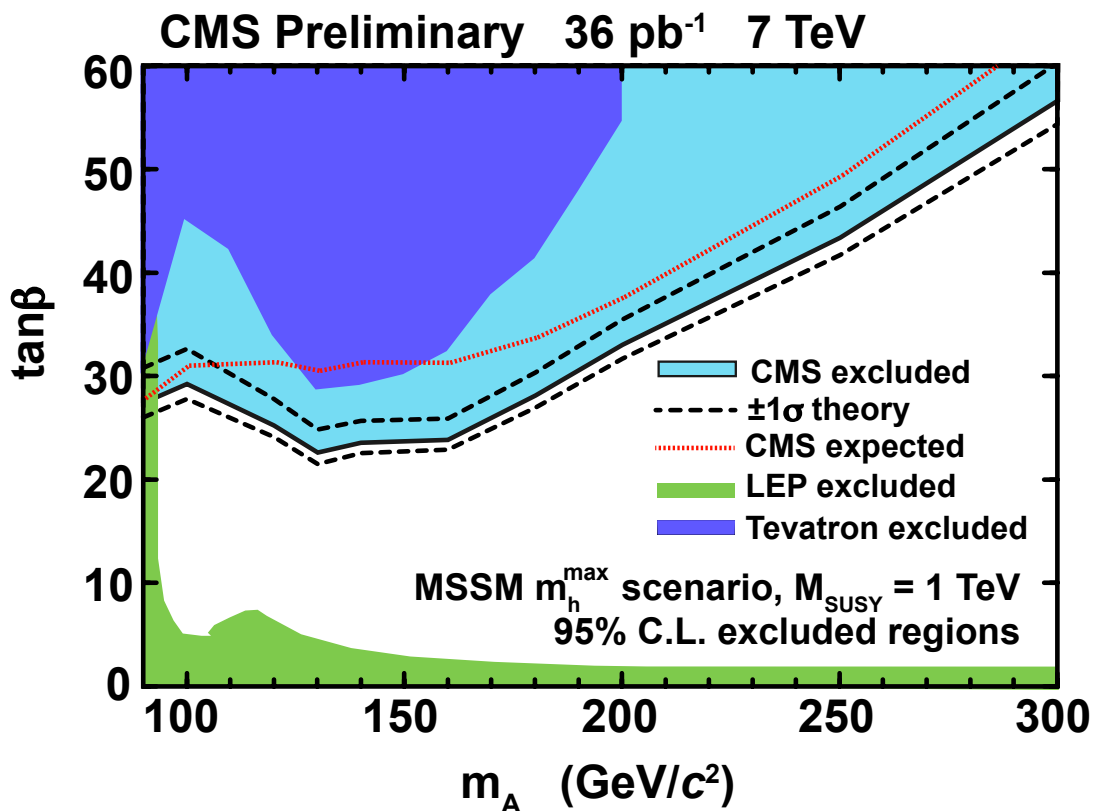


Figure 9.6: Region of MSSM $\tan\beta - m_{A^0}$ parameter space excluded by the CMS combined analysis [1].

2366 Bibliography

- 2367 [1] CMS Collaboration, “Search For Neutral MSSM Higgs Boson Production via Decays
2368 to Tau Pairs in pp Collisions at $\sqrt{s} = 7$ TeV”, *to be published* (2011).
- 2369 [2] J. Goldstone, “Field Theories with Superconductor Solutions”, *Nuovo Cim.* **19**
2370 (1961) 154–164. doi:10.1007/BF02812722.
- 2371 [3] J. Goldstone, A. Salam, and S. Weinberg, “Broken Symmetries”, *Phys. Rev.* **127**
2372 (Aug, 1962) 965–970. doi:10.1103/PhysRev.127.965.
- 2373 [4] F. Englert and R. Brout, “Broken Symmetry and the Mass of
2374 Gauge Vector Mesons”, *Phys. Rev. Lett.* **13** (Aug, 1964) 321–323.
2375 doi:10.1103/PhysRevLett.13.321.
- 2376 [5] P. W. Higgs, “Broken Symmetries and the Masses of Gauge Bosons”, *Phys. Rev.*
2377 *Lett.* **13** (Oct, 1964) 508–509. doi:10.1103/PhysRevLett.13.508.
- 2378 [6] G. S. Guralnik, C. R. Hagen, and T. W. B. Kibble, “Global Conservation
2379 Laws and Massless Particles”, *Phys. Rev. Lett.* **13** (Nov, 1964) 585–587.
2380 doi:10.1103/PhysRevLett.13.585.
- 2381 [7] S. Glashow, “Partial Symmetries of Weak Interactions”, *Nucl.Phys.* **22** (1961) 579–
2382 588. doi:10.1016/0029-5582(61)90469-2.
- 2383 [8] S. Weinberg, “A Model of Leptons”, *Phys.Rev.Lett.* **19** (1967) 1264–1266.
2384 doi:10.1103/PhysRevLett.19.1264.
- 2385 [9] A. Salam, “Weak and Electromagnetic Interactions”, Originally printed in
2386 *Svartholm: Elementary Particle Theory, Proceedings Of The Nobel Symposium
2387 Held 1968 At Lerum, Sweden*, Stockholm 1968, 367–377.
- 2388 [10] D. Griffiths, “Introduction to Elementary Particles”. Wiley-VCH, 2004.
- 2389 [11] E. Fermi, “An attempt of a theory of beta radiation. 1”, *Z. Phys.* **88** (1934) 161–
2390 177. doi:10.1007/BF01351864.
- 2391 [12] S. M. T. Morii, C.S. Lim, “The Physics of the Standard Model and Beyond”. World
2392 Scientific, 2004.
- 2393 [13] UA1 Collaboration, “Experimental observation of isolated large transverse energy
2394 electrons with associated missing energy at $\sqrt{s} = 540$ GeV”, *Phys. Lett.* **B122**
2395 (1983) 103–116.
- 2396 [14] UA2 Collaboration, “Observation of single isolated electrons of high transverse mo-
2397 mentum in events with missing transverse energy at the CERN $\bar{p}p$ collider”, *Phys.*
2398 *Lett.* **B122** (1983) 476–485. doi:10.1016/0370-2693(83)91605-2.

- 2399 [15] UA1 Collaboration, “Experimental observation of lepton pairs of invariant mass
 2400 around $95 \text{ GeV}/c^2$ at the CERN SPS collider”, *Phys. Lett.* **B126** (1983) 398–410.
 2401 doi:10.1016/0370-2693(83)90188-0.
- 2402 [16] UA2 Collaboration, “Evidence for $Z^0 \rightarrow e^+e^-$ at the CERN $\bar{p}p$ collider”, *Phys. Lett.*
 2403 **B129** (1983) 130–140. doi:10.1016/0370-2693(83)90744-X.
- 2404 [17] S. P. Martin, “A Supersymmetry Primer”, *arXiv hep-ph* (sep, 1997). 128 pages.
 2405 Version 5 (December 2008) contains a change in convention that flips the signs of
 2406 sigma and sigmabar matrices. It also contains a total of about 2 pages of updates,
 2407 mostly on supersymmetry breaking issues. Errata and a version with larger type (12
 2408 pt, 142 pages) can be found at <http://zippy.physics.niu.edu/primer.html>.
- 2409 [18] CERN Computing Newsletter.
- 2410 [19] D. L. Rainwater, D. Zeppenfeld, and K. Hagiwara, “Searching for $H \rightarrow \tau^+\tau^-$
 2411 in weak boson fusion at the LHC”, *Phys. Rev.* **D59** (1999) 014037, arXiv:hep-
 2412 ph/9808468. doi:10.1103/PhysRevD.59.014037.
- 2413 [20] Particle Data Group Collaboration, “Review of particle physics”, *J. Phys.* **G37**
 2414 (2010) 075021. doi:10.1088/0954-3899/37/7A/075021.
- 2415 [21]
- 2416 [22] LHC Higgs Cross Section Working Group Collaboration, “Handbook of LHC Higgs
 2417 Cross Sections: 1. Inclusive Observables”, arXiv:1101.0593.
- 2418 [23] M. Carena, S. Heinemeyer, C. Wagner et al., “MSSM Higgs boson searches at the
 2419 Tevatron and the LHC: Impact of different benchmark scenarios”, *The European
 2420 Physical Journal C - Particles and Fields* **45** (2006) 797–814. 10.1140/epjc/s2005-
 2421 02470-y.
- 2422 [24] CMS Collaboration, “The CMS experiment at the CERN LHC”, *JINST* **3** (2008)
 2423 S08004.
- 2424 [25] CMS Collaboration, “Measurement of Momentum Scale and Resolution using Low-
 2425 mass Resonances and Cosmic-Ray Muons”, *CMS PAS CMS-PAS-TRK-10-004*
 2426 (2010).
- 2427 [26] CMS Collaboration, “Tracking and Primary Vertex Results in First 7 TeV Collisions”,
 2428 *CMS PAS CMS-PAS-TRK-10-005* (2010).
- 2429 [27] G. L. Bayatian et al., “CMS Physics Technical Design Report Volume I: Detector
 2430 Performance and Software”. Technical Design Report CMS. CERN, Geneva, 2006.
- 2431 [28] CMS Collaboration, “CMS Strategies for tau reconstruction and identification using
 2432 particle-flow techniques”, *CMS PAS CMS-PAS-PFT-08-001* (2008).
- 2433 [29] CMS Collaboration, “Particle-Flow Event Reconstruction in CMS and Performance
 2434 for Jets, Taus, and MET”, *CMS PAS CMS-PAS-PFT-09-001* (2009).
- 2435 [30] A. Hoecker et al., “TMVA - Toolkit for Multivariate Data Analysis”, *ArXiv Physics
 2436 e-prints* (March, 2007) arXiv:arXiv:physics/0703039.

- 2437 [31] A. Kolmogorov, “On the representation of continuous functions of several variables
 2438 by superposition of continuous functions of one variable and addition”, *Doklady
 2439 Akademii Nauk SSSR* **114** (1957).
- 2440 [32] J. C. *et al.*, “Size of signal cones and isolation rings in the CMS tau identification
 2441 algorithm”, *CMS Note* **2008/026** (2008).
- 2442 [33] M. Bachtis, S. Dasu, and A. Savin, “Prospects for measurement of $\sigma(pp \rightarrow Z) \cdot B(Z \rightarrow \tau^+\tau^-)$ with CMS in pp Collisions at $\sqrt{s} = 7$ TeV”, *CMS Note*
 2443 **2010/082** (2010).
- 2444 [34] CMS Collaboration, “Study of tau reconstruction algorithms using pp collisions data
 2445 collected at $\sqrt{s} = 7$ TeV”, *CMS PAS CMS-PAS-PFT-10-004* (2010).
- 2446 [35] G. P. S. M. Cacciari and G. Soyez, “The anti-kt jet clustering algorithm”, *JHEP*
 2447 **04** (2008) 063, arXiv:0802.1189.
- 2448 [36] CMS Collaboration, “Commissioning of the Particle–Flow reconstruction in
 2449 Minimum–Bias and Jet Events from pp Collisions at 7 TeV”, *CMS PAS PFT-10-*
 2450 **002** (2010).
- 2451 [37] S. M. T. Sjöstrand and P. Skands, “PYTHIA 6.4 Physics and Manual”, 2000.
- 2452 [38] S. Jadach, Z. Was, R. Decker *et al.*, “The Tau Decay Library Tauola: Version 2.4”,
 2453 *Comput. Phys. Commun.* **76** (1993) 361.
- 2454 [39] S. Agostinelli, J. Allison, K. Amako *et al.*, “G4—a simulation toolkit”, *Nuclear
 2455 Instruments and Methods in Physics Research Section A: Accelerators, Spec-
 2456 trometers, Detectors and Associated Equipment* **506** (2003), no. 3, 250 – 303.
 2457 doi:10.1016/S0168-9002(03)01368-8.
- 2458 [40] CDF Collaboration, “Search for MSSM Higgs decaying to τ pairs in $p\bar{p}$ collision at
 2459 $\sqrt{s} = 1.96$ TeV at CDF”, *Phys. Rev. Lett.* **96** (2006).
- 2460 [41] CMS Collaboration, “CMS technical design report, volume II: Physics performance”,
 2461 *J. Phys.* **G34** (2007) 995–1579. doi:10.1088/0954-3899/34/6/S01.
- 2462 [42] L. Bianchini, “Improved Collinear Approximation for VBF $H \rightarrow \tau\tau \rightarrow 3\nu + \ell + \tau_{had}$ ”,
 2463 *CMS Note* **2010/226** (2010).
- 2464 [43] B. K. Bullock, K. Hagiwara, and A. D. Martin, “Tau Polarization And Its Corre-
 2465 lations As A Probe Of New Physics”, *Nucl. Phys.* **B 395** (1993) 499.
- 2466 [44] CMS Collaboration, “Measurements of Inclusive W and Z Cross Sections in pp Col-
 2467 lisions at $\sqrt{s} = 7$ TeV”, *CMS PAS EWK-10-002* (2010).
- 2468 [45] CMS Collaboration, “MET Performance in Events Containing Electroweak Bosons
 2469 from pp Collisions at $\sqrt{s} = 7$ TeV”, *CMS PAS JME-10-005* (2010).
- 2470 [46] C. C. Almenar, “Search for the neutral MSSM Higgs bosons in the $\tau\tau$ decay channels
 2471 at CDF Run II”. PhD thesis, Departament de Física Atomica, Molecular i Nuclear
 2472 (Universitat de València and IFIC (CSIC - Universitat de València), 2008.
- 2473

- 2474 [47] L. Lusito and C. Veelken, “Estimation of Background contributions to Tau analyses
2475 via Template Fitting”, *CMS Note* **2010/088** (2010).
- 2476 [48] CMS Collaboration, “Performance of tau reconstruction algorithms in 2010 data col-
2477 lected with CMS”, *CMS PAS TAU-11-001* (2011).
- 2478 [49] D. Jang, “Search for MSSM Higgs decaying to τ pairs in $p\bar{p}$ collision at $\sqrt{s} =$
2479 1.96 TeV at CDF”, *Ph.D. Thesis, Rutgers University* (2006).
- 2480 [50] J. Conway, E. Friis, and C. Veelken, “Measurement of the $Z/\gamma^* \rightarrow \tau^+\tau^-$ Production
2481 Cross-section in the $\mu + \tau_{had}$ final state using the HPS+TaNC Tau id. algorithm”,
2482 *CMS Note* **2011/021** (2011).
- 2483 [51] J. Conway, E. Friis, M. Squires et al., “The Tau Neural Classifier algorithm: tau
2484 identification and decay mode reconstruction using neural networks”, *CMS Note*
2485 **2010/099** (2010).
- 2486 [52] T. Früboes and M. Zeise, “The TauAnalysis/MCEmbeddingTools Package”.
2487 <https://twiki.cern.ch/twiki/bin/view/CMS/SWGuideTauAnalysisMCEmbeddingTools>.
- 2488 [53] CMS Collaboration, “Measurement of the Inclusive $Z \rightarrow \tau\tau$ Cross Section in pp Col-
2489 lisions at $\sqrt{s} = 7$ TeV”, *to be published* (2011).
- 2490 [54] S. Bolognesi, M. A. Borgia, R. Castello et al., “Calibration of track momentum using
2491 dimuon resonances in CMS”, *CMS Note* **2010/059** (2010).
- 2492 [55] CMS Collaboration, “Jet Energy Corrections determination at $\sqrt{s} = 7$ TeV”, *CMS
2493 PAS JME-10-010* (2010).
- 2494 [56] G. Bauer et al., “Modeling of $W \rightarrow \ell\nu$ MET with Boson Recoil”, *CMS Note*
2495 **2010/332** (2010).
- 2496 [57] G. Cerati et al., “Search for MSSM neutral Higgs $\rightarrow \tau^+\tau^-$ Production using the
2497 TaNC Tau id. algorithm”, *CMS Note* **2010/460** (2010).
- 2498 [58] CMS Collaboration, “Absolute luminosity normalization”, *CMS Detector Perfor-
2499 mance Summary* **CMS-DPS-2011-002** (2008).
- 2500 [59] J. Alcaraz. <https://twiki.cern.ch/twiki/bin/view/CMS/SWGuideEWKUtilities>.
- 2501 [60] P. M. Nadolsky et al., “Implications of CTEQ global analysis for collider observ-
2502 ables”, *Phys. Rev.* **D 78** (2008) 013004, arXiv:0802.0007.
- 2503 [61] PDF4LHC Working Group. <http://www.hep.ucl.ac.uk/pdf4lhc/PDF4LHCrecos.pdf>.
- 2504 [62] R. C. G. D. Bourilkov and M. R. Whalley, “LHAPDF: PDF use from the Tevatron
2505 to the LHC”, arXiv:0605.0240.
- 2506 [63] LHC Higgs Cross Section Working Group Collaboration *arXiv:hep-ex/1101.0593*
2507 (2011).